

# **Exploring Metal Organic Layer Based Composites for Selective Electrocatalytic CO<sub>2</sub> Reduction to Formate**

**Von der Fakultät Chemie der Universität Stuttgart  
zur Erlangung der Würde eines Doktors der Naturwissenschaften (Dr. rer. nat.)  
genehmigte Abhandlung**

vorgelegt von

**Hang Liu**  
aus Qingdao, China

Hauptberichter: Prof. Dr.-Ing. Elias Klemm

Mitberichter: Jun.-Prof. Dr. Deven Estes

Prüfungsvorsitzender: Prof. Dr. rer. nat. Biprajit Sarkar

Tag der mündlichen Prüfung: 13.07.2022

Institut für Technische Chemie der Universität Stuttgart

2022







---

**Erklärung über die Eigenständigkeit der Dissertation**

Ich versichere, dass ich die vorliegende Arbeit mit dem Titel

„.....“

selbständig verfasst und keine anderen als die angegebenen Quellen und Hilfsmittel benutzt habe; aus fremden Quellen entnommene Passagen und Gedanken sind als solche kenntlich gemacht.

**Declaration of Authorship**

I hereby certify that the dissertation entitled

“.....”

is entirely my own work except where otherwise indicated. Passages and ideas from other sources have been clearly indicated.

Name/Name: \_\_\_\_\_

Unterschrift/Signed: \_\_\_\_\_

Datum/Date: \_\_\_\_\_



## Acknowledgements

First of all, I would like to gratitude the China scholarship council for the financial support during my Ph.D. study in Germany. I would also like to extend my deepest gratitude to Prof. Elias Klemm, who provided me with this opportunity to continue my Ph.D. study and supervised me in my whole research and thesis. I believe the knowledge and experience I learned during the past four years will accompany me my entire life.

Secondly, I want to express my gratitude to our institute and university (Institut für Technische Chemie, Universität Stuttgart). I would greatly thank Prof. Deven Estes and Prof. Biprajit Sarkar for joining my thesis review and defense. I am also grateful for the generous helps and ample discussions from group leaders in our institute (Prof. Elias Klemm, Prof. Deven Estes, Dr. Michael Dyballa, Prof. Yvonne Traa, and Prof. Michael Hunger) and all my colleagues. I also would like to thank my colleagues (Dorothea Häussermann and Maximilian Schmidt) in my office for the patient assistance and interactive discussions during my staying in Germany.

Thirdly, I would like to sincerely thank my collaborators and colleagues for their assistance in my publication. Special acknowledgements are for my collaborators (Dr. Hongguang Wang, Prof. Peter van Aken, Dr. Kathrin Küster; Prof. Ulrich Starke) from Max-Planck-Institut für Festkörperforschung. I also wish to thank all my colleagues for facilitating my work in characterizations and synthesis, especially Dr. Qian Song, Heike Fingerle, Armin Löwe, Paul Rößner, and Dorothea Häussermann. Many thanks for the helps from Prof. Deven Estes and Dr. Carlos Lobo in polishing my English in the publication.

Last but not least, I'm deeply indebted to the full support and dedication from my parents (Tonghe Liu & Baomei Yang). I am sorry for not being able to fulfill the responsibilities of a child in the past time. I would also like to extend my deepest gratitude to my wife (Caiyun Xu) for accompanying me through master's and doctoral studies, which was really a hard time for me. I would also like to thank all my friends, who brought much fun during my stay in Germany.



# Contents

Acknowledgements.....	I
Contents.....	III
Abstract .....	VII
Zusammenfassung.....	IX
<b>1   Introduction .....</b>	<b>1</b>
1.1 Research background and motivations .....	1
1.1.1 Energy and environmental dilemmas .....	1
1.1.2 Strategies of CO <sub>2</sub> utilization.....	2
1.1.3 Opportunity of electrochemical CO <sub>2</sub> reduction.....	5
1.2 Progress of electrochemical CO <sub>2</sub> reduction (ECR) reaction.....	6
1.2.1 Principle and mechanism of ECR reaction.....	6
1.2.2 Reaction apparatus and environments.....	13
1.2.3 Catalyst design and optimization .....	22
1.3 Metal-Organic Frameworks (MOFs) for ECR reaction.....	30
1.3.1 Introduction to MOFs.....	30
1.3.2 MOF-based materials for ECR reaction.....	36
1.3.3 Challenge of MOFs for ECR reactions .....	43
<b>2   Motivation .....</b>	<b>47</b>
<b>3   Experimental Methods.....</b>	<b>49</b>
3.1 Chemicals .....	49
3.2 Characterization methods .....	49
3.3 Experimental synthesis .....	52
3.3.1 2D-MOFs .....	52
3.3.2 Bismuth-based composites.....	58
3.3.3 MOL composites with other metal sites.....	60
3.4 Methods of electrochemical CO <sub>2</sub> reduction.....	62

---

3.4.1 H-type cell .....	62
3.4.2 Gas Diffusion Electrodes .....	64
3.4.3 Data evaluation .....	65
<b>4   Development of Metal-Organic Layers (MOLs).....</b>	<b>67</b>
4.1 2D-MOF based materials for ECR reaction.....	67
4.1.1 Synthesis methods for 2D-MOFs.....	67
4.1.2 Stability of the 2D-MOFs in electrocatalysis.....	69
4.1.3 Suitable 2D-MOFs for ECR reactions .....	70
4.2 Zr-TATB MOL.....	76
4.2.1 Synthesis .....	76
4.2.2 Morphology and structure.....	79
4.2.3 Stability.....	85
4.2.4 Summary of Zr-TATB MOL .....	86
4.3 Porphyrin-based MOL .....	87
4.3.1 Synthesis strategy .....	87
4.3.2 Synthesis and characterizations .....	88
4.3.3 Summary.....	89
4.4 MOL derived materials.....	89
4.4.1 Design strategy .....	90
4.4.2 Synthesis and characterizations .....	91
4.4.3 Summary.....	92
<b>5   Development of Bi<sub>2</sub>O<sub>3</sub>/MOL Composites .....</b>	<b>95</b>
5.1 Basic principles to achieve MOL composites.....	95
5.2 Synthesis and characterizations of Bi <sub>2</sub> O <sub>3</sub> /MOL composites.....	97
5.2.1 Ultrafine BiO <sub>x</sub> /MOL composites .....	97
5.2.2 Bi <sub>2</sub> O <sub>3</sub> nanowires/MOL composite .....	100
5.3 Exploring the formation of Bi <sub>2</sub> O <sub>3</sub> /MOL composites .....	105
5.4 Synthesis and characterization of reference catalysts .....	107
5.4.1 Bi <sub>2</sub> O <sub>3</sub> /UiO .....	107
5.4.2 Bi <sub>2</sub> O <sub>3</sub> /AB .....	110

---

5.5 Summary of Bi <sub>2</sub> O <sub>3</sub> /MOL composites .....	112
<b>6   Electrochemical CO<sub>2</sub> Reduction to Formate by Bi/MOL Composites</b>	<b>113</b>
6.1 Optimization of the H-type cell .....	113
6.1.1 Selection of the backing electrode .....	113
6.1.2 Effect of the conductive additive .....	115
6.2 Comparison of the ECR performance of Bi <sub>2</sub> O <sub>3</sub> based composites .....	117
6.2.1 ECR performance of Bi <sub>2</sub> O <sub>3</sub> -based composites .....	118
6.2.2 Product detections of the ECR reaction .....	119
6.2.3 ECR performance of Bi <sub>2</sub> O <sub>3</sub> -based composites with similar loadings.....	121
6.2.4 ECR performance of Bi <sub>2</sub> O <sub>3</sub> /MOL with different loadings .....	122
6.2.5 Comparison of the ECR performance of BiO <sub>x</sub> and Bi <sub>2</sub> O <sub>3</sub> .....	126
6.3 Stability test of Bi <sub>2</sub> O <sub>3</sub> /MOL.....	127
6.3.1 Performance stability .....	128
6.3.2 Structure stability .....	128
6.4 Reasons for the high performance of Bi <sub>2</sub> O <sub>3</sub> /MOL.....	130
6.5 ECR performance using gas diffusion electrode .....	132
6.6 MOL composites with different bismuth compounds .....	134
6.6.1 Synthesis strategy of MOL composites with different bismuth compounds .....	134
6.6.2 Characterization of BiOCl/MOL(7) and Bi/MOL(8) .....	135
6.6.3 Comparison of ECR performance of the Bi-based MOL composites .....	137
6.6.4 Other bismuth-based MOL composites.....	138
6.7 Summary of ECR performance of Bi/MOL .....	143
<b>7   Electrochemical CO<sub>2</sub> Reduction by Other Metal/MOL Composites .</b>	<b>145</b>
7.1 MOL composites with tin-based active sites .....	145
7.1.1 Synthesis strategy of MOL composites of different tin species .....	145
7.1.2 Characterizations and ECR performance of tin based MOL composites .....	146
7.2 MOL composites with indium-based active sites .....	152
7.2.1 Synthesis strategy of MOL composites with different Indium species .....	152
7.2.2 Characterizations and ECR performance of indium-based MOL composites.....	153
7.3 MOL composites with other active sites.....	158

## Contents

---

7.3.1 Antimony (Sb) .....	158
7.3.2 Copper (Cu) .....	159
7.3.3 Palladium (Pd) .....	161
7.4 Comparison of MOLs composites of different active metal sites.....	163
7.5 Summary of ECR performance of MOL composites.....	164
<b>8   Summary and Outlook.....</b>	<b>165</b>
<b>9   Reference .....</b>	<b>167</b>
<b>10   Appendix .....</b>	<b>179</b>
10.1 Lists of chemicals and characterization instrunctments.....	179
10.2 ICP results.....	183
10.3 XPS results.....	184
10.4 Summary and comparsion of ECR reactions by MOFs.....	185
10.5 Nomenclature.....	187
10.5.1 Symbols .....	187
10.5.2 Abbreviations.....	187

## Abstract

The massive consumption of fossil fuels has led to a significant accumulation of carbon dioxide in the atmosphere, and a CO<sub>2</sub> concentration unprecedented over the past 3 million years. Capturing CO<sub>2</sub> and further converting it into valuable chemicals or fuels could contribute to solving this dilemma. In recent years, electrochemical CO<sub>2</sub> reduction technology has attracted increasing attention in research and development due to the tremendous advances in green and renewable electricity. This doctoral thesis provides a comprehensive summary of the progress in electrochemical CO<sub>2</sub> reduction, especially for the formation of formic acid/formate, due to its advantages in meeting techno-economic requirements. Furthermore, in terms of the catalyst selection, we opt for metal-organic framework (MOF) based materials as our target catalysts, which have received much attention in recent years due to their unique structures.

Firstly, considering the poor conductivity of most MOFs, electrocatalysts based on 2D-MOFs (also known as metal-organic layers, MOLs) would be a promising option. Based on the synthesis strategy and stability requirement, we decided to synthesize MOLs with a 2D-*kgd* lattice, consisting of Zr<sub>6</sub>-oxo clusters as metal nodes and tridentate linkers. Zr<sub>6</sub>-oxo-based MOFs, such as UiO-66, are usually found to exhibit good chemical stability. Furthermore, the addition of acetic acid as a capping agent can inhibit the stacking of the MOL layers and enable the direct synthesis of free-standing MOLs. As a result, Zr-TATB MOL was successfully constructed by a facile solvothermal process, using for the first time TATB (4,4',4''-s-triazine-2,4,6-triyl-tribenzoate) as a linker. Furthermore, multiple characterizations verified and validated its exact structure, which was in agreement with the expected MOL structure.

Secondly, Zr-TATB MOL with multiple anchoring sites on its surface shows a great potential of immobilizing different catalytic sites by post-modification strategies to form MOL composites. As a representative, uniformly dispersed Bi<sub>2</sub>O<sub>3</sub> nanowires were grown on the Zr-TATB MOL, denoted as Bi<sub>2</sub>O<sub>3</sub>/MOL. The structure of Bi<sub>2</sub>O<sub>3</sub>/MOL was exactly determined by advanced electron microscopy techniques. The post-modification process of Zr-TATB MOL was followed by ex-situ electron microscopy in order to determine the growth process from atomic level dispersion to Bi nanowires. The monolayer morphology of MOL facilitates the characterization of the structures, which provides a good basis for the rational design of MOF composites.

Thirdly, electrocatalytic CO<sub>2</sub> reduction (ECR) tests were conducted in a conventional H-type cell using carbon paper as a backing electrode. Bi<sub>2</sub>O<sub>3</sub>/MOL exhibited excellent ECR performance

with Faradaic efficiencies of over 85% to formate at a wide potential window ( $\sim 0.4$  V), and the best partial current density reached an impressive value of  $2.3 \text{ A}\cdot\text{mg}_{\text{Bi}}^{-1}$ . This performance far exceeded that of  $\text{Bi}_2\text{O}_3/\text{UiO}$  (a typical 3D-MOF-based composite) and  $\text{Bi}_2\text{O}_3/\text{AB}$  (a conductive carbon based composite), highlighting the superiority of 2D-MOF composites. The  $\text{Bi}_2\text{O}_3/\text{MOL}$  also exhibited good structural stability, verified by multiple characterizations. In addition, further ECR tests were conducted using gas diffusion electrodes (GDEs), achieving industrially relevant current densities towards formate of over  $300 \text{ mA}\cdot\text{cm}^{-2}$ . Among all MOFs reported for ECR reactions,  $\text{Bi}_2\text{O}_3/\text{MOL}$  exhibited excellent formate generation activity, whether using carbon paper in H-cells or GDEs.

Finally, we verified the universality of the post-modification strategy for the design of MOL-based composites. We were able to obtain a series of MOL composites bearing different metal species by tuning the reaction conditions, all of which exhibited good ECR activity. This research demonstrates the great potential of MOL-based composites as electrocatalysts and encourages further exploration of highly tunable MOLs for catalytic studies.

## Zusammenfassung

Der hohe Verbrauch fossiler Brennstoffe hat zu einer erheblichen Akkumulation von Kohlendioxid in der Atmosphäre geführt, wobei die CO<sub>2</sub>-Konzentration auf den höchsten Wert der letzten 3 Millionen Jahren angestiegen ist. Die Abscheidung von CO<sub>2</sub> und seine weitere Umwandlung in andere Chemikalien oder Kraftstoffe könnte zur Lösung dieses Problems beitragen. In den letzten Jahren hat das Verfahren der elektrochemischen CO<sub>2</sub>-Reduktion aufgrund der enormen Fortschritte bei grüner und erneuerbarer Elektrizität zunehmende Aufmerksamkeit in Forschung und Entwicklung auf sich gezogen. Die vorliegende Dissertation gibt einen umfassenden Überblick über die Fortschritte bei der elektrochemischen CO<sub>2</sub>-Reduktion, insbesondere bei der Bildung von Ameisensäure/Formiat, die aufgrund ihrer Vorteile für die Erfüllung der technisch-wirtschaftlichen Anforderungen von Vorteil ist. Bei der Auswahl des Katalysators haben wir uns für metallorganische Gerüstmaterialien (MOFs) entschieden, die in den letzten Jahren aufgrund ihrer einzigartigen Strukturen viel Aufmerksamkeit erhalten haben.

In Anbetracht der schlechten Leitfähigkeit der meisten MOFs wären Elektrokatalysatoren auf der Basis von 2D-MOFs (auch bekannt als metallorganische Schichten, MOLs) eine vielversprechende Option. Aufgrund der Synthesestrategie und der Stabilitätsanforderungen haben wir uns für die Synthese von MOLs mit einem 2D-*kgd*-Gitter entschieden, das aus Zr<sub>6</sub>-oxo-Clustern als Metallzentren und tridentale Linkern besteht. MOFs auf Zr<sub>6</sub>-Oxo-Basis, wie z. B. UiO-66, zeichnen sich in der Regel durch eine gute chemische Stabilität aus. Darüber hinaus kann die Zugabe von Essigsäure als Stabilisator die Stapelung der MOL-Schichten hemmen und die direkte Synthese von freistehenden MOLs ermöglichen. Infolgedessen wurde Zr-TATB MOL erfolgreich durch ein einfaches solvothermisches Verfahren hergestellt, wobei zum ersten Mal TATB (4,4',4''-s-triazin-2,4,6-triyl-tribenzoat) als Linker verwendet wurde. Darüber hinaus wurde seine genaue Struktur, die mit der erwarteten MOL-Struktur übereinstimmt, durch mehrere Charakterisierungen verifiziert und validiert.

Zweitens zeigt Zr-TATB MOL mit mehreren Verankerungsstellen auf seiner Oberfläche ein großes Potenzial für die Immobilisierung verschiedener Katalysatoren durch Nachbehandlungen zur Bildung von MOL-Kompositen. Stellvertretend dafür wurden homogen verteilte Bi<sub>2</sub>O<sub>3</sub>-Nanodrähte auf dem Zr-TATB MOL, bezeichnet als Bi<sub>2</sub>O<sub>3</sub>/MOL, synthetisiert. Die Struktur von Bi<sub>2</sub>O<sub>3</sub>/MOL wurde mit Hilfe modernster elektronenmikroskopischer Verfahren genau bestimmt. Der Nachbehandlungsprozess von Zr-TATB MOL wurde durch Ex-situ-Elektronenmikroskopie

verfolgt, um den Wachstumsprozess von der atomaren Dispersion bis zu den Bi-Nanodrähten zu bestimmen. Die Schichtmorphologie von MOLs ermöglicht die Charakterisierung der Strukturen, was eine solide Grundlage für das Entwickeln von MOL-Kompositen darstellt.

Drittens wurden elektrokatalytische CO<sub>2</sub>-Reduktionstests (ECR) in einer konventionellen H-Zelle mit Kohlepapier als Trägerelektrode durchgeführt. Bi<sub>2</sub>O<sub>3</sub>/MOL zeigte eine ausgezeichnete ECR-Leistung mit einer Faraday-Effizienz von über 85 % für Formiat in einem breiten Potenzialfenster (~0,4 V), und die beste Teilstromdichte erreichte einen beeindruckenden Wert von 2,3 A·mg<sub>Bi</sub><sup>-1</sup>. Diese Leistung übertraf bei weitem die von Bi<sub>2</sub>O<sub>3</sub>/UiO (einem typischen 3D-MOF-basierten Kompositen) und Bi<sub>2</sub>O<sub>3</sub>/AB (einem leitfähigen Kompositen auf Kohlenstoffbasis), was das Potential der 2D-MOF-Verbundwerkstoffe unterstreicht. Der Bi<sub>2</sub>O<sub>3</sub>/MOL zeigte ebenfalls eine gute Leistung und strukturelle Stabilität, was durch mehrere Charakterisierungen bestätigt wurde. Darüber hinaus wurden weitere ECR-Tests mit Gasdiffusionselektroden (GDEs) durchgeführt, wobei industriell relevante Stromdichten von über 300 mA·cm<sup>-2</sup> zu Formiat erreicht wurden. Unter allen MOFs, die für ECR-Reaktionen bekannt sind, zeigte Bi<sub>2</sub>O<sub>3</sub>/MOL eine ausgezeichnete Aktivität bei der Formiaterzeugung, sowohl mit Kohlepapier in der H-Zelle als auch mit Gasdiffusionselektroden (GDEs).

Abschließend haben wir die allgemeine Gültigkeit der Nachbehandlungsstrategie für das Design von MOL-basierten Kompositen überprüft. Durch Abstimmung der Reaktionsbedingungen konnten wir eine Reihe von MOL-Kompositen mit verschiedenen Metallspezies herstellen, die alle eine gute ECR-Aktivität aufwiesen. Diese Forschungsarbeit zeigt das große Potenzial von MOL-Kompositen als Elektrokatalysatoren und ermutigt zur weiteren Forschung an maßgeschneiderten MOLs für katalytische Untersuchungen.

# 1 | Introduction

## 1.1 Research background and motivations

### 1.1.1 Energy and environmental dilemmas

Energy consumption is widely considered to be highly correlated with social and economic development, as indicated by the increasing energy needs (**Figure 1.1**).<sup>[1-3]</sup> Among these energy sources, fossil fuels, mainly hydrocarbon-based materials, such as coal, petroleum, and natural gas, still play dominant roles in the energy market, covering 79.3 % of the worldwide energy consumption in 2019 (**Figure 1.1**).<sup>[1,2]</sup> However, the accessible fossil fuel resources with relatively low mining costs are limited and could be depleted in the near future (**Figure 1.1**).<sup>[1,2]</sup> As for such a dilemma, exploiting alternative and renewable energy sources is a widely recognized solution, of which tremendous progress has been witnessed in recent years.<sup>[3]</sup>

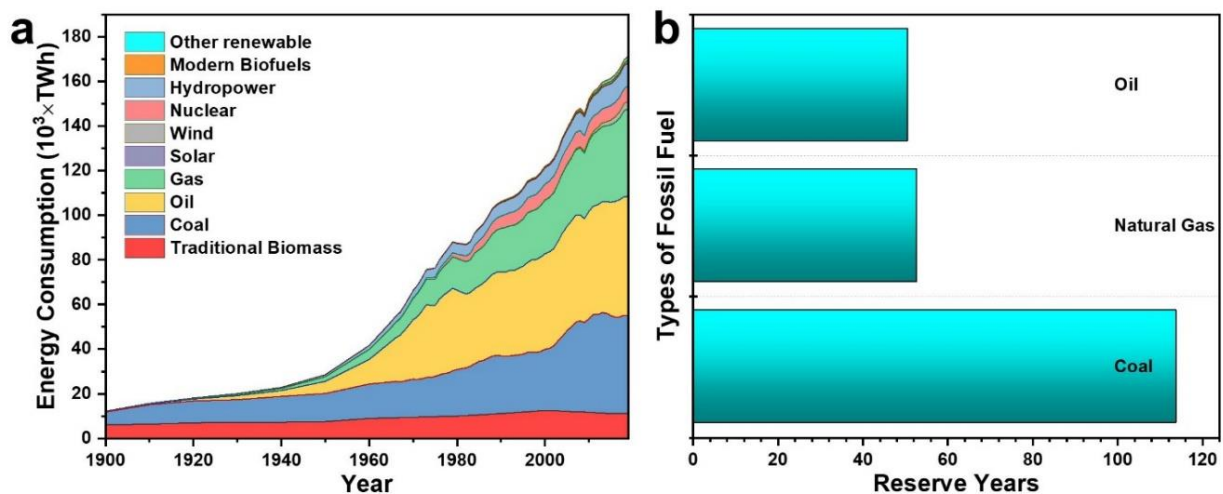


**Figure 1.1** (a) Global primary energy consumption by sources. (b) Years of fossil fuel reserve left. The assumption was based on the known reserves and annual production levels in 2015.<sup>[1,2]</sup>

Meanwhile, environmental issues also come along with the energy shortage globally. Combustion is a standard or intermediate step to convert fossil fuel into secondary energy carriers, such as heat or electricity, resulting in a significant release of  $\text{CO}_2$  and other pollution (**Figure 1.2a**). Before the industrial age, nature was able to close carbon cycle, mainly through green plants' photosynthesis. However, along with the fast development of society, the massive combustion of fossil fuels led to the rapid accumulation of atmospheric  $\text{CO}_2$ , reaching 416.71 ppm by Dec. 2021, breaking the natural carbon cycle.<sup>[4]</sup> Led by the  $\text{CO}_2$  emission (74.4 % contribution), anthropogenic

greenhouse gas (GHG) emissions have rapidly increased since the pre-industrial age, leading to the severe greenhouse effect.<sup>[3,5,6]</sup> Till now, the global temperature has risen by 1.2 °C, compared to the pre-industrial era (**Figure 1.2b**).<sup>[7]</sup> Abnormal global warming is the main form of climate change, leading to sea level rise, land desertification, species extinction, more extreme weather, and other severe consequences, demonstrated by the Intergovernmental Panel on Climate Change (IPCC).<sup>[8]</sup>

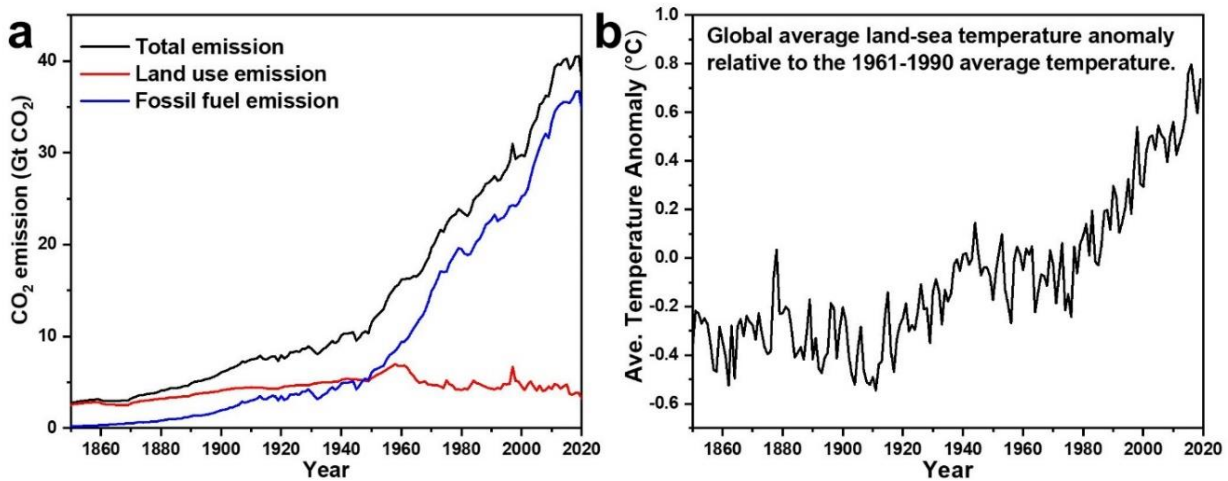


**Figure 1.2** (a) Global CO<sub>2</sub> emissions from fossil fuel and land use.<sup>[6]</sup> (b) Global average land-sea temperature change, anomaly relative to the 1961-1990 average temperature.<sup>[7]</sup>

## 1.1.2 Strategies of CO<sub>2</sub> utilization

### 1.1.2.1 Carbon capture, utilization, and storage (CCUS)

Carbon capture, utilization, and storage (**Figure 1.3**) are a series of artificial and effective methods to alleviate the greenhouse effect.<sup>[9]</sup> It starts with the CO<sub>2</sub> capture from enormous emission sources, considering that 78.4% of GHG emissions are from energy generation and industrial processes.<sup>[3]</sup> Direct capture from the atmosphere is also possible, even though the high cost. After capturing, the CO<sub>2</sub> can be compressed, transported and stored underground. By 2021, the installed capture capacity has reached 40 million tons of CO<sub>2</sub>.<sup>[3]</sup> Even though it was still a little far from the aim of net-zero CO<sub>2</sub> emission, it is still somehow encouraging. There will be more and more CCUS facilities worldwide in the future. By the International Energy Agency Sustainable Development Scenario (IEA-SDS), CCUS could contribute by 15% to reducing global CO<sub>2</sub> emissions to achieve net-zero emissions in 2070.<sup>[3]</sup> Considering the high cost of CCUS from business, it would be economically favorable to treat CO<sub>2</sub> as a raw material for valuable chemicals.

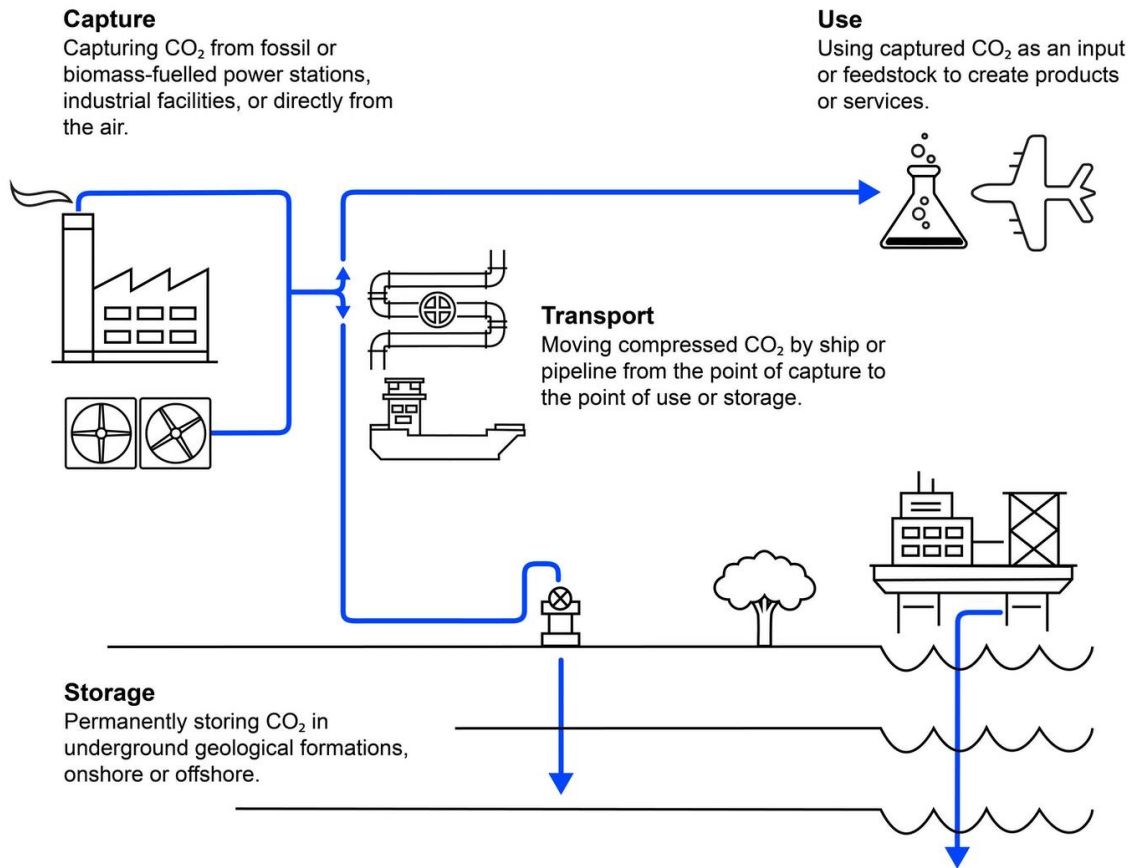


**Figure 1.3** Scheme of the CCUS procedures.<sup>[3]</sup>

### 1.1.2.2 Techniques for CO<sub>2</sub> utilization

Currently, 230 Mt CO<sub>2</sub> are utilized globally every year, mainly by fertilizer production (urea) and oil recovery.<sup>[3]</sup> In a perspective article from Cameron and co-workers in 2019, they summarized and compared conventional pathways (No.1-5) and non-conventional pathways (No. 6-10), totally ten ways of CO<sub>2</sub> utilization (**Figure 1.4**).<sup>[10]</sup> They also classified the pathways as “cycling”, “closed”, and “open” utilization pathways. The cycling pathways indicate a short-term CO<sub>2</sub> storage, such as converting CO<sub>2</sub> into fuels replacing massive combustion of fossil fuel, thus bringing the climate benefit. Closed pathways allow a nearly permanent CO<sub>2</sub> storage in the principle. The open pathways are mainly based on the biological system with a high risk of releasing CO<sub>2</sub> back into the atmosphere.

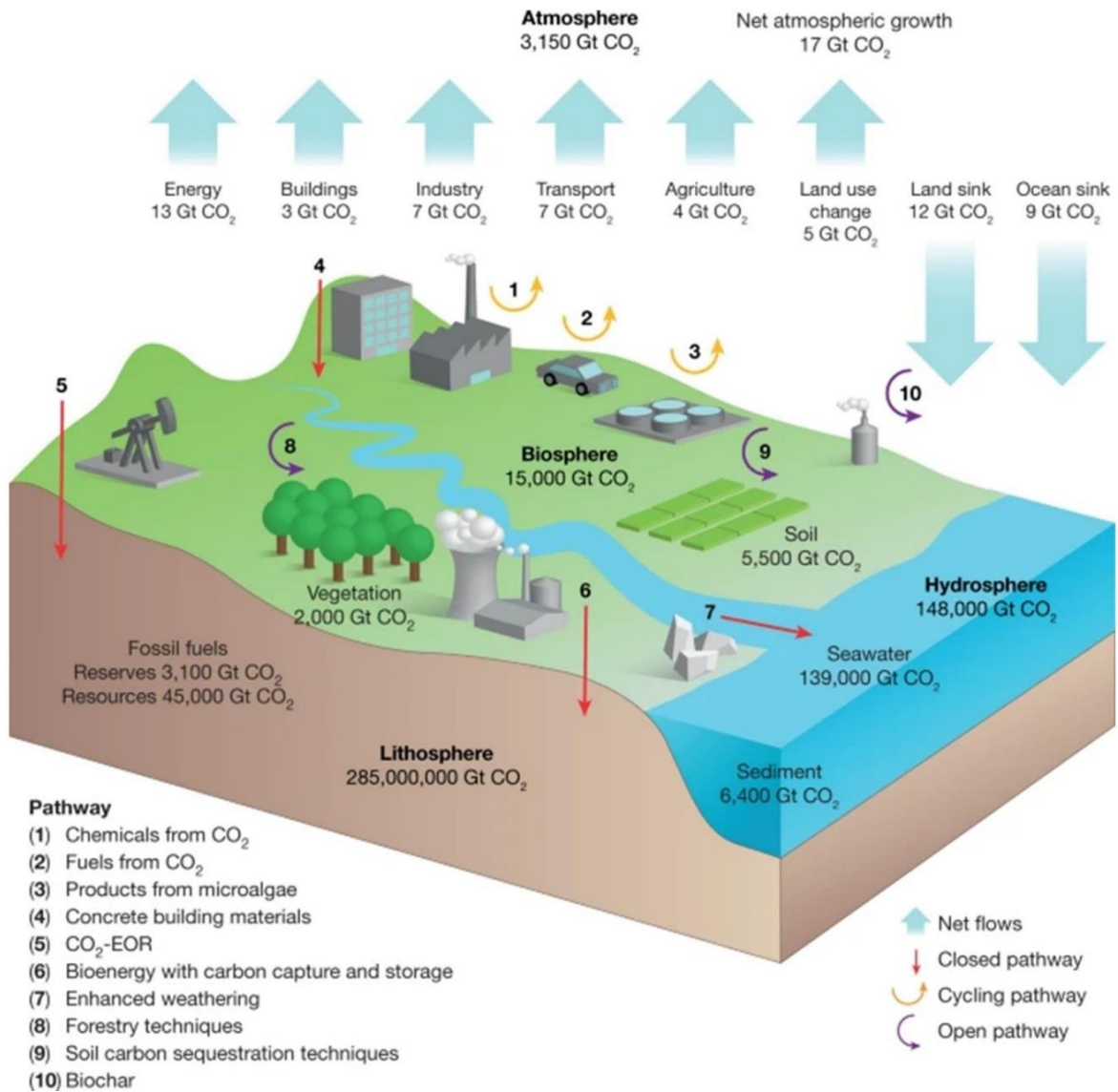


**Figure 1.4** Scheme of the pathways of CO<sub>2</sub> utilization.<sup>[10]</sup> EOR: Enhanced oil recovery.

The technical and economic barriers were discussed and evaluated by the perspective article.<sup>[10]</sup> The cycling pathways (No. 1,2,3) should be more competitive than the existing technologies and other alternatives before being applied, but they are still far from economically favorable yet. Promotions of cycling pathways can be achieved by reducing the costs of CO<sub>2</sub> capture and optimizing the reaction systems of CO<sub>2</sub> conversions.<sup>[11]</sup> The open pathways are theoretically profitable and technically feasible, but may risk high management costs. Except for CO<sub>2</sub> enhanced oil recovery (CO<sub>2</sub>-EOR), the closed pathways are mainly at low technology readiness levels (TRL). CO<sub>2</sub>-EOR could provide effective CO<sub>2</sub> removal but may not generate a net climate benefit. companies prefer to use as little CO<sub>2</sub> as possible to produce more oil. At the same time, the combustion of this oil will in turn release more CO<sub>2</sub> into the atmosphere. That is why CO<sub>2</sub>-EOR may not bring a net climate benefit.

### 1.1.3 Opportunity of electrochemical CO<sub>2</sub> reduction

The rapid development of renewable energy (solar, wind, etc.) is reducing our dependence on fossil fuels.<sup>[12-14]</sup> Thanks to the increasing availability of renewable electricity, the electrochemical process of CO<sub>2</sub> utilization is gaining more and more attention, referred to the “Fuel from CO<sub>2</sub>” in **Figure 1.4**. In the perspective article of Joshua in 2020, different electrochemical methods of CO<sub>2</sub> utilization are discussed and evaluated.<sup>[15]</sup> By comparison, the indirect pathway (H<sub>2</sub> production by electricity combined with CO<sub>2</sub> hydrogenation) presents the technically most feasible pathway yet, considering the highest yields and technology readiness levels (TRLs). However, the challenge posed by equilibrium conversion limitations could restrict its priority in the longer future. By comparison, the direct electrochemical pathway is estimated to be more promising in the longer run, for its potential to be coupled with the CO<sub>2</sub> capture and purification process.

Species	Rate of Formation <sup>a</sup>	Selectivity <sup>b</sup>	Energy Efficiency <sup>c</sup>	Current TRL <sup>d</sup>
<b>Carbon Monoxide</b>	High	High	High	High
<b>Ethylene</b>	High	Medium	Low	Low
<b>Formate</b>	Medium	High	Medium	Low
<b>Methane</b>	High	High	Medium	High
<b>Acetate</b>	Low	High	Medium	Low
<b>Methanol</b>	High	High	High	High

<sup>a</sup> High: >200 mA/cm<sup>2</sup> (or commercial TC), Medium: 200 >/>100 mA/cm<sup>2</sup>, Low: <100 mA/m<sup>2</sup>

<sup>b</sup> High: >80%, Medium 80% > FE > 60%, Low: < 60%

<sup>c</sup> High: >60%, Medium 60% > EE > 40%, Low: < 40%

<sup>d</sup> High: Operated at TRL > 6, Medium: Operated TRL 4-6, Low: Operated TRL 1-3

**Figure 1.5** Evaluation of product's ease of formation by direct and indirect electrochemical pathways.<sup>[15]</sup> TRL: technology readiness level.

Techno-economic analyses were estimated depending on the products.<sup>[15-18]</sup> **Figure 1.5** lists the product's ease of formation by the electrochemical pathways.<sup>[15]</sup> The order of the ease of formation: CO~CH<sub>3</sub>OH > CH<sub>4</sub> > Formate > Ethylene > Acetate. The good feasibility of methane and methanol is based more on the indirect pathway achieved by the CO<sub>2</sub> hydrogenation. Carbon monoxide (CO), formate, and ethylene are generated mainly by direct electrolysis. The very

positive evaluation of CO origins from the CO<sub>2</sub> direct electrolysis whether at room temperature or higher temperatures (> 400 °C). Compared with the product's market prices normalized to one mol electrons, formic acid/formate could be an attractive choice for the direct electrochemical product from CO<sub>2</sub> (Figure 1.6). At least, the recent work at our institute led to ultra-high current densities of more than 1 A·cm<sup>-2</sup>.<sup>[19-21]</sup>

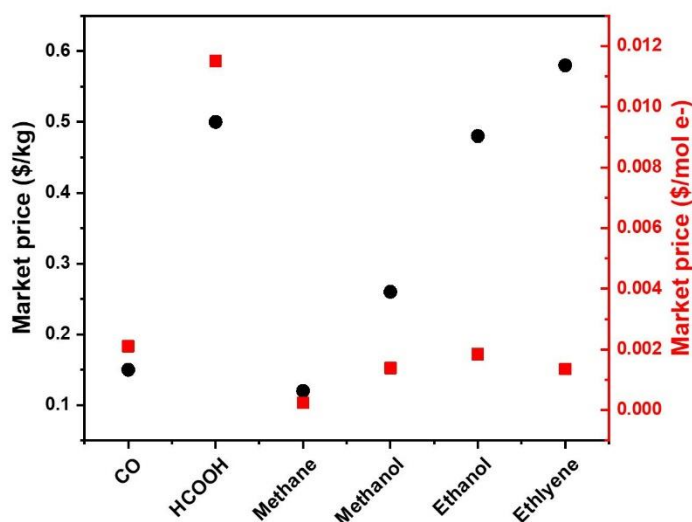


Figure 1.6 Market price from the US in 2019.<sup>[18]</sup>

## 1.2 Progress of electrochemical CO<sub>2</sub> reduction (ECR) reaction

As discussed in the last chapter, electrochemical CO<sub>2</sub> reduction (ECR), even though not economically profitable yet, is a promising method to achieve effective CO<sub>2</sub> removal and utilization, especially when considering the tremendous progress in CO<sub>2</sub> capture and renewable electricity. In this chapter, the focus will be placed on a brief summary of the principles and achievements of the ECR reaction at room temperature. The high-temperature CO<sub>2</sub> electrolysis is not included, because it's limited to the generation of CO.

### 1.2.1 Principle and mechanism of ECR reaction

Electrocatalytic CO<sub>2</sub> reduction (ECR) reaction is also commonly abbreviated as electrocatalytic CO<sub>2</sub>RR (CO<sub>2</sub> reduction reaction). Generally, the basic scheme of the ECR is composed of a cathode, an anode, a membrane, electrolytes, and an electrochemical workstation (Figure 1.7). Reduction half-reaction (ECR reaction) and oxidation half-reaction (mostly water oxidation) proceed on the cathode and anode, respectively. Considering the products from the ECR reaction could undergo re-oxidation at the anode side, the two electrodes are generally separated by the membrane (preferably, cation exchange membrane). The academic research in the lab generally

would adopt electrochemical workstations as a power supply, which also could be replaced by renewable electricity in industrial-relevant applications. As for the academic research, attention is mainly focused on the performance of the reduction half-reaction, which requires a reference electrode to detect and control the potential of the cathode (three-electrode system). Therefore, the general principle of ECR reaction will be discussed in this chapter.

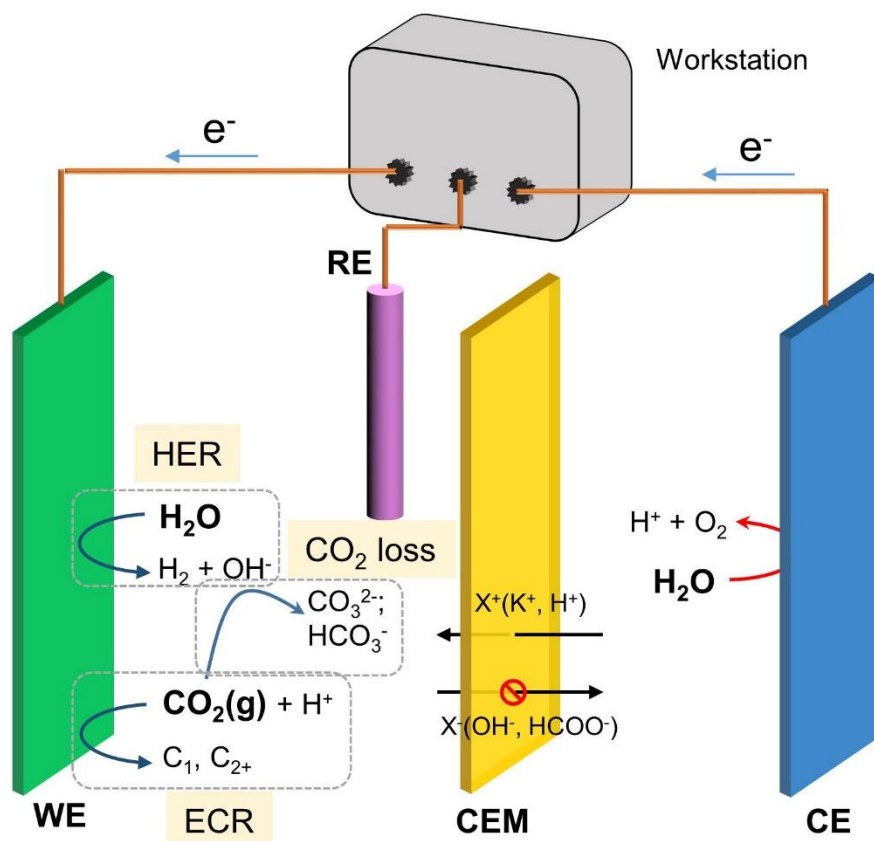


**Figure 1.7** Scheme of the ECR reaction system. WE: working electrode; CE: counter electrode; RE: reference electrode; CEM: cation exchange membrane.



**Figure 1.8** Scheme of the important progresses in ECR reaction.<sup>[22-33]</sup>

The successful conduction of the electrocatalytic CO<sub>2</sub> reduction was first reported in 1967 by Sawyer, who used gold and mercury electrodes as working electrodes in organic solvent (DMSO).<sup>[22]</sup> Hori achieved the more promising and pioneering works of ECR reaction in the aqueous electrolyte in 1985.<sup>[23]</sup> By systematic researches using different metal electrodes, a generic

link between metal species and product selectivity of ECR reaction was determined.<sup>[24,25]</sup> The following research mainly focused on the evaluation of the ECR performance by optimizing active sites (from bulk catalyst to nano/atomic level catalyst) and reaction engineering (from H-type cell to flow cell) (Figure 1.8).<sup>[22-33]</sup>

### 1.2.1.1 Reaction pathway of ECR reactions

Carbon dioxide is a linear and centrosymmetric molecule with  $D_{\infty h}$  symmetry. By valence-bond theory, a  $\text{CO}_2$  molecule possesses two  $sp$ -hybridized  $\sigma$  bonds and two delocalized  $\pi_3^4$  bonds. The  $\text{C}=\text{O}$  bonds are shorter (116 pm) and more robust than regular carbonyl groups (generally, 120 pm). The energy required to dissociate the  $\text{C}=\text{O}$  bond in  $\text{CO}_2$  ( $\sim 800 \text{ kJ}\cdot\text{mol}^{-1}$ ) is also higher than that of other carbonyl groups. As a result,  $\text{CO}_2$  is stable and relatively inert, with a large energy gap of 11.5 eV between the highest occupied molecular orbital (HOMO) and the lowest unoccupied molecular orbital (LUMO).<sup>[34]</sup> The stability of the  $\text{CO}_2$  structure determines that it is not easily activated to participate in chemical reactions.

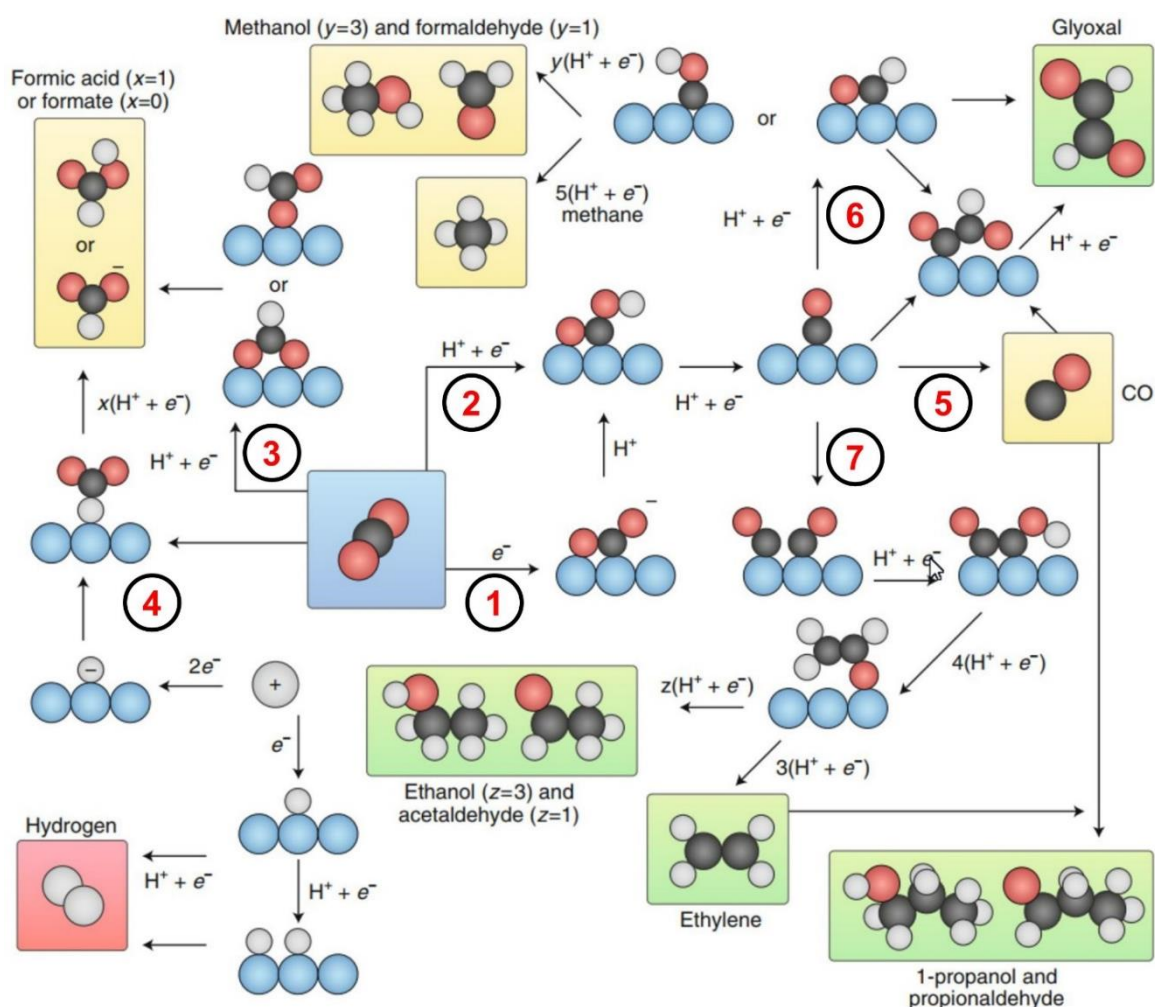


**Figure 1.9** Scheme of the reaction pathways of the ECR reaction to different products. The square of different color backgrounds:  $\text{CO}_2$  (blue),  $\text{C}_1$  product (yellow),  $\text{C}_{2+}$  product (green), and  $\text{H}_2$  (red). Spheres of different colors: catalytic sites (blue), H (white), C (black), and O (red).<sup>[35]</sup>

The general ECR reaction pathways are demonstrated in **Figure 1.9**.<sup>[35-39]</sup> The first step of the ECR reaction is the chemical absorption and activation of the CO<sub>2</sub> molecule. Considering the very stable molecule of CO<sub>2</sub>, direct electron transfer to CO<sub>2</sub> forming \*CO<sub>2</sub><sup>-</sup> intermediate (step 1) is rather difficult, as indicated by the very negative redox potential (-1.9 V vs. SHE) (**Table 1.1**).<sup>[40]</sup> The participation of a suitable electrocatalyst could significantly decrease the potential needed for CO<sub>2</sub> activation through a chemical bonding between the catalyst and CO<sub>2</sub>. Besides, proton-coupled electron transfer (PCET) processes (steps 2&3) are also considered to be an effective way to achieve CO<sub>2</sub> activation. Generally, the carbon bonded \*COOH and oxygen bonded \*OCOH are recognized to be the intermediate for CO and formic acid generation, respectively. Further reduction of these intermediates by PCET can lead to CO and formic acid formation. Similar to the thermalcatalytic CO<sub>2</sub> hydrogenation mechanism, the critical step can also be the proton reduction on the surface, forming a metal hydride (step 4). The formation of formic acid can also proceed by the CO<sub>2</sub> insertion into a metal hydride, and further reduction with a proton. The desorption of \*CO can lead to CO as a final product (step 5). However, for the Cu-based catalyst, the strong binding with \*CO can allow further reductions, forming aldehyde, methanol, and methane (step 6). Neighboring \*CO or \*CHO can be coupled to form carbon-carbon bonds, which are the key steps towards multiple carbon products (step 7), such as ethylene (C<sub>2</sub>H<sub>4</sub>), ethanol (C<sub>2</sub>H<sub>5</sub>OH), ethane (C<sub>2</sub>H<sub>6</sub>), and n-propanol (C<sub>3</sub>H<sub>7</sub>OH).

**Table 1.1** Standard redox potentials of electrochemical CO<sub>2</sub> reduction reactions towards different products.

Possible half-reaction during ECR	Standard potential (V vs. SHE) at pH=7
$2\text{H}^+ + 2\text{e}^- \rightarrow \text{H}_2$	-0.42
$\text{CO}_2 + \text{e}^- \rightarrow \text{CO}_2^-$	-1.90
$\text{CO}_2 + 2\text{H}^+ + 2\text{e}^- \rightarrow \text{HCOOH}$	-0.61
$\text{CO}_2 + 2\text{H}^+ + 2\text{e}^- \rightarrow \text{CO} + \text{H}_2\text{O}$	-0.53
$\text{CO}_2 + 6\text{H}^+ + 6\text{e}^- \rightarrow \text{CH}_3\text{OH} + \text{H}_2\text{O}$	-0.38
$\text{CO}_2 + 8\text{H}^+ + 8\text{e}^- \rightarrow \text{CH}_4 + 2\text{H}_2\text{O}$	-0.24
$2\text{CO}_2 + 12\text{H}^+ + 12\text{e}^- \rightarrow \text{CH}_2\text{CH}_2 + 4\text{H}_2\text{O}$	0.06
$2\text{CO}_2 + 12\text{H}^+ + 12\text{e}^- \rightarrow \text{CH}_3\text{CH}_2\text{OH} + 3\text{H}_2\text{O}$	0.08

### 1.2.1.2 Key performance indicators for the evaluation of the ECR reactions

It is necessary to introduce some key performance indicators for the performance evaluation.<sup>[36,41]</sup>

## (1) Onset potential

Generally, the onset potential is the minimal potential (most positive for cathode) required to produce certain products. This value is generally more negative than the equilibrium redox potential, and the difference between the two is defined as the overpotential. Lower overpotentials generally indicate a lower activation barrier at the catalytic sites, which is an important parameter for mechanistic investigations. Precise detection methods are required to approach the real value as much as possible, considering the current density at this point would be rather low. It might also be meaningful to indicate the corresponding applied potential to reach an industrially relevant current density. **Figure 1.10** depicts the correlations of the maximum FEs in ECR reactions towards different products and corresponding overpotentials.<sup>[42]</sup>

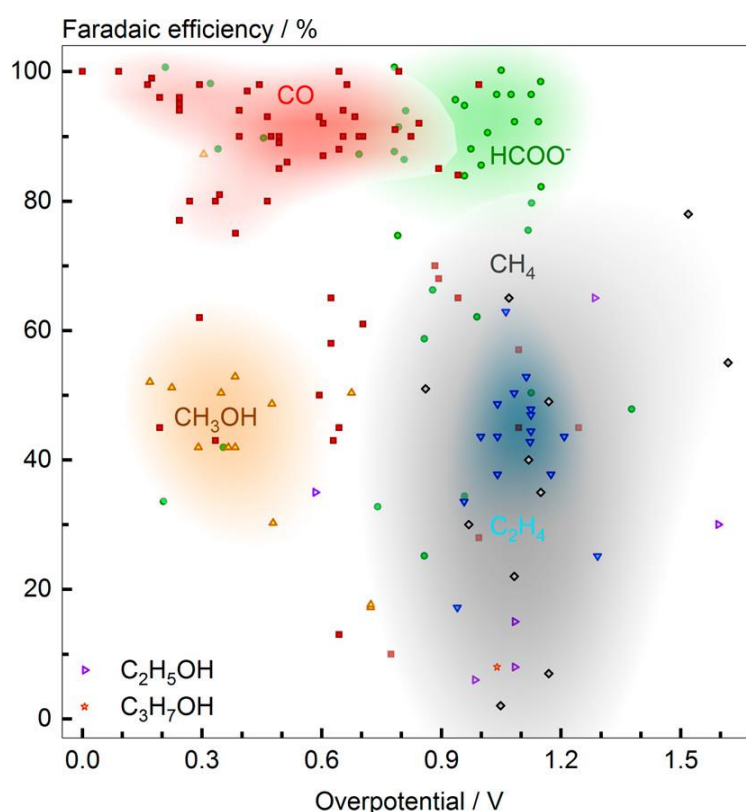


**Figure 1.10** Performance maps of the maximum Faradaic efficiencies in ECR reaction towards different products and corresponding overpotentials.<sup>[42]</sup>

## (2) Faradaic efficiency (FE)

The FE is defined as the percentage of the electrons consumed for specific products at a certain applied potential. For electrocatalysis, the FE is a direct indicator of product selectivity. As the main side reaction, proton reduction (HER, hydrogen evolution reaction) will gradually dominate as the applied potential becomes more negative.

## (3) Current density (j)

Generally, the current density is the current response normalized to the surface area of the

working electrode. In principle, the surface area can be the electrochemical surface area (ECSA), the precise surface area or the geometrical area of the electrode. The geometrical area of the working electrode is the most common and most easily controlled when operating the ECR experiments. The ECSA can be estimated by measuring double-layer capacitance (DLC).<sup>[36]</sup> The calculation is based on the approximation that the double-layer capacitance is proportional to the ECSA. A standard sample (generally, a metal foil) with a defined active area is used to determine the surface-specific DLC as a reference. This method is not suitable for complex systems, in which multiple components can contribute to the value of DLC. The most precise measurement can be achieved by the Pb underpotential deposition method.<sup>[43]</sup>

When comparing the current at different catalyst loadings, the current can also be normalized to the mass of the catalyst or the mass of the active sites (directly related to turnover frequency (TOF)). Partial current density indicates the current density of certain products, which is widely adopted to represent the yield rate of a certain product.

#### (4) Energy efficiency (EE)

Energy efficiency is defined as the percentage of energy transferred towards certain products. As for a half-reaction, the EE depends on the overpotential and the FE at certain potentials. As the current densities in industrial applications are high, the internal Ohmic resistances will significantly contribute to the cell voltage and thus decrease the energy efficiency, which requires the optimization of the cell design.

#### (5) Tafel slope

The Tafel plot is a graph of the overpotential versus the logarithm of the partial current density, according to the Tafel equation.<sup>[44-46]</sup> The Tafel slope can be calculated by linear fitting of data at low current densities. The Tafel slope is an indicator of the reaction pathway and the rate-determining step. For the slope of 118 mV per decade, the rate-determining step is the single electron transfer to generate the  $\text{CO}_2^{\bullet-}$  intermediate. For a slope of 59 mV per decade, the reaction pathway includes a fast electron transfer to form  $\text{CO}_2^{\bullet-}$  and a subsequent rate-determining chemical reaction (probably an  $\text{H}^+$  transfer step). The current densities should be based on the ECSA, not geometrical area, making it more challenging to measure in composite systems.

### 1.2.1.3 Primary judgments of the product selectivity

Determining the exact reaction pathways at specific active sites needs experimental and theoretical methods. However, empirical rules can be established based on former publications. The product selectivity is largely determined by the type of the catalytic sites. The pioneering research by Hori investigated the product distributions for diverse metal electrodes (**Figure**

**1.11a).**<sup>[24,25,47]</sup> These elements can be classified into four groups, based on the selectivity of ECR reaction. Firstly, most first-row transition metals (Mn, Fe Co, etc.) and part of the noble metals (Pd, Pt, etc.) catalyze only HER, which can be ascribed to the H<sub>2</sub>-group. Secondly, part of the noble metals and ds-block transition metals (groups 11&12), such as Zn, Ag, and Au, generally catalyze CO<sub>2</sub> into CO, which is the CO-group. Thirdly, most p-block metals exhibit selectivity mainly to formic acid/formate, which form the HCOOH-group. Finally, Cu-based catalysts exhibit unprecedented activity towards multiple-carbon products, which form the C<sub>2+</sub>-group. This empirical rule can be extended to metal-supported catalysts to find suitable catalytic sites, as summarized in **Figure 1.11b**. However, the selectivity of different elements in electrocatalysis is not invariable. For example, tin-based catalysts can also selectively produce CO by ECR reaction. The metallic Co or Ni can only produce H<sub>2</sub>, while the corresponding compounds (Co<sub>3</sub>O<sub>4</sub>, Ni-NC, etc.) are possible selectively produce HCOO<sup>-</sup> or CO (**Figure 1.11b,c**).

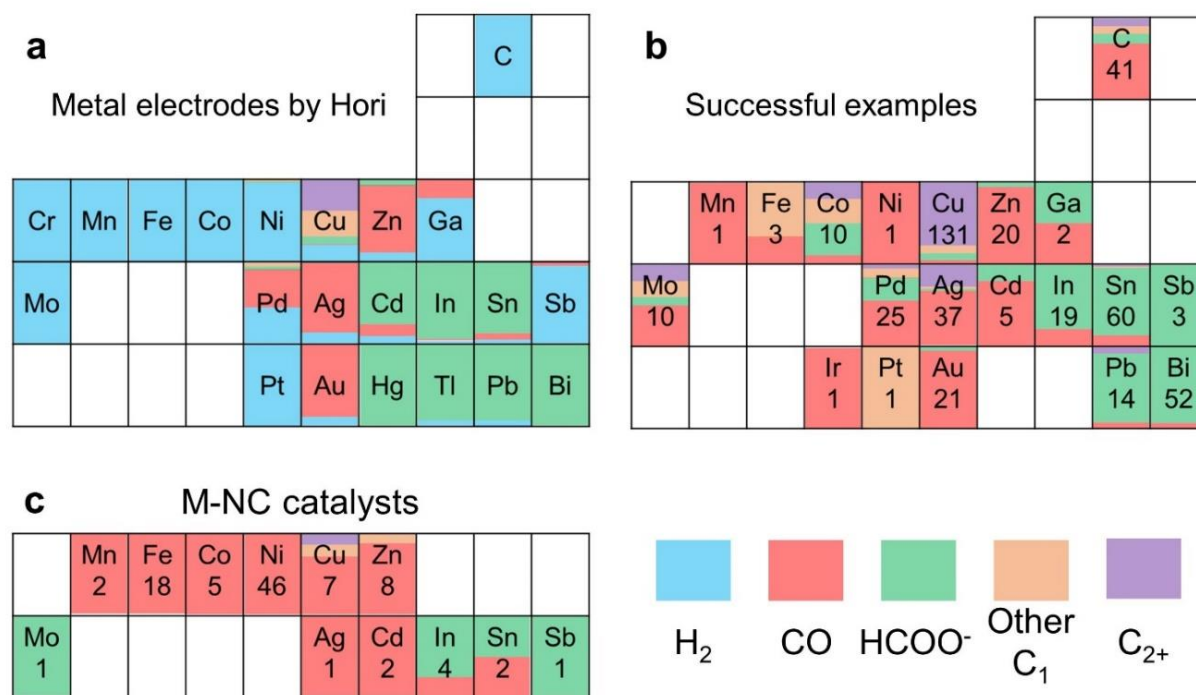


**Figure 1.11** Scheme of product selectivity of the periodic table elements in ECR reaction. (a) Data from Hori's research using metal foil electrodes.<sup>[24,25,47]</sup> (b) Data from a personal summary of the successful ECR examples in the aqueous electrolyte from publications (metal-nitrogen-doped carbon catalysts (M-NC) and molecular catalysts are not included). (c) Data from a personal summary of the successful ECR examples of M-NC catalyst from publications. The number below the element symbols indicates the statistical samples.

The product selectivity of an electrocatalyst can be explained by the adsorption energies of the critical intermediates (\*H, \*CO, \*COOH, and \*OCHO) in the mechanism, which is discussed by Rossmeisl and co-workers (**Figure 1.12**).<sup>[48]</sup> The classification depends on the results of metal foil electrodes by Hori (**Figure 1.11a**). The adsorption energies of \*H and \*CO were found to play a key role in this classification. As for the H<sub>2</sub>-group, the significantly stronger adsorption of \*CO

(all below -1.0 eV in **Figure 1.12b**) on the surface prohibits its desorption or further reduction, leading to mainly H<sub>2</sub> evolution. As for the CO-group, the catalysts possess nearly the most negative values of  $\Delta E_{*H} - \Delta E_{*COOH}$  (**Figure 1.12a**), indicating the thermodynamically preferred generation of the \*COOH intermediate. Compared with the H<sub>2</sub>-group, the proper interaction of \*CO allows its effective desorption, generating CO predominately. As for the HCOOH-group, the very positive  $\Delta E_{*H}$  and nearly positive value of  $\Delta E_{*H} - \Delta E_{*COOH}$  indicate the low possibility of HER reaction and CO formation. The relatively high oxophilicity of the p block metals favors the formation of oxygen bonded intermediate (\*OCHO) and thus the formation of HCOOH. However, considering the need of the proton or \*H, especially the PCET process, the low proton affinity of p block metals causes the generally higher overpotential to generate HCOOH (**Figure 1.10**). The moderate interaction of \*CO determines the Cu-based catalyst's ability to form carbon-carbon bonds, which is typical for the C<sub>2+</sub>-group.

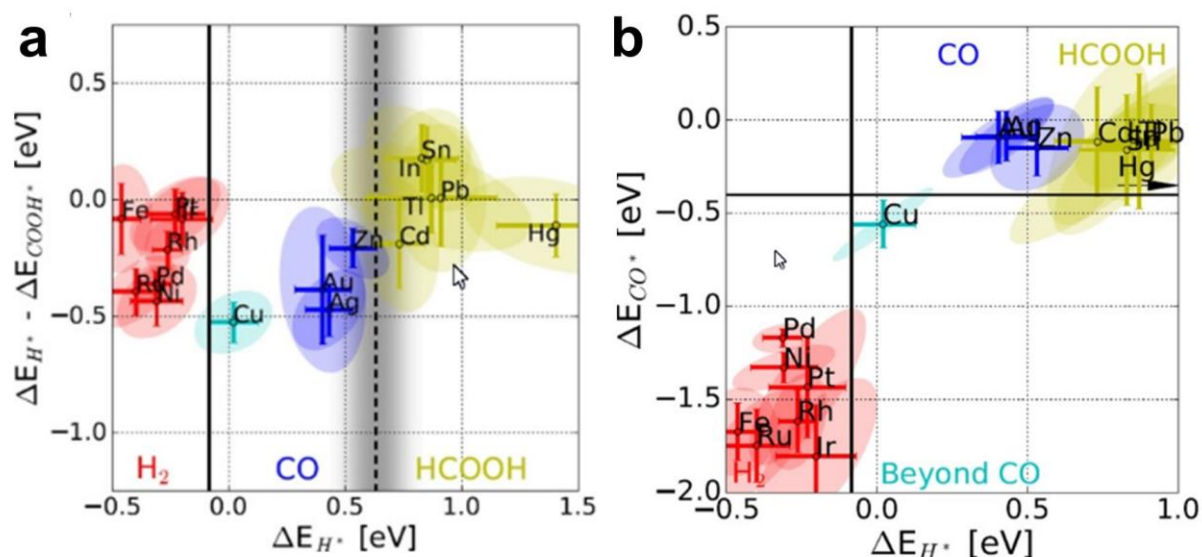


**Figure 1.12** Relationships diagram of adsorption energy ( $\Delta E_{*H}$ ,  $\Delta E_{*CO}$ ), adsorption energy difference ( $\Delta E_{*H} - \Delta E_{*COOH}$ ), and the ECR selectivities for different metal electrodes. The color indicates the different selectivities: H<sub>2</sub>-group (Red), CO-group (Blue), HCOOH-group (Yellow), and C<sub>2+</sub>-group (Cyan). A lower  $\Delta E$  means a stronger adsorption ability.<sup>[48]</sup>

## 1.2.2 Reaction apparatus and environments

### 1.2.2.1 Electrochemical set-up for ECR reaction

#### 1. H-type cell

The H-type cell is a conventional setup and is mainly adopted in academic research because of its advantage of facile assembly and operation.<sup>[49]</sup> The general scheme of the H-type cell is shown in **Figure 1.13a**, generally containing a three-electrode system (**Figure 1.7**). The electrodes are immersed in the electrolyte with dissolved CO<sub>2</sub> as the reactant. Considering the very low solubility

of the  $\text{CO}_2$  in aqueous solutions (34 mM, 1 atm  $\text{CO}_2$ ), the current density is strongly limited (mostly below  $30 \text{ mA}\cdot\text{cm}^{-2}$ ). The H-type cells are more suitable for investigating the structure-activity relationship of different catalysts, which generally need the reactions to proceed at a low current density. For example, the Tafel slope is a key and popular method to investigate the kinetics of the ECR reaction. To measure the Tafel slope, the partial current density generally should be below  $1 \text{ mA}\cdot\text{cm}^{-2}$ .<sup>[44-46]</sup> Besides, it is also suitable for comparing the intrinsic catalytic performance of different catalysts. This is because the H-cell environment is relatively well-defined and well-reproducible.

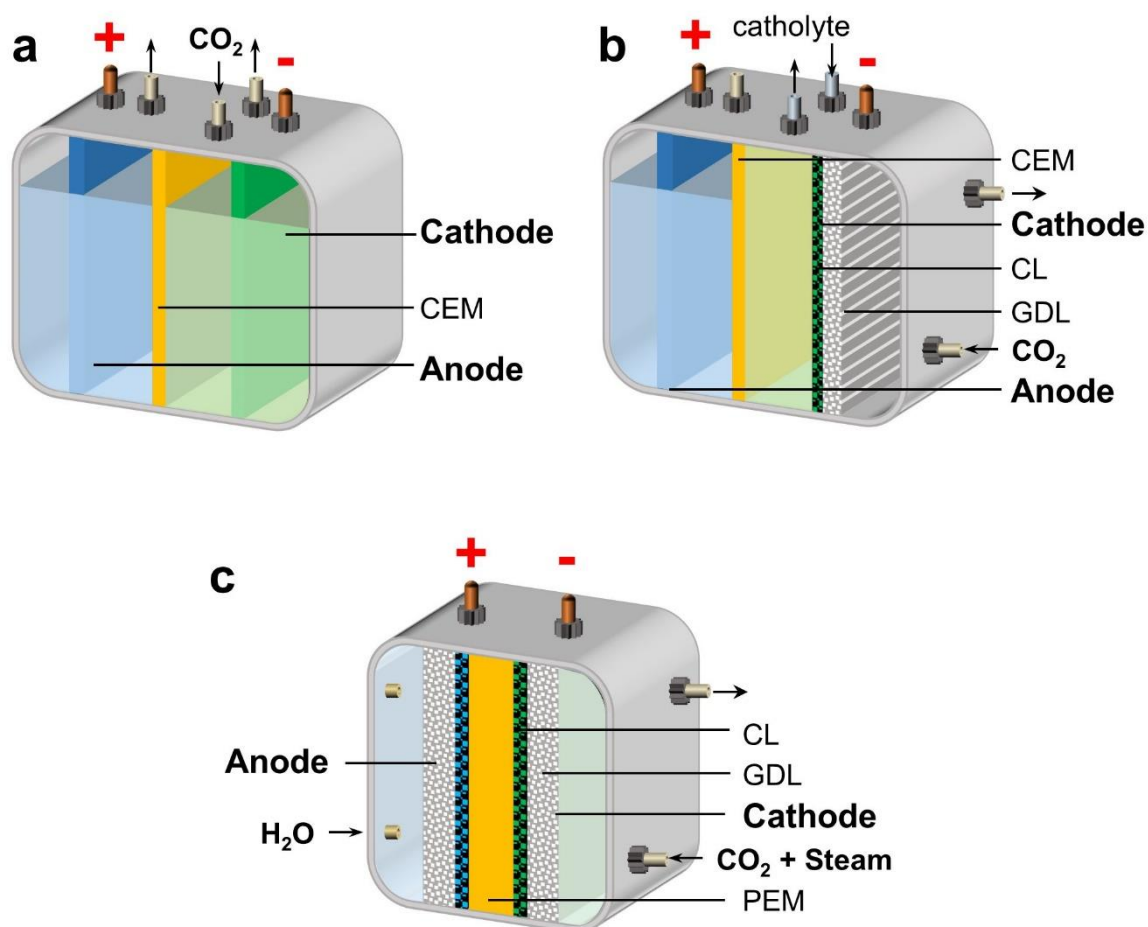


**Figure 1.13** Scheme of the setup of (a) H-type cell, (b) gas diffusion electrode (GDE), and (c) Membrane Electrode Assembly (MEA). CEM: cation exchange membrane. PEM: Proton exchange membrane.

## 2. Gas diffusion electrode (GDE) based flow cell

To improve the performance of ECR reactions up to the industrial level, gas diffusion electrodes were introduced to overcome the  $\text{CO}_2$  depletion problem in H-cells.<sup>[41,49-51]</sup> The GDE is a type of catalyst-loaded porous electrode, which consists of a catalyst layer (CL) and a gas diffusion layer (GDL) (**Figure 1.13b**). The GDL is a hydrophobic, porous, and conductive layer, generally including a macroporous layer (mostly conductive carbon fibers) and microporous layer (MPL). The hydrophobicity is usually achieved by PTFE coating on the surface, which is crucial in

prohibiting electrode flooding. However, too much PTFE could block the gas diffusion channel and decrease the conductivity of the GDL. A proper GDL should exhibit a good balance between conductivity, hydrophobicity, and gas transport. The catalyst layer is commonly deposited on the top of GDL, with the electrolyte being in direct contact with the front and the gas supplied from the back, making the reaction zone a triple-phase boundary.<sup>[52]</sup> A large three-phase interface can significantly facilitate the mass transfer of CO<sub>2</sub>, thus promoting the ECR performance, which generally needs optimizations of the design and every component of the GDEs.

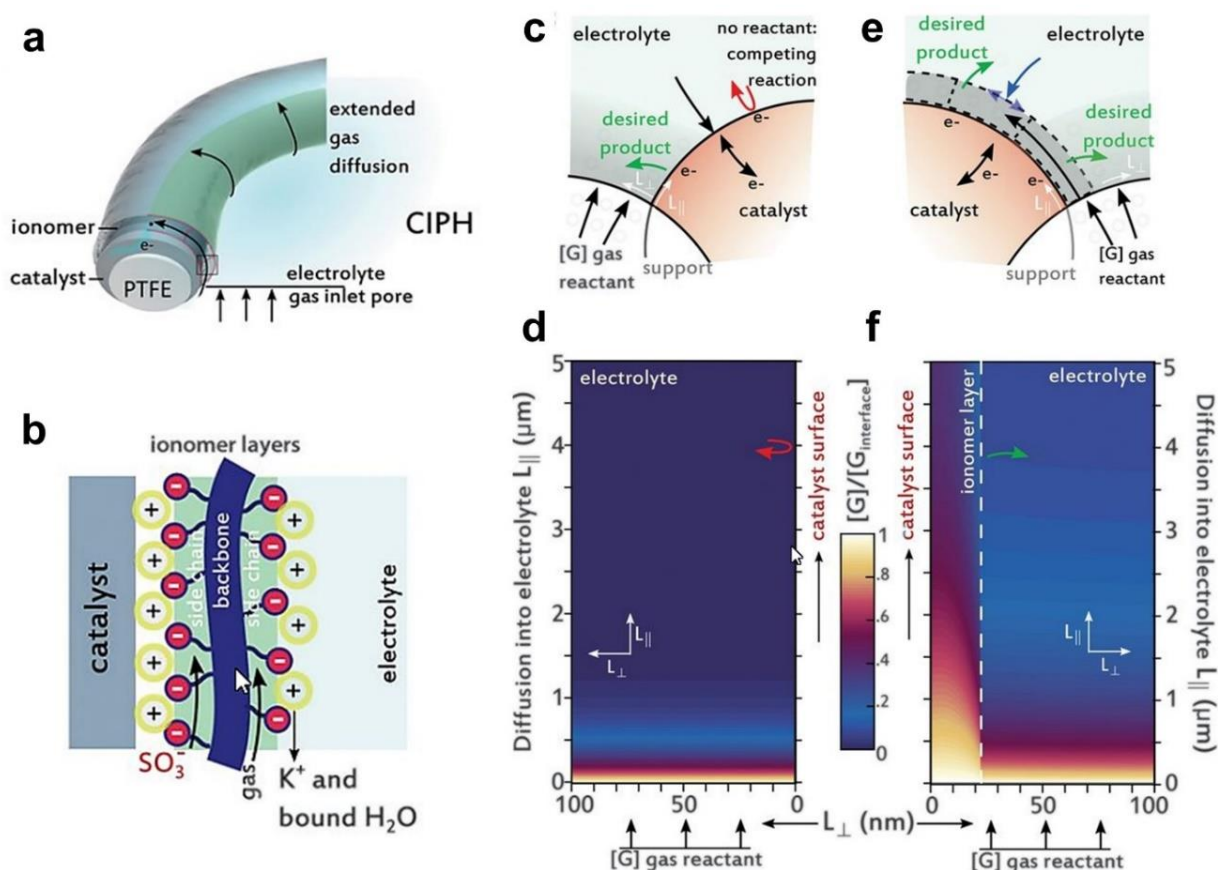


**Figure 1.14** (a) Scheme of the catalyst:ionomer planar heterojunction (CIPH) system. (b) Scheme of the effect of the ionomer on the surface of the catalyst. Scheme of the triple-phase boundary and modeled CO<sub>2</sub> availability of the GDE (c,d) without or (e,f) with ionomer coating.<sup>[53]</sup>

Recently, the GDE design has achieved significant progress in reaching the current densities of the ECR reaction beyond 1 A·cm<sup>-2</sup>.<sup>[19,53,54]</sup> As presented by Sargent and co-workers, a catalyst:ionomer planar heterojunction (CIPH) was constructed by coating a thin layer of the ionomer (several nm) on the surface of the catalyst (Figure 1.14a). The adopted ionomer here is the perfluorosulfonic acid (PFSA) ionomer, which contains both hydrophilic and hydrophobic groups. Furthermore, the ionomer layer facilitates the mass transport and accumulation of cations at the electrode surface (Figure 1.14b).<sup>[53,54]</sup> The effect of promoting CO<sub>2</sub> transport was investigated by modeling CO<sub>2</sub> availability (Figure 1.14c-f). Compared to the conventional GDE design without

ionomer, the CIPH systems could significantly promote CO<sub>2</sub> transport, contributing to ethylene partial current densities of 1.3 A·cm<sup>-2</sup>.

Despite significant progress regarding satisfactory current densities by adopting and optimizing GDEs, there are still several challenges to be solved before an industrial application.<sup>[50,51]</sup> Firstly, long-term stability remains a challenge. The progressing electrode flooding is a crucial problem that restricts a long-term operation at large current densities, especially using carbon-based GDEs. This problem is also referred to as the “alkalinity problem”, which will be discussed later.<sup>[55,56]</sup> A high local pH occurring at high current densities essentially promotes the hydrophilic transformation of the GDE by the hydroxylation of carbon materials, leading to flooding issues. An alternative choice is to avoid carbon-based GDEs and optimize the design of the GDEs.<sup>[53,54]</sup> Moreover, some other problems are amplified in the GDE setup at high current densities. The high local pH leads to a high CO<sub>2</sub> loss and catalyst leaching by the reaction with generated OH<sup>-</sup> (**Figure 1.7**). In addition, the Ohmic drop due to internal resistance can result in a large energy loss at high current densities.

Besides GDE design, the ECR performance enhancement also relies on optimizing the active sites. Therefore, the transfer between H-type cells and GDE cells also needs attention.

### 3. Membrane electrode assembly (MEA) based flow cell

MEAs can be a promising solution to overcome some issues arising from the liquid electrolyte, which is characterized as “zero-gap”, “catholyte-free”.<sup>[51,58]</sup> In a typical MEA design (**Figure 1.13c**), GDEs are attached directly to the membrane without a liquid electrolyte. The membrane can be regarded as a solid electrolyte. A proton exchange membrane (PEM) is mostly applied to transport protons, generated through water oxidation at the anode, and then transported to the cathode to react with gas CO<sub>2</sub>. The removal of the aqueous electrolyte reduces the flooding issues in normal GDEs, thus potentially improving the system's stability. As for the liquid products, the electrolyte-free mode can avoid the product separation cost afterwards. Besides, the zero-gap design could possibly reduce the Ohmic resistance of the cells, thus improving the energy efficiency of ECR reactions. Until today, MEA-based ECR reactions have achieved current densities of more than 100 mA·cm<sup>-2</sup>, outputting >13 wt% EtOH and 15 wt% HCOOH.<sup>[59,60]</sup>

#### 1.2.2.2 Reaction environments

The actual electrode reaction during the electrolysis can be described by the model of the electrochemical double layer (EDL) (**Figure 1.15**).<sup>[61]</sup> Based on EDL theory, the Helmholtz layer (area ①) was first beyond the charged electrode (negative for ECR reactions). It can be divided into the inner Helmholtz plane (IHP) and the outer Helmholtz plane (OHP). IHP contains directly

absorbed species, such as solvent molecules, reactants, products, etc. The OHP lies above the IHP, composed of solvated ions of opposite charge (cations for ECR reactions) with the nearest distance to the electrode. Beyond the Helmholtz layer is the diffusion layer (area ② ③), where the potential decreases rapidly with the distance to the electrode.

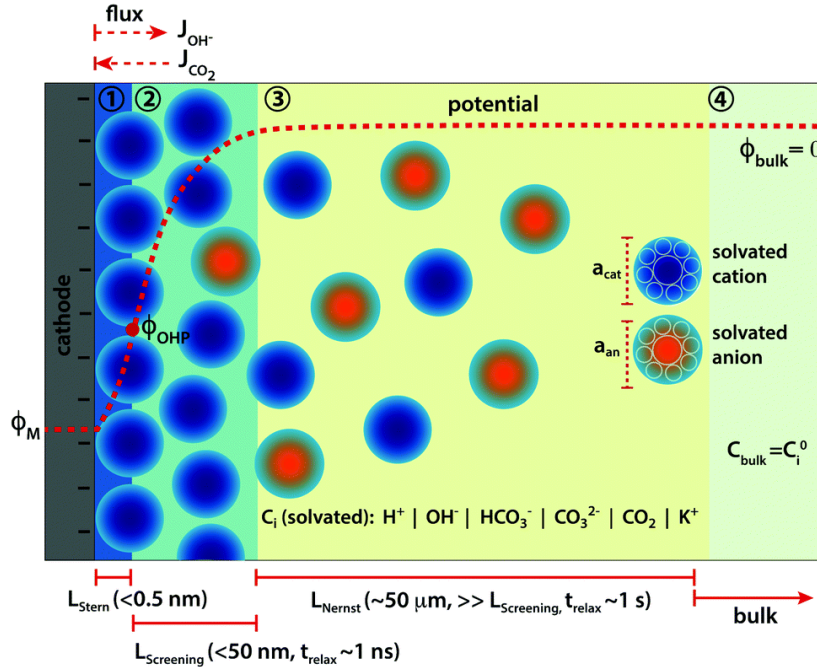


**Figure 1.15** Scheme illustrating the electrical double layer (EDL) at the cathode in ECR reaction.  $\Phi_M$ ,  $\Phi_{OHP}$  and  $\Phi_{bulk}$  indicate the potential of the metal electrode, outer Helmholtz plane (OHP) and bulk electrolyte, respectively.<sup>[61]</sup>

## 1. Electrolytes

Aqueous electrolyte systems are the most commonly used liquid electrolyte systems in research and practical applications because of their low cost, environmental friendliness, wide availability, good solubility, and high ionic conductivity. In addition, the aqueous electrolyte itself can participate in chemical reactions as a proton donor and proton acceptor, where the pH, cations, anions, and concentration of supporting electrolyte can affect the ECR performance.

### (1) Anionic effects

According to the EDL theory, the anions could hardly influence the ECR reaction directly. Because the ECR reaction needs the participation of protons, which are mainly from the water molecules, generating the  $\text{OH}^-$  simultaneously. Mostly, the anionic effect can be roughly described as the buffer effect or pH effect.

As for the H-type cell, bicarbonate ( $\text{HCO}_3^-$ ) is regarded as the most common choice, with the advantage of being relatively inexpensive and environmentally friendly. Bicarbonate can hardly participate in the ECR reaction directly. However, it can serve as the proton and  $\text{CO}_2$  carrier, based

on the equilibrium between the  $\text{CO}_3^{2-}$  and  $\text{H}_2\text{CO}_3$ , promoting the ECR reaction. The  $\text{HCO}_3^-$  could buffer the pH change near the electrode, accelerating the proton transfer. The latter effect has been proven through the experiment of using  $^{13}\text{C}$  labeled  $\text{KHCO}_3$  by Shao and co-workers (**Figure 1.16**). The  $^{13}\text{CO}$  was found to be absorbed on the Cu (catalyst) surface by operando surface-enhanced infrared absorption spectroscopy.<sup>[62]</sup>

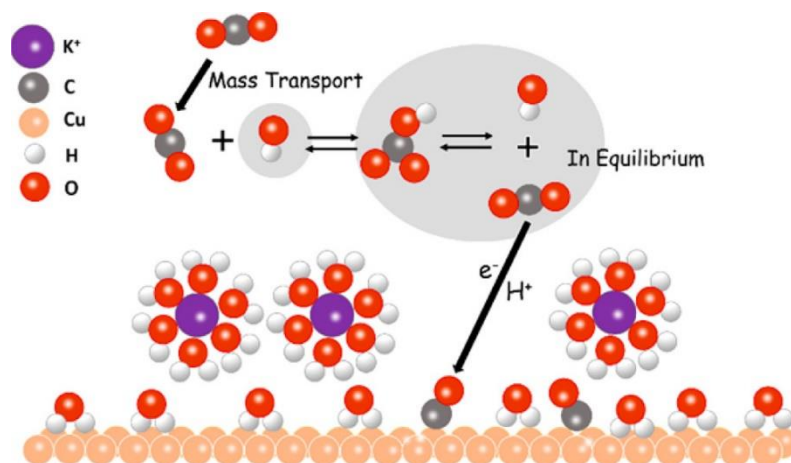


**Figure 1.16** Scheme of the effect of bicarbonate in ECR reaction.<sup>[62]</sup>

When one switches from the H-type cell to the GDE-based flow cell, KOH (alkaline solution) becomes a preferred choice. In principle, an alkaline environment could suppress the HER reaction by shifting its redox potential to a more negative value. However, it doesn't make sense to adopt highly alkaline catholyte in H-type cells. Considering the long  $\text{CO}_2$  diffusion pathway in the H-type cell, the high pH will significantly impede the mass transport of  $\text{CO}_2$  towards the electrode, for the formation of the  $\text{CO}_3^{2-}$ . On the contrary, GDEs possess a much shorter diffusion pathway, making them less prone to the influence of high pH values. Besides the suppressed HER reaction, an alkaline environment will also influence the product distribution, especially promoting  $\text{C}_{2+}$  product generation.<sup>[63]</sup> However, the high alkalinity brings serious stability problems, probably because of the massive precipitation of carbonate (**Table 1.2**).<sup>[55-56,64]</sup> Avoiding too alkaline electrolytes or even using acidic electrolytes has recently attracted more attention.<sup>[54, 65]</sup>

**Table 1.2** Effect of the high alkaline catholyte on ECR reaction.<sup>[57]</sup>

Advantages	Disadvantages
Suppressed HER	Aggravated $\text{CO}_2$ loss and electrolyte consumption
High yield of $\text{C}_{2+}$ products	Precipitation of the carbonates inside GDE
Possibly new reaction pathways	Accelerated electrode flooding

## (2) Cationic effects

The investigations of the cationic effect mainly focus on the alternation of the alkali metals (IA group), considering the requirement of high solubility and chemical inertness. In 1991, Hori and co-workers found the effect of alkali metal ions on selectivity, of which larger alkali metal ions ( $\text{Cs}^+$ ) promote the generation of ethylene.<sup>[66]</sup> The promotion effect is well recognized and investigated in the following research.<sup>[67]</sup> Generally, the larger alkali metal ions possess weaker hydration and smaller hydration shells, making them more likely to adsorb at the electrode. As more metal ions are adsorbed, the potential of the outer Helmholtz plane will be positively shifted and less proton will be adsorbed competitively, leading to the suppression of the HER reaction. Additionally, the alkali metal ions in the Helmholtz layer can stabilize the  $^*\text{CO}_2^-$  intermediate by polarization effects.<sup>[54]</sup> The buffering effect is also applied to explain the enhanced performance using larger alkali metal ions, which can buffer the pH change and increase the local  $\text{CO}_2$  concentration.<sup>[68]</sup>

### (3) Other electrolytes

Besides aqueous electrolytes, organic solvents (such as acetonitrile, dimethylformamide, dimethyl sulfoxide, etc.) are also widely used for ECR reactions, mainly for molecular catalysts, such as porphyrin, phthalocyanine, and other organometallic complexes.<sup>[22,23,69,70]</sup> Most molecular catalysts need to be dissolved in the organic catholyte before the ECR reaction can occur. The advantages and disadvantages are listed in **Table 1.3**. Since there are nearly no ions to transport charges, no reactants (like the  $\text{H}^+$ ) to complete the electrode reaction in the organic electrolyte, the addition of organic salts (e.g., tetrabutylammonium based salts) and reactants (proton donor, e.g., trifluoroethanol) is compulsory.

Ionic liquids (ILs) are a series of ionic compounds that remain liquid at room temperature. Unlike the conventional aqueous/non-aqueous solvents, ILs are characterized by nearly no evaporation, good conductivity, high chemical stability, and high solubility.<sup>[71]</sup> Imidazolium cation based ILs are one of the most commonly used for ECR reactions. The imidazolium cation can combine with the  $^*\text{CO}_2^-$  intermediate, serving as a co-catalyst and promoting the  $\text{CO}_2$  activation. The respective advantages and disadvantages are listed in **Table 1.3**. CO is the most common ECR product under a relatively low overpotential using IL-based electrolytes. Using IL-based electrolytes may lead to the formation of a unique product. For example, Bismuth-based catalysts are mostly found to produce formate as the main product in aqueous electrolytes (**Figure 1.11b**), while producing CO as the main product in IL-based electrolytes.<sup>[72]</sup> Some unusual products are also commonly reported using IL-based electrolytes, such as oxalate and dimethyl carbonate. The high cost is the main obstacle for industrial applications, which can be compensated by improving the catalytic performance.<sup>[73]</sup>

**Table 1.3** Summary of the advantages and disadvantages of using organic electrolytes and ionic liquid electrolytes.

Advantages	Disadvantages
<b>Organic solvent</b>	
Better CO <sub>2</sub> solubility	Need addition of the reactants
Suppressed HER	Mostly C <sub>1</sub> products
Probably different reaction mechanism	Mainly H-type cell, not established for GDE
	Expensive
	Not environmentally friendly
<b>Ionic liquids</b>	
High conductivity	Need addition of the reactants
Better CO <sub>2</sub> solubility	Expensive
Promote CO <sub>2</sub> activation	
Suppressed HER	
Probably different reaction mechanism	

## 2. Temperature

As for every chemical reaction, the temperature is always one inevitable parameter to be discussed. Higher temperatures will increase the electrode reaction rate, while the ECR selectivity may differ. Considering that higher temperature will lead to a decreased solubility of the CO<sub>2</sub>, a temperature optimization with maximum output is desired.<sup>[74]</sup> Mizuno and co-workers investigated the temperature effect on the ECR reaction by In, Sn, and Pb in a high-pressure H-type cell.<sup>[75]</sup> The results indicated that very high temperatures lead to a decreased FE of formate and an increased proportion of HER. Different metal species also possess different sensitivity to temperature. In their conditions, the best FE of formate was achieved by Sn at 20 °C, In at 20-60 °C, and Pb at 60 °C. Overall, selecting the optimum reaction temperature depends on the type of active sites, electrolyte, and reaction setup.<sup>[74,75]</sup>

## 3. Pressure

In gas | liquid reactions, the pressure of the gas will directly influence the concentration of the reactants, thus influencing the performance. Todoroki and co-workers confirmed the enhancement of the performance by increasing pressure in an H-type cell.<sup>[76]</sup> They found that both selectivity and current density increase rapidly when increasing air pressure and then level off after exceeding

20 atm.

### 1.2.2.3 Coupling with other reactions

As discussed before, exploring CO<sub>2</sub> utilization would be a great strategy to tackle the environmental and energy dilemmas (**Chapter 1.1**). However, the techniques of the ECR reactions are still not economically favorable. Coupling with other reactions to enhance the economic output has been considered recently (**Figure 1.17**).<sup>[77]</sup>

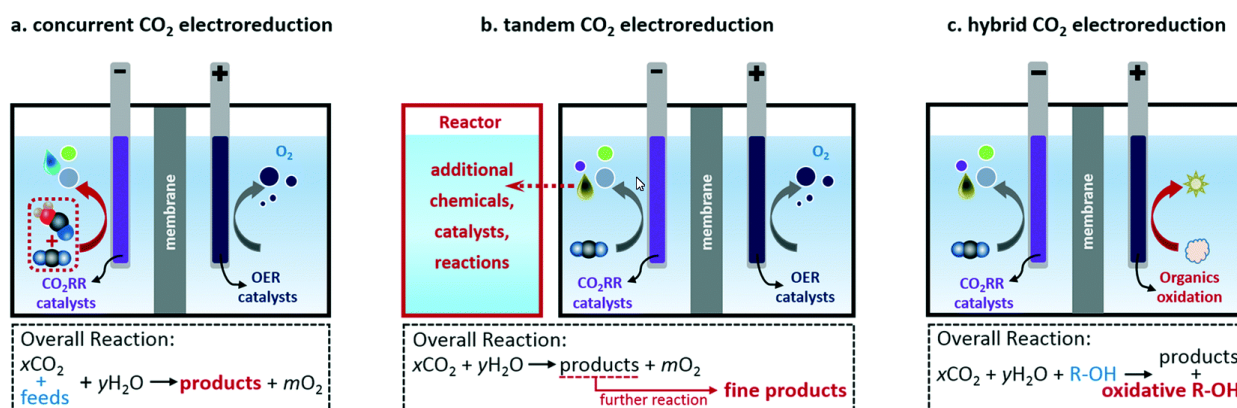


**Figure 1.17** Three strategies for coupling ECR reaction: (a) concurrent ECR, (b) tandem ECR, (c) hybrid ECR.<sup>[77]</sup>

A first option is the concurrent ECR reaction, which indicates the co-electrolysis of CO<sub>2</sub> with another reactant at the cathode. Examples are the combination of N<sub>2</sub> and CO<sub>2</sub> reduction ( $\text{N}_2 + \text{CO}_2 \rightarrow \text{CO}(\text{NH}_2)_2$ )<sup>[78]</sup> and the combination of the CO<sub>2</sub> and NO<sub>3</sub><sup>-</sup> reduction ( $\text{NO}_3^- + \text{CO}_2 \rightarrow \text{CO}(\text{NH}_2)_2$ )<sup>[79]</sup>, both giving urea as products.

A second option is the tandem ECR reaction, which means using the product of the ECR reaction as a reactant to perform another reaction. Considering the currently low concentration of liquid ECR products (typically below 1 M), microbial biocatalysis can be combined, converting formate into other valuable products.<sup>[80]</sup> Furthermore, gaseous products, such as CO, can be further converted, e.g., from CO into hexanol and butanol.<sup>[81]</sup>

The former two strategies are still at a rather early stage, considering the relatively low utilization and conversion. The third option is to replace the typical OER reaction with other organic transformation reactions at the anode. Most academic research only reports and tracks the applied potentials upon the cathode with iR compensation. When applying the ECR reaction of industrial scale, cell voltage, which includes the cathode potential, is a more applicable parameter. The cell voltages are expected to be below specific values to meet the industrial requirement, which is 1.8 V for CO, 2.3 V for EtOH, 3.2 V for HCOOH.<sup>[16]</sup> Oxygen from OER is of low value and its formation possesses a high thermodynamic potential and overpotentials. Besides, active O species damage the components in the cell (e.g., organic membrane). Alternative organic

transformations could be alcohol oxidation,<sup>[82]</sup> biomass oxidation,<sup>[83]</sup> or chloride oxidation<sup>[84]</sup>.

### 1.2.3 Catalyst design and optimization

#### 1.2.3.1 General strategies of catalyst optimization

Efficient catalytic sites are still the primary and critical part of realizing applicable ECR reactions. Therefore, the critical aspects concerning the development of such catalysts are briefly summarized below:

(1) High efficiency to certain desired products. The first requirement of the catalyst relies on a good performance, i.e., high current density, good Faradaic efficiency and low overpotentials. Therefore, the rational selection of active sites to selectively generate certain products and the corresponding structural optimization of catalysts are vital solutions to achieve the desired performance.

(2) High stability. Even though the operational stability relies a lot on the design of the cell and the electrode engineering, as discussed before, the intrinsic stability of the active sites should not be ignored. Structural damage to the catalyst is the one of main reasons for the performance deactivation.

(3) Deep understanding of the mechanism. Unravelling the structure-activity relationship is the ultimate goal of academic research, which can guide the rational design of the catalyst. However, exploring the key factors of activity remains a challenge because it requires precise structural elucidation, operando investigation, and computational methods.

Based on the great progress of the recent academic research, general strategies to achieve superior active sites are summarized in the following two parts: defect and interface engineering (**Figure 1.18**).<sup>[85-88]</sup> Defects are irregular structures compared to the perfect crystal. Open metal sites at the surface of the catalyst can be regarded as defects, which differ from the inner structure of the crystal. It is generally recognized that catalysis happens at the surface, initialized by the chemical adsorption at the catalyst's surface. More specifically, the defect's influence includes size, shape, heteroatom doping, and vacancy effects, which are typical principles for creating unsaturated coordination sites. Besides, strain effects and grain boundary effects generally originate from the interaction between particles forming the homo-junction. As for the multiple-component composites, a performance enhancement can often be ascribed to the interface. The hybrid surface from the different components can provide unique interaction with CO<sub>2</sub> and its intermediates occurring during ECR reactions.

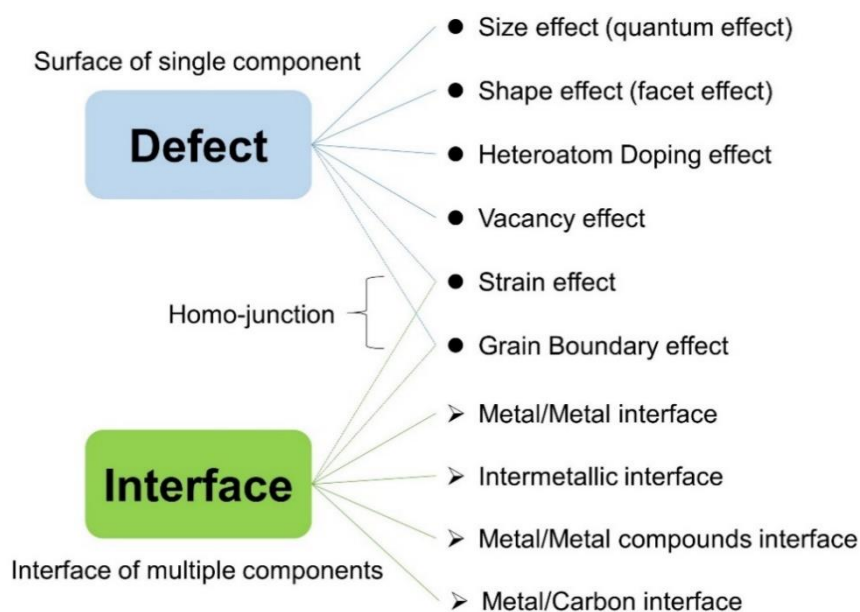


**Figure 1.18** Scheme of strategies based on defect and interface engineering. <sup>[85-88]</sup>

The above described two strategies are both from the intrinsic property of the catalytic sites. There is also another factor which is the pore effect. Mostly, it takes effect by changing the local environments. The restricted mass transport between the bulk and pore surface can cause concentration profiles, increasing local pH.<sup>[89]</sup>

### 1.2.3.2 Molecular catalyst

Considering their well-defined structure, molecular catalysts are thought to be good for investigating structure-activity relationships in ECR reactions. Organometallic coordination compounds are the most important molecular catalysts (**Figure 1.19**).<sup>[23,69,90]</sup> The atomic metal centers are the active site for CO<sub>2</sub> activation, mainly transition and p-block metals. The typical reaction mechanism starts by forming an M-CO<sub>2</sub> complex intermediate or a metal hydride intermediate. Therefore, the performance of molecular catalysts relies a lot on the coordination sphere and functional groups.

CO is the easiest product to obtain, mainly relying on the transition metals sites, such as Ru, Re, Rh, Mn, Fe, Co, or Ni. The selectivity to formate is also reported, of which metal hydride is mainly believed to be the active intermediate. P-block metal sites are preferred to generate formate, which is also true for molecular catalysts. The formation of C<sub>2+</sub> products occurs mainly on Cu sites. Besides, there are also metal-free molecules, mainly pyridine and its derivatives. The examples and corresponding products are listed in **Figure 1.19**.

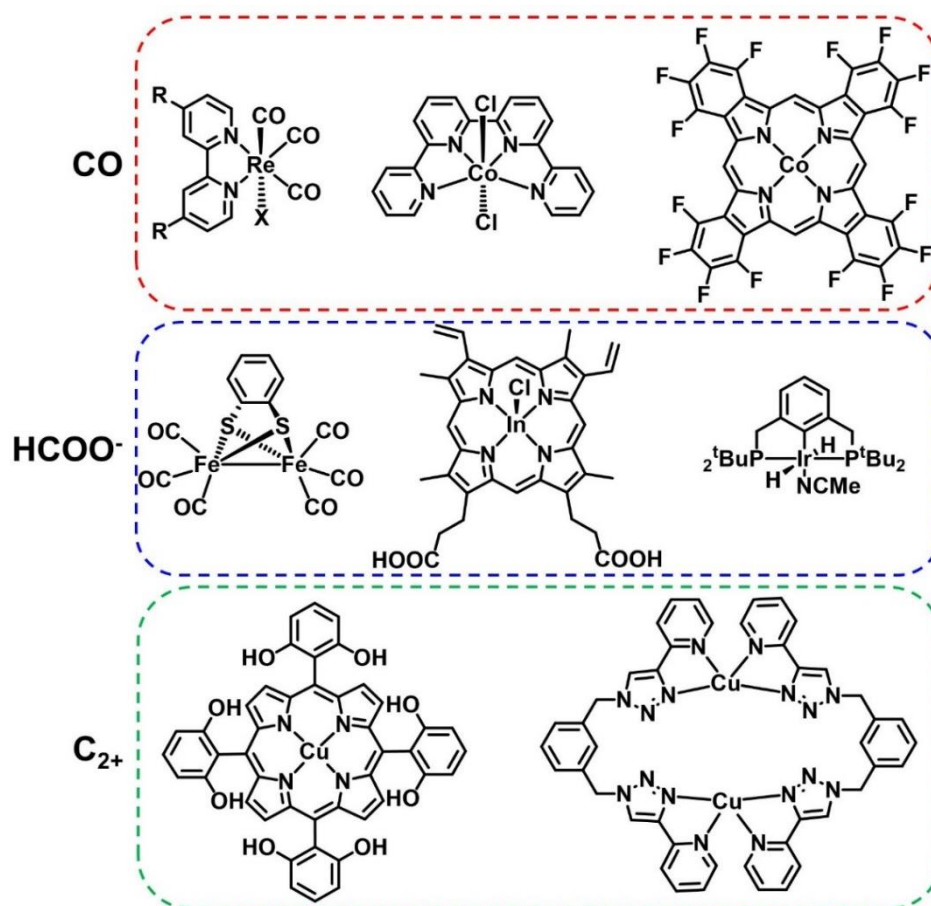


**Figure 1.19** Examples of the organometallic coordination compounds for ECR reaction.<sup>[23,69,90]</sup>

The poor solubility and insufficient stability of most organometallic coordination compounds in water also determine that it is more suitable for testing in organic electrolytes, which is not preferred in practical applications. Based on this consideration, it would be desired to immobilize these catalysts on the surface of solid supports to meet the need to achieve higher current densities.<sup>[91]</sup> The immobilization strategies can be classified as non-covalent bonding, covalent bonding, and forming periodic frameworks, based on the interaction types (Figure 1.20).<sup>[92]</sup> As for the first two methods, supports are needed, mainly carbon materials, such as acetylene black, graphene or carbon nanotubes. Carbon materials are cheap, conductive, and can supply different functional groups. Non-covalent methods, suitable for highly conjugated molecules, are the most facile to handle, generally by an ultra-sonication. However, they may also suffer from aggregation and leaching. By contrast, covalent bonding can provide better dispersion and durability, which needs the existence of the functional groups on both catalysts and supports. Additionally, molecular catalysts as building blocks into porous materials, such as porous organic polymer, MOFs, or COFs, are gaining more attention in recent years, introduced more in the following chapter. An evaluation of these immobilization methods is given in Figure 1.20b.

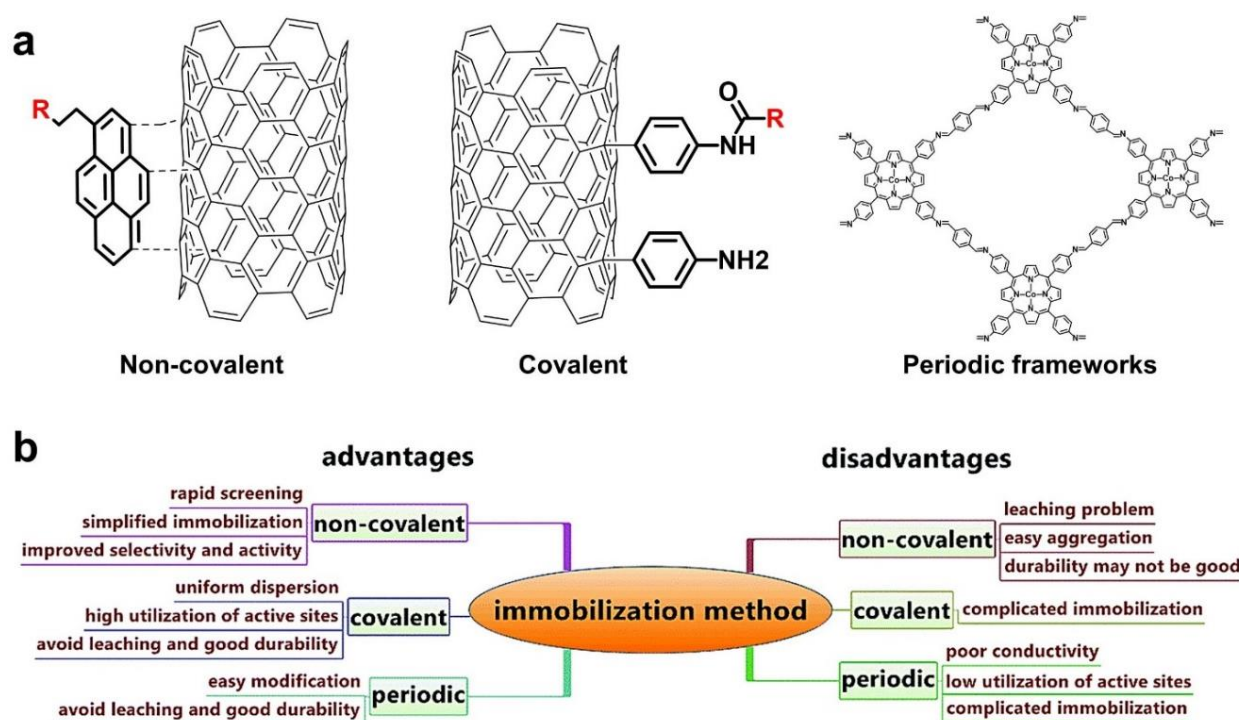


**Figure 1.20** Scheme of the immobilization strategies of molecular catalysts and their advantages and disadvantages.<sup>[92]</sup>

### 1.2.3.3 Carbon-based catalyst

Carbon-based materials attract much attention for many intrinsic advantages, including high surface area, excellent conductivity, low cost, wide availability, and environmental friendliness.<sup>[93-95]</sup> The introduction will be divided into metal-free carbon and metal-nitrogen-doped carbon (M-NC).

#### 1. Metal-free Carbon

Pristine carbon materials possess nearly no activity of CO<sub>2</sub> reduction (**Figure 1.11a**). However, Carbons doped with heteroatoms, mainly N-doped Carbon (NC), can conduct the ECR reaction.<sup>[93-94]</sup> Because of the similar radius of N and C, N can be well doped into the carbon structure. The possible configurations of the N are pyridinic N, pyrrolic N, graphitic N, and oxidized N (**Figure 1.20**).<sup>[94]</sup> Either Pyridinic N<sup>[96]</sup> or Pyrrolic N<sup>[97]</sup> are considered to be the active sites for ECR reaction. Nitrogen-doped carbons prepared by different methods often possess different catalytic properties, giving different conclusions. Changing the pyrolysis temperature or post thermal treatment (e.g., in H<sub>2</sub>, NH<sub>3</sub>) can influence the distribution of the N species in NC materials. However, it is still impossible to get a pure pyridinic N or pyrrolic N doped carbon material to draw a final conclusion. Additionally, a new active site complicates the discussion, which is the carbon defect generated upon N removal.<sup>[98]</sup> Moreover, previous descriptions of the actual active sites may still be inaccurate or insufficient, given the structural complexity of amorphous carbon

and the difficulty of accurate characterizations. The surrounding environments of the active sites may also play a role in determining their activity. Besides N-doped carbon, other non-metal atom doped carbons can also be active, such as B doped carbon/diamond, or F doped carbon.<sup>[93,94, 99,100]</sup>

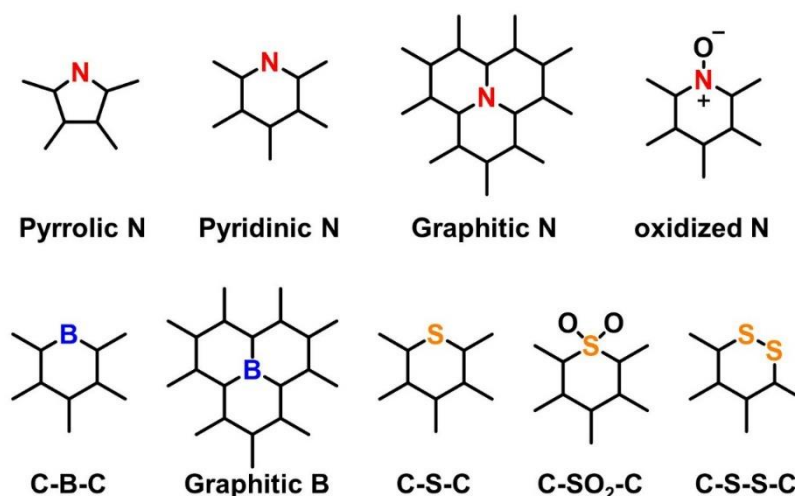


**Figure 1.21** Scheme of the N configuration in N-doped carbon materials.<sup>[94]</sup>

As for the product distribution of the ECR reaction, metal-free carbon catalysts mainly selectively produce CO, whereas fewer examples of producing formate or C<sub>2</sub> products (**Figure 1.11b**). The N sites (pyridinic N or pyrrolic N) are commonly identified as the active sites of CO<sub>2</sub> reduction, no matter if CO, formate, or C<sub>2</sub> is the product.<sup>[93-94]</sup> B-doped sites (**Figure 1.21**) are reported to produce formic acid or C<sub>2</sub> products, especially B-doped diamond.<sup>[98,99]</sup> Other elements, such as phosphorus or sulfur, play more the role of a promoter and are often not decisive for the selectivity of the ECR reaction.<sup>[101]</sup> This could be due to the fact that their larger atom radius does not fit well into the lattice of carbon materials (**Figure 1.21**).

## 2. Metal-Nitrogen-Doped Carbon

Single-atom catalysts (SACs) are considered to have a well-defined structure and maximize atomic utilization, which has recently attracted much attention.<sup>[102]</sup> As a critical member of SACs, M-NC catalysts are expected to replace traditional metal or metal compounds based catalysts, especially noble metal based catalysts, e.g., in fuel cells' ORR process.<sup>[95]</sup> The structural motif of M-NC is similar to that of N-macrocyclic metal complexes, such as metal-porphyrins and phthalocyanines), which have been widely recognized to be active in ECR reaction (**Figure 1.19**). A brief procedure to synthesize M-NC is the pyrolysis of a mixture of metal precursors and N-containing carbon precursors. Modulations of the coordination environment were expected to be the key strategy for optimizing their catalytic performance.<sup>[102]</sup> The coordination environments can be facilely and flexibly modulated by three main experimental approaches.

Firstly, changing the metal center. The metal center is the key factor for determining the ECR

reactions' selectivity. The corresponding products are summarized in **Figure 1.11**. Based on literatures, first-row transition metals are mainly applied,<sup>[104-106]</sup> possibly due to the suitable radius fitting into planar tetra-coordinated macrocyclic molecule. CO is the main product in this case. Ni and Fe are the most active metal sites for producing CO, while the corresponding metal or metal compounds produce almost only H<sub>2</sub> (**Figure 1.11**). Generally, Ni-NCs achieve the highest performance concerning the Faradaic efficiencies and current densities. Ni-NCs are not compulsory to be atomic dispersion and even Ni particles embedded in the NCs can also possess good ECR performance. As for the Fe-NC, it needs a stricter synthesis of the single site, because the existence of metal particles decreases the selectivity. The striking advantage of the Fe-NC lies in the lowest overpotential reported for the ECR reaction to CO.<sup>[106]</sup> As reported by Hu and co-workers, Fe-NC exhibited over 80% Faradaic efficiency towards CO starting from -0.2 V vs. RHE (reversible hydrogen electrode) and reached a CO current density of around 100 mA·cm<sup>-2</sup> at -0.45 V vs. RHE. By comparison, Ni-NC generally exhibited over 80 % Faradaic efficiencies towards CO, but starting from around -0.6 V vs. RHE. Except for CO, formate and C<sub>2+</sub> products can be produced by choosing p-block metals and Cu-based M-NC catalysts, respectively.

Secondly, optimizing thermal treatment conditions. Tailoring pyrolysis conditions or conducting post-pyrolysis is also a common strategy to optimize the ECR performance by changing coordination environments. Specifically, the coordination number of the metal (creation of the vacancy) and the proportion of N species will be changed (**Figure 1.22**).<sup>[103]</sup> As the pyrolysis temperature increases, there will be less N coordination, less proportion of the pyridinic/pyrrolic N sites, and more vacancies.

Thirdly, heteroatom co-doping. Co-doping is also an effective way to enhance the activity of the M-NC catalysts, the most common of which is S doping (**Figure 1.22**). This can be effective even if it is not directly coordinated to the central metal.<sup>[107]</sup>

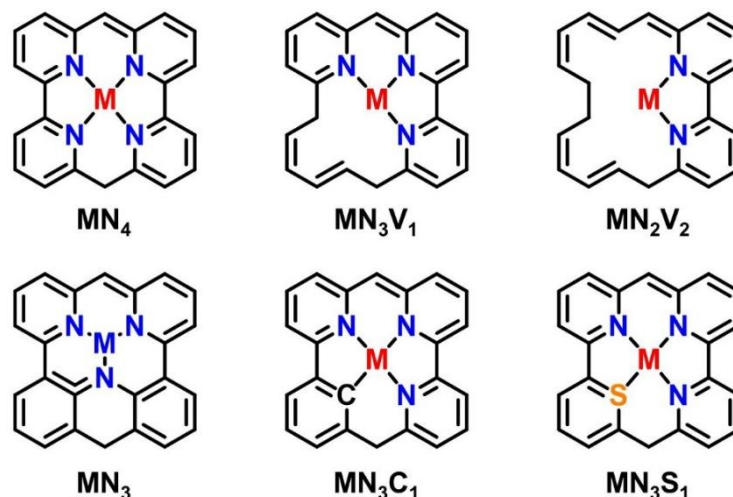


**Figure 1.22** Scheme of the reported structure of the M-NC. V: vacancy.<sup>[103]</sup>

### 1.2.3.4 Metal or metal compounds based catalyst

#### 1. CO as the main product

ECR reaction selectively producing CO is considered to be the most economically and technologically favorable ECR process. CO generation of high current densities has so far exhibited excellent one of the lowest overpotential (**Figure 1.10**), selectivity and energy efficiency, which is one of the most technically feasible ECR reactions (**Figure 1.5**).<sup>[15,108]</sup> A two-step strategy of coupling ECR to syngas (CO+H<sub>2</sub>) with Fischer-Tropsch synthesis to multiple-carbon products is also a practical option. Nearly all known ECR-active elements have the potential to generate CO selectively (**Figure 1.11**). The key strategy for optimizing active sites for CO lies in enhancing the CO<sub>2</sub> activation, stabilizing the \*COOH intermediate, and suppressing HER processes.<sup>[37,87]</sup>

Firstly, noble metals such as Ag, Au, and Pd are the most studied elements for highly selective CO generation.<sup>[87,109]</sup> The overpotentials required for the ECR reaction to CO by these noble metals are generally low, typically achieving over 90% FE at around -0.5 to -0.6 vs. RHE. To enhance the atomic utilization and increase the active surface, smaller particle sizes are preferred, contributing to a higher proportion of surface atoms and more defects. However, smaller particles are not necessarily better because the size effect often shows a volcano-shaped tendency.<sup>[110-113]</sup> Morphology engineering (facet effect) is also a common strategy. High-index crystal face, due to their higher surface energy and more unsaturated sites, generally enhances performance.<sup>[113]</sup> Moreover, interfacial engineering is also a common strategy, such as forming alloys<sup>[114]</sup> and surface modifications<sup>[115,116]</sup>.

The *ds*-block elements (mainly Zn) are also suitable ECR catalysts producing CO. Zn is considered an excellent candidate for replacing noble metals due to its relatively low price. However, the overpotentials required are larger than with noble metals, achieving over 90% FE at around -0.9 V vs. RHE. The surface oxidation state plays a vital role in controlling the selectivity to CO.<sup>[117,118]</sup> The investigation of the size effect implies that ultrasmall particles (< 3 nm) are less preferred for CO production.<sup>[118]</sup> The commonly adopted catalysts are ZnO, followed by Zn, and ZnS. Cd-based catalysts are less reported, due to their high toxicity. CdS-type materials are mainly adopted,<sup>[119]</sup> which possess a similar overpotential to Zn-based catalysts.

Even though p-block metals mainly possess the ability to produce formate/formic acid, CO can also be selectively produced through appropriate regulations, such as using SnS<sub>2</sub>.<sup>[120]</sup>

#### 2. Formate/Formic acid as the main product

Considering the high market value of formic acid, the production of formic acid by ECR reaction is still an attractive option, even if the current technology is not fully mature (**Figure 1.5&1.6**).

P-block metals (Sn, In, Bi, etc.) based catalysts are widely developed for ECR reactions with selectivities of over 90% to formate/formic acid (**Figure 1.11b**).<sup>[121-123]</sup> However, compared to ECR to CO, the generation of formic acid catalyzed by p-block metals often requires high overpotentials (around -0.9 V vs. RHE to reach over 90% FE) (**Figure 1.10**), which corresponds to lower energy efficiencies than ECR to CO. Most of the adopted catalysts are metal oxides (SnO<sub>2</sub>, In<sub>2</sub>O<sub>3</sub>, Bi<sub>2</sub>O<sub>3</sub>, etc.), which must be partially reduced before or during the reaction. A residual amount of oxide on the surface is essential for getting high selectivities by various operando characterizations.<sup>[124-126]</sup> General strategies to improve ECR performance comprise morphology optimization, doping, and alloying.<sup>[121-123]</sup>

Recently, Xie and co-workers reported a partially oxidized Co layer exhibiting excellent performance in ECR to formate.<sup>[46]</sup> Unlike the p-block catalysts, this ECR reaction can proceed at a very low overpotential (reaching 90% FE at -0.35 V vs. RHE). After that, further investigation using cobalt oxides (Co<sub>3</sub>O<sub>4</sub>) also verified the high selectivity of Cobalt towards formic acid.<sup>[127]</sup> However, an obvious drawback for such catalysts lies in their very narrow potential window (< 0.1 V).

In addition, palladium-based catalysts can selectively produce formic acid at very low overpotentials (around -0.15 V vs. RHE). The size dependency also exhibits a volcano shape with a peak at a particle size of 6.5 nm.<sup>[128]</sup> The main drawback is that the current density rapidly deactivates during ECR reactions.<sup>[109,129]</sup>

### 3. C<sub>2+</sub> as main products

The generation of multi-carbon products often requires a relatively high overpotential, and the FE is hardly above 80% (mostly in the range of 40-60%), which causes a relatively low energy efficiency of the ECR to C<sub>2+</sub> products (**Figure 1.10**) According to the techno-economic analysis, the non-direct pathway (CO<sub>2</sub>-CO-C<sub>2+</sub>) needs to be considered as an alternative,<sup>[15,16,130]</sup> which increases the challenge of direct ECR to C<sub>2+</sub>. In terms of catalytic sites, copper catalysts are almost the only catalysts capable of selective ECR reactions to C<sub>2+</sub>, even though very few non-copper catalysts such as Pd, NiAl, NiGa have been reported (**Figure 1.11**).<sup>[108,131]</sup> The desired active sites can provide appropriate adsorption of CO, which is an intermediate in the formation of C-C bonds (**Figure 1.9, 1.12**). Therefore, the strategies of enhancing the selectivity for C<sub>2+</sub> products are often focused on optimizing the adsorption capacity and improving the coverage of \*CO. The specific experimental choices can be divided into two categories:

#### (1) Oxide derived (OD) Cu catalyst

Grain boundaries are widely recognized to provide a strong binding of CO and validated for

promoting the generation of multi-carbon products in direct ECR reaction.<sup>[132]</sup> Among these catalysts, oxide-derived Cu, generally prepared by partial reduction of Cu oxides, was mostly adopted for being rich in grain boundaries. Besides, the mechanism for the superior activity of C<sub>2+</sub> products is often thought to be strongly related to the oxidation state of Cu.<sup>[133]</sup> The residual Cu<sup>+</sup> in OD-Cu is thought to be a key site to guarantee good selectivity (Figure 1.23).<sup>[134,135]</sup>

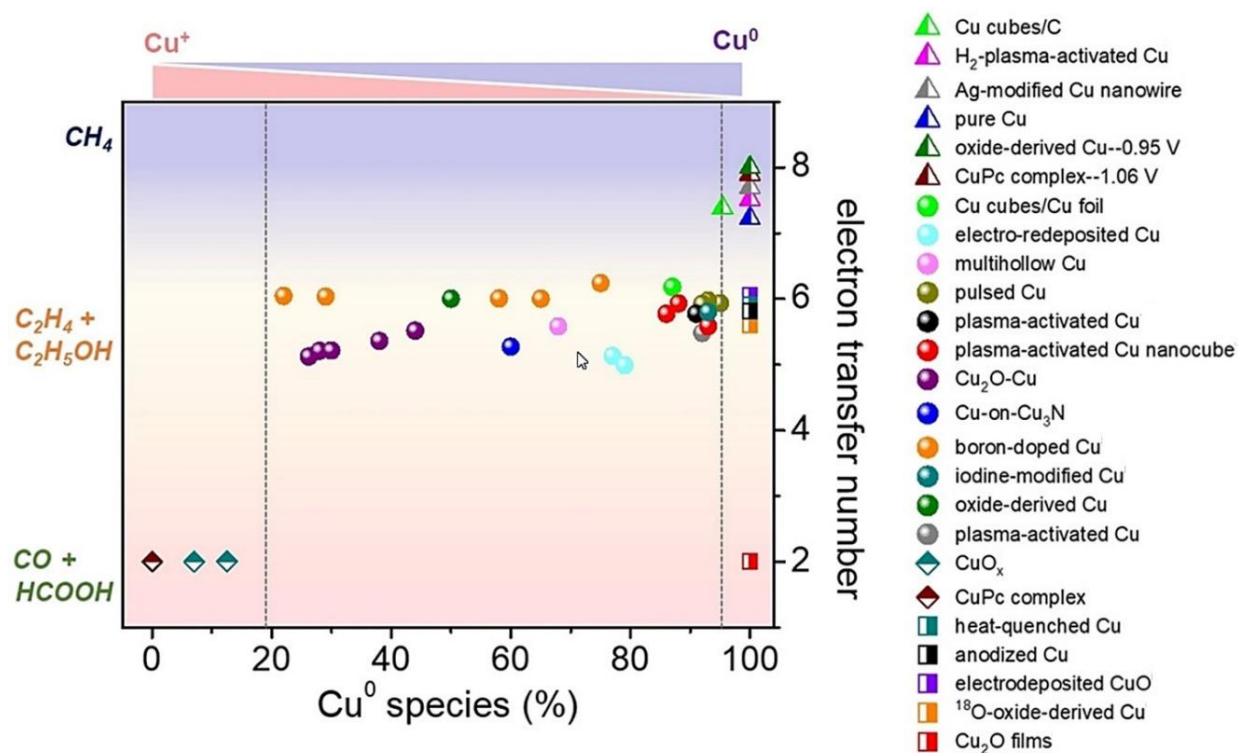


**Figure 1.23** Correlation between the selectivity and oxidation state of Cu catalyst.<sup>[133]</sup>

## (2) Cu-alloy based catalyst

Alloying with a second metal allows for optimizing the band structure, which enhances the adsorption and coverage of the key intermediate CO.<sup>[136]</sup> Elements capable of selective CO generation (e.g., Ag,<sup>[137]</sup> Pd,<sup>[138]</sup> Zn<sup>[139]</sup>) are the most adapted for alloying. The \*CO generated on the metal surface, such as Ag, can be rapidly transferred to the Cu surface, enhancing the coverage of CO on the Cu surface, which is presumed to be the key intermediate for getting the high C<sub>2+</sub> selectivity.

## 1.3 Metal-Organic Frameworks (MOFs) for ECR reaction

### 1.3.1 Introduction to MOFs

Metal-organic frameworks (MOFs) are a series of crystalline porous frameworks constructed by metal-based secondary building units (SBUs) and organic bridging linkers through coordination

bonds.<sup>[140-144]</sup> Along with Covalent Organic Frameworks (COFs) and Hydrogen-bonded Organic Frameworks (HOFs), MOFs are a crucial member of the reticular chemistry, established by O. M. Yaghi.<sup>[142]</sup> By 2022, over 10,000 structures have been recorded by the Cambridge Structural Database (CSD).<sup>[145]</sup> Due to their ultra-high specific surface area, porosity, flexibility, and well-defined structure, MOFs are considered promising candidates for various applications, including gas storage and separation, sensing, optics, energy conversion, or catalysis.<sup>[146]</sup>

MOFs are regarded as a promising platform for catalysis research. Compared to traditional solid catalysts, MOFs exhibit the following advantages: (1) Ultra-high surface areas to increase the dispersion of active sites.<sup>[141]</sup> (2) High porosities to immobilize guest materials.<sup>[147]</sup> (3) Crystalline nature determines the well-defined structure.<sup>[148-151]</sup> (4) The flexible structure facilitates microenvironment regulation.<sup>[149]</sup> In summary, MOFs are solid catalysts with an active site dispersion close to molecular catalysts, which is expected to upgrade the catalytic performance and investigate the structure-activity relationship.

### 1.3.1.1 Elements of MOFs

#### 1. Metal nodes (metal-based SBUs)

The metal nodes, representing the inorganic part in MOFs, are also called secondary building units (SBUs). These can be mononuclear or multinuclear, i.e., metal nodes contain one or multiple metal species. The linker mainly provides the coordinating atoms, but can also come from the solvent or the anion of the metal precursor. The metal centers and the coordination atoms constitute the metal SBUs, which contribute significantly to the structural diversity of MOFs. The formation of metal SBUs depends mainly on the type of metals, linkers, synthesis conditions, and framework geometry. Metal species with similar properties often have isomorphic metal SBUs. For example, Zr, Hf, and Ce often form octahedral  $M_6$  clusters. Divalent first-row transition metals often form paddle-wheel type  $M_2$  clusters. Trivalent first-row transition metals often form triangular  $M_3$  clusters. Some common metal SBUs can be found in [Figure 1.24](#).

#### 2. Organic bridging linkers

As the organic component of MOFs, linkers play a relatively decisive role with regard to porosity by connecting the metal nodes to form a framework. The organic linkers commonly used in MOFs are rigid or semi-rigid, as shown in [Figure 1.24](#). The linkers in MOFs are usually O-coordinating (mostly carboxylic acid groups or hydroxyl groups) or N-coordinating (mostly azole groups or amine groups). Still, they can also be sulfur-coordinating, sulfonate-coordinating, or phosphonate-coordinated. It is worth noting that organic linkers may also contain metal components, forming metallized linkers. These linkers are generally derived from organometallic



filler (usually solvent molecules) from the MOFs. This was initially catered for gas adsorption,<sup>[140]</sup> but was subsequently adopted for further applications.

### 1.3.1.2 Ultra-high surface area and porosity

Compared to conventional porous materials, using rigid organic bridging linkers greatly enhances the porosity of the material (Figure 1.25).<sup>[141]</sup> For example, the classical MOF-5 has a porosity of 61%, and some MOFs can even reach 90%.<sup>[140,141]</sup> The ultra-high porosity opens up the promising potential of using MOFs for gas storage (hydrogen, methane). As for catalysis, a high specific surface area implies a good exposure of catalytic sites. The ultra-high porosity and crystalline nature of MOFs imply that the dispersion of active sites in MOFs is approaching that of molecular catalysts. In addition, a high pore volume can also be used to immobilize guest compounds, providing additional catalytic sites.

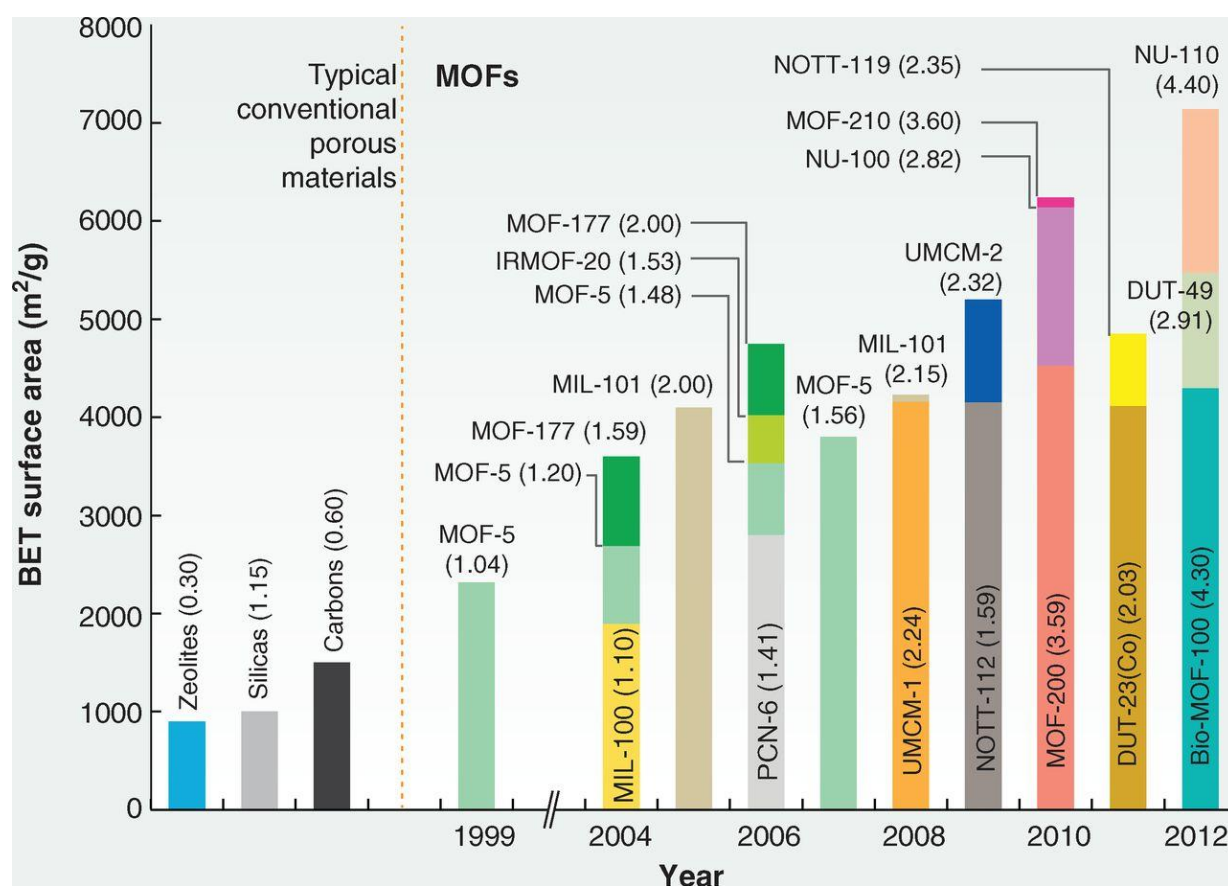


**Figure 1.25** The development of MOFs' specific surface area and pore volume.<sup>[141]</sup> Conventional porous materials were provided for comparison. The numbers in the parentheses represent the corresponding pore volume (cm<sup>3</sup>/g).

### 1.3.1.3 Formation mechanism and stability

The crystallization process of MOFs is Gibbs free energy-driven (Figure 1.26).<sup>[150,151]</sup> The crystallization process depends strongly on the conditions of synthesis. Generally, MOFs are obtained by solvothermal treatment of a mixture containing metal precursors, linkers, solvents,

and possibly modulators. High boiling point organic solvents (e.g., DMF) are mostly adopted, since the solvothermal process is generally at a high temperature (mostly 85-150 °C), thus promoting crystallization's kinetic parameters. Besides, organic solvents can inhibit the over-hydrolysis of metal precursors as well as provide good solubility for organic linkers. The modulators are sometimes added to regulate the crystallization rate by reducing the effective concentration of metal ions in the system through the coordination effect. The ease of crystallization indicates the high periodicity of the MOFs, which facilitates their precise structural resolution. Beyond solvothermal synthesis, more and more synthetic methods have been developed, such as room-temperature synthesis, green synthesis, and solid-phase synthesis.<sup>[152]</sup>

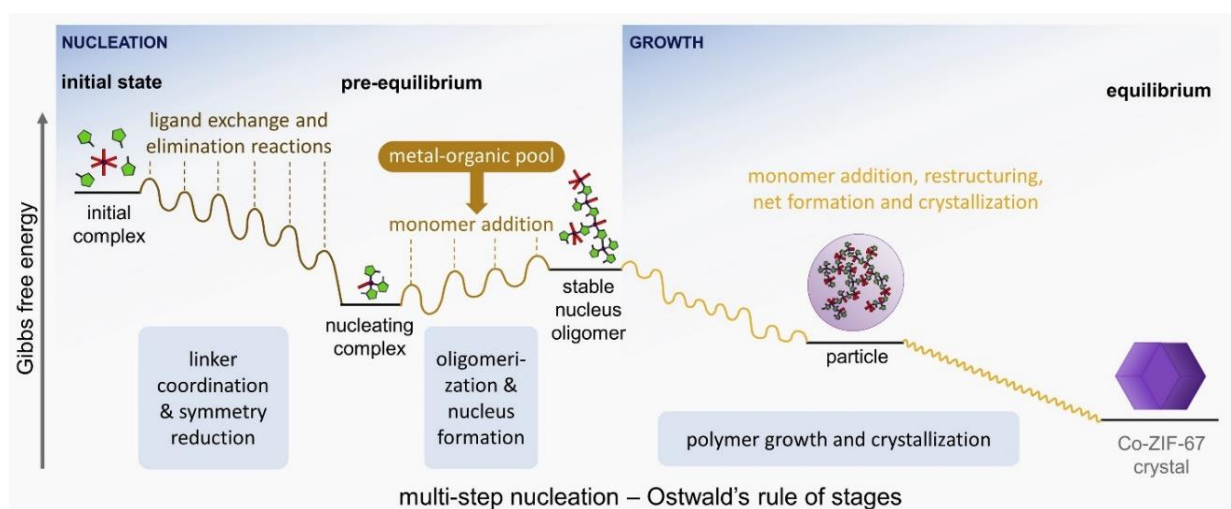


**Figure 1.26** The scheme of MOF formation mechanism, exemplified by Co-ZIF-67.<sup>[151]</sup>

The ease of crystallization of MOFs also brings stability issues of MOFs. The bond energy of coordination bonds tends to be lower than that of conventional covalent bonds, which dictates that the coordination bonds are flexible and facilitate a conformational optimization during crystallization (Figure 1.26), but can also lead to relatively unstable frameworks. Therefore, the strength of coordination bonds is usually used as an important indicator for the stability of MOFs. As an empirical rule, the soft-hard acid-base (HSAB) theory is often used to give a rough but quick judgment of the coordination bond strength.<sup>[153,154]</sup> Usually, the combinations of hard acid-hard base or soft acid-soft base can form a stronger bond. Based on this theory, the linkers and metal SBUs in MOFs can be categorized. Most tetravalent or trivalent metal ions (e.g.,  $Zr^{4+}$ ,  $Al^{3+}$ ) (hard acids) and O-coordinating linkers (hard bases) can form stable coordination bonds. Divalent metal ions (e.g.,  $Zn^{2+}$ ,  $Cu^{2+}$ ) (soft acids) tend to form stable bonds with N-coordinating linkers (soft bases). In addition to bond strength, the coordination number of the SBUs also influences the stability, of which a higher coordination number is preferred. As for the linkers, short and rigid linkers could better resist structural damage.<sup>[154]</sup> The stability of different MOFs varies greatly. Some MOFs undergo apparent destruction or phase transformation once exposed to the air,<sup>[155]</sup>

while some remain stable even in concentrated  $\text{HNO}_3$ ,  $\text{H}_2\text{SO}_4$  or  $\text{HCl}$ .<sup>[156]</sup>

### 1.3.1.4 Microenvironment modulations for catalysis

Metal-organic frameworks can provide various catalytic sites originating from the three compositions mentioned above. (Figure 1.27).<sup>[149,157]</sup> In the case of metal SBUs, the metal sites provide Lewis acidity, corresponding coordination atoms have a certain Lewis basicity, and the metastable metals also have redox properties. In the case of linkers, functional groups of the linkers may have versatile chemical properties. For example, a carboxylic acid group or a sulfonic acid group is Brønsted acidic, and an amino group or a sulfhydryl group is Lewis basic. If the linker is metallized, it is Lewis acidic and can be redox-active. The pore space can be used to host diverse guest compounds serving as active sites.

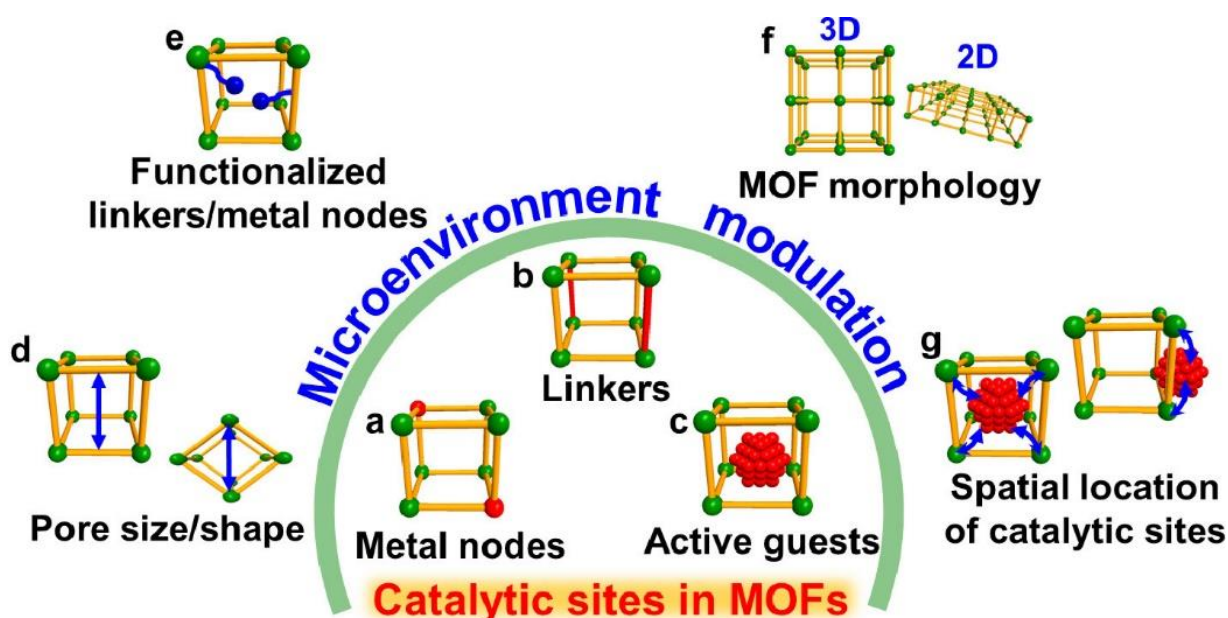


**Figure 1.27** Scheme of the active sites in MOFs and strategies of microenvironment modulation.<sup>[149]</sup>

Metal-organic frameworks are very flexible and highly tunable in structure.<sup>[144]</sup> Linkers or metal SBUs can often be substituted by alternatives of similar conformation to form isorecticular structures. A pioneering example is IRMOFs (isorecticular MOFs) series illustrated by Yaghi and co-workers in 2000 (Figure 1.27).<sup>[158]</sup> The linkers adopted for IRMOFs are all linearly dentate, carboxylic acid-based linkers. Although the specific structures are different, the formed IRMOFs are all consistent in their structural conformation. Besides, similar metal SBUs conformation of different metal species can also be flexibly exchanged without the influence of the conformation of the frameworks, such as Zr, Hf, or Ce.<sup>[144]</sup>

Topology was introduced as a mathematical approach to simplify the understanding of the framework diversity of MOFs.<sup>[159]</sup> Every framework can be simplified by a ball-stick model based on every component's geometric features and connection numbers. The topology can be described

by so-called Schläfli symbols, which can be calculated by *TopoPro* software. The RCSR (Reticular Chemistry Structure Resource) database provides more topology information on reticular chemistry.<sup>[160]</sup> The topology symbol of the IRMOF is *pcu*, shown in **Figure 1.28**.

Their superior potential for post-modification also demonstrates the structural flexibility of MOFs. The three components (metal-based SBUs, linkers, and frameworks) are open to being modified (**Figure 1.27**).<sup>[147,149,161-163]</sup> Such a flexible modification of the MOF structure, when it appeared in the field of catalysis, can be regarded as a modulation of the catalytic environment.

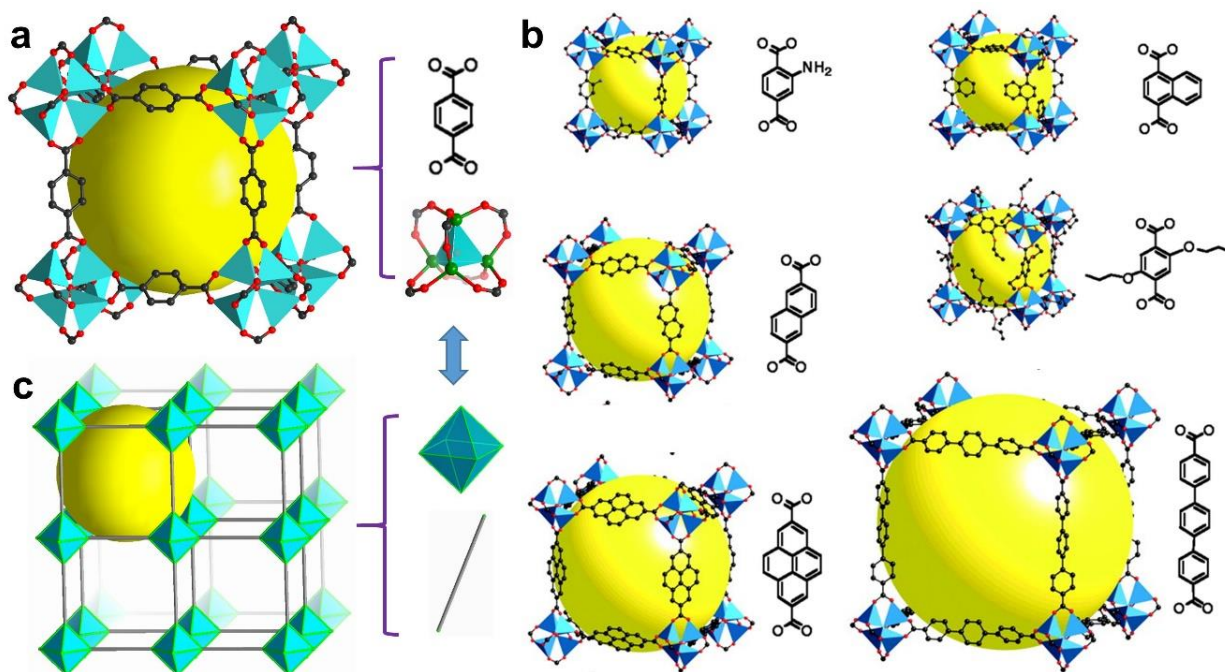


**Figure 1.28** (a) Scheme of the MOF-5 framework. (b) Examples of the isoreticular MOFs (IRMOFs).<sup>[158]</sup> (c) Scheme of the *pcu* net framework of the IRMOFs. The Zn<sub>4</sub>O SBUs and linkers are simplified as light blue octahedral and grey line, respectively.

### 1.3.2 MOF-based materials for ECR reaction

Due to the structural advantages of MOFs, MOF-based materials have attracted significant attention as electrocatalysts (**Figure 1.29**). Although their application in ECR reactions started late, they are developing rapidly.<sup>[164-168]</sup> In this section, we will summarize the application of MOF-based catalysts in the field of ECR.

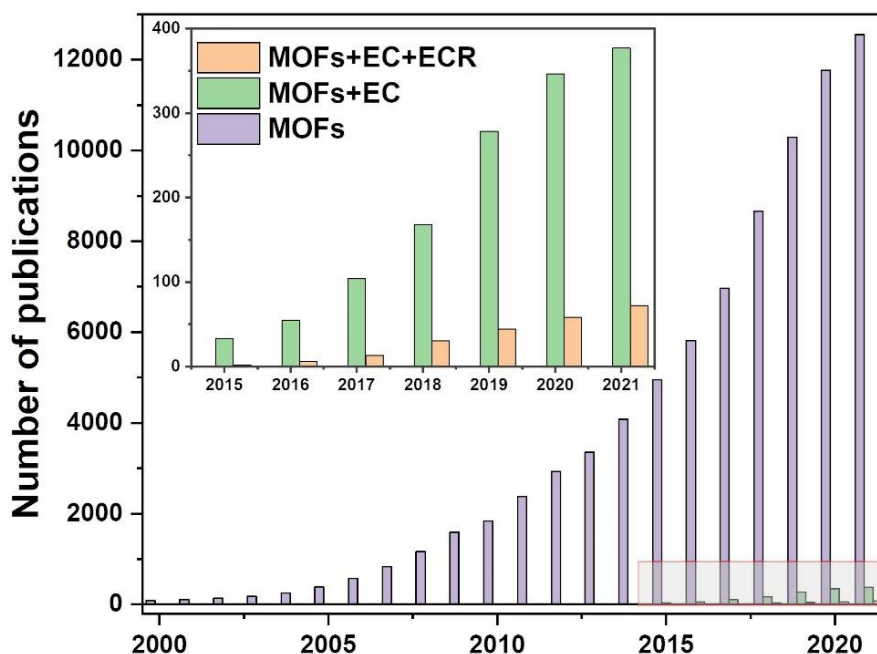


**Figure 1.29** Publications concerning the MOFs/electrocatalysis (EC)/Electrocatalytic CO<sub>2</sub> reduction (ECR) every year since 2000. Data collected from *Web of Science* in 2022.<sup>[169]</sup>

### 1.3.2.1 MOF-derived materials

Considering that pristine MOFs are mostly poorly electrically conductive and not very stable when directly used as electrocatalysts, the development of MOF derivatives is a practical strategy to overcome these limitations.<sup>[170]</sup> Given the decreasing synthesis cost of certain MOFs, MOF derivatives can be expected to be suitable for applications in ECR reactions.<sup>[152]</sup>

#### 1. MOFs pyrolysis

Pyrolysis is a very common and efficient method to produce stable and electrically conductive electrocatalysts from MOF precursors. Generally, through pyrolysis, the organic fractions of MOFs can be converted into conductive carbon supports, and the metal fractions can be converted into metal or metal compounds serving as active sites. For example, Xia and co-workers<sup>[171]</sup> pyrolyzed Bi-based MOFs (Bi-BTC) to obtain Bi@C composites, which were further oxidized to obtain Bi<sub>2</sub>O<sub>3</sub>@C composites. These Bi<sub>2</sub>O<sub>3</sub>@C composites exhibited excellent ECR performance towards formate, reaching a current density of over 200 mA·cm<sup>-2</sup> with a gas diffusion electrode. Similar strategies have been conducted to obtain CuO<sub>x</sub>/C for producing C<sub>2+</sub> products.<sup>[172]</sup> However, considering that the metal content in MOFs can often be up to several tens of wt%, direct pyrolysis of MOFs mostly leads to the formation of large metal particles, which may be unfavorable for catalysis.

More studies have focused on using MOFs as precursors to obtain single-atom catalysts (mainly M-NC catalysts) by pyrolysis.<sup>[173]</sup> The commonly used MOFs are zeolitic imidazolate frameworks

(mainly ZIF-8(Zn)). Active metal sites can be introduced by SBU replacements or impregnation with metal precursors. The Zn component of ZIF-8(Zn) itself can be removed by sublimation at 1000 °C during pyrolysis, leaving only M-NC (**Figure 1.30**). This property of Zn-based MOFs causes their frequent use as precursors for pyrolysis. The use of other metal-based MOFs as precursors often requires a subsequent acid etching step to remove the excess metal compounds. Based on this strategy, environmental modulation of M-NC can be achieved by adding other heteroatomic precursors.

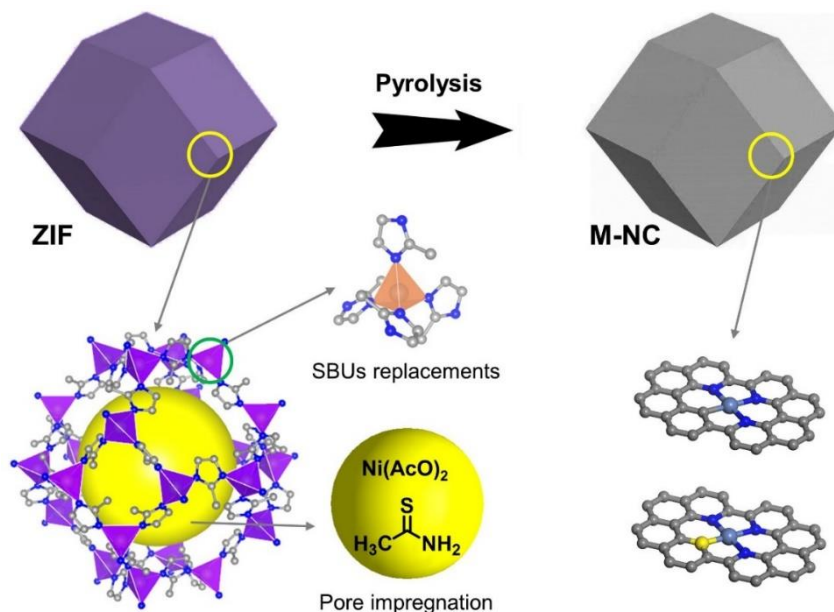


**Figure 1.30** Scheme illustrating the pyrolysis of ZIFs into M-NC.

## 2. MOFs decomposition

Besides pyrolysis, the conversion of MOFs into other metal compounds by utilizing their instability is also an important method. An example is the in-situ conversion of MOFs to metal compounds by electroreduction, where MOFs are considered pre-catalysts.<sup>[174-176]</sup> For example, the reduction of Bi-MOF to Bi-ene (Bismuthene)<sup>[174]</sup> or the hydrolysis to Bi<sub>2</sub>O<sub>2</sub>CO<sub>3</sub><sup>[175]</sup> achieved efficient ECR electrocatalysts.

### 1.3.2.2 Pristine MOFs

The MOFs-derived materials lose the structural advantage of MOFs as crystalline porous materials. Moreover, using MOFs as precursors is sometimes an expensive option. Applying MOFs directly as electrocatalysts is a more attractive option for exploiting the structural advantages of MOFs. Up to now, there are about 60 publications using MOFs directly as electrocatalysts, which is still subject to rapid developments. A summary is listed in **Table 1.4**.

**Table 1.4** Summary of MOFs used directly for aqueous ECR reactions.<sup>[a]</sup>

Catalyst	Product (FE%) <sup>[b]</sup>	$j_{\text{total}}$ (mA·cm <sup>-2</sup> ) <sup>[c]</sup>	Potential (V vs. RHE) <sup>[d]</sup>	Stability (h)	Ref.
CR-MOF	HCOO <sup>-</sup> (30)	-1.1	-1.18	2.2	[27]
Al-TCPP(Co)	CO(76)	-1	-0.7	7	[177]
Cu/NU-1000	HCOO <sup>-</sup> (28)	-1.2	-0.82	0.5	[178]
ZIF-8/MWCNT	CO(100)	-7.7	-0.86	10	[179]
HKUST-1	Alcohol(16)	-10	-0.29	5	[180]
ZIF-8	CO(65)	-3.5	-1.8	4	[181]
Ag <sub>2</sub> O/layered ZIF-7	CO(78)	-40	-1.3	--	[182]
Co-PMOF	CO(94)	-28	-1.0	36	[183]
Ru doped HKUST-1	Alcohol(47)	-20	--	5	[184]
PCN-222(Fe)/C	CO(91)	-1.2	-0.6	10	[185]
ZIF-8	CO(78)	-14	-1.2	--	[186]
Cu <sub>2</sub> O/HKUST-1	CH <sub>4</sub> (63.2)	-14	-1.7	1	[187]
CAU-17	HCOO <sup>-</sup> (41)	-20	--	5	[188]
Cu-ade NSs	C <sub>2</sub> H <sub>4</sub> (45)	-8.5	-1.4	8	[189]
MOF-1992	CO(80)	-16.5	-0.63	2	[190]
MOL-Py-CoPP	CO(92.2)	-29	-0.86	--	[191]
ZIF-8-A-LD	CO(90.6)	-3.5	-1.2	10	[192]
Ni(Im) <sub>2</sub> NSs	CO(78.8)	-5	-0.85	14	[193]
Ag/Al-PMOF	CO(55)	-1	-1.1	12	[194]
STPyP-C	CO(96)	-6.5	-0.62	48	[195]
HNTM-Au <sup>[e]</sup>	CO(95.2)	-9.6	-0.8	24	[196]
CoCp <sub>2</sub> @MOF-545(Co)	CO(97)	-8.5	-0.8	8	[197]
TCPP(Co)/Zr-BTB	CO(75)	-7.2	-0.76	18	[198]
In-BDC	HCOO <sup>-</sup> (88)	-15	-0.76	21	[199]
PcCu-O <sub>3</sub> -Zn/CNT	CO(88)	-4	-0.7	11	[200]
Bi-BTC	HCOO <sup>-</sup> (90)	-17.8	-1.06	12	[201]

Fe/BIF-73-NS	CO(88.6)	--	-1.16	--	[202]
Cu-TCPP(Cu)	HCOO <sup>-</sup> (81)	-2.1	-0.7	5	[203]
PCN-222(Cu)/C	HCOO <sup>-</sup> (44)	-3.2	-0.7	2	[204]
Sn doped ZIF-8	HCOO <sup>-</sup> (90)	-27	-1.1	--	[205]
Zr-PP-Co	CO(82.4)	-2	-0.6	10	[206]
MOF-NS-Co <sup>[e]</sup>	CO(98)	-17.9	-1.0	12	[207]
NNU-17	CO(90)	-9	-1.0	30	[208]
Ag/UiO	CO(90)	-40	-1.18	1	[209]
Cu <sub>2</sub> O/Cu-HHTP	CH <sub>4</sub> (73)	-10.8	-1.4	5	[210]
MOL-CoN <sub>x</sub>	CO(99)	-2.3 <sup>[f]</sup>	-0.5	4	[211]
CoPc-Cu-O	CO(85)	-17.3	-0.74	--	[212]
PCN-223	CO(90.7)	-6	-0.76	20	[213]
NNS-33	CH <sub>4</sub> (73)	-10.8	-1.4	5	[214]
UiO film on Ag	CO(80)	-0.4	-0.8	5	[215]
Cu <sub>3</sub> (HHTQ) <sub>2</sub>	MeOH(53.6)	-0.5	-0.4	10	[216]
PcCu-Cu-O/CNT	C <sub>2</sub> H <sub>4</sub> (50)	-7.3	-1.2	4	[217]
HATNA-Cu	CH <sub>4</sub> (78)	-10.5	-1.5	12	[218]
BIF-102 NSs	C <sub>2</sub> H <sub>4</sub> (11.3)	-14	-1.0	5	[219]
Ni-Pc-NiO <sub>4</sub>	CO(90)	-37.8	-1.15	10	[220]
POM@PCN-222(Co)	CO(90)	-16.1	-0.9	--	[221]
Zr/Ti-PCN-224(Co) <sup>[e]</sup>	CO(93.6)	-4.8	-0.7	11	[222]
C@In-BCP	HCOO <sup>-</sup> (90)	-7.7	-0.84	20	[223]
In-MOF-[NiS <sub>4</sub> ]	HCOO <sup>-</sup> (90)	-40.2	-1.3	12	[224]
Cu(111)@Cu-THQ	C <sub>2</sub> H <sub>4</sub> (57.2)	-14.3	-1.4	8.5	[225]
2Bn-Cu@UiO-67 <sup>[g]</sup>	CH <sub>4</sub> (81)	-420	--	0.16	[226]
Su-100	HCOO <sup>-</sup> (90)	-8	-0.97	0.5	[227]
monolayer Cu-TCPP <sup>[e]</sup>	C <sub>2</sub> (41.1)	--	-1.4	7	[228]

[a] Non-aqueous electrolysis is excluded. [b] FE to a certain product. [c,d] The best performance with a good FE. [e] Photo-coupled ECR reaction. [f] Unit: A·mg<sub>Co</sub><sup>-1</sup>. [g] Test in GDE.

## 1. Metal SBUs as active sites

The occurrence of the ECR reaction is mainly dependent on metal sites, mainly provided by the metal SBUs of MOF catalysts. The first example using SBUs as active sites for ECR reduction is a copper rubeanate framework, reported by Yamada and co-workers in 2012.<sup>[27]</sup> This MOF exhibited 30% Faradaic efficiency towards formic acid. The relationship between metal sites and product selectivity can be found in **Figure 1.11**. Common metal SBUs as catalytic sites are the following: Cu-based MOFs (mainly to  $C_{2+}$ ,  $CH_4$ ),<sup>[27,180,184,189,210,214,216,217,218,219,225,228]</sup> Ni-based MOFs (to CO),<sup>[193,220]</sup> Fe-based MOFs (to CO),<sup>[190,202]</sup> Co-based MOFs (to CO),<sup>[195]</sup> Zn-based MOFs (to CO),<sup>[179,181,186,192,200]</sup> Cd-based MOFs (to CO),<sup>[208]</sup> and p-block metal based MOFs (to formate)<sup>[188,199,201,223,224,227]</sup>. Common metal SBUs adopted for ECR reactions are depicted in **Figure 1.31**.

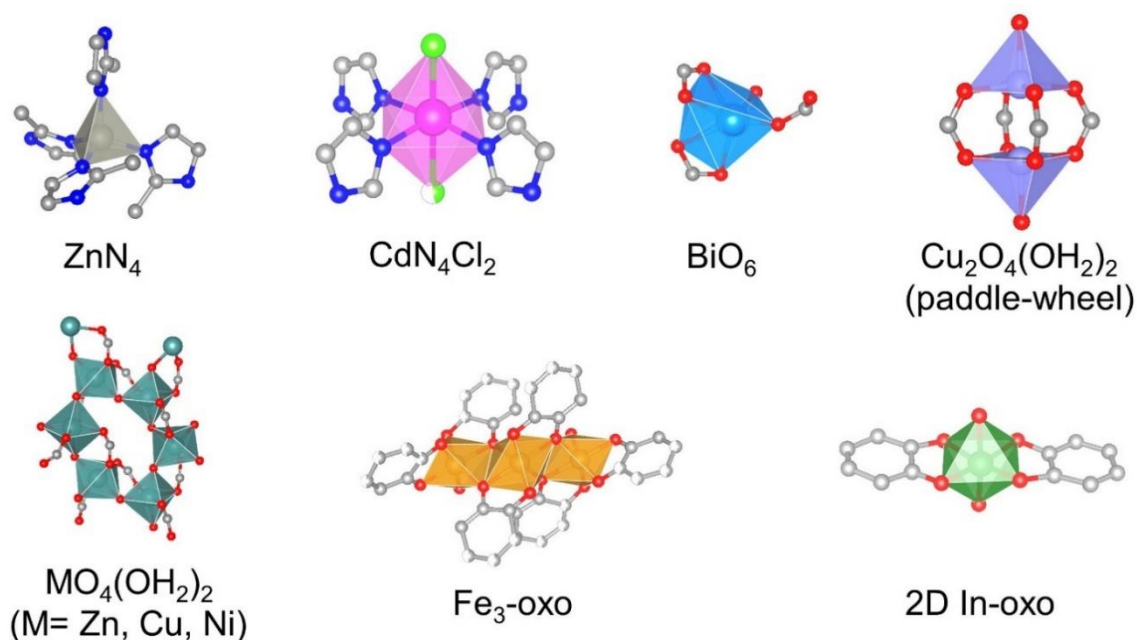


**Figure 1.31** Scheme of the common metal SBUs as active sites of MOFs for ECR reaction.

## 2. Linkers as active sites

In addition to metal SBUs, various linkers are often used as catalytic sites for ECR reactions. Some organometallic catalysts can be functionalized to construct MOFs, such as metal-porphyrins and metal-phthalocyanines (**Figure 1.32**).<sup>[229]</sup> Lin and co-workers reported the immobilization of active  $CoN_x$  metal complexes on linkers for catalytic ECR to  $CO$ .<sup>[211]</sup> When coordinated with metal ions, such linkers yield perfectly dispersed solid catalysts.<sup>[177,183,185,196, 204,206,207,213,218,221]</sup>

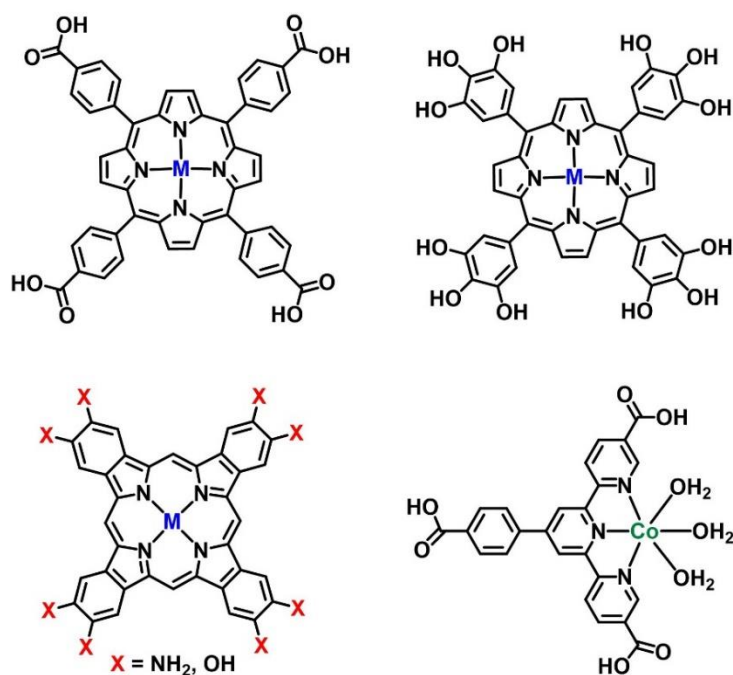


**Figure 1.32** Scheme of the common linkers as active sites of MOFs for ECR reaction.

### 3. Guest compounds as active sites

Taking advantage of the superior porosity of MOFs, guest compounds can be immobilized therein. The catalytic sites thus introduced can be metal compound particles<sup>[178,182,187,194,205,209,210,215]</sup> or molecular catalysts<sup>[191,197,198,226]</sup>.

In such composite systems, the functions of MOFs fall into the following categories: 1. They serve as templates, supports, and offer protections.<sup>[194,210]</sup> 2. They modulate the catalyst's electronic structure and surface states and stabilize intermediates.<sup>[194,209,215]</sup> 3. The confined pore space can enrich the reactants (CO<sub>2</sub>)<sup>[209]</sup> and improve the local pH.<sup>[194]</sup> A typical example came from Cao and his co-workers, shown in **Figure 1.33**. They constructed a two-dimensional conductive MOF (Cu-HHTP), followed by partial destruction to form a uniform distribution of 3.5 nm Cu<sub>2</sub>O particles on the MOF. The Cu-HHTP acted as a Cu precursor and as a template to produce, disperse and protect the tiny Cu<sub>2</sub>O nanoparticles. DFT calculations indicated that the hydroxyl groups from the linker could stabilize various intermediates, especially \*CHO, through hydrogen bonding, inhibiting the production of formaldehyde and methanol, thus facilitating the formation of CH<sub>4</sub>.



one dimension, such as constructing two-dimensional large-conjugated MOFs.<sup>[231]</sup> When using two-dimensional or ultrasmall three-dimensional MOFs, even if the conductivity is not significantly improved, they can avoid conductivity dilemmas due to their higher exposure of catalytic sites. However, although many MOFs are two-dimensional in the crystal structure, the actual synthesis often does not result in two-dimensional nanosheets. Direct synthesis of monolayer 2D-MOFs for electrochemical applications is still in its infancy.<sup>[191,211]</sup>

Another strategy focuses on encapsulating conductive substances (e.g., carbon particles,<sup>[223]</sup> conductive molecules<sup>[197,221]</sup>) in the pores of MOFs to enhance the overall electrical conductivity. This approach has the advantage of being more versatile and can be applied to a wide range of MOFs; however, the filler, while enhancing the conductivity, may also be accompanied by blockage of the diffusion channels.

### 1.3.3.2 Stability issues

The stability of MOF materials has been a central issue that has plagued the direct use of MOFs as electrocatalysts. If MOFs are actually unstable under electrocatalytic conditions, these MOFs could be attributed to the MOF-derived materials.<sup>[176]</sup> These MOF catalysts are actually pre-catalysts (**Figure 1.34**). Unfortunately, this issue did not receive much attention in the early days. Moreover, the development of operando characterization techniques limited the ability to reveal the structural evolution of MOFs during electrocatalysis.

The stability of the MOFs during electrocatalysis should be seriously considered and examined. If metal SBUs are used as catalytic sites, their structural stability can be quickly evaluated using the HSAB theory. It should be noted that in the actual catalytic process, the valence state of central metals is often reduced or partially reduced, and the effect of this on the structural stability should be taken into account when applying the HSAB theory. If the linkers are used as the active sites, the metal SBUs are usually inert metals, such as  $Zr^{4+}$  and  $Al^{3+}$ . Zr and Al-based MOFs were believed to remain relatively stable in ECR reactions, because of their limited redox properties.<sup>[209]</sup> It is noteworthy that when electrocatalysis occurs, electrons are transferred to the metal sites coordinated to the linkers. These reduced metal sites should become correspondingly larger in radius and potentially detach from the linkers, which is destructive to the active sites.<sup>[232]</sup> This detachment process may be intensified with the increase of the applied potential and higher current densities.

The characterization of the stability of MOFs should be evaluated not only by electrocatalytic performance stability, but also by various structural and surface state characterizations, such as AFM, XPS, XAS, XRD, and electron microscopy.<sup>[176]</sup>

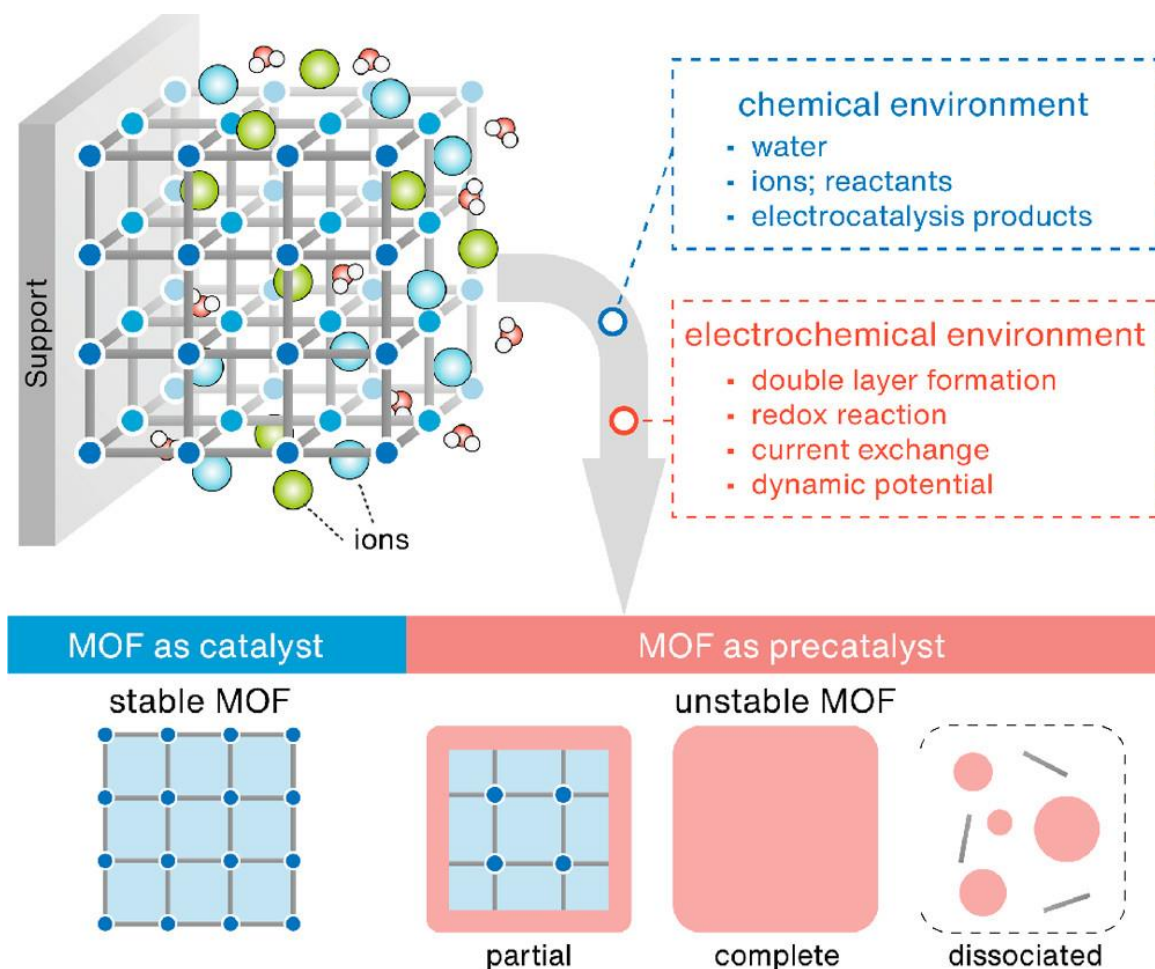


**Figure 1.34** Scheme illustrating the environmental factors that may affect the stability of MOFs in electrocatalytic reactions and the classification of MOFs according to the degree of damage.<sup>[176]</sup>

### 1.3.3.3 Understanding of the effect of the structural optimizations

Whether MOFs are used directly as electrocatalysts or as MOF-derived electrocatalysts<sup>[233]</sup>, their versatile structures and high structural tunability could provide convenience and advantages to achieve catalyst optimizations. Maintaining the structural integrity of MOFs in the electrocatalytic process is essential to provide a well-defined reaction environment, which is an advantage to study structure-activity relationships.<sup>[176]</sup> This requires explicit structural characterizations, mechanistic studies and the support of theoretical calculations.<sup>[200,209]</sup> However, the very large primitive cells of MOF crystals place higher demands on computational performance.



## 2 | Motivation

Electrocatalytic carbon dioxide reduction (ECR) reactions are a well-recognized pathway to achieve carbon neutrality. In recent years, with significant advances in renewable electricity, the electricity-driven conversion of CO<sub>2</sub> to fuels or valuable chemicals has become more economically attractive. However, no industrial plants are available yet, because reductions in reactor costs and improvements in catalytic performance and stability are still needed. Among the many ECR products, formic acid/formate can compensate installation costs by a higher economic yield, due to its highest market price per mol of consumed electrons.<sup>[15,16]</sup> Therefore, formic acid/formate was chosen as the ideal target product in this thesis.

In academic research, chemists prefer to focus on the investigation of potential structure-activity relationships of catalysts, which provide a basis for the rational design of advanced catalysts. As emerging materials, metal-organic frameworks (MOFs) are widely used in catalysis research due to their ultra-high specific surface area, high porosity, well-defined structure, and high structural tunability. The first study using MOFs as catalysts can be dated to 2007,<sup>[234]</sup> while the major beginning of electrocatalysis by MOFs appeared only five years ago (**Figure 1.29**). The main obstacle is the poor electrical conductivity of most MOFs, which was considered unsuitable for electrocatalysis.<sup>[165]</sup> In addition, stability issues are a pitfall when using MOFs to study structure-activity relationships.

To address this challenge, the present work intends to develop efficient MOF electrocatalysts for ECR reactions. The keys of using MOFs as direct electrocatalysts are to solve the problem of poor electrical conductivity and structural instability during electrocatalytic reactions. A straightforward idea to improve the conductivity is to select conductive MOFs (mainly highly conjugated two-dimensional MOFs)<sup>[228]</sup> that have been reported several times for ECR reactions.<sup>[197,207,209,213,214,217]</sup> However, the metal SBUs used in these catalysts, namely divalent metal sites coordinated to O atoms, are predicted to be unstable according to HSAB theory and generally possess many unsaturated sites (lower coordination number), indicating an instability during ECR reaction. Moreover, considering that the metal SBUs in these catalysts are active sites, they will be reduced to catalyze the reaction, which will exacerbate the instability.<sup>[207]</sup> Therefore, we discarded this strategy. Considering that the main drawback of poor conductivity is the waste of catalytic sites located on the inner surface, the construction of 2D-MOFs would be an applicable way to avoid the described problems even if the conductivity is still low.

In order to maintain the stability of MOFs during electrocatalysis, the desired choice is that its components do not serve as catalytic sites for direct ECR reactions, which dictates that the catalytic sites are provided by the guest compounds. Zr-based MOFs, while being stable, have a good diversity of coordination conformations, which facilitates the formation of 2D-MOFs. In addition, the abundance of functional groups on their surfaces is beneficial for facile post-modification to immobilize guest compounds and modulate the micro-environments.<sup>[162,235]</sup> As for the generation of formic acid/formate, the p-block metals are the best choice (**Figure 1.11**).

The catalytic performance will be preferably tested in H-type cells, which are often widely adopted in academic research, for the convenience of a quick comparison of the intrinsic catalytic performance of different catalysts. Furthermore, based on the ample experience of our institute on gas diffusion electrodes, such electrodes will also be applied.

Thus, the specific targets of this work were:

- (1) Design and synthesize 2D-MOF as thin as possible, with good stability to allow the direct ECR reactions.
- (2) Develop post-modification strategies to immobilize the active guest species.
- (3) Achieve an efficient ECR catalyst to formic acid/formate.
- (4) Investigate the structure-activity relationship of the ECR reaction by tuning the microenvironment of the active sites.

## 3 | Experimental Methods

### 3.1 Chemicals

Unless otherwise stated, all chemicals were purchased from commercial suppliers and used without further purification. The abbreviations and supplies of the chemicals are listed in the [Table 10.1](#).

### 3.2 Characterization methods

The characterization instruments used in work are listed in [Table 10.2](#).

#### 1 Chemical analysis

Metal contents were determined by Inductively Coupled Plasma Atomic Emission Spectroscopy (ICP-AES, Varian Vista-MPX). Since the samples used for ICP-AES must be an aqueous solution without any organic components, the catalyst samples had to be digested first. For Zirconium-containing samples, the samples were entirely digested in a mixture of nitric acid and hydrofluoric acid. For acetylene black based samples, a mixture of nitric acid and perchloric acid was chosen as the digestion agent. The non-dissolved fraction (carbon residue) can be removed by filtration to obtain a homogeneous aqueous solution for ICP-AES. The metal content was quantified using calibration plots of known concentrations. These measurements were carried out by Heike Fingerle (Institute of Technical Chemistry, University of Stuttgart). A summary of the ICP-AES results is listed in [Table 10.3](#).

#### 2 X-Ray Diffraction

X-ray diffraction (XRD) patterns were analyzed by a BrukerD8 Advance diffractometer of 35 kV and 40 mA with a Cu K $\alpha$  ( $\lambda = 0.154$  nm) radiation. The powder samples were pressed into a recessed Si plate. As for the dispersed samples, a drop of dispersion was drop-casted on a mirror Si plate, followed by XRD measurements.

#### 3 Porosity measurements

The porosities of the sample were determined by N<sub>2</sub> physisorption measurements, which were conducted on an Autosorb 3B (Quantachrome) at 77 K. Before the measurements, the samples

were degassed at 150 °C for 12 h under vacuum to remove the adsorbed solvents (DMF, Acetone or MeOH) without destroying the structures. The measurements were carried out by Dorothea Häussermann (Institute of Technical Chemistry, University of Stuttgart).

#### 4 Thermogravimetric analysis

Thermogravimetric analysis (TGA) was performed on a Setaram Thermogravimetric Analyzer Setsys TG-16/18 to determine the thermal stability. The measurements were done under air with a ramping rate of 2 °C·min<sup>-1</sup> and carried out by Jan Florenski (Institute of Technical Chemistry, University of Stuttgart).

#### 5 Nuclear Magnetic Resonance

Nuclear Magnetic Resonance was performed on a Bruker Advance 300. Three kinds of measurements were conducted. (1) Analysis of the synthesized linkers. Deuterated solvent (DMSO-d<sub>6</sub> or CDCl<sub>3</sub>) was selected based on the compound's solubility. The chemical shift was calibrated by the peak of the pristine solvent ( $\delta = 2.50$  ppm for DMSO;  $\delta = 7.24$  ppm for CHCl<sub>3</sub>). (2) Quantification of the liquid products of the ECR reaction. Samples were prepared by mixing 300  $\mu$ L electrolyte and 200  $\mu$ L D<sub>2</sub>O (with a known amount of TMSP as an internal standard for quantification). The concentration of TMSP in commercial D<sub>2</sub>O was quantified by the DMSO<sub>2</sub> standard. The <sup>1</sup>H-NMR was conducted by a solvent suppression method (*zgpr* method). The chemical shifts of the products of CO<sub>2</sub> reduction can be determined based on a former publication.<sup>[236]</sup> (3) Dissolution/NMR tests. The MOFs samples were firstly dissolved into KOH/D<sub>2</sub>O (around 1 M). The supernatant can be collected by filtration and then subjected to the NMR test.

#### 6 Scanning Electron Microscopy

TESCAN VEGA3 XM collected conventional Scanning electron microscopy (SEM) images with tungsten filament electron source and SE (secondary electron) detector. Limited to the poor resolution, it can only be used to distinguish roughly the morphology of the samples. Field emission scanning electron microscopy (FE-SEM) images were collected using a Zeiss Supra 40 with a field S3 emission scanning electron microanalyzer to get a better resolution.

#### 7 Atomic Force Microscopy

Atomic force microscopy (AFM) analysis was conducted on a Bruker Multi-mode 8 Atomic Force Microscope. The AFM sample was prepared by a drop-casting method, using mica as support. The dispersion should be thoroughly ultra-sonicated before use. The measurements were carried out by Qian Song (Institute of Technical Chemistry, University of Stuttgart) at Max Planck Institute for Solid State Research.

### 8 Product quantification (HPLC+GC)

The liquid products, especially formate, were detected by high-performance liquid chromatography (HPLC, Agilent 1260 Infinity) equipped with a NUCLEOGEL Sugar 810 H column and a refractive index detector (RID), using 0.5 mM H<sub>2</sub>SO<sub>4</sub> as an eluent. The concentration can be calculated using a calibration plot. The standard formate samples were prepared by dissolving a certain amount of HCOOK into 0.5 M KHCO<sub>3</sub>, a common electrolyte.

The gaseous products were analyzed by offline/online gas chromatography (GC, Agilent 7890A), equipped with PLOT&MOLESIEVE columns, a thermal conductivity detector (TCD), and a flame ionization detector (FID), using He as carrier gas. The concentration can be calculated using a calibration plot. The standard gas bottles were purchased from Westfalen AG. One main drawback of using He as the carrier gas is the insensitivity towards the detection of H<sub>2</sub>, considering the very close molecular weights of H<sub>2</sub> and He. The main reason to adopt He rather than Ar or N<sub>2</sub> as the carrier gas is to increase the sensitivity towards CO, one of ECR reactions' main products. As a result, the detection limit of H<sub>2</sub> starts at around 1 %, while that for CO was 100 ppm.

### 9 X-ray Photoelectron Spectroscopy

X-ray photoelectron spectroscopy (XPS) was performed on a Kratos Axis Ultra, equipped with a monochromated Al K $\alpha$  X-ray source ( $h\nu = 1486.6$  eV). A charge neutralizer was applied, to compensate for the poor conductivity of the samples. The calibration was done by setting C 1s from adventitious carbon to 284.8 eV. Survey scans are performed before and after detailed scans to check for potential beam damage. The fitting conditions and results are listed in [Table S10.4](#). These measurements are carried out by Kathrin Küster (Max Planck Institute for Solid State Research, Stuttgart).

### 10 Transmission Electron Microscopy

The sample for the microscopy study was prepared using the drop-casting method: a drop of the sample dispersion was placed on a carbon-coated Cu grid (TEM grid) and dried in air. There were two types of TEM grids used in this work. One is the conventional TEM grid with the surface covered by a complete carbon film (several layers of carbon atoms). This TEM grid is common and suitable for ultrafine nanoparticles. However, it may also bring background interference, especially for the ultrathin 2D-materials. Hence, a TEM grid of lacey carbon (holey carbon films) was also adopted, especially for a clean background for high-resolution HAADF-STEM and EELS images.

Conventional Transmission electron microscopy (TEM) images were collected on a Philips CM-200 FEG TEM. The phase analysis of TEM images is based on contrast mechanisms,

including mass-thickness contrast, Z contrast, and diffraction contrast.

Aberration corrected HRTEM was performed using a JEOL ARM200F TEM equipped with a cold-field emission gun and a post specimen spherical aberration corrector (Cs) operated at an acceleration voltage of 80 kV. For STEM and EELS, we used a JEOL ARM200F equipped with a DCOR corrector (CEOS GmbH), a cold-field emission electron gun, and a Gatan GIF Quantum ERS electron energy-loss spectrometer. The acceleration voltage was set to 200 kV. HAADF-STEM imaging was performed with a convergent semi-angle of 20.4 mrad and the collection semi-angle of 70-300 mrad. A collection semi-angle of 111 mrad was used for EELS measurements with a Gatan K2 Summit camera. EELS spectrum imaging was performed with a dispersion of 0.5 eV/channel and 1900 eV drift tube energy with a 4000-pixel wide detector for the simultaneous acquisition of Zr and Bi spectrum images. The raw spectrum image data were first denoised by applying the principal component analysis (PCA) with a multivariate statistical analysis (MSA) plugin (HREM Research Inc.) in Gatan DigitalMicrograph and then smoothed using a spatial filter in Gatan DigitalMicrograph. 4D-STEM datasets were acquired with a Merlin direct electron detector ( $256 \times 256$  pixels, Quantum Detectors), operating in the 1-bit mode with continuous reading/writing at a pixel dwell time of  $4.8 \times 10^{-5}$  s. All the high-resolution electron microscopy measurements were carried out by Hongguang Wang (Max Planck Institute for Solid State Research, Stuttgart).

### 3.3 Experimental synthesis

#### 3.3.1 2D-MOFs

##### 3.3.1.1 Zr-TATB

###### 1. H<sub>3</sub>TATB Linker synthesis

The 4,4',4''-s-triazine-2,4,6-triyl-tribenzoic acid (H<sub>3</sub>TATB) was synthesized according to the previous literature.<sup>[237]</sup> The typical synthesis route is illustrated in **Figure 3.1**.

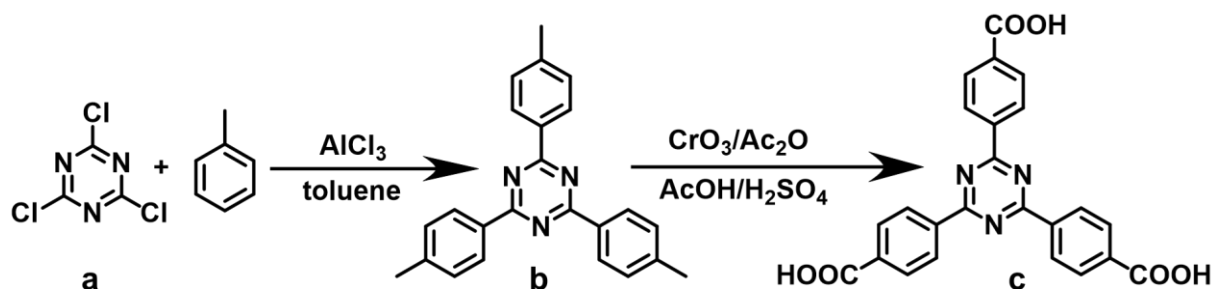


**Figure 3.1** Scheme illustrating the procedure of the H<sub>3</sub>TATB synthesis.

1) Synthesis of 2,4,6-tri-*p*-tolyl-*s*-triazine (**b**)

Generally, 20 g anhydrous AlCl<sub>3</sub> was added into a 250 mL two-necked flask containing 50 mL dry toluene (de-watered by molecule sieve), and the temperature was set to 60 °C. Then, 8.3 g Cyanuric chloride (C<sub>3</sub>N<sub>3</sub>Cl<sub>3</sub>, **a**) was added slowly over ~1 hour. After all the C<sub>3</sub>N<sub>3</sub>Cl<sub>3</sub> was added, the mixture was stirred overnight at 60 °C. The resulting red sticky oil was poured into a large amount of ice water to destroy the AlCl<sub>3</sub>, followed by extraction using 100 mL CHCl<sub>3</sub>. The organic layer was filtered. Methanol was added into CHCl<sub>3</sub> until the needle-like solid precipitated completely. The rest of the solid was recrystallized with hot toluene to harvest white needle-like crystalline solids. The successful synthesis was confirmed by <sup>1</sup>H NMR (δ, CDCl<sub>3</sub>): 2.40 (s, 9H), 7.25 (d, 6H), 8.57 (d, 6H) (Figure 3.2).

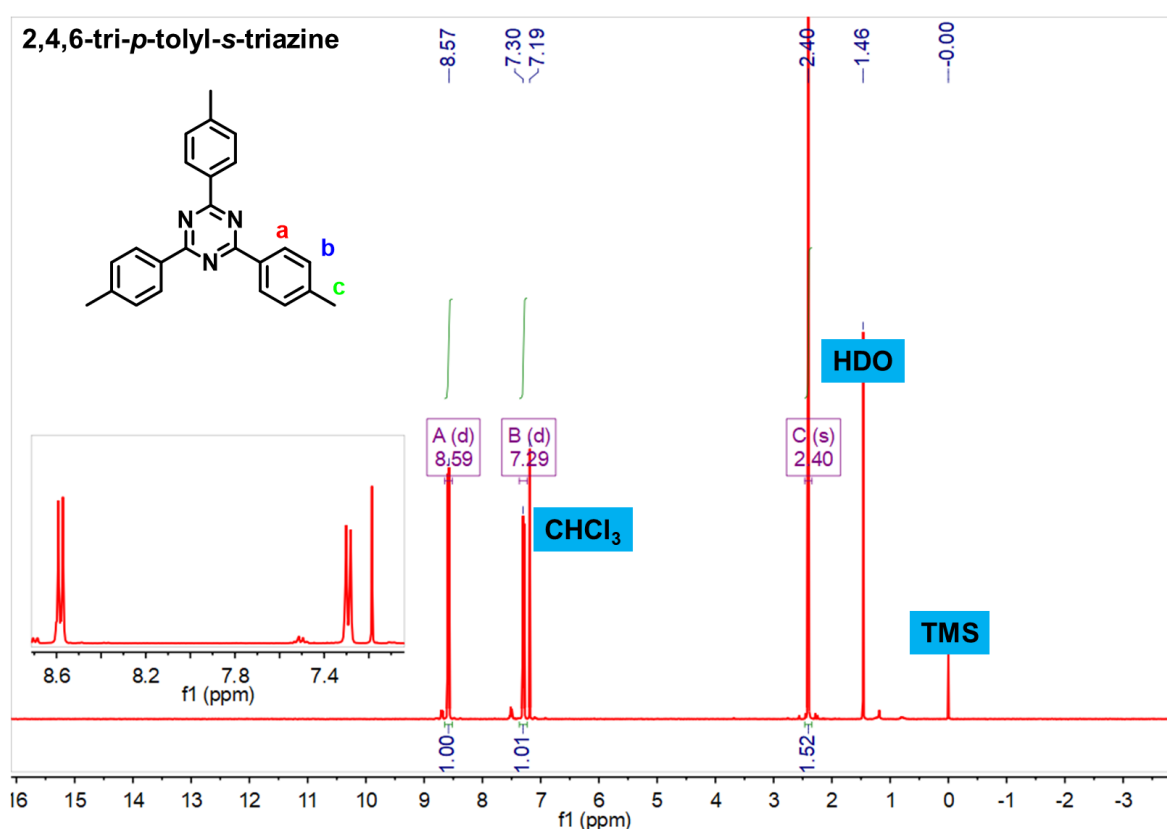


**Figure 3.2** <sup>1</sup>H-NMR spectrum of the 2,4,6-tri-*p*-tolyl-*s*-triazine, using CDCl<sub>3</sub> as a solvent.

2) Synthesis of H<sub>3</sub>TATB (**c**)

A 500 mL conical flask was charged with 2.78 g 2,4,6-tri-*p*-tolyl-*s*-triazine (**b**) dissolved in 70 mL acetic acid, then 4.4 mL of H<sub>2</sub>SO<sub>4</sub> was added under a cold water-ice bath. Subsequently, 7.2 g chromium oxide was slowly added in 4.8 mL acetic anhydride under stirring, which was then slowly added into the flask under a cold ice-water bath. The resulting brown slurry was stirred overnight at room temperature. Next, the mixture was redispersed into 300 mL ice water. The solid product was collected by centrifugation and washed with water to remove the Cr<sup>3+</sup> and HOAc until the solid color became light-yellow. The solid product was then dissolved in 200 mL of 2 M NaOH

solution. After the unreacted starting material was removed by centrifugation, the solution was acidified with 10% HCl to give a creamy white precipitate (until pH < 3). Next, the crude product was filtered and dried in an oven. Recrystallization of the crude product with DMF gave the pure product as a white solid. The successful synthesis was confirmed by  $^1\text{H}$  NMR ( $\delta$ ,  $d_6$ -DMSO): 8.22 (d, 6 H), 8.83 (d, 6 H), 13.33 (s, 3 H) (Figure 3.3).

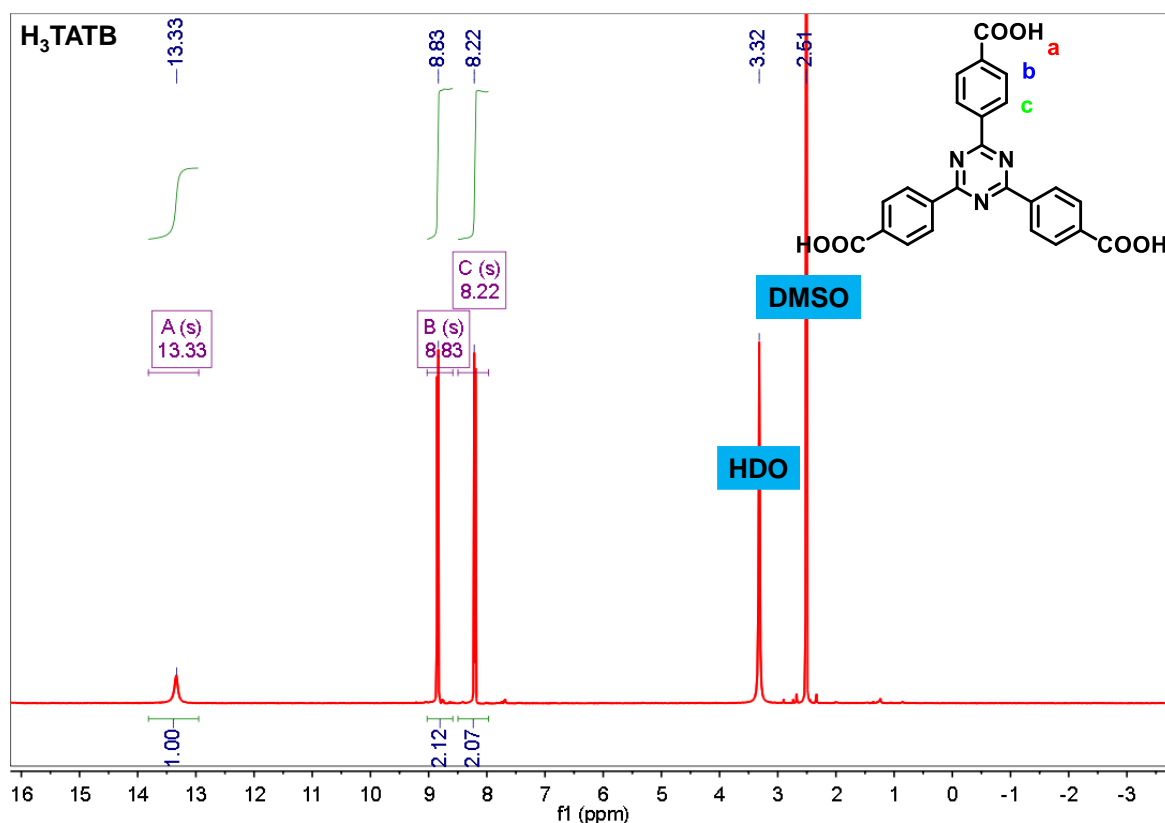


**Figure 3.3**  $^1\text{H}$ -NMR spectrum of the  $\text{H}_3\text{TATB}$ , using  $d_6$ -DMSO as a solvent.

## 2. Zr-TATB MOL

Generally, 190 mg  $\text{ZrOCl}_2 \cdot 8\text{H}_2\text{O}$  was dissolved into a mixture of 6 mL DMF and 4 mL glacial HOAc, further transferred into a 20 mL vial with a cap. The vial was placed in an oven at  $85^\circ\text{C}$  for 2 hours to accelerate cluster formation. Then, 44 mg  $\text{H}_3\text{TATB}$  was added to the above solution, followed by ultrasonication. The vial was solvothermally treated in an oven at  $120^\circ\text{C}$  for 24 hours. After the reaction, as-synthesized Zr-TATB MOL can be separated by centrifugation and washed with DMF and acetone/MeOH. After drying in an oven at  $85^\circ\text{C}$ , the white powder can be harvested.

Here are some comments on the synthesis of the Zr-TATB MOL. 1. The addition of  $\text{ZrOCl}_2 \cdot 8\text{H}_2\text{O}$  is flexible, of which amounts ranging from 96 mg to 190 mg do all work. 2. The thermal treatment of the mixture of  $\text{Zr}^{4+}$ /DMF/HOAc was to promote the formation of the  $\text{Zr}_6$ -oxo clusters, which is not compulsory. 3. The solvothermal time can be from 12 hours to 48 hours. 4. Besides static synthesis, continuously stirring at  $100^\circ\text{C}$  in an oil bath for 12 hours also works, confirmed by PXRD and TEM.

### 3. Worm-like Zr-TATB

17.2 mg  $\text{ZrCl}_4$  was firstly dissolved into a mixture of 2 mL DMF, 1.25 mL concentrated HCl, and 0.9 mL  $\text{H}_2\text{O}$ . And then, 22 mg  $\text{H}_3\text{TATB}$  was added and well-dispersed by the assistance of ultrasonication. The mixture was filled into a 20 mL vial, which was sealed with a cap and placed in an oven at  $120\text{ }^\circ\text{C}$  for 2 days. After the reaction, as-synthesized Zr-TATB MOL can be separated by centrifugation and washed with DMF and acetone/MeOH. After drying in an oven at  $85\text{ }^\circ\text{C}$ , the white powder can be harvested.

#### 3.3.1.2 Al-TCPP

##### 1 $\text{H}_4\text{TCPP}$ Linker synthesis

According to the previous literature, the tetrakis(4-carboxyphenyl)porphyrin linker ( $\text{H}_4\text{TCPP}$ ) was synthesized.<sup>[238]</sup> The typical synthesis route is illustrated in [Figure 3.4](#).

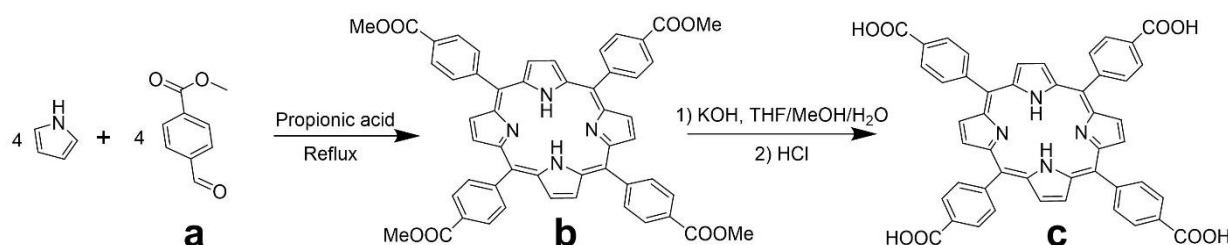


**Figure 3.4** Scheme illustrating the procedure of the  $\text{H}_4\text{TCPP}$  synthesis.

##### 1) Synthesis of 5,10,15,20-Tetrakis(4-methoxycarbonylphenyl)porphyrin (TPPCOOMe) (**b**)

6 g pyrrole and 13.8 g methyl p-formylbenzoate were added into a 500 mL flask, followed by adding 200 mL propionic acid. The mixture was stirred and refluxed overnight to finish the condensation. After the reaction, the mixture was filtered through a sand core funnel and washed with 200 mL EtOH, sufficient ethyl acetate, and a small amount of THF, respectively. The light purple powder can be collected after being dried at  $85\text{ }^\circ\text{C}$ . The successful synthesis was confirmed by  $^1\text{H}$  NMR ( $\delta$ ,  $\text{CDCl}_3$ ): -2.89 (s, 2H), 4.04 (s, 12 H), 8.22 (d, 8 H), 8.37 (d, 8 H), 8.74 (s, 8 H) ([Figure 3.5](#)).

##### 2) Synthesis of $\text{H}_4\text{TCPP}$ (**c**)

1.95 g TPPCOOMe (**b**) and 6.82 g KOH was dissolved into a mixture of 60 mL THF, 60 mL MeOH, and 60 mL  $\text{H}_2\text{O}$  in a 500 mL flask. The mixture was stirred and refluxed overnight to finish the hydrolysis. After the reaction, the mixture was cooled down to room temperature. 200 mL water was added to dilute the mixture, followed by neutralized by 1 M HCl solution until a pH of 5. This step is to precipitate the  $\text{H}_4\text{TCPP}$ . The dispersion was filtered through a sand core funnel and washed with water until the pH was around 7. The purple solid can be collected after drying

at 85 °C. The successful synthesis was confirmed by  $^1\text{H}$  NMR ( $\delta$ ,  $d_6$ -DMSO): -2.92 (s, 2H), 8.36 (dd, 16 H), 8.86 (s, 8 H) (Figure 3.6).

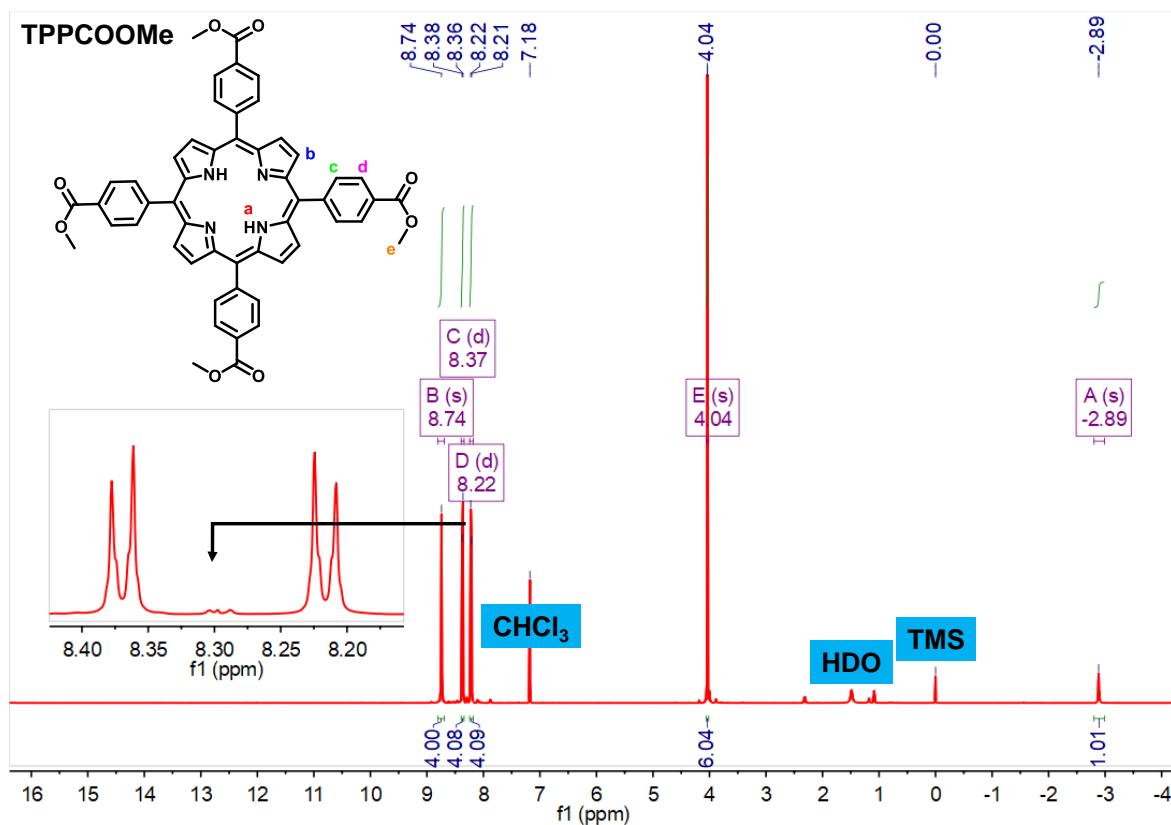


Figure 3.5 NMR spectrum of the TPPCOOMe, using  $\text{CDCl}_3$  as a solvent.

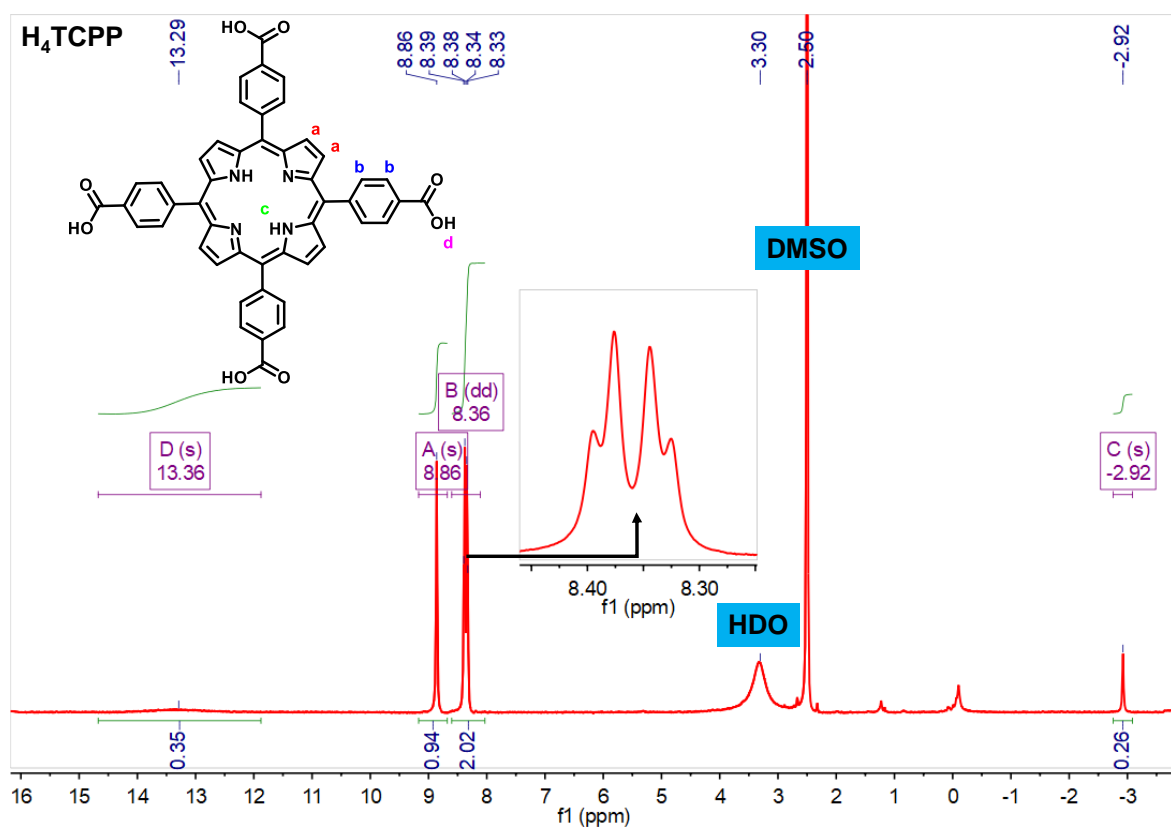


Figure 3.6 NMR spectrum of the  $\text{H}_4\text{TCPP}$ , using  $d_6$ -DMSO as a solvent.

## 2. Conventional Al-TCPP

The conventional synthesis of the Al-TCPP was modified from a previous report.<sup>[239]</sup> Typically, 150 mg  $\text{AlCl}_3 \cdot 6\text{H}_2\text{O}$  and 200 mg  $\text{H}_4\text{TCPP}$  were dispersed in 25 mL  $\text{H}_2\text{O}$  by ultrasonication. The mixture was then transferred into a 150 mL autoclave and sealed. The autoclave was placed in an oven at 180 °C for 16 hours. After the reaction, the solid was separated from the mother liquid by centrifugation and washed with DMF and acetone. The final product was collected after drying at 85 °C.

## 3. AlOOH precursors

The layered AlOOH was synthesized based on a previous report.<sup>[240]</sup> 5 g  $\text{Al}(\text{NO}_3)_3 \cdot 9\text{H}_2\text{O}$  and 1.52 g Urea were dissolved into 10 mL  $\text{H}_2\text{O}$ , followed by stirring at 50 °C for 1 hour. After that, the mixture was filled into a 60 mL autoclave, which was sealed and placed in an oven at 160 °C for 24 hours. After the reaction, the solid can be collected by filtration, washed with water, and dried at room temperature.

## 4. 2D Al-TCPP by AlOOH

37 mg AlOOH and 100 mg  $\text{H}_4\text{TCPP}$  were dispersed in 25 mL  $\text{H}_2\text{O}$  by ultrasonication. 3 mL concentrated HCl was added afterwards. The mixture was then filled into a 150 mL autoclave, which was sealed and placed in an oven at 180 °C for 16 hours. After the reaction, the solid was separated from the mother liquid by centrifugation and washed with DMF and acetone. The final product was collected after drying at 85 °C.

### 3.3.1.3 Co-ATA and derived materials

#### 1. Lamellar Co-ATA

Generally, 45 mg  $\text{CoCl}_2 \cdot 6\text{H}_2\text{O}$  and 34 mg ATA were dissolved into a mixture of 8 mL DMF, 0.5 mL EtOH, and 0.5 mL  $\text{H}_2\text{O}$ . 5 drops of triethylamine were added afterwards. The mixture was filled into a 20 mL vial, which was sealed with a cap and placed in an ultrasonication bath for 8 hours. After the reaction, the purple solid can be collected by filtration, washed with water, and dried at room temperature.

#### 2. Pyrolysis of Co-ATA

Certain amount of the Co-ATA was placed in a ceramic boat and placed into a tube furnace. The pyrolysis proceeded at 400 °C with a heating rate of 5 °C /min under vacuum for 2 hours. The product was denoted as Co-ATA-400.

### 3.3.2 Bismuth-based composites

#### 3.3.2.1 BiO<sub>x</sub>/MOL

Generally, 40 mg Zr-TATB MOL and 60 mg Bi(NO<sub>3</sub>)<sub>3</sub>·5H<sub>2</sub>O were dispersed in 4 mL DMF. The mixture was transferred into a 20 mL vial, which was sealed with a cap and stirred at room temperature overnight. The catalysts were harvested by centrifugation, washed with DMF, H<sub>2</sub>O, and acetone, and finally dried at 85 °C.

#### 3.3.2.2 Bi<sub>2</sub>O<sub>3</sub>-based composites using different supports (MOL, UiO, AB)

##### 1. UiO-66

UiO-66 synthesis: Generally, 186 mg ZrCl<sub>4</sub> and 138 mg BDC were dissolved in 50 mL DMF containing 6 mL HOAc. After adding 2 drops of H<sub>2</sub>O, the mixture was transferred into a 100 mL glass flask. The flask was kept at 120 °C for 12 h under continuously stirring. After cooling down to room temperature, the solid was isolated by centrifuging and fully washed with DMF and acetone.

##### 2. Bi<sub>2</sub>O<sub>3</sub>/MOL, Bi<sub>2</sub>O<sub>3</sub>/UiO-66, Bi<sub>2</sub>O<sub>3</sub>/AB

Generally, 40 mg support (Zr-TATB MOL, UiO-66 or Acetylene Black) and 60 mg Bi(NO<sub>3</sub>)<sub>3</sub>·5H<sub>2</sub>O were dispersed in 4 mL DMF. The mixture was transferred into a 20 mL vial sealed with a cap and solvothermally treated in an oven at 85 °C for 12 hours. The catalysts were harvested by centrifugation, fully washed with DMF, H<sub>2</sub>O, and acetone, and finally dried at 85 °C. The catalysts were denoted as Bi<sub>2</sub>O<sub>3</sub>/MOL, Bi<sub>2</sub>O<sub>3</sub>/UiO, and Bi<sub>2</sub>O<sub>3</sub>/AB, respectively.

##### 3. Bi<sub>2</sub>O<sub>3</sub>/UiO and Bi<sub>2</sub>O<sub>3</sub>/AB loaded with 2.6 wt% Bi

The loading procedures are consistent with Bi<sub>2</sub>O<sub>3</sub>/MOL, except for the amount of added precursors Bi(NO<sub>3</sub>)<sub>3</sub>·5H<sub>2</sub>O: 72 mg for Bi<sub>2</sub>O<sub>3</sub>/UiO-2.6, 128 mg for Bi<sub>2</sub>O<sub>3</sub>/AB-2.6.

##### 4. Bi<sub>2</sub>O<sub>3</sub>/MOL with different Bi loadings (Bi<sub>2</sub>O<sub>3</sub>/MOL-X)

The loading procedures are consistent with the synthesis of Bi<sub>2</sub>O<sub>3</sub>/MOL, except for the amount of added precursors Bi(NO<sub>3</sub>)<sub>3</sub>·5H<sub>2</sub>O: 8 mg for Bi<sub>2</sub>O<sub>3</sub>/MOL-0.6, 30 mg for Bi<sub>2</sub>O<sub>3</sub>/MOL-1.4, 120 mg for Bi<sub>2</sub>O<sub>3</sub>/MOL-3.1.

#### 3.3.2.3 Other bismuth-based MOL composites

##### 1. BiOCl/MOL(1)

40 mg Zr-TATB MOL and 40 mg BiCl<sub>3</sub> were dispersed in 4 mL DMF by ultrasonication. The mixture was transferred in a 20 mL vial sealed with a cap and placed in an oven at 85 °C for 24

hours. A white powder was harvested by centrifugation, fully washed with DMF and acetone, and finally dried at 85 °C.

#### 2. BiO<sub>x</sub>/MOL(2)

30 mg Zr-TATB MOL and 60 mg Bi(NO<sub>3</sub>)<sub>3</sub>·5H<sub>2</sub>O were dispersed in 10 mL acetone by ultrasonication. The mixture was transferred in a flask and refluxed for 2 hours. A white powder was harvested by centrifugation, fully washed with acetone, and finally dried at 85 °C.

#### 3 [Bi<sub>6</sub>O<sub>6</sub>]<sup>6+</sup>/MOL(4)

40 mg Zr-TATB MOL and 60 mg Bi(NO<sub>3</sub>)<sub>3</sub>·5H<sub>2</sub>O were dispersed in 4 mL MeCN by ultrasonication. The mixture was transferred in a 20 mL vial sealed with a cap and placed in an oven at 85 °C for 24 hours. A white powder was harvested by centrifugation, fully washed with MeCN and acetone, and finally dried at 85 °C.

#### 4. Bi/MOL(5)

30 mg Zr-TATB MOL and 40 mg Bi(NO<sub>3</sub>)<sub>3</sub>·5H<sub>2</sub>O were dispersed in 4 mL DMF by ultrasonication. The mixture was sealed in an autoclave and placed in an oven at 150 °C for 16 hours. A grey powder was harvested by centrifugation, fully washed with DMF and acetone, and finally dried at 85 °C.

#### 5. BiO<sub>x</sub>I<sub>y</sub>/MOL(6)

BiO<sub>x</sub>I<sub>y</sub>/MOL(6) could be obtained by post-treatment of Bi<sub>2</sub>O<sub>3</sub>/MOL with KI. Specifically, 50 mg KI was added in a fresh Bi<sub>2</sub>O<sub>3</sub>/MOL dispersion (40 mg in 4 mL DMF). The mixture was in an ultrasonic bath for 15 minutes. An orange powder was harvested by centrifugation, washed with acetone, and finally dried at 85 °C.

#### 6. BiOCl/MOL(7)

BiOCl/MOL(7) could be obtained by a hydrothermal post-treatment of Bi<sub>2</sub>O<sub>3</sub>/MOL. To be precise, 20 mg Bi<sub>2</sub>O<sub>3</sub>/MOL was dispersed in 5 mL tap water and sealed into an autoclave. The hydrothermal treatment was done at 160 °C for 10 hours in an oven. A white powder can be harvested by centrifugation, washed with acetone, and dried at 85 °C. The chloride from natural water is enough for the phase transformation to BiOCl.

#### 7. Bi/MOL(8)

Metallic Bi/MOL (8) could be prepared by post-synthetic treatment of Bi<sub>2</sub>O<sub>3</sub>/MOL. First, 30 mg NaBH<sub>4</sub> as a reductant were dissolved in 2 mL cold MeOH. Then, 20 mg Bi<sub>2</sub>O<sub>3</sub>/MOL was dispersed into 8 mL MeOH, followed by quick addition of the reductant solution. After 30 seconds,

the resulting black powder was separated through centrifugation, washed with MeOH, and dried at room temperature under vacuum.

#### 8. Bi/MOL(9)

Bi/MOL(9) could be obtained by a hydrothermal post-treatment of Bi<sub>2</sub>O<sub>3</sub>/MOL. 20 mg Bi<sub>2</sub>O<sub>3</sub>/MOL was dispersed in 5 mL DMF and sealed into an autoclave. The solvothermal treatment was done at 160 °C for 10 hours in an oven. A grey powder was harvested by centrifugation, washed with acetone, and dried at 85 °C.

### 3.3.3 MOL composites with other metal sites

#### 3.3.3.1 Tin-based MOL composites

##### 1. Sn<sup>2+</sup>/MOL(1) and SnO<sub>x</sub>/MOL(2)

The Sn<sup>2+</sup> modification was carried out first to get Sn<sup>2+</sup>/MOL(1). 40 mg Zr-TATB MOL and 40 mg SnCl<sub>2</sub>·2H<sub>2</sub>O were dispersed in 4 mL DMF by ultrasonication. The mixture was transferred in a 20 mL vial sealed with a cap and placed in an oven at 85 °C for 24 hours. The Sn<sup>2+</sup>/MOL(1) could be harvested by centrifugation and subsequently washed with DMF and MeCN. The powder was re-dispersed in 5 mL MeCN without prior drying.

Because of the weak bonds between divalent metal ions and MOL, the appearance of proton solvents or other proton resources will lead to the detachment of the immobilized metal sites from MOLs. To stabilize the immobilized Sn species on Zr-TATB MOL, 100 μL H<sub>2</sub>O<sub>2</sub> was added into the above dispersion. The mixture was stirred at 85 °C for half an hour. A white powder was harvested by centrifugation, washed with acetone, and dried at 85 °C, which was named as SnO<sub>x</sub>/MOL(2).

##### 2. Sn<sup>4+</sup>/MOL(3)

40 mg Zr-TATB MOL and 40 mg SnCl<sub>4</sub>·5H<sub>2</sub>O were dispersed in 4 mL DMF by ultrasonication. The mixture was transferred in a 20 mL vial sealed with a cap and placed in an oven at 85 °C for 24 hours. A white powder was harvested by centrifugation, washed with DMF, H<sub>2</sub>O, and acetone, and finally dried at 85 °C.

##### 3. SnS<sub>2</sub>/MOL(4)

25 mg Zr-TATB MOL, 12.5 mg SnCl<sub>4</sub>·5H<sub>2</sub>O, and thioacetamide (TAA) were dispersed in 4 mL DMF by ultrasonication. The mixture was sealed in an autoclave. A solvothermal treatment was done at 150 °C for 8 hours in an oven. A brown powder can be harvested by centrifugation, washed with DMF, H<sub>2</sub>O, and acetone, and was finally dried at 85 °C.

#### 4. SnO<sub>2</sub>/MOL(5)

Generally, 20 mg Zr-TATB MOL and 10 mg SnCl<sub>2</sub>·2H<sub>2</sub>O were dispersed into 4 mL DMF. The mixture was sealed in an autoclave and solvothermally treated at 160 °C for 10 hours. A white powder was separated by centrifugation, washed with H<sub>2</sub>O/acetone, and dried at 85 °C, giving SnO<sub>2</sub>/MOL.

#### 3.3.3.2 Indium-based MOL composites

##### 1. InO<sub>x</sub>/MOL(1)

40 mg Zr-TATB MOL and 40 mg InCl<sub>3</sub> were dispersed in 4 mL DMF by ultrasonication. The mixture was transferred in a 20 mL vial sealed with a cap and placed in an oven of 85 °C for 24 hours. A white powder can be harvested by centrifugation, washed with DMF and acetone, and finally dried at 85 °C.

##### 2. InO<sub>x</sub>/MOL(2)

40 mg Zr-TATB MOL and 50 mg In(NO<sub>3</sub>)<sub>3</sub>·xH<sub>2</sub>O were dispersed in 4 mL DMF by ultrasonication. The mixture was transferred in a 20 mL vial sealed with a cap and placed in an oven at 85 °C for 12 hours. The white powder was harvested by centrifugation, washed with DMF, H<sub>2</sub>O, and acetone, and finally dried at 85 °C.

##### 3. In<sub>2</sub>O<sub>3</sub>/MOL(3)

Generally, 20 mg Zr-TATB MOL and 10 mg In(NO<sub>3</sub>)<sub>3</sub>·xH<sub>2</sub>O were dispersed in 4 mL DMF. The mixture was sealed in an autoclave and solvothermally treated at 160 °C for 10 hours. The white powder was separated by centrifugation, washed with H<sub>2</sub>O/acetone, and dried at 85 °C, giving In<sub>2</sub>O<sub>3</sub>/MOL(3).

#### 3.3.3.3 Antimony-based MOL composites (SbO<sub>x</sub>/MOL)

20 mg Zr-TATB MOL and 40 mg SbCl<sub>3</sub> were dispersed in 4 mL DMF by ultrasonication. The mixture was transferred in a 20 mL vial sealed with a cap and placed in an oven at 85 °C for 12 hours. A white powder was harvested by centrifugation, washed with DMF, H<sub>2</sub>O, and acetone, and finally dried at 85 °C.

#### 3.3.3.4 Copper-based MOL composites (CuI/MOF)

The Cu<sup>2+</sup> modification was carried out first to get Cu<sup>2+</sup>/MOL. 40 mg Zr-TATB MOL and 50 mg Cu(NO<sub>3</sub>)<sub>2</sub>·3H<sub>2</sub>O were dispersed in 4 mL DMF by ultrasonication. The mixture was transferred in a 20 mL vial sealed with a cap and placed in an oven at 85 °C for 12 hours. The Cu<sup>2+</sup>/MOL was harvested by centrifugation and washed with DMF. The powder was re-dispersed in 4 mL DMF

without prior drying. 50 mg KI was added in the above dispersion to precipitate the Cu species. The mixture was placed in an ultrasonica bath for 10 minutes. A light green powder was harvested by centrifugation, washed with acetone, and dried at 85 °C.

### 3.3.3.5 Palladium-based MOL composites (Pd/MOF)

20 mg Zr-TATB MOL and 15 mg Pd(NO<sub>3</sub>)<sub>2</sub> were dispersed in 2 mL DMF by ultrasonication. The mixture was transferred into a 20 mL vial sealed with a cap and placed in an oven of 85 °C for 12 hours. A dark-brown powder was harvested by centrifugation, washed with DMF and acetone, and finally dried at 85 °C.

## 3.4 Methods of electrochemical CO<sub>2</sub> reduction

### 3.4.1 H-type cell

#### 3.4.1.1 Preparation of working electrodes

The working electrodes were prepared by a standard drop-casting method (**Figure 3.7**). The catalyst ink was obtained by dispersing 1 mg catalyst, 1 mg acetylene black and 10 μL Nafion solution (5 wt% in mixture of lower aliphatic alcohols and water) into 1 mL isopropanol. After thorough ultrasonication, 200 μL ink was drop-casted onto the carbon paper (Toray paper, TGP-H-060) with an area of 1.0 × 1.0 cm<sup>2</sup>, followed by drying overnight in an oven at 85 °C. The loading of the catalyst was 0.2 mg·cm<sup>-2</sup>.

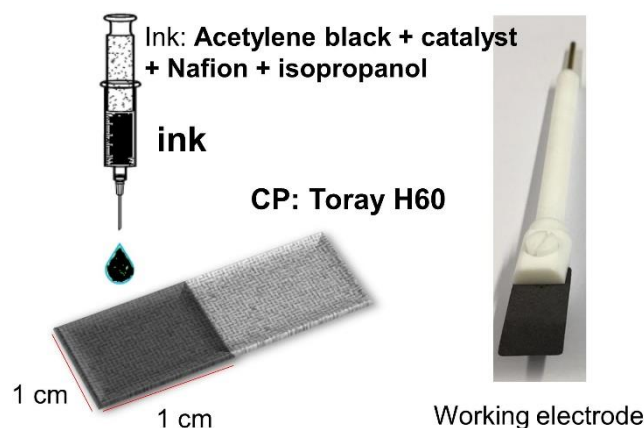


**Figure 3.7** Scheme of the drop-casting method to prepare the working electrodes for H-type cell.

#### 3.4.1.2 Set-up and ECR procedure

The scheme of the H-type cell with a three-electrode configuration is shown in **Figure 3.8**. The cell volume of the cathode chamber was measured to be 85 mL by water displacement method. The working electrode consisted of a PTFE coated electrode clip and the catalyst-loaded carbon

paper (Figure 3.7). The reference and counter electrodes were saturated Ag/AgCl (+0.199 V vs. SHE, 25 °C) and Pt foil, respectively. A cation exchange membrane (CEM, Nafion 117) was placed between the cathode and anode chamber. 0.5 M KHCO<sub>3</sub>, prepared using bi-distilled water, was adopted as the electrolyte in both cathode and anode chambers. The electrochemical workstation was an Orignalys OGF500 pack. All applied potentials were measured with auto-IR-compensation.

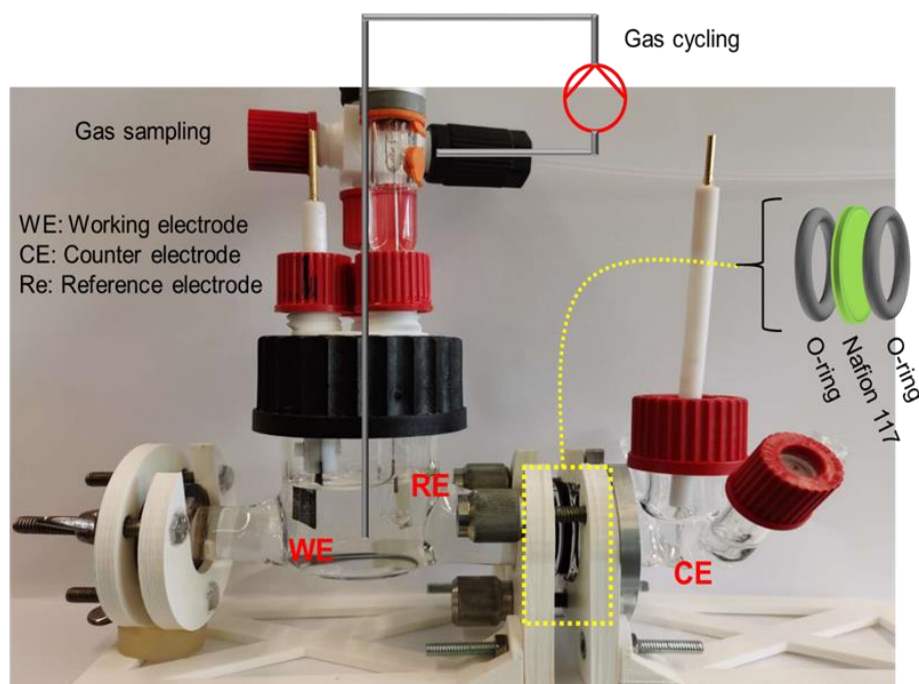


**Figure 3.8** Scheme of the used H-type cell with a three-electrode configuration for ECR measurements.

Pre-conditioning is required before the ECR measurements, comprising cyclic voltammetry (-1.5 to +1.0 V, vs. Ag/AgCl, 50 mV/s, 10 cycles) and pre-electrolysis (-1.8 V vs. Ag/AgCl, 10 min) under CO<sub>2</sub> atmosphere. The pre-conditioning can help to wet the electrode, form and stabilize the active sites on the reaction surface. To determine the preferred potential range of the ECR reaction, linear sweep voltammetry (LSV) measurements were conducted with a scan rate of 10 mV/s with CO<sub>2</sub> or Ar continuously bubbling. Prior to the chrono amperometric measurements, the electrolyte was purged with CO<sub>2</sub> to remove air. During the reaction, CO<sub>2</sub> was recirculated by a peristaltic pump. The speed of the magnetic stirrer was controlled to be 1000 rpm for every experiment. After certain reaction times, gas samples were taken and analyzed by offline GC. Liquid products were quantified by HPLC, and <sup>1</sup>H-NMR with a solvent suppression method. Considering it is a closed system without continuous supplies of fresh electrolyte and CO<sub>2</sub>, the accumulated amount of the products increases and the CO<sub>2</sub> concentration decreases along with the reaction time. This decides that the reaction time should be well controlled to ensure that there is enough product for quantification and that the concentration of CO<sub>2</sub> is not too low. CO<sub>2</sub> concentration should be above 80% during the entire reaction time. That is why most chrono amperometric experiments last only around 30 min. Key experiments were repeated at least twice to determine an error margin.

### 3.4.2 Gas Diffusion Electrodes

#### 3.4.2.1 Preparation of gas diffusion electrode

Gas diffusion electrodes were prepared by drop-casting the ink on homemade gas diffusion layers (GDLs). The ink was the same as the one used for the H-type cell test. The catalyst loading was controlled to be  $1.4 \text{ mg per cm}^2$ . We didn't adopt commercial GDLs (Carbon paper with microporous layer (MPL)) for preparing gas diffusion electrodes. The reason is the rapid wetting and flooding of the catalyst layer, which leads to a rapid drop in activity. The structure scheme of these two types is shown in **Figure 3.9**. The key advance of the homemade GDL is the higher hydrophobicity, considering the higher content of PTFE (35 wt%).<sup>[19]</sup>

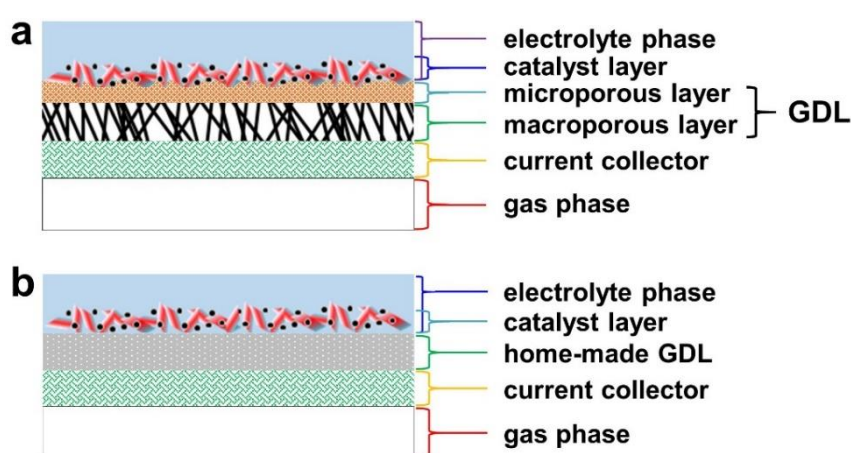


**Figure 3.9** Scheme of the structures of GDEs using (a) commercial GDL cell and (b) home-made GDL.

The homemade GDLs were prepared by dry-pressing as follows<sup>[19]</sup>: (1) Knife-milling of a mixture containing 35 wt% polytetrafluoroethylene powder (PTFE,  $350 \mu\text{m}$ ) and 65 wt% acetylene black; (2) Dry-pressing 400 mg PTFE/AB mixture ( $10 \text{ kN cm}^{-2}$ ); (3) Sintering at  $340 \text{ }^\circ\text{C}$  under  $\text{N}_2$  atmosphere for 10 min.

#### 3.4.2.2 Set-up and ECR procedure

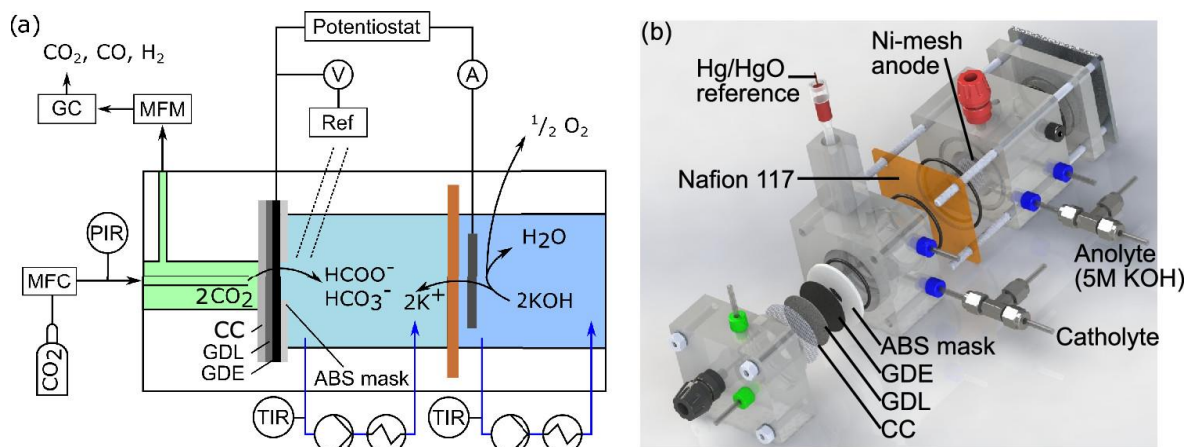


**Figure 3.10** Scheme of the GDE cell for ECR reaction.<sup>[19]</sup>

The experimental setup (**Figure 3.10**) for gas diffusion electrode tests was developed in previous work.<sup>[19]</sup> The working electrodes are a sandwich of a current collector (Ni mesh), a gas diffusion electrode, and an ABS mask. The ABS mask restricted the electrode area to an open circle of around 1 cm<sup>2</sup>. The reference and counter electrodes are a Hg/HgO (1M KOH, +0.140 V vs. SHE, 25 °C) electrode and a Ni mesh, respectively. 1.0 M KHCO<sub>3</sub> (99%, Carl Roth) and 5.0 M KOH (99%, Carl Roth) were adopted as electrolytes for the cathode and anode chamber, respectively. A cation exchange membrane (CEM, Nafion 117) was placed between the cathode and anode chamber. The electrochemical workstation was a Gamry Reference 3000 potentiostat. All the applied potentials were with auto IR compensation.

Pre-conditioning is required before measurements, which is cyclic voltammetry (-1.6 to +0.3 V, vs. Hg/HgO, 50 mV/s, 5 cycles) under CO<sub>2</sub> atmosphere. The pre-conditioning can help to wet the electrode, form and stabilize the active sites on the reaction surface. The inlet of CO<sub>2</sub> flow rate is adjusted by a mass flow controller (MFC). To reduce the influence of the CO<sub>2</sub> concentration on activity, the concentration of CO<sub>2</sub> in the outlet gas flow should be controlled to be above 80%, e.g., 10 ml/min for 200 mA·cm<sup>-2</sup>. The flow rate of the gas outlet was monitored by a mass flow meter (MFM). The gas sample was analyzed by an online GC. Liquid products were quantified by HPLC. The experiments were repeated at least twice to determine an error margin.

### 3.4.3 Data evaluation

The transformation of the measured potential to RHE as reference is based on the **equations (3.1)** and **(3.2)**. The pH value of the CO<sub>2</sub> saturated 0.5 M KHCO<sub>3</sub> in the H-type cell was 7.23.<sup>[241]</sup> The pH value of the 1.0 M KHCO<sub>3</sub> in the GDE cell was 8.4.<sup>[242]</sup>

$$E(\text{vs. RHE}) = E(\text{vs. Ag/AgCl}) + 0.199 + 0.0591 \times pH \quad \text{Eq(3.1)}$$

$$E(\text{vs. RHE}) = E(\text{vs. Hg/HgO}) + 0.150 + 0.0591 \times pH \quad \text{Eq(3.2)}$$

The Faradaic efficiencies (FEs) of the products are calculated according to **equation (3.3)**:

$$FE_i(\%) = \frac{j_i}{j_{total}} = \frac{n_i}{n_{total}} \times 100\% \quad \text{Eq(3.3)}$$

**FE<sub>i</sub>**: Faradaic efficiency for product i (%); **j**: Current density (A·cm<sup>-2</sup>); **n<sub>i</sub>**: Mole amount (mol) of the transferred electrons to certain product i; **n<sub>total</sub>**: Total transferred mole amount of the electron;

**S**: Reaction area (cm<sup>2</sup>); **t**: Reaction time (s).

Precisely, the liquid products in the H-type cell or GDE cell are calculated using **equation (3.4)**:

$$FE_i(\%) = \frac{n_i}{n_{total}} = \frac{c_i \cdot V_l \cdot z_i}{\left(\int_0^t I \cdot dt\right)/F} \times 100\%$$

Eq(3.4)

**c<sub>i</sub>**: Concentration (mol·L<sup>-1</sup>) of a certain liquid product; **z<sub>i</sub>**: Electron transfer number for a certain product *i*, which is 2 for CO, H<sub>2</sub>, or formate; **V<sub>l</sub>**: Volume (L) of the catholyte **I**: Current (A); **t**: Reaction time (s); **F**: Faraday constant, 96485 C/mol.

The gas products in H-type cell are calculated using **equation (3.5)**:

$$FE_i(\%) = \frac{n_i}{n_{total}} = \frac{z_i \cdot x_i \cdot V_g/V_m}{\left(\int_0^t I \cdot dt\right)/F} \times 100\%$$

Eq(3.5)

**V<sub>g</sub>**: Gas volume (L) in the cathode cell; **x<sub>i</sub>**: Mole fraction of certain gas product; **V<sub>m</sub>**: Molar volume of the gas, 22.4 L/mol.

The gas products in GDE cell are calculated using **equation (3.6)**:

$$FE_i(\%) = \frac{j_i}{j_{total}} = \frac{(z_i \cdot x_i \cdot V_g/V_m) \cdot F/t}{I_{total}} = \frac{(z_i \cdot x_i \cdot q_g/V_m) \cdot F}{I_{total}} \times 100\%$$

Eq(3.6)

**q<sub>g</sub>**: The flow rate (L/s) of the gas outlet.

The turnover frequency (TOF) is defined as the transferred electron for a certain product per active site and hour, which was calculated according to **equation (3.7)**:

$$TOF (s^{-1}) = \frac{n_i}{n_M \cdot t} = \frac{j_i/F}{m \cdot w/M_M}$$

Eq(3.7)

**TOF**: Turnover frequency (s<sup>-1</sup>); **n<sub>i</sub>**: Mole amount (mol) of the transferred electrons to a certain product. **n<sub>M</sub>**: Total mole number (mol) of the active metal; **t**: Reaction time (s); **j<sub>i</sub>**: Partial current density (A·cm<sup>-2</sup>) of a certain product; **F**: Faraday constant, 96485 C/mol; **m**: Loading of the catalyst (g/cm<sup>2</sup>); **w**: Mass fraction of the active metal in the catalyst; **M<sub>M</sub>**: Molar weight of the active metal, g/mol.

## 4 | Development of Metal-Organic Layers (MOLs)

Constructing two-dimensional MOFs with ultra-exposed external surfaces should be a promising strategy to avoid the disadvantage of poor conductivity.<sup>[164-168,230,243,244]</sup> The beginning of this research was the selection and synthesis of proper 2D-MOFs having as much exposed surface as possible. Besides, good structural flexibility and stability are aimed for immobilizing active sites for electrocatalysis.

### 4.1 2D-MOF based materials for ECR reaction

#### 4.1.1 Synthesis methods for 2D-MOFs

The synthesis methods for 2D-materials can be classified into top-down and bottom-up methods. This classification also applies to the synthesis of 2D-MOFs. The top-down methods, i.e. exfoliating lamellar structures from the 3D bulk materials, are widely used in synthesizing 2D-materials. A well-known example is the preparation of graphene from bulk graphite using Scotch tapes. This approach generally requires the periodic structure of the material to be two-dimensional. The interactions between the layers are mostly non-covalent, such as van der Waals forces, hydrogen bonds, or  $\pi$ - $\pi$  stacking effects.<sup>[168]</sup> The methods to date have been ultrasonic exfoliation, mechanical exfoliation, solvent-induced exfoliation, and freeze-thaw exfoliation. Generally, the weaker the interactions between the layers are, the easier the exfoliations. However, when the interactions are covalent, more harsh conditions must be applied, such as chemical exfoliation. In the case of Xu's research,<sup>[245]</sup> the pillars between layers are disulfide bonds (-S-S-), which can be selectively broken by moderate chemical reaction without damaging the in-plane structure (**Figure 4.1a**). The advantage of these top-down methods is that they are facile. However, these methods are not easy to control because the destruction of the entire material can occur, especially when the interlayer interactions are different to be broken. In addition, another drawback is the low yield. To summarize, these methods still don't guarantee the formation of 2D-MOFs as a single-crystal layer.

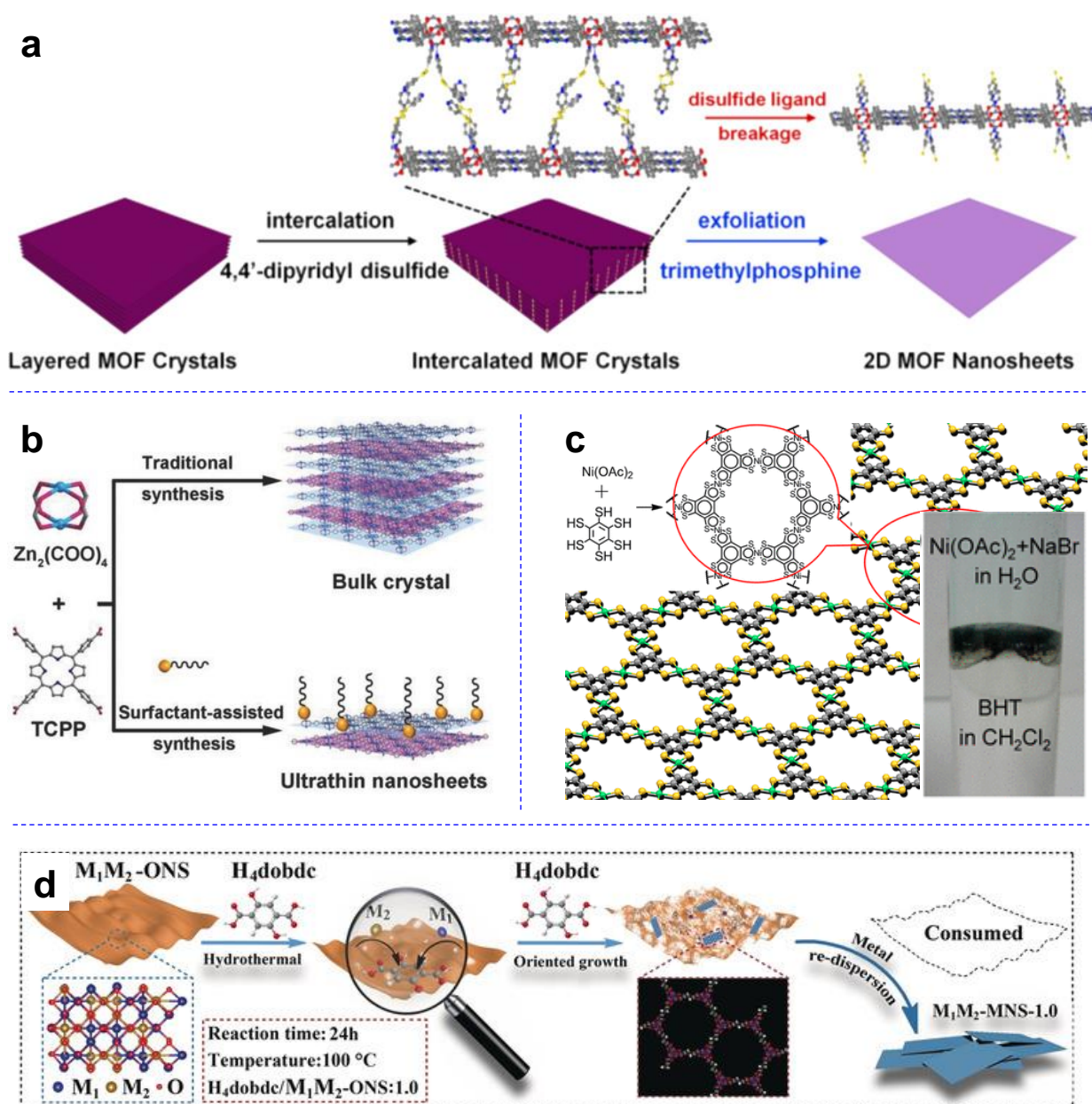


**Figure 4.1** Examples of the syntheses of 2D-MOFs. (a) Schematic illustration of the preparation of Zn-TCPP(Pd) nanosheets via a chemical exfoliation method.<sup>[245]</sup> (b) Schematic illustration of surfactant-assisted synthesis and conventional synthesis of Zn-TCPP.<sup>[246]</sup> (c) Schematic illustration of the liquid-liquid interfacial growth of Ni-BHT nanosheets.<sup>[247]</sup> (d) Schematic illustration of the self-sacrificing template method by converting metal oxide nanosheets into MOF nanosheets.<sup>[248]</sup> ONS: oxide nanosheets; MNS: MOFs nanosheets.

The bottom-up method is the reverse process in which the synthesis starts from small molecules to form layers. The critical point is to achieve preferential growth along specific orientations and inhibit the stacking process.<sup>[168]</sup> Compared to the top-down method, this method has a higher potential to produce 2D-MOFs with more uniform thickness in a high yield. There are two main approaches: the surfactant-assisted method and the interfacial growth method.

As well-known, the growth of nanoparticles is driven by the need to compensate for the high surface energy on the external surface. Surfactants were applied to interact with certain crystal

surfaces closely, achieving their restricted growth leading to certain morphology. These surfactants are also known as capping agents in inorganic synthesis. Modulators in MOF synthesis can also have this effect. A representative example is the synthesis of ultrathin PPF-1 layers (7.6 nm, 8-layers) with the assistance of polyvinylpyrrolidone (PVP) (Figure 4.1b).<sup>[246]</sup>

As for the interfacial growth, the key is to control the reaction, preferably occurring at the interface, an ultrathin reaction zone. The interface can be a gas-liquid interface, liquid-liquid interface, liquid-solid interface, or gas-solid interface. For example, liquid-liquid interfacial growth can be based on the solubility difference of two reactants in two non-miscible liquids, and the two reactants can only meet at the interface (Figure 4.1c).<sup>[247]</sup> Using a self-sacrificing template to synthesize layers can also be regarded as the solid-liquid interfacial growth, in which the metal ion reactants can only be available at the interface (Figure 4.1d).<sup>[248]</sup> CVD methods can also be classified as gas-solid interfacial growth.<sup>[249]</sup> The drawback of this interfacial method can be the low yield because the reaction zone is mostly minimal.

#### 4.1.2 Stability of the 2D-MOFs in electrocatalysis

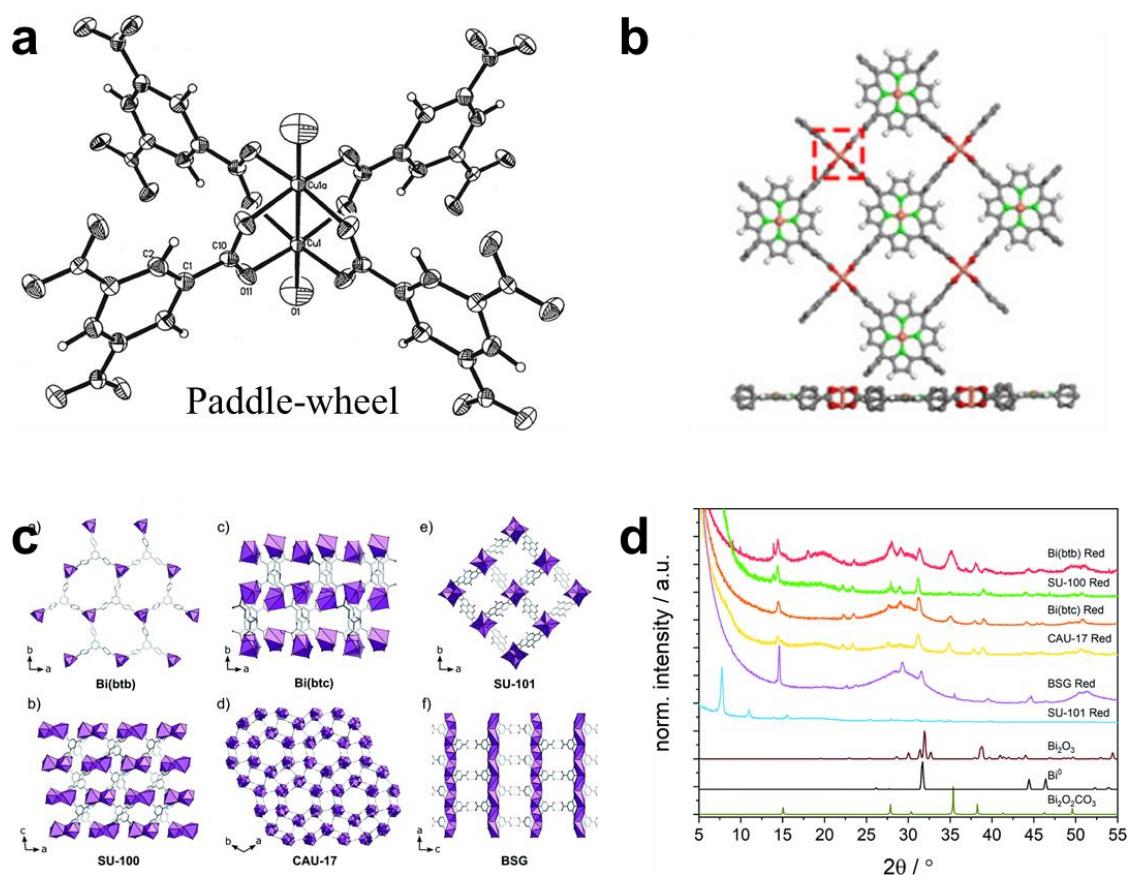


**Figure 4.2** (a) Scheme of the paddle-wheel type SBU in HKUST-1.<sup>[250]</sup> (b) Scheme of the structure of the 2D Cu-TCPP(Cu) built by paddle-wheel type SBUs.<sup>[203]</sup> (c) Scheme of several Bi-based MOFs for ECR reaction and (d) their PXRD patterns after the ECR tests.<sup>[227]</sup>

The basic principles of MOF stability are discussed in **Chapter 1.3.1.3**. Here the focus is on the stability of MOFs when applied to electrocatalysis. One example is HKUST-1 (also called  $\text{Cu}_3\text{BTC}_2$ ), which was firstly reported in 1999.<sup>[250]</sup> This structure has attracted significant attention owing to its ample pore space. Its SBU is a classical paddle-wheel structure, which has two open metal sites (OMSs) per SBU (**Figure 4.2a**). The strength of the coordination bonds in HKUST-1 is not high based on HSAB theory. HKUST-1 is famous for its poor water resistance, which is impossible for aqueous electrolysis. Some other MOFs based on this cluster, such as the PPF series<sup>[251]</sup>, are also impossible to be stable during electrocatalysis (**Figure 4.2b**).<sup>[203]</sup> Another famous example is the Ni/Co-BDC, which is applied for the oxygen evolution reaction (OER).<sup>[252]</sup> However, the in-situ formed Co/Ni oxides are proven to be the actual catalytic sites rather than Ni/Co-BDC.<sup>[179]</sup>

Even though MOFs comply with the HSAB theory, their stability needs to be examined carefully. One recent work used a series of Bi-based MOFs for ECR reaction, which turns out that most Bi-MOFs have been deconstructed and transformed into other Bi species during the tests (**Figure 4.2c,d**).<sup>[227]</sup> The in-situ generated metallic or low-valent states are generally recognized as the active sites to drive electrocatalytic  $\text{CO}_2$  reduction. Once the central metals are reduced, hard or soft acid recognition will change. For example, one would expect that  $\text{Bi}^{3+}$  is a hard acid that can form stable coordination with the carboxylate group. However, the real oxidation state during the test can be  $\text{Bi}^0$ , which is not able to form a MOF.

Hence, these facts suggest to us three points that need to be considered to achieve MOFs-based electrocatalysis: (1) choose rigid frameworks according to HSAB theory; (2) avoid MOFs, whose central metals/SBUs can be easily reduced at negative potentials; (3) carefully examine the structural integrity after reactions.

### 4.1.3 Suitable 2D-MOFs for ECR reactions

#### 4.1.3.1 The choice of $\text{Zr}(\text{Hf})_6$ -oxo based 2D-MOFs

For electrocatalytic reduction reaction, it may not be a good choice that the active sites are from the SBUs of MOFs, because of stability issues. Introducing guest compounds to form MOF composites should be more promising. Herein, Zr (or Hf) based MOFs are selected, a famous MOF family known to be stable.<sup>[154,253]</sup> Zirconium and Hafnium, both belonging to group 4 elements, can form isomorphic  $\text{M}_6$  clusters for their very similar chemical properties. Another advantage of Zr (or Hf) based MOFs is the high structural flexibility that allows for multivariate post-modifications.<sup>[162,253]</sup>

As a component of MOFs, Zirconium exists mostly in the form of  $Zr_6$  clusters ( $Zr_6$ -oxo, Octahedral shape) (Figure 4.3a,b). The carboxylate groups from the linkers will coordinate through the edge positions of the octahedron, in which two oxygen atoms of the carboxylates coordinate with two adjacent Zr atoms. The maximum coordination number by carboxylate groups is 12, corresponding to the 12 edges of an octahedron. There are mostly three situations of the  $Zr_6$ -oxo cluster when constructing 2D-MOFs (Figure 4.3c-e). The coordination orientations can be classified by the symmetry of the octahedron. The vectors perpendicular to the 2D-MOF layers can be along the  $C_4$ ,  $C_3$ , or  $C_2$  rotatory axis of an octahedron, respectively (Figure 4.3c-e). The former publications on  $Zr_6$ -oxo based MOFs reported a minimum coordination number of 6.<sup>[253]</sup> Too low coordination number (Figure 4.3c) means too many unsaturated SBUs, which may result in the instability of the framework. Examples in Figure 4.3d,e may be the reliable coordination orientations.

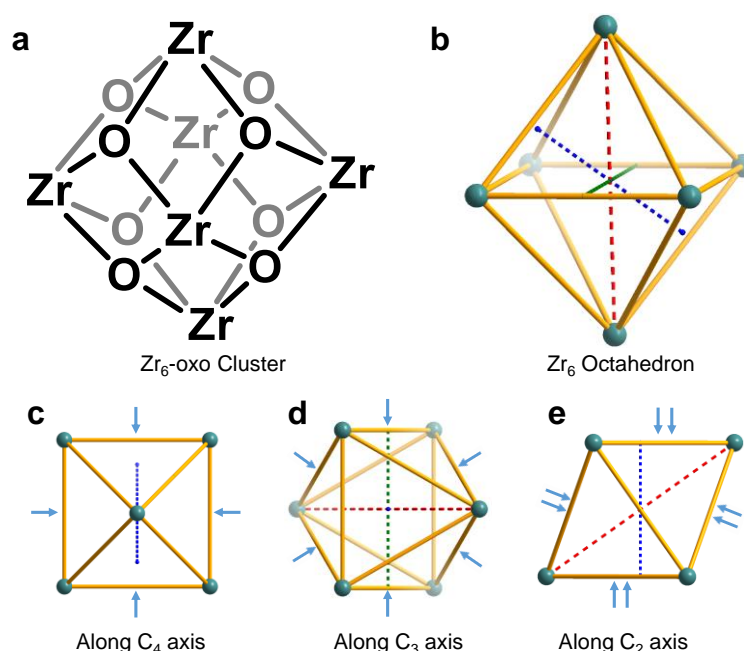


**Figure 4.3** (a) Scheme illustrating the structure of the  $Zr_6$ -oxo cluster and (b) its simplified  $Zr_6$ -octahedron. The green, blue, and red dashed lines represent two-fold, three-fold, and four-fold rotational symmetry axes, respectively. Cyan balls indicate the Zr atoms. (c-e) Projections of the  $Zr_6$ -octahedron, when applied to 2D-MOFs, viewed along specific symmetry axes. The blue arrows mark the coordination directions.

#### 4.1.3.2 The significance of topology in designing 2D-MOFs

Topology is an important tool to guide the synthesis of the 2D-MOFs. In Figure 4.4, some classic 2-periodic nets that are usually encountered in the family of 2D-MOFs are depicted. The structures are simplified as nodes interconnected nets to present the topology of MOFs. In the examples of *hxl* and *sql*, the nodes are 6 and 4 connected with each other by the angle of  $30^\circ$  and  $90^\circ$ , respectively. As for the *kgd* net, both 3- and 6-connected nodes are linked to each other.

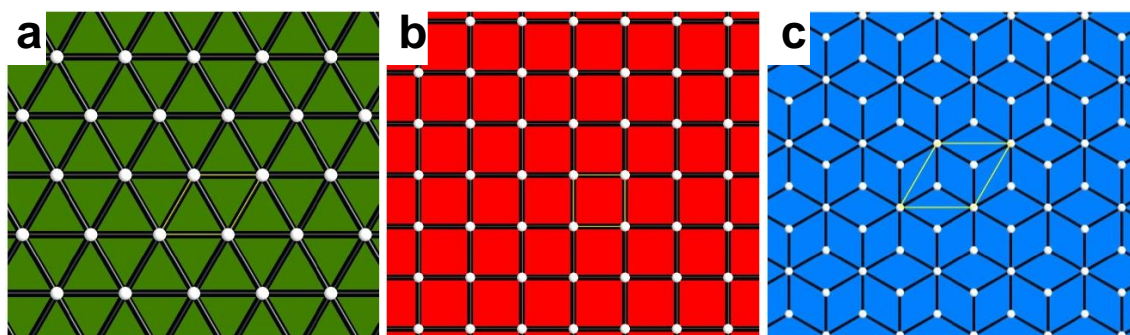


**Figure 4.4** Nets of classic 2D periodic frameworks: (a) 6-connected *hxl*, (b) 4-connected *sql*, and (c) (3,6)-connected *kgd*.<sup>[159,160]</sup>

#### 4.1.3.3 Examples of Zr(Hf)<sub>6</sub>-oxo based 2D-MOFs

Herein, a summary of published 2D-MOFs based on Zr<sub>6</sub>-oxo is given, which is classified by topology. The examples discussed in this summary are two-dimensional in terms of their crystal structure, which does not imply that monolayers have been successfully synthesized.

##### 1. Zr(Hf)<sub>6</sub>-oxo based 2D-MOFs with *hxl* topology

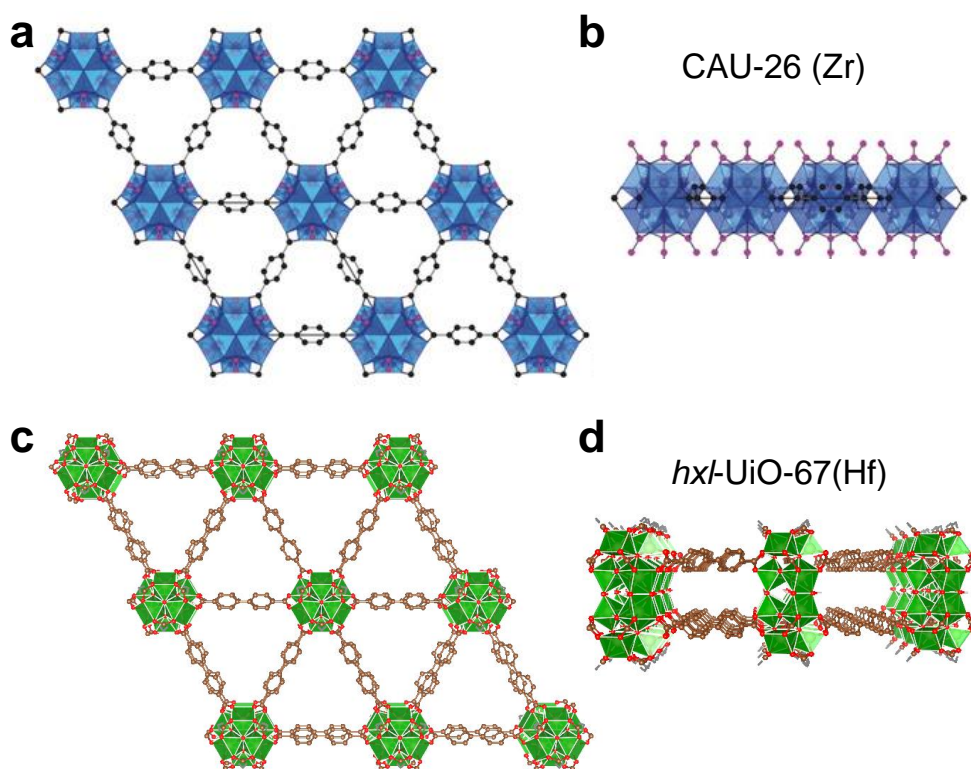


**Figure 4.5** Examples of Zr(Hf)<sub>6</sub>-oxo based 2D-MOFs with *hxl* topology. Scheme illustrating the structure of the CAU-26 (Zr), viewed along (a) *c*-axis (b) [110] direction.<sup>[254]</sup> Scheme illustrating the structure of *hxl*-UiO-67 (Hf), viewed from (c) *c* axis (d) *a* axis.<sup>[255]</sup> Blue polyhedrons: Zr<sub>6</sub>-oxo clusters; Green polyhedron: Hf<sub>6</sub>-oxo clusters; Red/Purple balls: O atoms; Black/Brown balls: C atoms.

The adopted ligands are all linear shapes, which are simplified as a line in the topology scheme. The six-connection nodes in the *hxl* topology are provided by the Zr<sub>6</sub>-oxo cluster, and the coordination orientation is shown in **Figure 4.3d**. As for the examples, Stock's group reported the

synthesis of CAU-26 using the most simple linker (1,4-benzene dicarboxylic acid, BDC) in 2019 (Figure 4.5a,b).<sup>[254]</sup> However, the synthesis method is imperfect, which needs special purifications afterward. The morphology is characterized by electron microscopy, including the existence of the non-2D particles. Before that, Grey's group reported the synthesis of the *hxl*-UiO-67(Hf) nanosheet with a thickness of 11 nm (Figure 4.5c,d).<sup>[255]</sup> The single-layer thickness, according to its crystal structure, should be around 1.6 nm. The methods were top-down methods, which may suffer from low yield and non-uniform layer formation. Considering the costs of the linker, these two examples are very attractive. However, both BDC and BPDC (biphenyl-4,4'-dicarboxylate) have a strong tendency to form three-dimensional MOFs UiO-66 and UiO-67, respectively, which adds additional difficulties to the synthesis of pure 2D-MOFs.

## 2. Zr(Hf)<sub>6</sub>-oxo based 2D-MOFs with *sql* topology

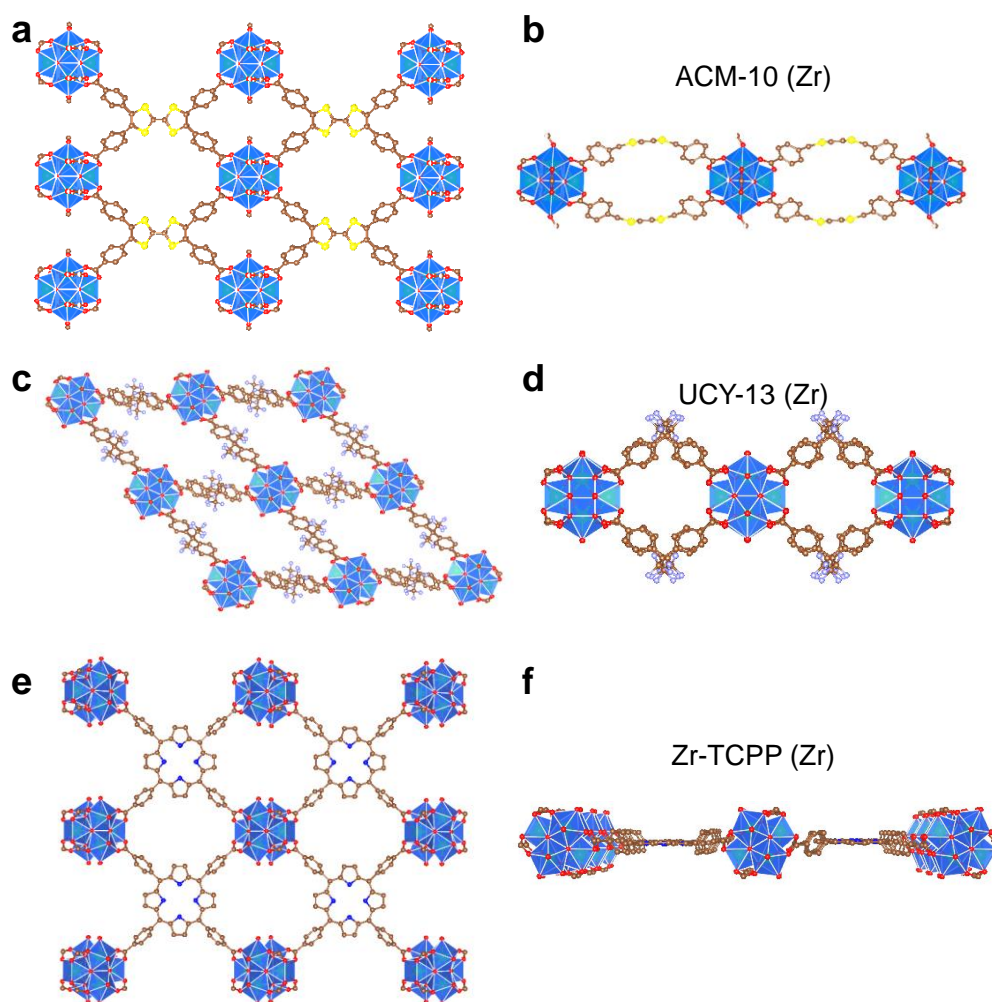


**Figure 4.6** Examples of Zr(Hf)<sub>6</sub>-oxo based 2D-MOFs with *sql* topology. Scheme illustrating the structure of ACM-10 (Zr), viewed along (a) *a* axis (b) *b* axis.<sup>[256]</sup> Scheme illustrating the structure of UCY-13 (Zr), viewed along (c) *c* axis and (d) *a* axis.<sup>[258]</sup> Scheme illustrating the proposed structure of Zr-TCPP, viewed along (e) *a* axis and (f) *c* axis.<sup>[259]</sup> The simulated Zr-TCPP structure is exfoliated from the PCN-222 (Zr). Blue polyhedrons: Zr<sub>6</sub>-oxo clusters; Red balls: O atoms; Brown balls: C atoms; Yellow balls: S atoms; Purple balls: F atoms.

There are several different examples reported for the *sql* topology. For ACM-10 (Figure 4.6a,b), the connection of the  $Zr_6$ -oxo cluster and linker are 8 and 4, respectively.<sup>[256]</sup> From its projection to the plane, the  $Zr_6$ -oxo clusters are connected from four directions by the ligands, resulting in *sql* topology. A similar structure can be found in another publication.<sup>[257]</sup> Another example is UCY-13, having SBU with a connection number of 8, equal to 4 from its projection to the plane (Figure 4.6c,d).<sup>[258]</sup> Whether ACM-10 or UCY-13, the coordination orientations are more like in Figure 4.3e. It is a pity that these two publications didn't characterize the morphology or thickness. The last sample is Zr-TCPP, with both SBU and linker connections of 4 (Figure 4.6e,f). The structure is said to be extracted from PCN-222 (3D MOF).<sup>[258]</sup> Electron microscopy and AFM analysis could prove the formation of a single layer. The coordination orientation is more similar to Figure 4.3d (CN is 6), which causes unsaturated coordination (CN is 4 for Zr-TCPP). As discussed before, the stability is uncertain for a CN of 4. It is a pity that the authors didn't show the structural stability of Zr-TCPP.<sup>[259]</sup>

### 3. Zr(Hf)<sub>6</sub>-oxo based 2D-MOFs with *kfd* topology

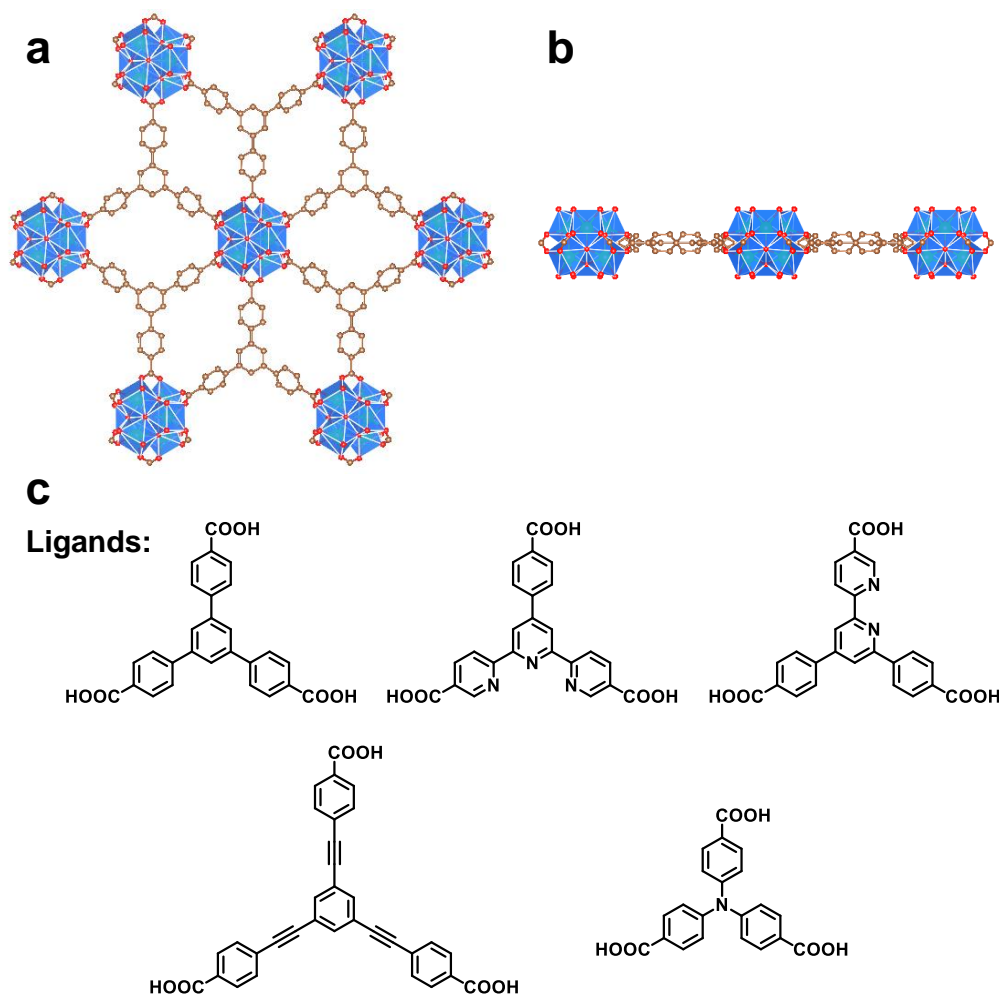


**Figure 4.7** Examples of Zr(Hf)<sub>6</sub>-oxo based 2D-MOFs with *kfd* topology. Scheme illustrating the structure of Zr-BTB MOL, viewed along (a) *c* axis (b) *a* axis.<sup>[260,261]</sup> Blue polyhedrons:  $Zr_6$ -oxo clusters; Red balls: O atoms; Brown balls: C atoms. (c) Linkers that are reported to achieve 2D-*kfd* net yet.<sup>[260-264]</sup>

Speaking of  $\text{Zr}(\text{Hf})_6$ -oxo cluster based 2D-MOFs, *kgd* topology is the most famous one (Figure 4.7). The connection numbers of SBUs and linkers are 6 and 3, respectively, corresponding to the coordination orientation shown in Figure 4.3e. This *kgd* topology is commonly reported to give 2D-MOFs with monolayer (1.2 nm) or bilayer (2-2.2 nm) thickness. The synthesis of this kind of Zr-BTB MOL needs a large amount of modulators (formic acid), which can be ascribed to the bottom-up synthesis by the surfactant method. Besides, several other linkers have been applied to give isorecticular 2D-MOFs, proving the high structural flexibility. Lin's group, which has done many significant works in this field, refers to these two-dimensional MOFs as metal-organic layers (MOLs).

#### 4.1.3.4 Chosen design strategy,

To sum up, 2D-MOFs of the *kgd* topology would be a promising strategy, regardless of the stability, thickness, synthesis difficulty, or cost of linkers. Based on the former example of Zr-BTB, we would like to add a modification by changing BTB into TATB (4,4',4''-s-triazine-2,4,6-triyl-tribenzoate). This is to improve the stability of the whole MOL further. Generally, a more rigid linker would be better regarding stability. For the BTB, the biphenyl structures are twisted by certain angles ( $\sim 17^\circ$ ) (Figure 4.8). The twisting can happen under excitation by heat, light, or other energy sources. Replacing the central benzene ring with a triazine ring can significantly increase the  $\pi$ -conjugations and makes the linker more rigid. Considering that there is no report using TATB solely for MOLs constructions, the research should start with the synthesis of Zr-TATB MOL and its careful structural characterization.

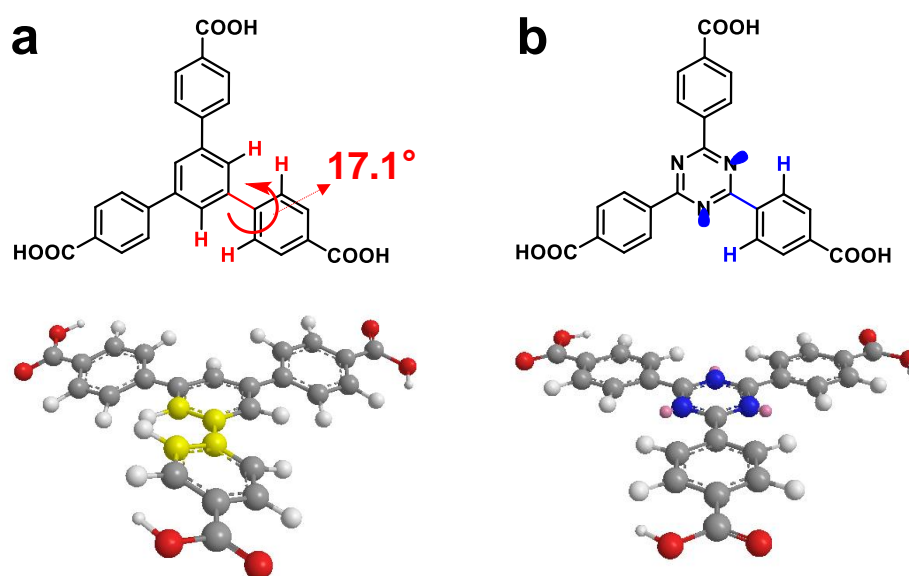


**Figure 4.8** Structure of (a) BTB and (b) TATB linkers. The twisted structure is presently in ball-stick mode. Grey/yellow balls: C atoms; White balls: H atoms; Red balls: O atoms; Blue balls: N atoms; Pink balls: lone pair electrons.

## 4.2 Zr-TATB MOL

### 4.2.1 Synthesis

Preliminary trials were carried out according to the synthesis protocol of Zr-BTB<sup>[261]</sup>. Considering the very similar size of the linkers (BTB vs. TATB) and the isorecticular structure, the PXRD pattern of Zr-TATB should be nearly the same as the simulated Zr-BTB structure. However, the synthesis failed when using the same synthesis conditions. In the beginning, we thought the reason could be the insufficient amount of the modulator (formic acid). However, very few precipitations occurred when enhancing the formic acid content. This could be due to too strong acidity after massive formic acid, especially considering water is also added to the reaction system. Too strong acidity may dissolve the intermediate species (or seeds for crystal growth). The effect of the modulator can be found in **Chapter 1.3.1.3**. Hence, we turned to the modulator acetic acid (HOAc) and reduced the water content simultaneously. We don't need to completely avoid water, since water is necessary to form the Zr<sub>6</sub>-oxo cluster. However, the water residue in solvent or reactant would be enough.

After several trials, Zr-TATB was successfully synthesized by a facile solvothermal reaction of ZrOCl<sub>2</sub>·8H<sub>2</sub>O and TATB linker in an acetic acid (HOAc)/N, N-dimethylformamide (DMF) mixture (**Chapter 3.3.1.1**). The obtained PXRD patterns matched well with the pattern of the simulated Zr-BTB (**Figure 4.9a**).<sup>[261]</sup> Considering several known 3D-MOFs concerning Zr and TATB/BTB linkers, it is necessary to exclude these 3D structures by PXRD. One unwanted phase is a 3D-MOF of zeotype *mtn* topology, called PCN-777 (**Figure 4.9b**).<sup>[237]</sup> Another unwanted phase is the interlocked Zr-BTB, in which the two layers of the Zr-BTB are interlocked with each other (**Figure 4.9c**).<sup>[265]</sup> The Zr-TATB is possible to form such an isorecticular structure. By comparison, as-synthesized Zr-TATB is free of impurities of the mentioned unwanted phases (**Figure 4.9d**).

The solid composition is examined by the dissolution/NMR test (**Figure 4.10a**). The powder was firstly dissolved into 1M KOH/D<sub>2</sub>O, followed by the <sup>1</sup>H-NMR measurement of its supernatant. The TATB linker was identified ( $\delta = 7.7(\text{d})$  ppm,  $8.0(\text{d})$  ppm) in the <sup>1</sup>H-NMR spectrum, proving the existence of the linker in the solid. The structure of TATB didn't undergo any destruction during the solvothermal reaction. The presence of the acetate ( $\delta = 1.9(\text{s})$  ppm) can be explained by the acetic acid used as a modulator. Tiny peaks at 8.5 ppm and 2.3 ppm can be ascribed to formate and dimethylamine derivatives, respectively, originating from the decomposition of residues of the solvent DMF.<sup>[266]</sup> The mole ratio of TATB:acetate can be calculated by the integrations of the

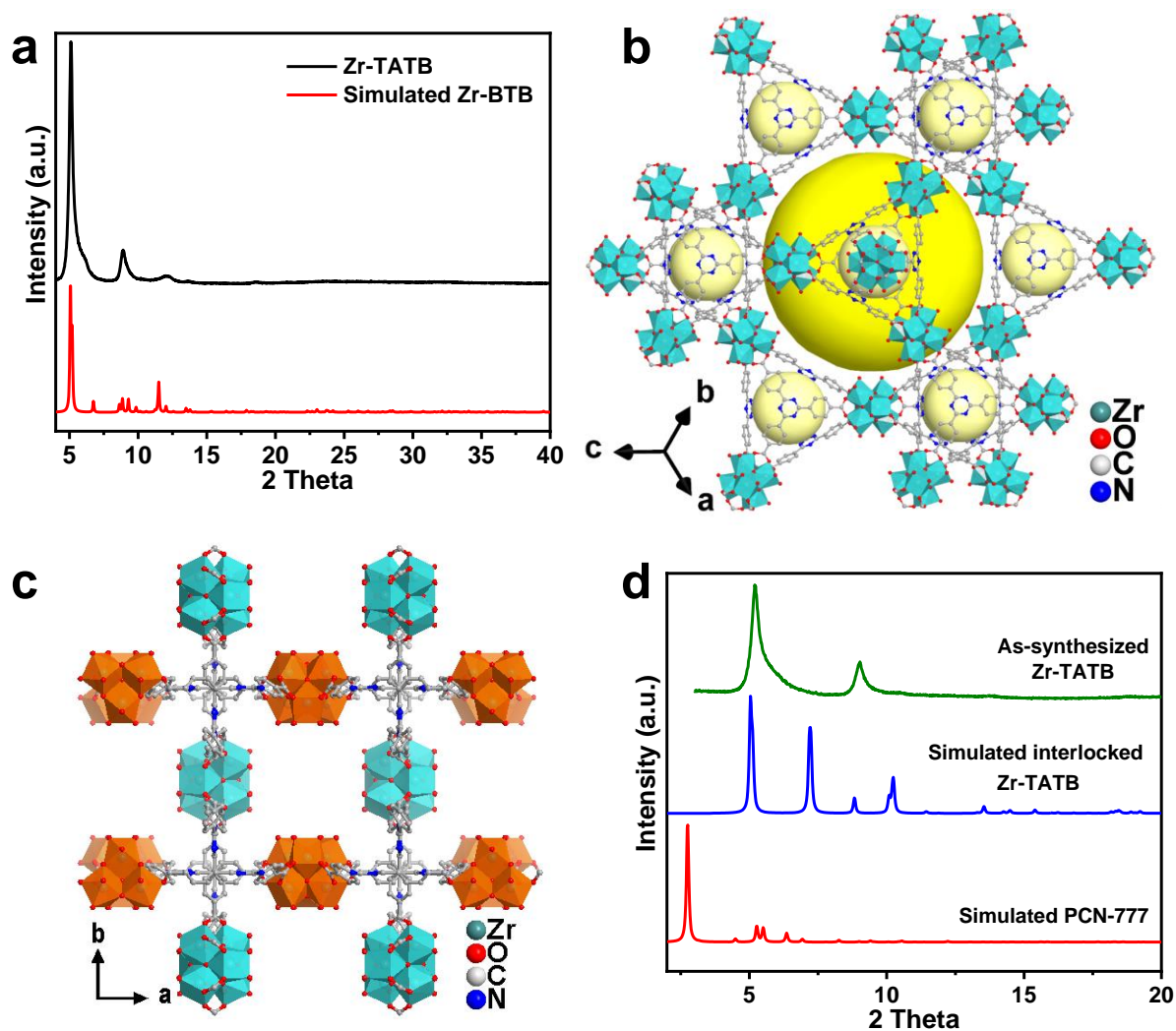


**Figure 4.9** (a) PXRD patterns of simulated Zr-BTB MOL and as-synthesized Zr-TATB. Scheme of possible 3D MOFs constructed by  $Zr_6$ -oxo SBUs and TATB linkers. (b) PCN-777, viewed along [111] direction.<sup>[237]</sup> (c) Proposed interlocked Zr-TATB, viewed along  $c$  axis.<sup>[265]</sup> Blue/Orange polyhedron:  $Zr_6$ -oxo cluster; Grey balls: C atoms; Red balls: O atoms; Blue balls: N atoms. (d) PXRD patterns of the simulated PCN-777, interlocked Zr-TATB, and as-synthesized Zr-TATB.

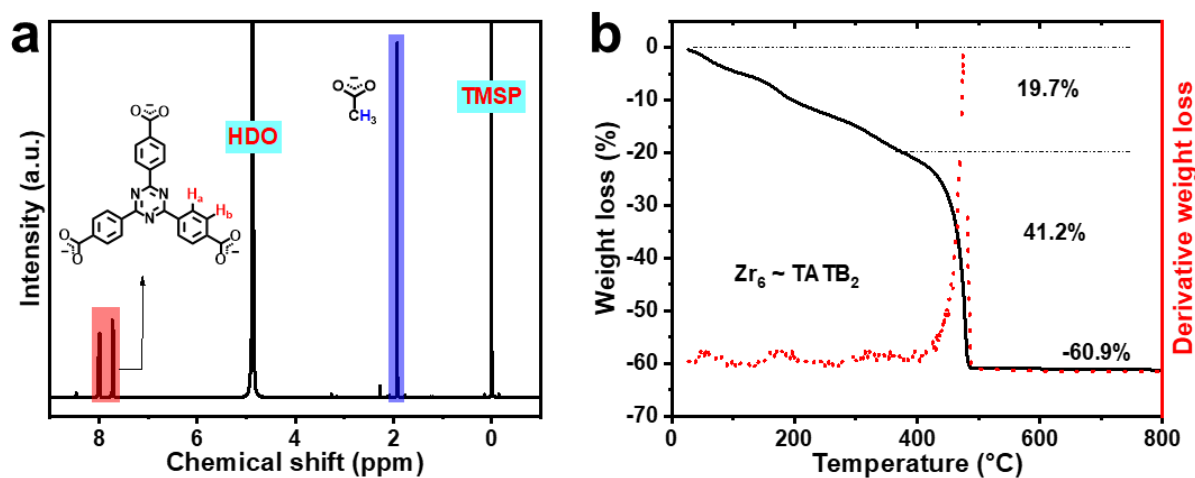


**Figure 4.10** (a) Dissolution/NMR analysis of Zr-TATB MOL, adopting  $d_4$ -TMS of known concentration as an internal standard (b) TGA plots of the Zr-TATB MOL under air with a heating rate of  $2\text{ }^\circ\text{C}\cdot\text{min}^{-1}$ .

peaks to be 1:2.8, close to the theoretical value (1:3). The composition can also be evaluated by the Thermogravimetric analysis (TGA) (Figure 4.10b).<sup>[237,265]</sup> The weight loss below 160 °C could be attributed to the evaporation of water and DMF, which serve as reactant/solvent during synthesis. Starting from 180 °C, the dehydration of surface O/OH groups will occur. Decomposition of acetate and linker happens at around 310 and 450 °C, respectively, finally resulting in ZrO<sub>2</sub>. The Zr and TATB linker ratio can be determined to 3.3:1, close to the theoretical value (3:1) of Zr-BTB.

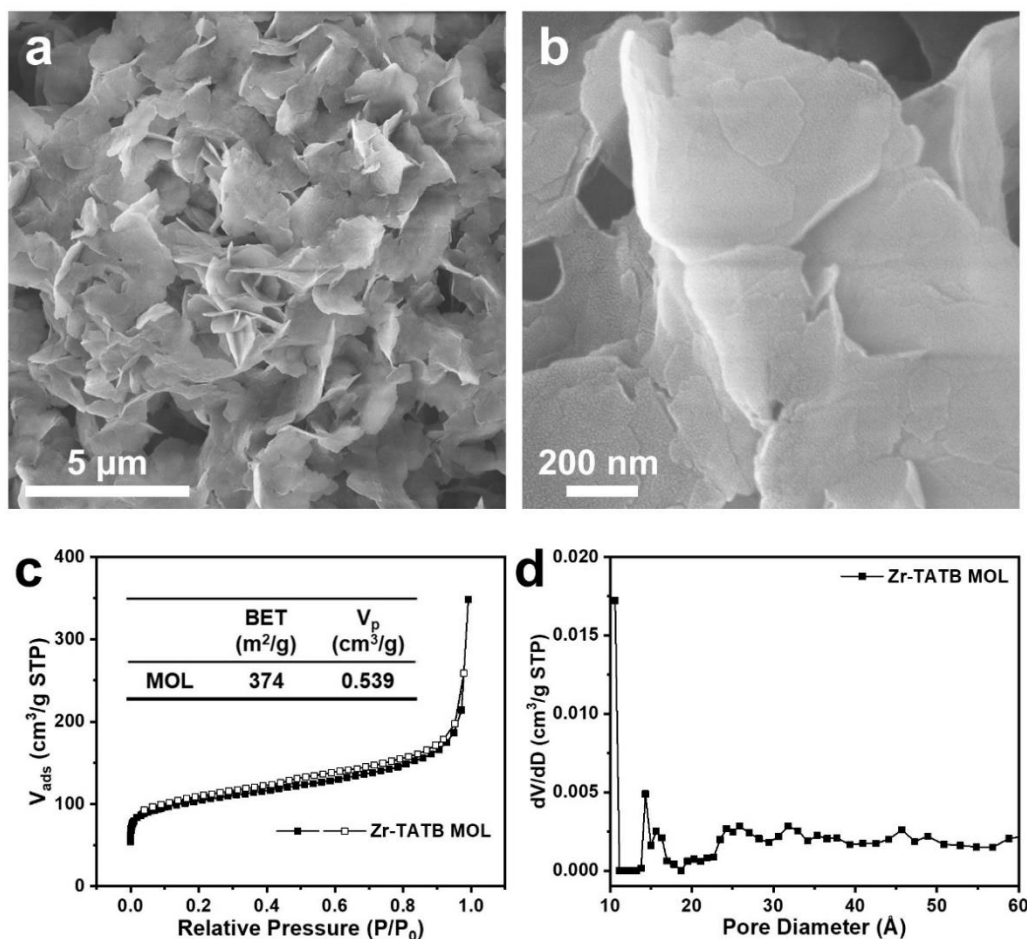


**Figure 4.11** (a,b) FE-SEM images and (c) N<sub>2</sub> sorption isotherms (solid: adsorption curve; open: desorption curve) of Zr-TATB MOL at 77 K (Inserted table: BET surface area and pore volume(V<sub>p</sub>)). (d) DFT-based pore size distribution of Zr-TATB MOL. The used DFT mode: N<sub>2</sub> at 77K on silica (cylindr./sphere pore, NLDFT ads. model).

The rough morphology is characterized by Scanning electron microscopy (SEM) (Figure 4.11a,b). The images prove the layer structure without any 3D-nanoparticles. The size of the layer varies from hundreds of nanometers to several micrometers. N<sub>2</sub> physisorption (77 K) experiment was conducted to get information on the porosity of Zr-TATB MOL (Figure 4.11c,d). The measurement shows a type II isotherm plot, indicating the non-porous structure. The DFT-based pore size distribution gives a large amount of the pores originating from the stacked layers, ranging from micropores to mesopores.

## 4.2.2 Morphology and structure

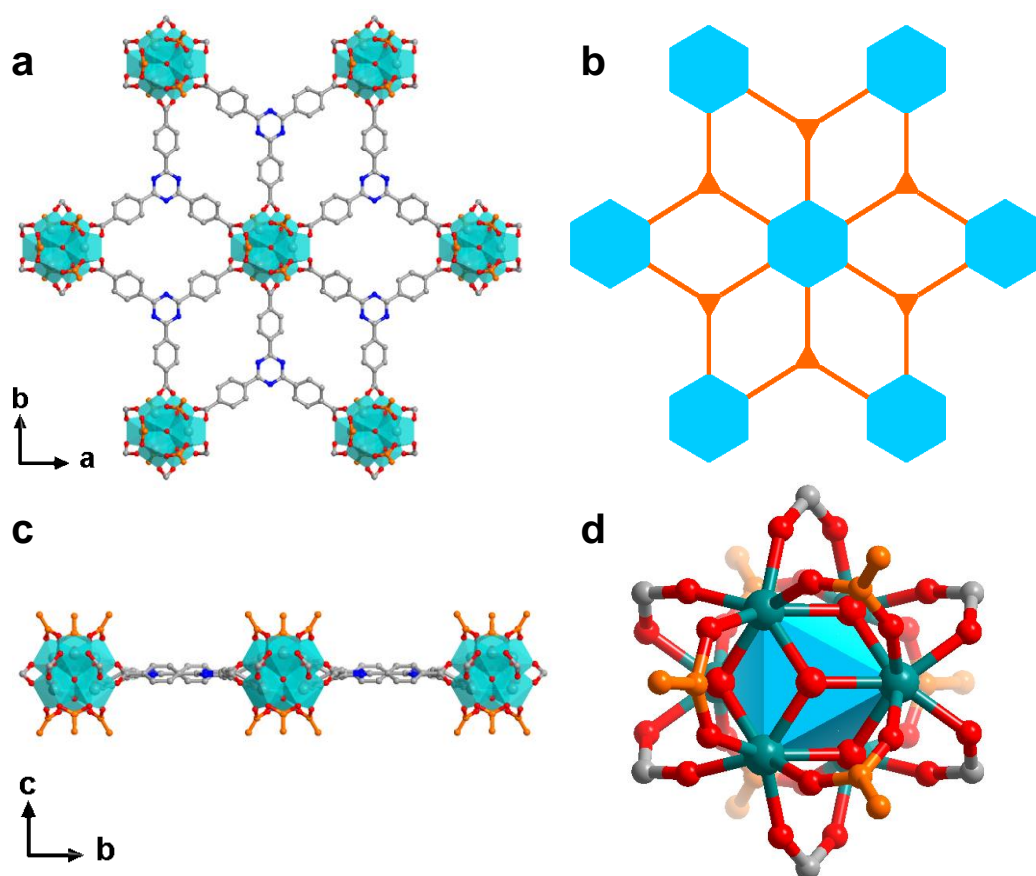


**Figure 4.12** Scheme illustrating the structure of the Zr-TATB MOL viewed from (a)  $c$  axis and (c)  $a$  axis. (b) 2D- $kgd$  topology of Zr-TATB MOL, where the 6-connected  $Zr_6$ -oxo clusters and the 3-connected TATB linkers were simplified as blue hexagons and orange triangles, respectively. (d) The cluster structure of  $Zr_6$ -oxo cluster in Zr-TATB MOL. Cyan: Zr; Light blue polyhedron:  $Zr_6$ -oxo cluster; Blue balls: N atoms; Red: O atoms; Grey balls: C atoms from linkers; Orange balls: C atoms from acetate.

The exact crystal structure should be determined due to the new linker. Because we can not get larger single crystals to reveal the precise structure by single-crystal diffraction, we resorted to other methods to elucidate the exact structure. The crystal structure of Zr-TATB was proposed based on Zr-BTB.<sup>[261]</sup> Energy and geometry optimizations are followed by the Forcite tool of *Material studio* software.<sup>[267]</sup> An optimized structure and simulated PXRD patterns of Zr-TATB can be obtained (Table 4.1&4.2). The stacking mode adopted here is AA stacking. The reflexes originating from layer stacking, such as (001), didn't appear in the pattern of the as-synthesized Zr-TATB (Figure 4.13b). Further confirmation was obtained with the assistance of the *Mercury* software. It can extract diffraction information with the preferred orientation, corresponding to the preferred crystallographic plane.<sup>[245]</sup> The preferred orientation of the layer is expected to be (001) orientation. As we can recognize, the diffractions of the stacked layers, corresponding to (001) in the PXRD pattern, are nearly invisible (Figure 4.13b). For a better understanding, the PXRD with the preference of (110) was given to compare with the preference of (001). These results confirm

the layer structure of the Zr-TATB without apparent stacking.

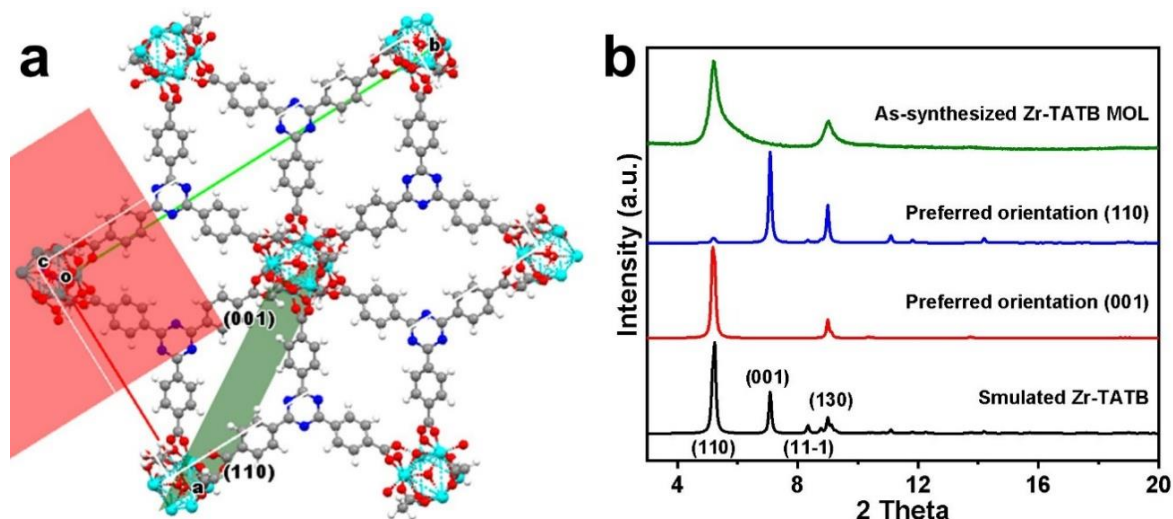


**Figure 4.13** (a) Scheme of the structure of the Zr-TATB MOL. Light blue balls: Zr atoms, Red balls: O atoms, Grey balls: C, Blue balls: N, White balls: H. The (001) and (110) planes are highlighted by red and olive colors, respectively. Acetates are capped to the Zr<sub>6</sub>-oxo clusters from the *c* axis direction. (b) PXRD patterns of simulated Zr-TATB, simulated Zr-TATB with preferred (001) orientation, simulated Zr-TATB with preferred (110) orientation, and as-synthesized Zr-TATB MOL.

**Table 4.1** Crystallographic information of simulated Zr-TATB.

Parameters	Zr-TATB
Chemical formula	Zr <sub>6</sub> (μ <sub>3</sub> -O) <sub>4</sub> (μ <sub>3</sub> -OH) <sub>4</sub> (TATB) <sub>2</sub> (AcO) <sub>6</sub>
Space group	C2/m
<i>a</i> [Å]	19.52
<i>b</i> [Å]	34.18
<i>c</i> [Å]	12.57
α [deg]	90
β [deg]	97.29
γ [deg]	90

**Table 4.2** Table of the diffractions of the simulated Zr-TATB.

Miller index			2θ [deg]	d [Å]	I [a.u.]
h	k	l			
0	2	0	5.166	17.09	54.29
1	1	0	5.240	16.85	100.0
0	0	1	7.085	12.47	53.20
1	1	-1	8.337	10.60	10.05

0	2	1	8.772	10.07	5.906
1	3	0	8.997	9.821	19.01
2	0	0	9.125	9.684	8.675
1	1	1	9.271	9.532	2.746

The structure of the Zr-TATB MOL was further characterized by electron microscopy. TEM can observe the highly creased layers without bulk particles, similar to other 2D-materials (Figure 4.14a). The enlarged areas show an apparent honeycomb-type lattice fringe pattern (Figure 4.14b,c). In the bright-field image, the darker parts can be ascribed to the position of heavier or denser components according to the contrast mechanisms of TEM. As for the Zr-TATB, the darker parts can be taken as the  $Zr_6$ -oxo clusters, presenting a hexagonal symmetry. The Fast Fourier Transform (FFT) is an effective mathematic tool to analyze and characterize periodic signals. The corresponding FFT pattern of the Zr-TATB is a set of bright dots (Figure 4.14d), presenting a hexagonal symmetry as expected from the simulated structure. Moiré fringes, resulting from layer stackings with a displacement, didn't appear in the FFT pattern.<sup>[268]</sup> This is further proof for the simulated crystal structure based on the AA stacking.

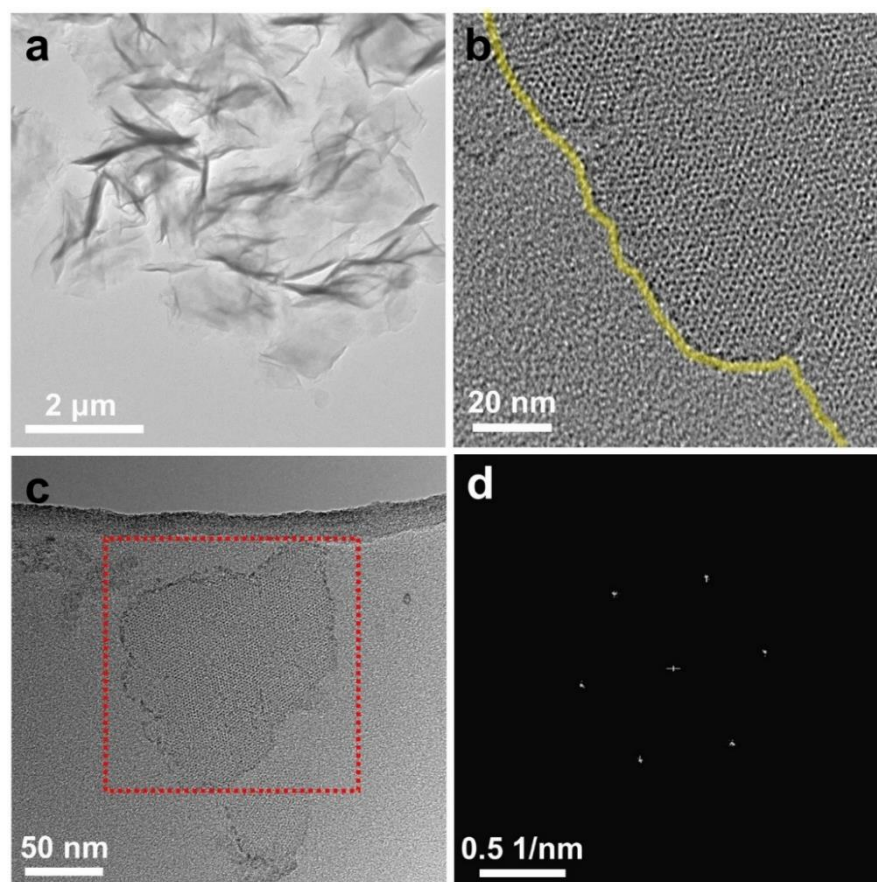


**Figure 4.14** (a-c) TEM bright-field images of the Zr-TATB MOL. The border of the MOL is highlighted by the yellow line in (b). (d) Corresponding FFT patterns of the box region in (c), where a monolayer MOL is displayed.

Further high-resolution TEM (HRTEM) images give a clear view of the lattice structure of Zr-TATB MOL (**Figure 4.15a,b**). The  $Zr_6$ -oxo clusters appear as black dots arranged with hexagonal symmetry. The distance of the two adjacent  $Zr_6$ -oxo clusters can be measured to be 1.94 nm, close to the theoretical value of 1.95 nm (**Figure 4.15b**). The selected area electron diffraction (SAED) pattern also confirms the results and conclusions of the FFT pattern. The pattern is indexed to be (110), (020), (1-10), (-1-10), (0-20), and (1-10) with [001] zone axis by the simulated Zr-TATB structure.

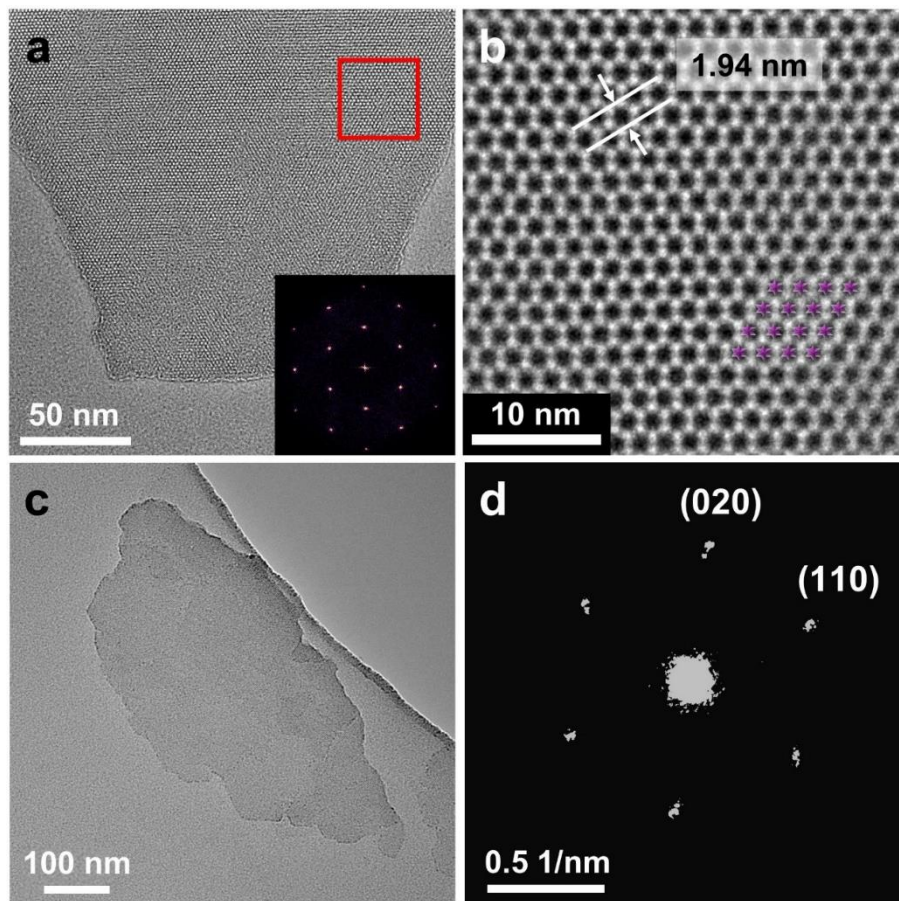


**Figure 4.15** (a,c) TEM and (b) HRTEM bright-field images of the Zr-TATB MOL (inserted: FFT pattern). (d) Selected area electron diffraction (SAED) pattern of the Zr-TATB MOL in (c).

Over the past decades, scanning transmission electron microscopy has been developed and applied to direct observation of the nanostructure of materials. Compared to conventional TEM, STEM images are generated by focusing the electron beam to a tiny spot which is then scanned over the sample. The electron beams at every spot in the view field are parallel to the optical axis to reduce the influence of the phase difference on the image. The application of the aberration correction allows to achieve atomic resolution (sub-ångström). The contrast mechanism is nearly only Z-contrast because of the high-angle annular dark-field (HAADF) detector. These characters make STEM a promising method for structure characterization. 2D-materials, for their ultrathin and uniform thickness, are very suitable for STEM analysis. Herein, the STEM was conducted,

giving an annular dark-field (ADF) image and an annular bright-field (ABF) image (Figure 4.16). The  $Zr_6$ -oxo clusters exhibit bright dots in the HAADF image and dark dots in the ABF image, respectively, because of their higher atomic number. Again, no Moiré fringes were observed, excluding the possibility of twisted stacking.<sup>[268]</sup> Unfortunately, we could not reach an atomic resolution for the radiation damage. Cryogenic electron microscopy may be expected to solve this dilemma.<sup>[269]</sup>

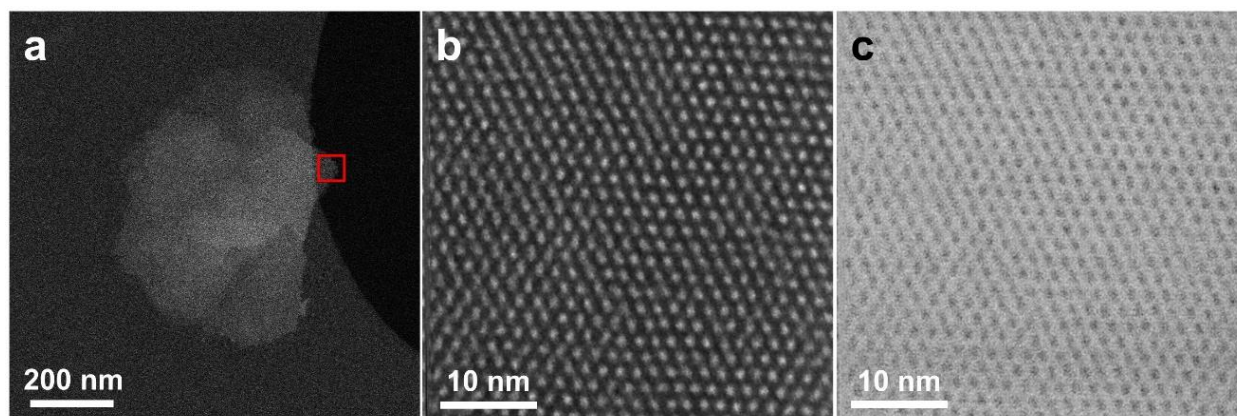


**Figure 4.16** (a) Low-magnification annular dark-field scanning transmission electron microscopy (ADF-STEM) of the Zr-TATB MOL. (b,c) Ptychography reconstructed modulus and phase image of the Zr-TATB MOL using a 4D dataset acquired with a Merlin electron detector.

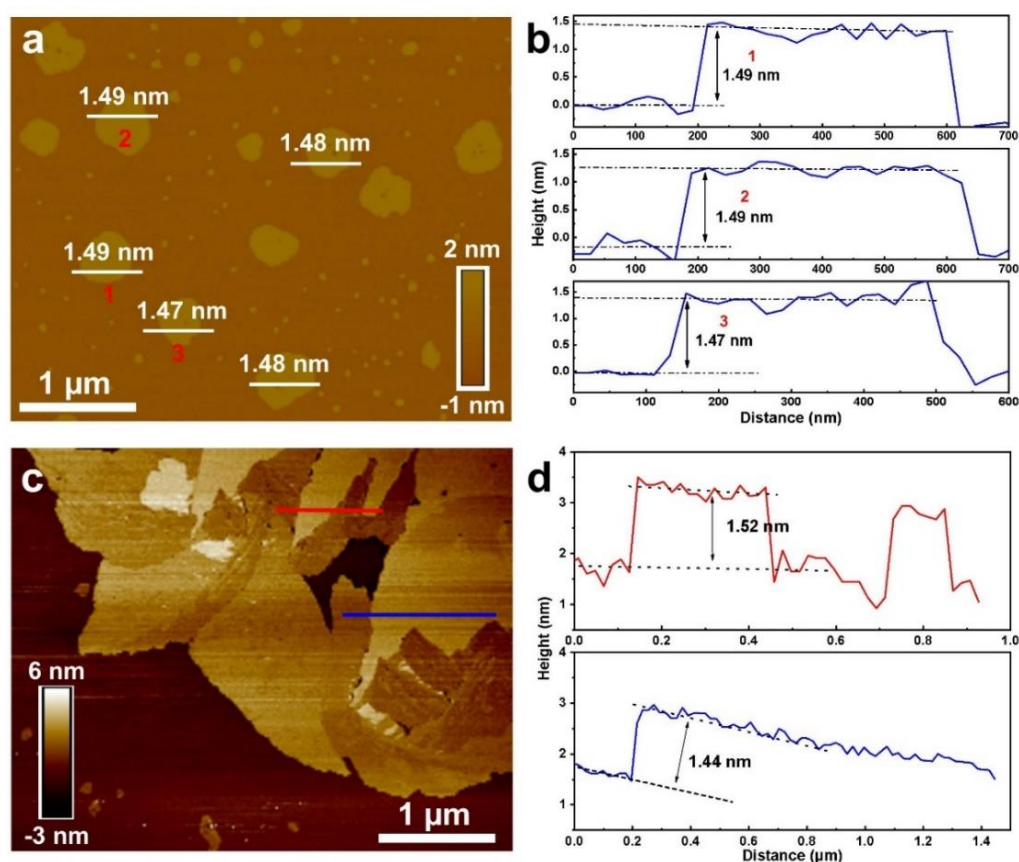


**Figure 4.17** AFM images of the Zr-TATB MOL and the corresponding height profiles (marked in colored numbers/lines). The thicknesses of the Zr-TATB MOL are marked in the figure.

After confirming the layer structure of the Zr-TATB, the thickness is one key parameter, which can be determined by atomic force microscopy (AFM) analysis. The sample was prepared by drop-casting using a highly diluted and ultrasonicated Zr-TATB dispersion on a mica. The thickness can be measured to be 1.48 nm on average (**Figure 4.17**), corresponding to the thickness of the single layer. This thickness is somewhat thicker than the isorecticular Zr-BTB<sup>[261]</sup>, due to the capping acetate being larger than the hydroxyl groups in Zr-BTB.

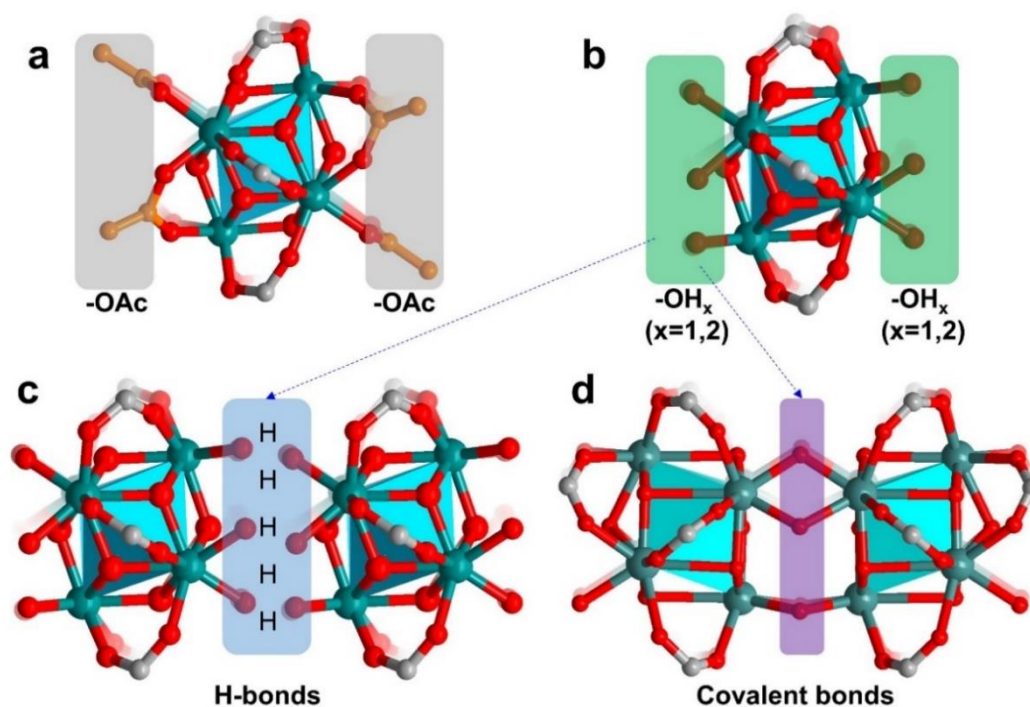


**Figure 4.18** Scheme illustrating the capping effect in synthesizing the free-standing monolayer Zr-TATB MOL. (a) Zr<sub>6</sub>-oxo cluster capped with acetates. (b) Zr<sub>6</sub>-oxo cluster without capping agents. The stacking mode of the Zr<sub>6</sub>-oxo cluster by the (c) H-bonds and (d) covalent bonds

No apparent post-treatment (top-down method) is required to synthesize monolayers of the Zr-TATB. The bottom-up synthesis principle can be classified as one of the surfactant-assisted methods. Here, the modulators could modulate the synthesis speed and serve as capping agents during the synthesis. The acetate groups, perpendicularly bonded to the plane of the Zr-TATB MOL, can prohibit the stacking of the synthesized MOL (**Figure 4.18a**). This speculation was verified by a comparative experiment adopting HCl for the synthesis of Zr-TATB (**Chapter 3.3.1.1**). From the SEM images, apparent stacking can be recognized, which leads to the formation of worm-like morphologies (**Figure 4.19a,b**). The layer structure can be confirmed by the PXRD patterns, similar to Zr-TATB MOL (**Figure 4.19c**). Besides, the N<sub>2</sub> physisorption experiment shows an isotherm plot closer to type I, corresponding to its microporous structure (**Figure 4.19d**). The layer stacking can be in the form of hydrogen bonds or the covalent bonds based on surface hydroxyl groups (**Figure 4.18**), highlighting the significance of the capping acetates. In short, we confirm the successful synthesis of a free-standing monolayer Zr-TATB MOL of *kgd* lattice.

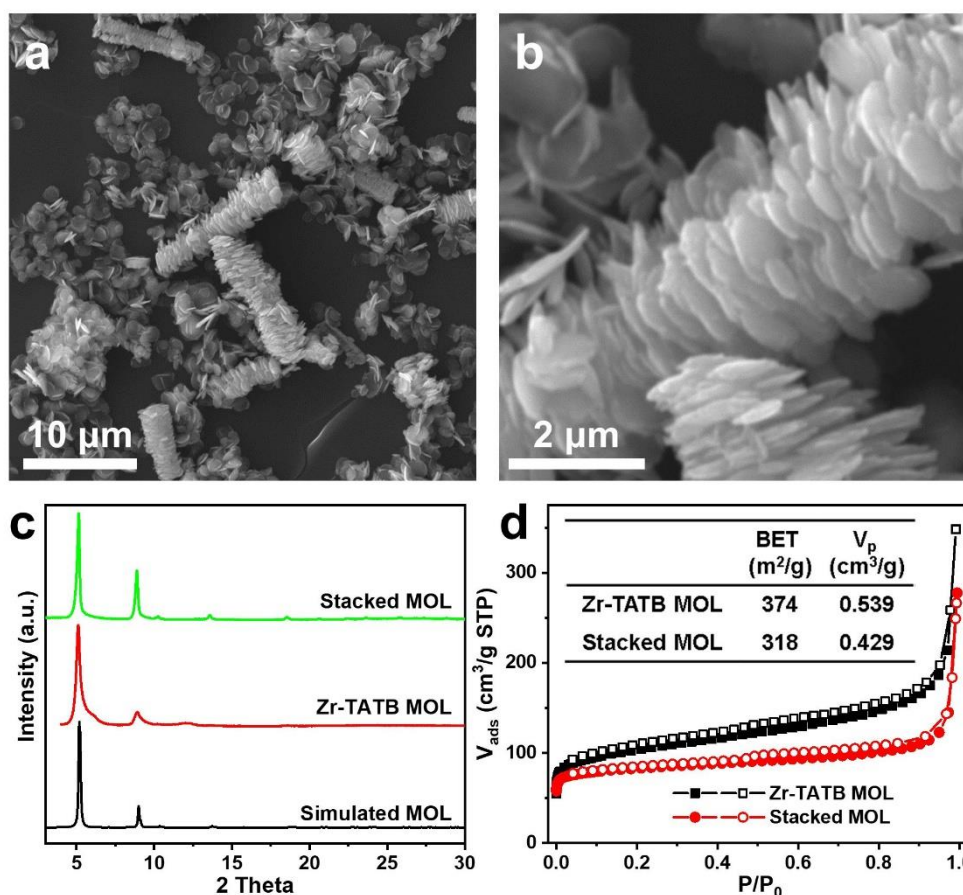


**Figure 4.19** (a,b) SEM images of the stacked Zr-TATB (stacked MOL) (c) PXRD patterns of simulated Zr-TATB MOL, as-synthesized Zr-TATB MOL and stacked MOL. (d) N<sub>2</sub> sorption isotherms (solid: adsorption curve; open: desorption curve) of Zr-TATB MOL and stacked MOL at 77 K (Inserted table: BET surface area and pore volume( $V_p$ )).

### 4.2.3 Stability

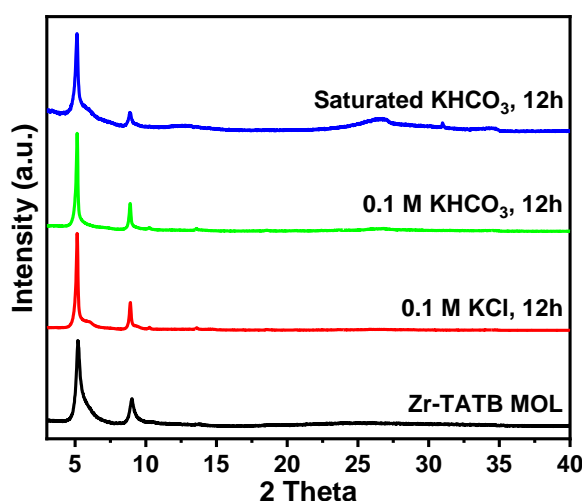


**Figure 4.20** PXRD patterns of the Zr-TATB MOL after exposure to different electrolytes.

The good thermal stability can be proven by TGA analysis, in which the structure was found to be stable up to at least 400 °C in air (**Figure 4.10b**). Furthermore, the chemical stability was demonstrated by soaking in common electrolytes overnight, followed by PXRD measurements

(**Figure 4.20**). Such chemical stabilities are in accordance with our expectations for electrocatalysis.

#### 4.2.4 Summary of Zr-TATB MOL

Considering the need for good stability and the advantage of the monolayer, a 2D-*kgd* framework based on  $Zr_6$ -oxo clusters was chosen as the target structure. Accordingly, a free-standing Zr-TATB MOL of monolayer thickness was successfully constructed by a  $Zr_6$ -oxo cluster and a TATB linker, which is used for the first time as a linker for MOL construction. The synthesis method is a facile surfactant-assisted solvothermal synthesis method, in which acetic acid was applied as a capping agent to prohibit stacking. The structure was precisely determined by multiple characterization methods. A 2D-*kgd* topology was demonstrated and free-standing monolayers were proven. The free-standing 2D structure ensures a sufficiently exposed surface for loading active sites and applying electricity, which is a prerequisite for electrocatalysis. The chemical stability indicates the expected robustness of the structure in the electrocatalytic process. The multivariate characteristics of Zr-TATB MOL also demonstrate its great potential for catalytic studies using tunable microenvironments.

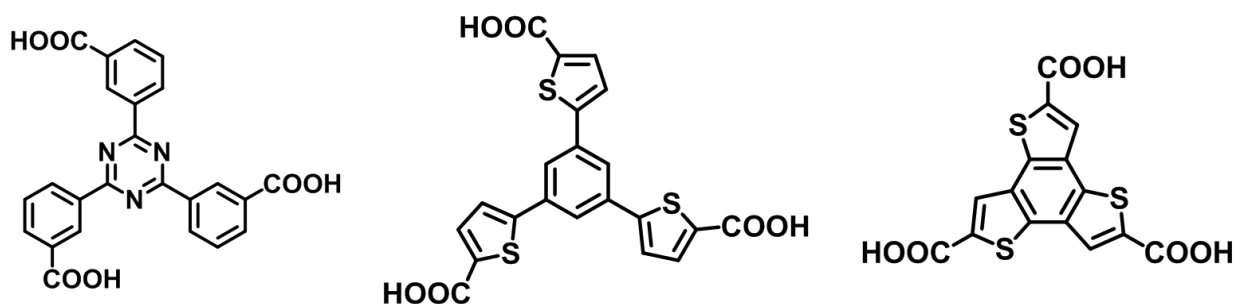


**Figure 4.21** Possible but not reported linkers for MOL composites.

The high structural flexibility determines the high possibility of getting a family of isorecticular MOLs. The components can be flexibly exchanged without changing the topology. 1. Metal SBUs. Considering that Ce and Hf are found to form isostructural metal SBUs in MOFs, it is highly expected to replace Zr by Ce and Hf.<sup>[261,270]</sup> 2. Linkers. Based on the *kgd* topology, the TATB linker can be freely exchanged by other tridentate linkers, which are roughly planar and of  $C_3$  symmetry. Some examples are possible but not achieved yet for MOL constructions (**Figure 4.21**). 3. The capping agents. Other carboxylic acids can also serve as modulators during synthesis and capping agents prohibiting the stacking.<sup>[260,271]</sup> These multivariate components jointly contribute to the adjustable micro-environments for catalysis, making MOLs an attractive candidate for investigating the structure-activity relationship.

## 4.3 Porphyrin-based MOL

Besides Zr-TATB MOL, porphyrin-based compounds have received much attention in catalysis, including ECR reactions, as a popular molecular catalyst.<sup>[226,272,273]</sup> As highly conjugated molecules, porphyrin-based compounds generally suffer from  $\pi$ - $\pi$  stacking, leading to the deactivation of many active sites.

### 4.3.1 Synthesis strategy

Porphyrins can be integrated into the linkers for constructing MOFs. Porphyrins-based MOFs can achieve the ultimate dispersion of the active sites as the building blocks of MOFs are restricted and isolated by the rigid porous framework. Considering the stability and accessibility of active sites during electrocatalysis, developing 2D aluminum-based porphyrin frameworks could be a promising choice, such as Al-TCPP. Even though the Al-TCPP is not structurally 2D, some layers always existed in the as-synthesized products (Figure 4.22).<sup>[239]</sup> The main target hereafter is to synthesize 2D layers of Al-TCPP selectively.

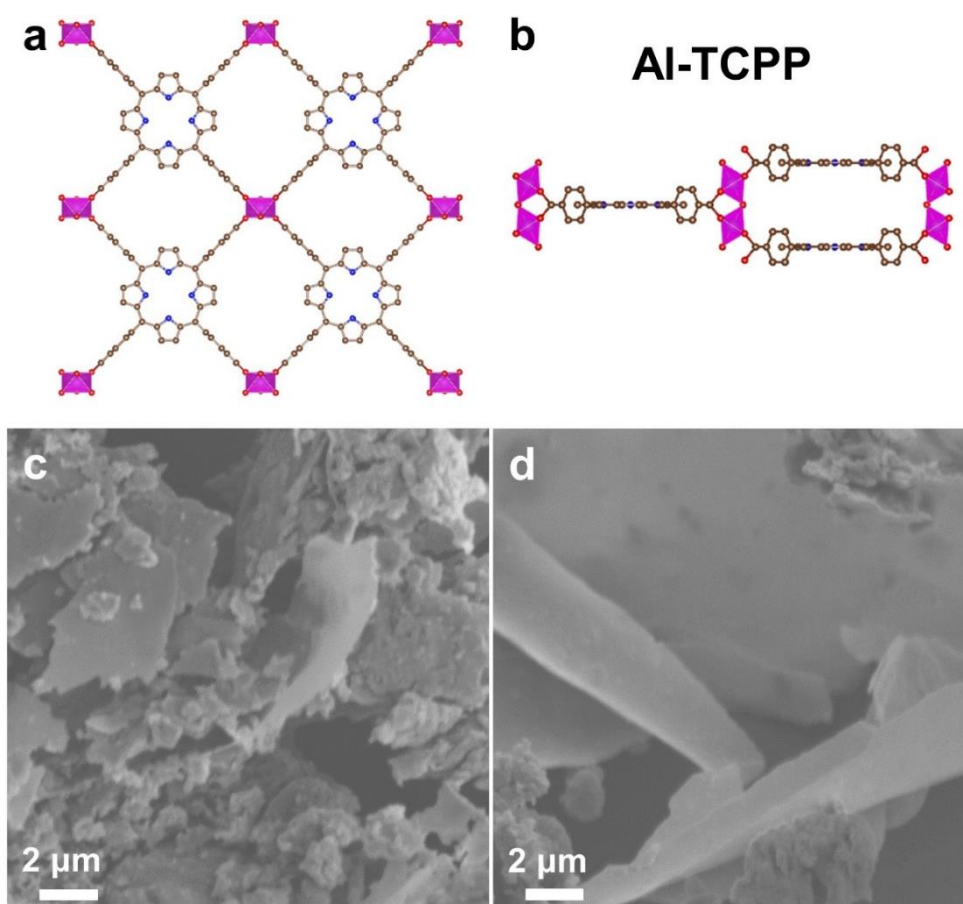


**Figure 4.22** Scheme illustrating the structure of Al-TCPP, viewed along (a) *b* axis (b) *c* axis. Pink polyhedron: Al-oxo cluster; Brown balls: C atoms; Blue balls: N atoms. (c,d) SEM images of the Al-TCPP, using conventional methods.<sup>[239]</sup>

One reliable strategy could be the application of the self-sacrificing template method.<sup>[272]</sup> As described by Yaghi's group, an ultrathin layer of Al<sub>2</sub>O<sub>3</sub> was deposited on the surface of the Ag octahedron by Atomic Layer Deposition (ALD). The Al<sub>2</sub>O<sub>3</sub> layer was used as the sacrificing template and precursor to construct Al-TCPP. Al-CTPP turned out to be in the form of a layer structure. Based on this principle, 2D self-sacrificing templates for the synthesis of 2D Al-TCPP could be found, which are NiAl-LDH and AlOOH, as shown in **Figure 4.23**.

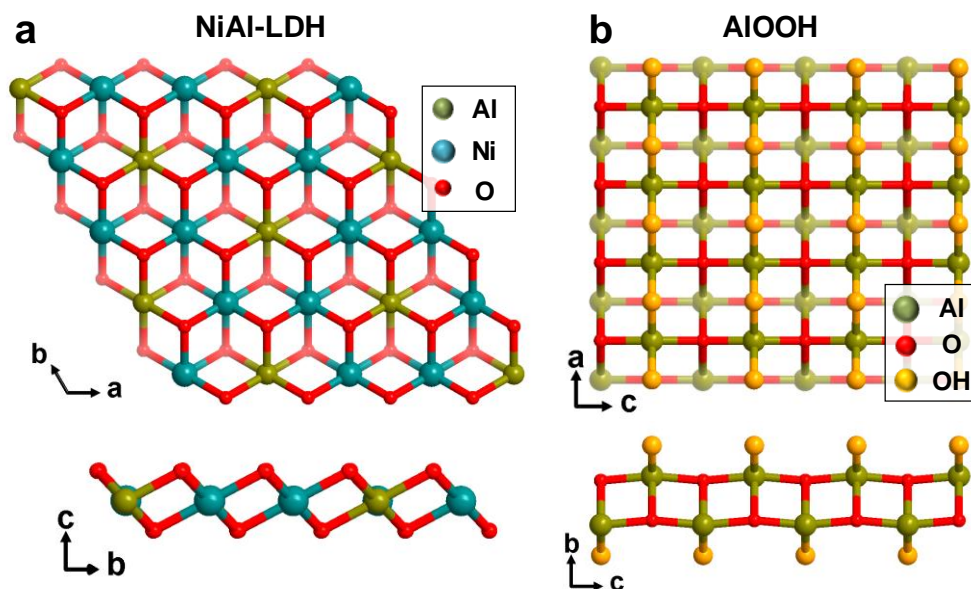


**Figure 4.23** Scheme of the structures of (a) NiAl-LDH and (b) AlOOH.

### 4.3.2 Synthesis and characterizations

NiAl-LDH and AlOOH are structurally two-dimensional and can be used as sacrificing templates and precursors (**Figure 4.23**). They will slowly dissolve to Al<sup>3+</sup> and coordinate with porphyrin linkers (TCPP) under solvothermal conditions. Through the experiments, it was found that the Ni ions in NiAl-LDH will coordinate into porphyrin centers during the synthesis. This one-pot metallization of the porphyrin will lead to the difficulty of further metallization by other metal sites. Thus, AlOOH may be a wiser choice.

The successful synthesis (**Chapter 3.3.1.2**) of the Al-TCPP from AlOOH can be confirmed using PXRD by comparison with the simulated pattern (**Figure 4.24a**). A small amount of the unreacted AlOOH may exist because of a tiny and broad peak at  $2\theta=14.5^\circ$  in the PXRD pattern of Al-TCPP. From the morphology characterizations by SEM and TEM, apparent layer structures can be observed (**Figure 4.24c,d**), demonstrating the feasibility of this synthesis strategy. However, large 3D particles also exist, as can be seen in the SEM image (**Figure 4.24b**), indicating that the synthesis needs to be improved.

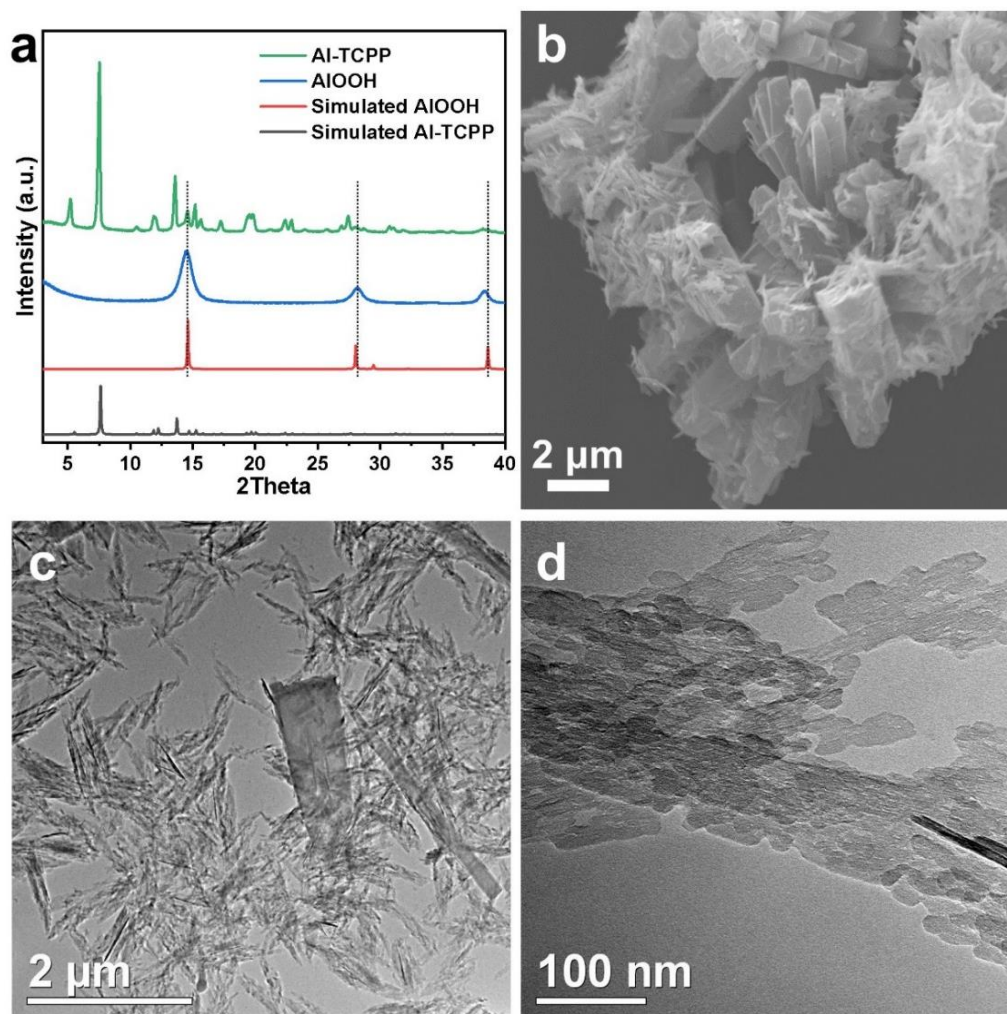


**Figure 4.24** (a) PXRD patterns of the simulated Al-TCPP, simulated AIOOH, as-synthesized AIOOH, and Al-TCPP. (b) SEM image and (c,d) TEM images of the Al-TCPP, using self-sacrificing template methods.

### 4.3.3 Summary

The principle of using a self-sacrificing template to construct 2D-Al-TCPP is proven to be possible. However, the optimization of synthesizing 2D Al-TCPP was not continued, because the synthesis of Zr-TATB MOL was more promising. In addition, competing publications showed up in 2020,<sup>[274,275]</sup> which weakened the innovation of my work.

## 4.4 MOL derived materials

The 2D-MOFs described in the former chapter are intended to be directly used in electrocatalysis. However, the conductivity problem still exists even for most 2D-MOFs. Constructing 2D-MOFs can compensate for conductivity problems by exposing more external surfaces. The pyrolysis of MOFs is still a common strategy for electrocatalysis, as discussed in the introduction. Hereafter, a strategy to develop 2D MOF-derived materials is presented.

## 4.4.1 Design strategy

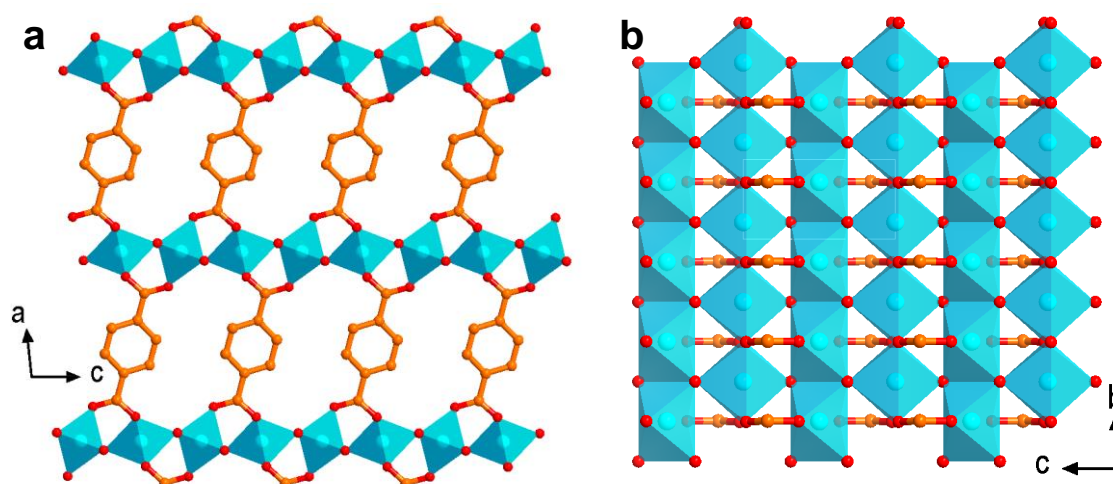


**Figure 4.25** Scheme illustrating the structure of  $M^{II}$ -BDC ( $M = Ni, Co$ ), viewed along (a)  $b$  axis (b)  $a$  axis.<sup>[252]</sup>

The precursor adopted here is  $M^{II}$ -BDC ( $M = Co, Ni$ ), which has been famous for electrocatalysis since its publication in 2016<sup>[252]</sup>. The advantages of this kind of MOFs are their facile and scalable synthesis and low cost. It is not a two-dimensional MOF, but tends to form a laminar structure (**Figure 4.25**). The layer's orientation is along the plane of the planar metal SBUs (Co or Ni). By performing different variations of the precursor, a series of related materials can be obtained: 1. Metal doping of SBUs. Other divalent or trivalent metal ions can be partially exchanged into the metal SBUs. 2. Linker modification. The linker can be exchanged or post-modified. Herein, I would like to exchange the original 1,4-benzene dicarboxylic acid (BDC) linker by the 2-aminoterephthalic acid (ATA) linker, due to the similar coordination features. The amino groups in ATA can be post-synthetically modified into Salen-type compounds (**Figure 4.26**), which bring additional possibilities for the sake of environment modulations of the active sites.

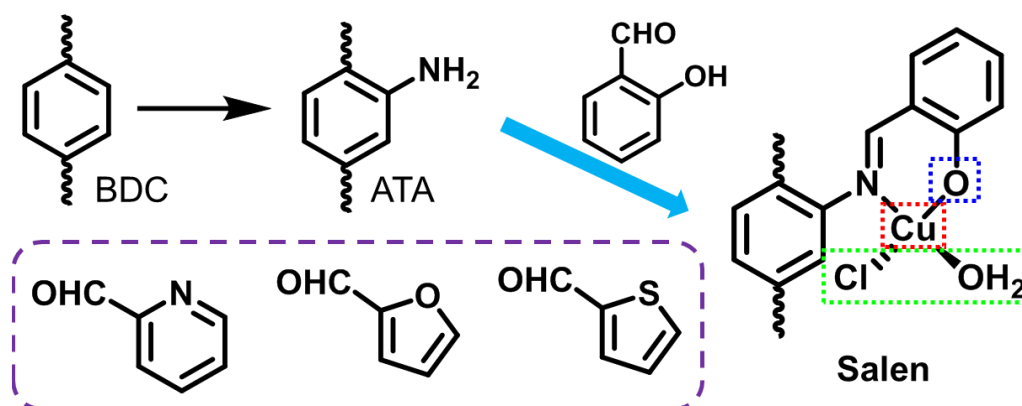


**Figure 4.26** Scheme illustrating the possible post-synthetic modifications after replacing BDC with ATA. The dashed box represents the tunable coordination sites.

#### 4.4.2 Synthesis and characterizations

Considering that the materials are designed for the ECR reaction, I would mainly focus on the Co-based MOFs because a recent work by Xie's group reported a high performance of ECR to formate by Co species.<sup>[46]</sup> The synthesis was based on the Co-BDC literature with the slight modification that the linker was replaced by the same amount of the ATA (**Chapter 3.3.1.3**).<sup>[252]</sup> We checked the morphology of the as-synthesized Co-ATA powder by SEM/TEM, and found a layer structure (**Figure 4.27**). However, its PXRD pattern could not match the simulated Co-BDC pattern (**Figure 4.28a**), which indicates that Co-ATA is not an isorecticular structure of Co-BDC. Considering the possible existence of various isomers of Co-ATA/BDC compatible with our system, we searched the CCDC database to find the possible structure. Luckily, we could find one structure (Co<sub>3</sub>-BDC), which matches our experiment data at least partially (**Figure 4.28a-c**).<sup>[276]</sup> The main difference is the strength of the prominent diffraction peak, indicating that the as-synthesized powder possesses a certain preferred orientation, as was the case for Zr-TATB MOL. By indexing the diffraction peaks, we could find that Co-ATA exhibits relatively enhanced (002) peaks and weakened (200) peaks. Therefore, we can infer that the preferred orientation of the Co-ATA layer is (200) (**Figure 4.28d**). Since the diffraction at the (200) plane didn't totally disappear, the thickness corresponds to several layers.

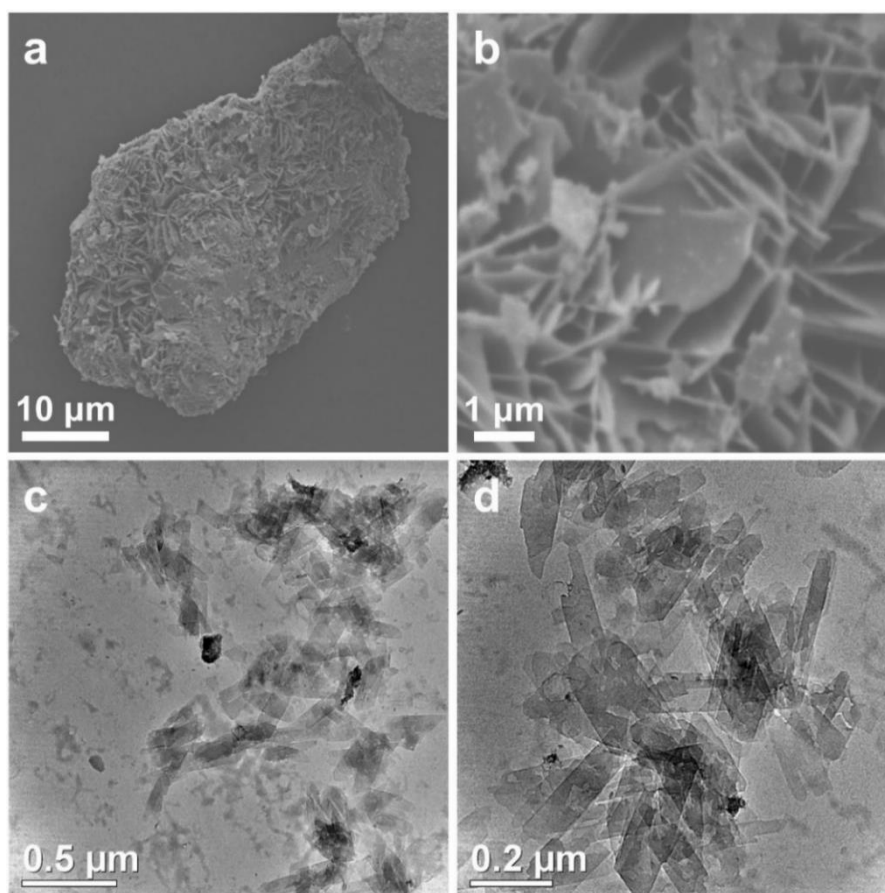


**Figure 4.27** (a,b) SEM images of Co-ATA. (c,d) TEM images of Co-ATA.

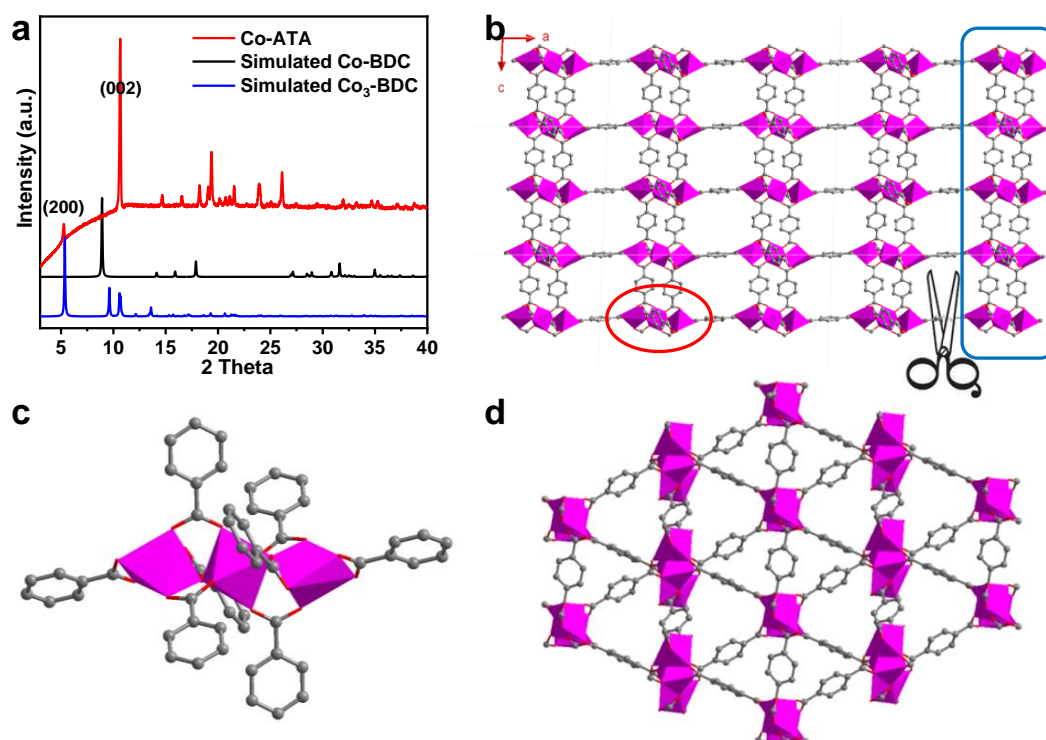


**Figure 4.28** (a) PXRD patterns of simulated Co-BDC, simulated Co<sub>3</sub>-BDC, and as-synthesized Co-ATA. Scheme illustrating (b) the structure of Co<sub>3</sub>-BDC viewed along *b* axis (c) the structure of the Co<sub>3</sub> SBU. (d) Co<sub>3</sub>-BDC with preferred (200) orientation.

We made a preliminary trial of the Co-ATA pyrolysis at 400 °C under vacuum (**Figure 4.29**). It turned out that layer structure could be maintained after pyrolysis. Aggregated nanoparticles could be observed on the layer by the contrast difference, ascribed to the Co oxide (**Figure 4.29**). The dispersion of the nanoparticles is not well controlled in this preliminary trial, which needs optimizations of the reaction conditions.

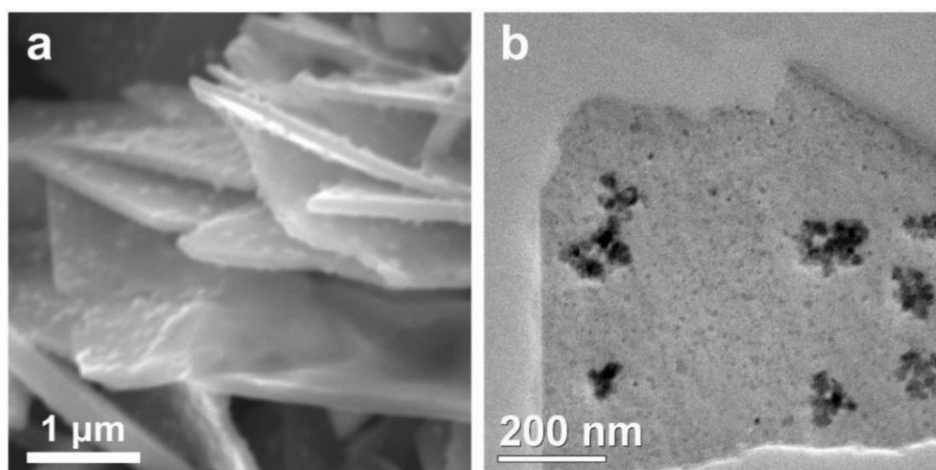


**Figure 4.29** (a) SEM images and (b) TEM images of Co-ATA-400.

#### 4.4.3 Summary

We found a successful synthesis of lamellar Co-ATA. The morphology and structure were

primarily discussed and confirmed by electron microscopy and X-ray diffraction studies. The preliminary results of the pyrolysis show the great potential to achieve a well-dispersed Co-based material. However, considering the limited time, further investigations were suspended, and the focus was placed on the investigation of Zr-TATB MOL.



## 5 | Development of Bi<sub>2</sub>O<sub>3</sub>/MOL Composites

To ensure stability in the ECR reaction and avoid the influence of poor conductivity, we selected Zr<sub>6</sub>-oxo based 2D-MOFs as our key research subject. Considering the inertness of Zr in the ECR reaction, the introduction of exogenous catalytic sites to form composites is a primary and necessary step to achieve good performance. Due to the exposed surface, abundant/uniform surface groups, well-defined structure, and good stability, Zr-TATB MOL is ideal for constructing and optimizing MOL composites for ECR reaction. In this chapter, the mechanism of creating MOL composites and the development of a superior MOL composite will be discussed.

### 5.1 Basic principles to achieve MOL composites

Besides the outstanding stability of the Zr<sub>6</sub>-oxo clusters, another advantage is their flexible structures in constructing MOFs, which significantly promotes the diversity of MOFs structures, which are discussed in **Chapter 1.3.1.4**. The general chemical formula of Zr<sub>6</sub>-oxo based MOFs is shown in **Figure 5.1**.<sup>[253]</sup>

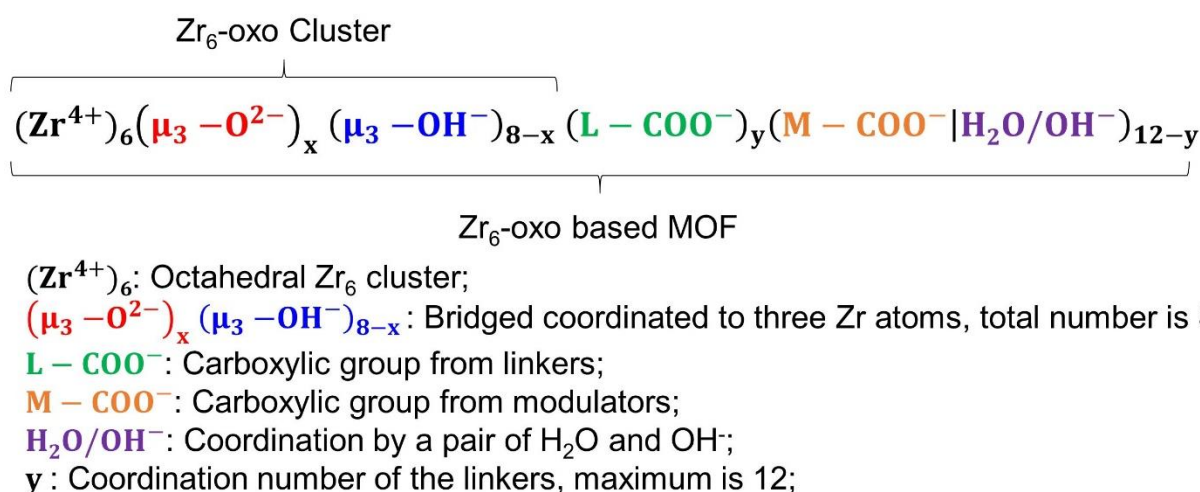


**Figure 5.1** The formula and components of Zr<sub>6</sub>-oxo based MOFs.

The structures of most MOFs are determined by single-crystal X-ray diffraction (SC-XRD), which is still one of the most accurate characterization methods to determine the material structure. The drawback is that a high-quality single crystal is needed. Besides, H atoms and small amounts of non-periodical components can not be detected by SC-XRD. Therefore, another charge balance principle is combined to get the exact formula of the Zr<sub>6</sub>-oxo clusters and corresponding MOFs.

The octahedral Zr<sub>6</sub>-oxo clusters could have an asymmetry of O<sub>h</sub>, D<sub>3d</sub>, D<sub>4h</sub>, and so on, depending on the exact coordination environments. At every face of the octahedron, there would be one bridging O or OH, which is coordinated to three Zr atoms. The exact ratio of O:OH is determined by the charge balance. The μ<sub>3</sub>-OH exhibits a weak acidity, of which other metal ions can replace the protons. Generally, Zr<sub>6</sub>-oxo clusters have a maximum coordination number of 12 towards carboxylate groups of the linkers. Restricted to the asymmetry and spatial obstruction of linkers, the coordination number can be 10, 8, or 6, which means the existence of unsaturated coordination sites. The uncoordinated sites can be capped by the modulators (monocarboxylic acids, such as formic acid, acetic acid, etc.) or a pair of H<sub>2</sub>O/OH<sup>-</sup>, or other possibilities.<sup>[162,277,278]</sup> The unsaturated coordination widely exists in the Zr<sub>6</sub>-oxo based MOF due to inevitable structural defects.<sup>[277]</sup>

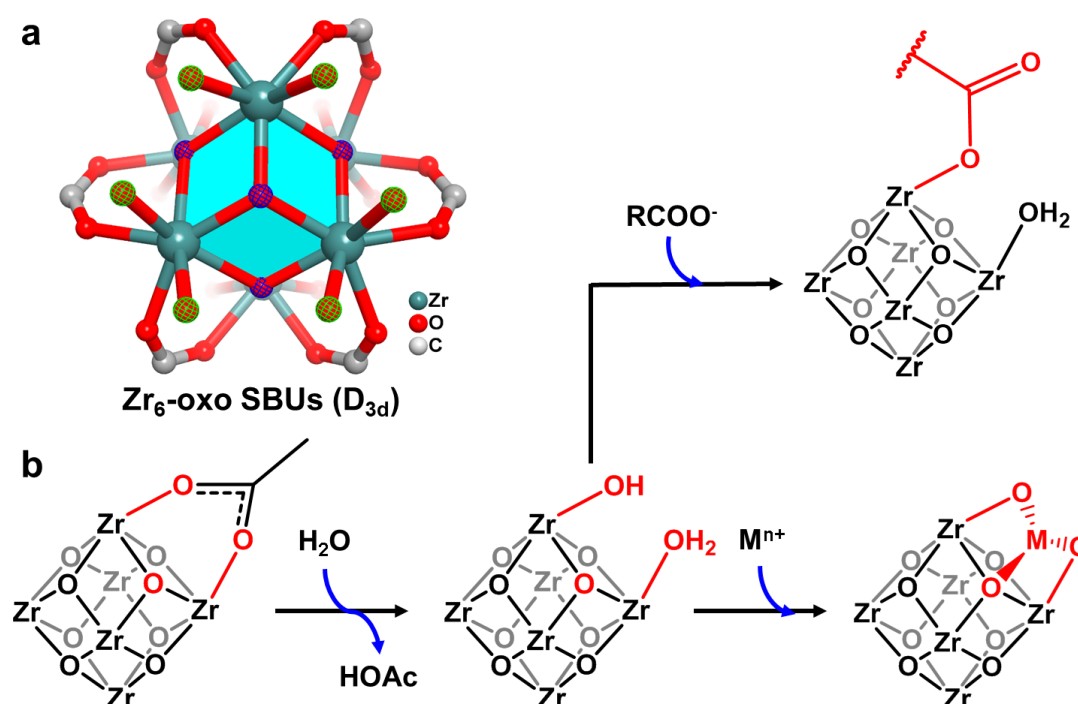


**Figure 5.2** (a) Structure of the Zr<sub>6</sub>-oxo cluster, with open anchoring sites. Symbols with green /blue nets represent -OH/OH<sub>2</sub> and -μ<sub>3</sub>-O/OH, respectively. Cyan balls: Zr atoms; Red balls: O atoms; Grey balls: C atoms. (b) Scheme illustrating the post-modifications upon Zr<sub>6</sub>-oxo cluster, including metal ions modification and organic group modification.

The Zr<sub>6</sub>-oxo cluster is quite an oxygen-rich structure compared to ZrO<sub>2</sub>, with a stoichiometric ratio of Zr:O of 6:32. It is an amphoteric compound bearing multiple sites: (1) the unsaturated Zr can provide Lewis acid sites; (2) the μ<sub>3</sub>-OH can provide Brønsted acid sites; (3) The lone pair electron of O atoms from the linkers or -OH can serve as Lewis base sites. These dense and versatile surface groups open up a great potential for post-modifications.<sup>[162,279]</sup>

The Zr-TATB MOL inherits the high tunability of the Zr<sub>6</sub>-oxo cluster for versatile post-modifications. Considering the surface is fully accessible, the post-modifications will not be blocked by the restricted pore volume. There are three neighboring pairs of H<sub>2</sub>O/OH<sup>-</sup> and one μ<sub>3</sub>-

O/OH, perpendicular to the plane, which can be used to immobilize guest metal ions strongly (Figure 5.2).<sup>[235,279]</sup> The surface OH groups can also undergo more synthetic modifications, such as acylation into a carboxylic acid. If these unsaturated sites are occupied by the modulators (monocarboxylic acid), this process can be regarded as an exchange of the capping molecule.<sup>[162]</sup> As discussed in Chapter 4.2.1, the successful synthesis of the Zr-TATB MOL requires the capping effect of the acetate, which is proven by dissolution/NMR analysis (Figure 5.3). However, the capping by the acetate does not prevent the post-modifications, because the coordination or capping by the acetate is reversible and flexible, which is indicated by the possible hydrolysis to restore the surface -OH (Figure 5.2b). This reverse coordination can be proven through a vacuum treatment of the sample at 160 °C. Under such a condition, the acetate will combine with the proton sources ( $\mu_3$ -OH, H<sub>2</sub>O, etc.) to an acetic acid molecule and then is removed by the evaporation under vacuum. The slight shift of the peaks of TATB<sup>3-</sup> can result from the difference in pH and water content when conducting the characterization.<sup>[280]</sup>

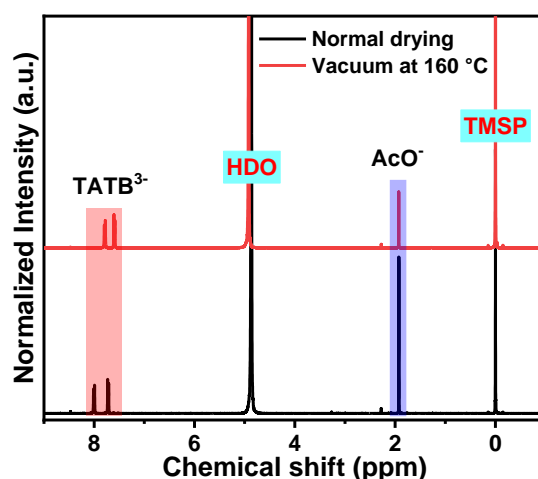


**Figure 5.3** <sup>1</sup>H-NMR spectrum of the dissolved Zr-TATB MOL treated under different conditions, using *d*4-TMSP as an internal standard. The intensities are normalized by the area of the TATB<sup>3-</sup> signal.

## 5.2 Synthesis and characterizations of Bi<sub>2</sub>O<sub>3</sub>/MOL composites

Among the active sites for formate generation, Bismuth-based active sites are receiving much attention due to their excellent performance (Figure 1.11). Herein, Bi was adopted to the construction of MOL composites.

### 5.2.1 Ultrafine BiO<sub>x</sub>/MOL composites

The trivalent Bi ion should interact strongly with the multiple surface -OH<sub>x</sub> groups of Zr-TATB MOL.<sup>[281]</sup> Many examples have been reported based on this loading principle to construct single-

atom materials based on MOFs (**Figure 5.2**).<sup>[159,235,279]</sup> This was done by stirring the Bi precursor (Bi(NO<sub>3</sub>)<sub>3</sub>) and Zr-TATB MOL in DMF solution at room temperature (**Chapter 3.3.2.1**). After the reaction, the solid was separated and thoroughly washed. ICP-AES confirmed that Bi was successfully loaded with 0.56 wt% (**Table 10.3**).

By electron microscopy techniques, the morphology of the loaded Bi was examined. From the TEM images, only the lattice of the Zr-TATB MOL can be observed without apparent heterogeneous particles being observed (**Figure 5.4a,b**). Considering the complexity of the imaging mechanism of the conventional TEM, we resort to the HAADF-STEM, in which the contrast can give direct evidence of the Z (atomic number) difference. In the dark-field image, a higher atomic number causes a brighter plot. The thickness will also influence the contrast in the HAADF-STEM images, however, with a minor influence than the Z contrast. Generally, the thicker the layer is, the brighter it would be. In the overall view, the layer number difference can be directly observed by a contrast difference, which is marked by the yellow curves in **Figure 5.4c**. Besides, some bright dots occurring on the layer can be Bi nanoparticles or MOL fragments. In the magnified view, a hexagonal symmetric arrangement of bright dots can be seen, corresponding to the 2D-*kgd* net of the MOL and the Zr<sub>6</sub>-oxo clusters presented as bright dots (**Figure 5.4d-f**). Heterogeneous particles are rarely observed in most of the images.

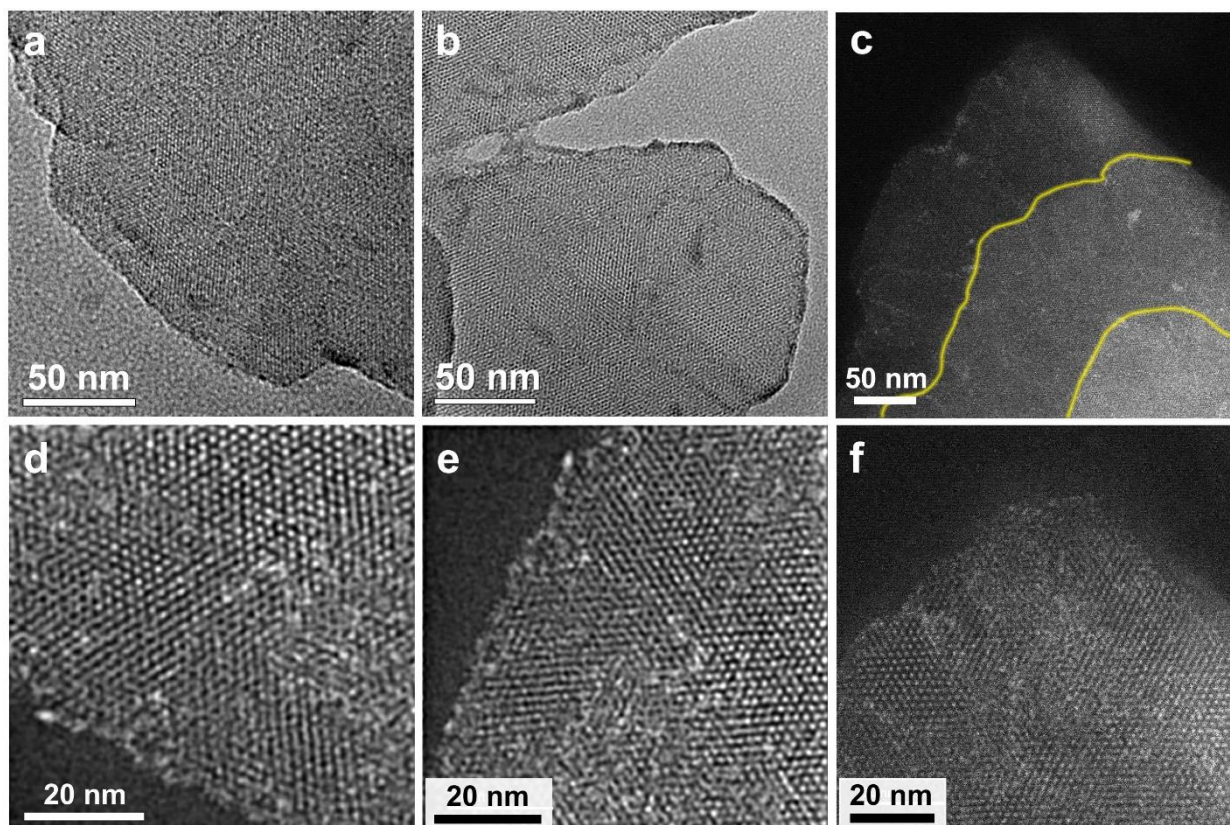


**Figure 5.4** (a,b) TEM images and (c-f) HAADF-STEM images of the BiO<sub>x</sub>/MOL. The edges of the stacked MOL layers are marked by yellow curves in (c).

EELS was applied to give element maps to confirm the dispersion of the introduced Bi sites. The distribution of the Zr can originate from the Zr-TATB MOL. The scanned area is marked by a red square in **Figure 5.5a**, corresponding to the magnified image of **Figure 5.4e**. From the element maps, the spatial coincidence of the Bi and Zr signals can prove the uniform distribution of the Bi on the MOL (**Figure 5.5**), even though it is not clearly observed from the HAADF-STEM image. As for the background, there is nearly no signal belonging to Zr-TATB MOL or Bi species, verifying the reliability of signals. Considering such a mild post-modification, no reduction ability of Bi can be expected, and the state of the Bi can be proposed to be amorphous Bismuth oxide. Here, we can speculate that most Bi species are sub-nanometer BiO<sub>x</sub> species, obtained by the described post-modification of MOL (**Figure 5.2b**).<sup>[162]</sup> From here on, this material is denoted as BiO<sub>x</sub>/MOL.

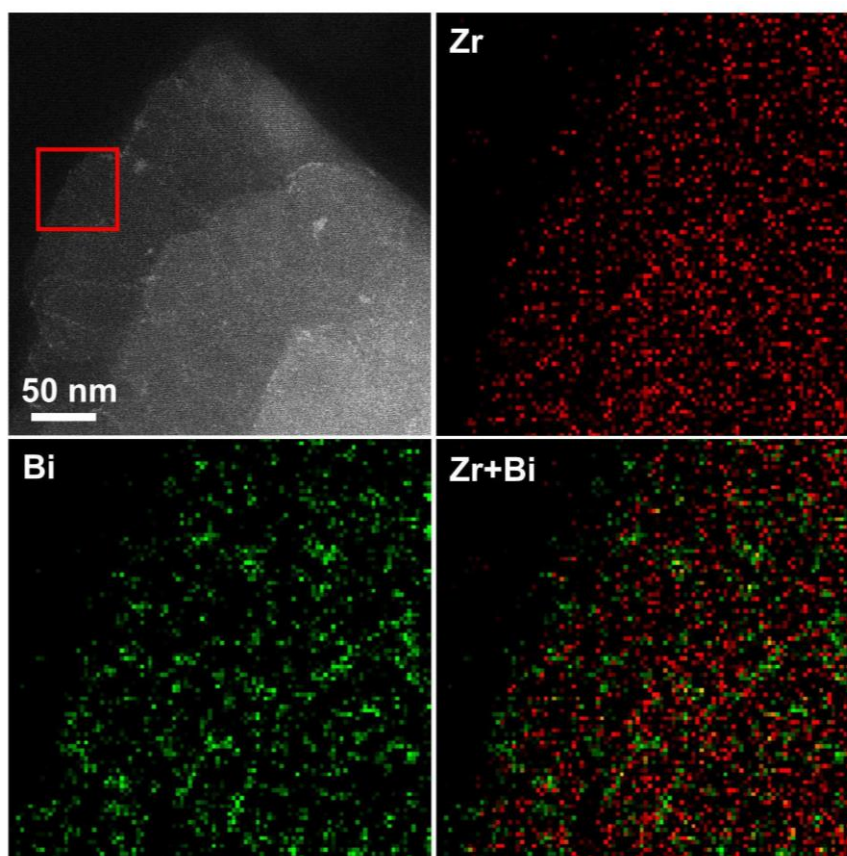


**Figure 5.5** HAADF-STEM images of the BiO<sub>x</sub>/MOL and corresponding EELS maps for Bi, Zr, and the composite map, respectively. The selected area for the EELS mapping is marked by the red box (**Figure 5.4e**).

More element maps were examined to figure out the composition of suspicious particles in **Figure 5.6a-c**. As marked by the ellipse, the particle here can be confirmed as Bi species (**Figure 5.6d-f**). The occurrence of the few nanoparticles can originate from aggregation during the drying process.

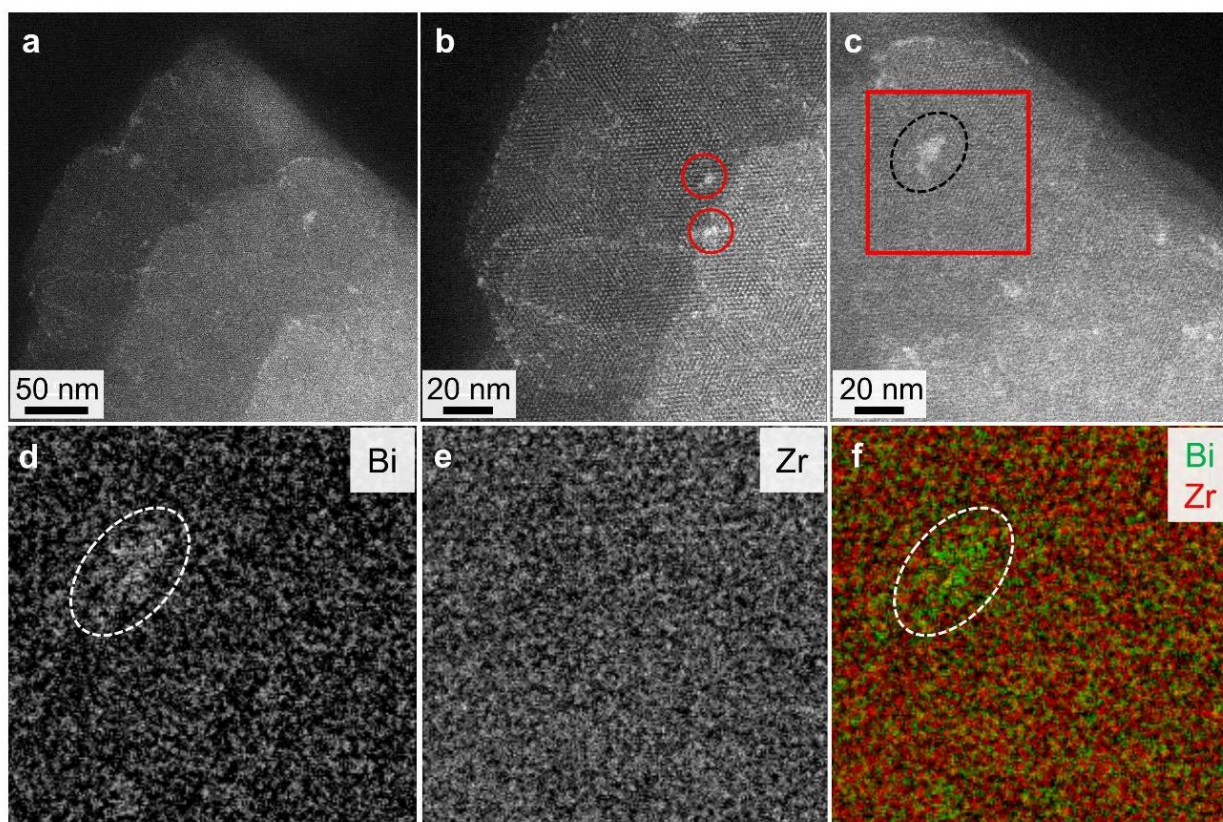


**Figure 5.6** (a-c) HAADF-STEM images of the Zr-TATB MOL. (d-f) The STEM-EELS maps for Bi, Zr, and the composite map, respectively.

### 5.2.2 Bi<sub>2</sub>O<sub>3</sub> nanowires/MOL composite

Considering the loading of the Bi is only 0.56 wt% for BiO<sub>x</sub>/MOL, a hydrothermal post-modification treatment was introduced to increase the Bi loading (Chapter 3.3.2.2). The hydrothermal conditions increased the loading to 2.6 wt%, measured by ICP-AES (Table 10.3). The morphology was investigated by electron microscopy (Figure 5.7). Unlike BiO<sub>x</sub>/MOL, apparent heterogeneous nanowires can be observed to be uniformly distributed on the Zr-TATB MOL. The hydrothermal conditions seem to be mild enough, because the MOL lattice can still be identified (Figure 5.7d). The de-noised TEM image combined with the FFT pattern clearly exhibits a lattice of hexagonal symmetry (Figure 5.7e). The particle size distribution is given in Figure 5.7f, with an average diameter of 5.8 nm. The successful synthesis of such tiny nanowire without the assistance of capping agents highlights the template effect of the MOL.<sup>[282,283]</sup>

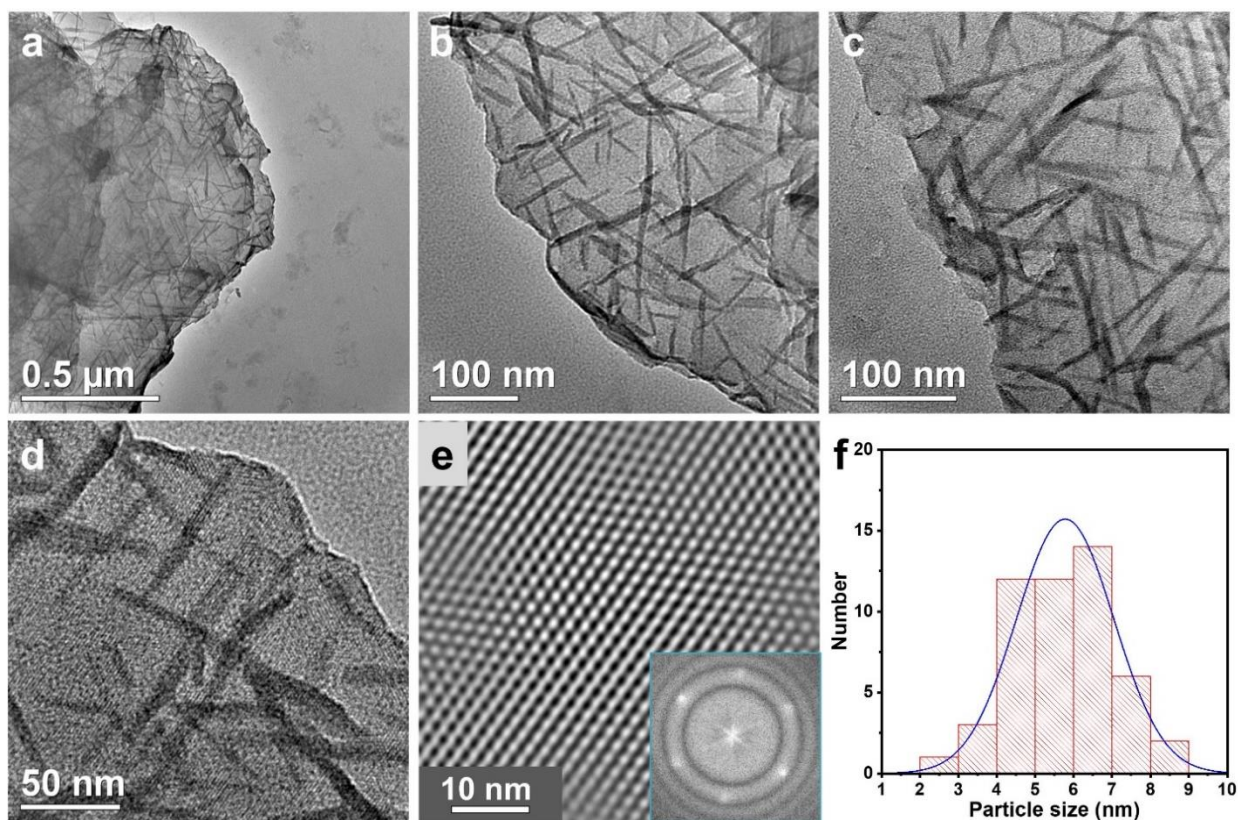


**Figure 5.7** (a-d) TEM images of the Bi<sub>2</sub>O<sub>3</sub>/MOL. (e) De-noised TEM image of the lattice of the MOL and FFT pattern of (d). (f) Diameter distribution diagram of the Bi<sub>2</sub>O<sub>3</sub> nanowires.

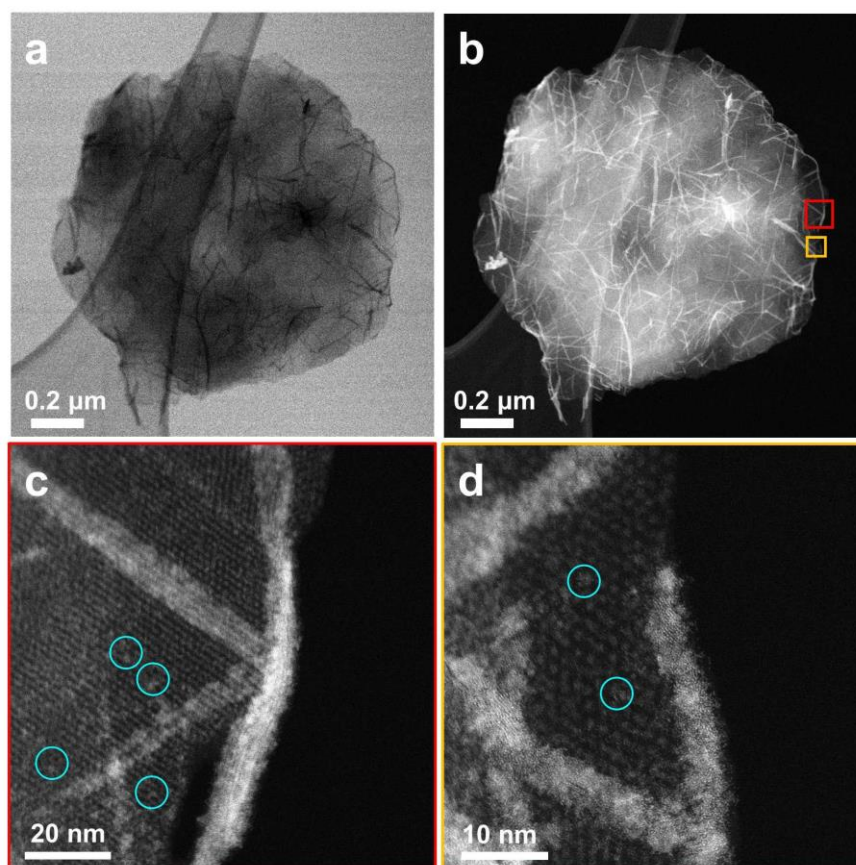


**Figure 5.8** (a) Bright-field and (b) Dark-field STEM images of Bi<sub>2</sub>O<sub>3</sub>/MOL. (c,d) High-resolution HAADF images of the selected areas marked with red and orange borders. Some ultrafine clusters highlighted by blue circles can be observed, independent of nanowires.

Even though the contrast difference indicates the existence of nanowires, this is still not a solid evidence that these are Bi species. Further STEM measurements were conducted, confirming Bi nanowires onto the Zr-TATB MOL (**Figure 5.8**). The apparent contrast difference in the image can reflect the Z difference between the nanowires and the MOL. The brighter the nanowires are in the dark-field images, the larger the atomic number is they have, indicating the nanowires are Bismuth species. From the magnified HAADF-STEM image, we can recognize the lattice of the MOL, demonstrating the integrity of the Zr-TATB MOL after post-modification (**Figure 5.8c,d**). Besides, some small bright dots (highlighted by cyan circles) can be found on the MOL, which do not belong to nanowires. These ultrafine nanoparticles may inherit from the BiO<sub>x</sub>/MOL, which can be regarded as the primary stage before the hydrothermal treatment. Further confirmation of the Bi-based nanowires was achieved by EELS maps (**Figure 5.9**). The signal of the Bi mainly concentrates on the bright nanowires in the dark-filed images, confirming the Bi species of the nanowires.

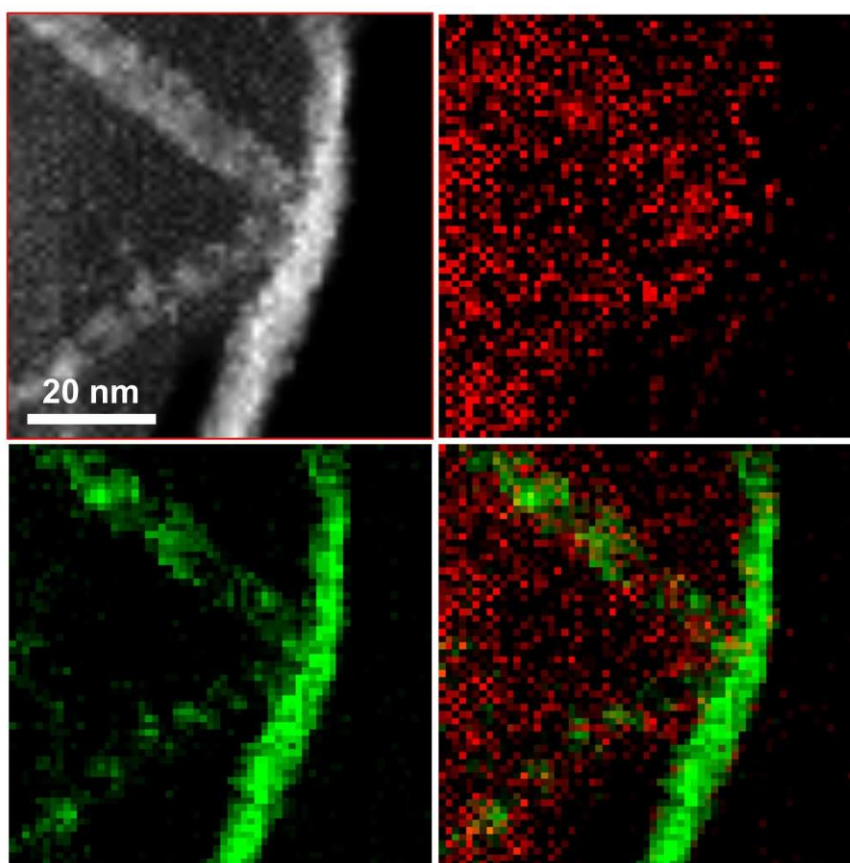


**Figure 5.9** HAADF-STEM images of the Bi<sub>2</sub>O<sub>3</sub>/MOL and corresponding EELS maps for Bi, Zr, and the composite map, respectively.

We turned to the question of what is the structure of the nanowires. The High-Resolution HAADF-STEM image shows a clear crystal lattice from the nanowire, indicating its crystalline nature (**Figure 5.10**). The FFT patterns at different positions of the nanowire all give similar patterns, which indicates a uniform structure of the whole nanowire. The lattice spacing can be

measured to be 3.408 Å (Figure 5.11), ruling out the possibility of metallic Bi (R-3m, 3.280 Å; Im3m, 2.67 Å). Considering the synthesis condition, it can only be a kind of bismuth oxide. As for the Bi<sub>2</sub>O<sub>3</sub>, there are commonly four crystallographic phases, which is  $\alpha$ -Bi<sub>2</sub>O<sub>3</sub> (monoclinic),  $\beta$ -Bi<sub>2</sub>O<sub>3</sub> (tetragonal),  $\gamma$ -Bi<sub>2</sub>O<sub>3</sub> (bcc), and  $\delta$ -Bi<sub>2</sub>O<sub>3</sub> (fcc). The FFT pattern shows the diffraction spots corresponding to a simple cubic symmetry. The structure elucidation was assisted by PXRD patterns (Figure 5.12a), which show the main peak at 28.1°. After searching the COD<sup>[284]</sup> and *jade* PDF cards, we found the best match to  $\beta$ -Bi<sub>2</sub>O<sub>3</sub> (PDF#18-0244, COD-9007723). Besides,  $\gamma$ -Bi<sub>2</sub>O<sub>3</sub> (bcc) and  $\delta$ -Bi<sub>2</sub>O<sub>3</sub> (fcc) are less inclined to exhibit such a simple cubic symmetry. Hence, we are able to index the FFT pattern, which is (210), (-120), (-2-10), (1-20), (-310) and (3-10) with [001] zone axis of  $\beta$ -Bi<sub>2</sub>O<sub>3</sub> (Figure 5.11). From here on, this material is denoted as Bi<sub>2</sub>O<sub>3</sub>/MOL.

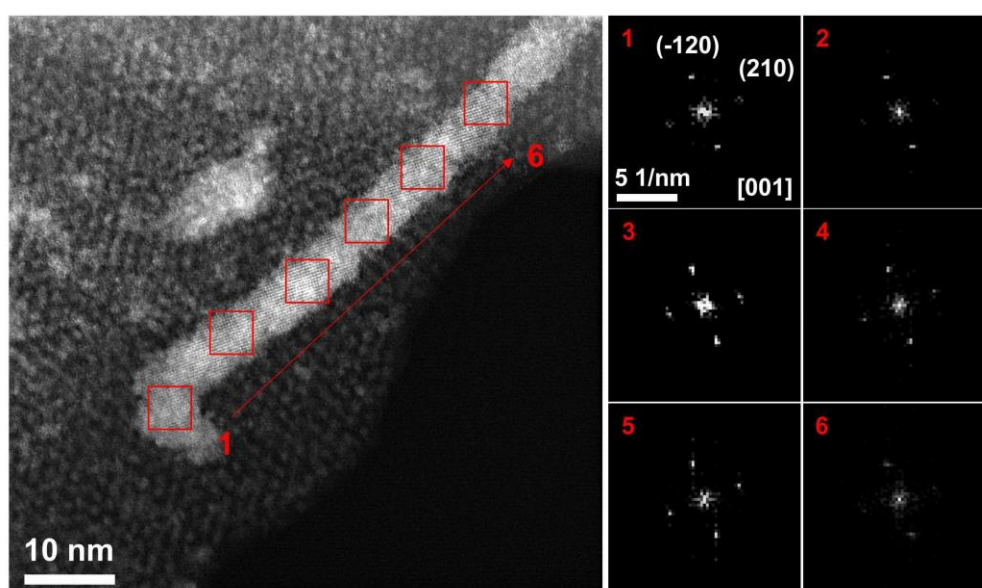


**Figure 5.10** HAADF-STEM image of Bi<sub>2</sub>O<sub>3</sub>/MOL and localized FFT patterns. Six selected squares along the nanowire were selected, all exhibiting cubic diffraction, corresponding to [001] zone axis of crystalline tetragonal Bi<sub>2</sub>O<sub>3</sub>

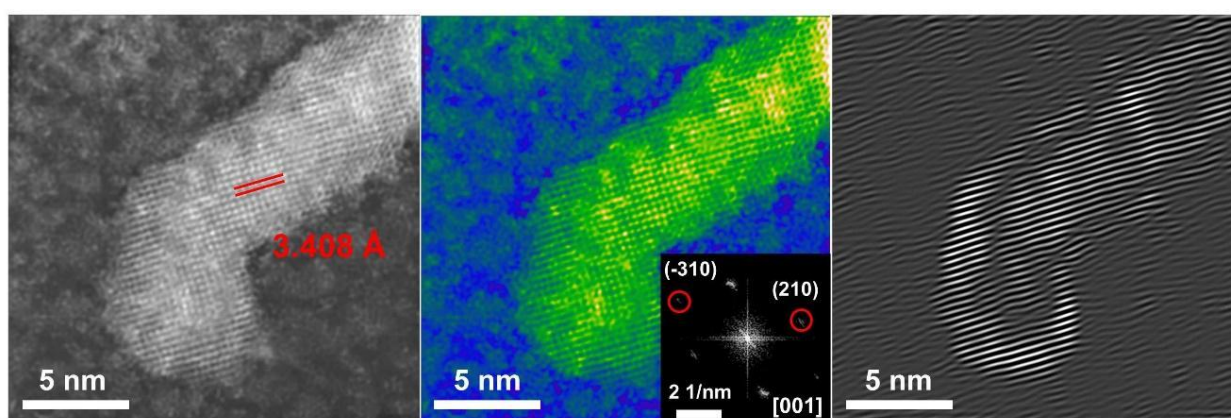


**Figure 5.11** (a) Conventional, (b) recolored, and (c) de-noised HAADF-STEM image of the Bi<sub>2</sub>O<sub>3</sub> nanowires on the Zr-TATB MOL. The corresponding FFT pattern is inserted in (b).

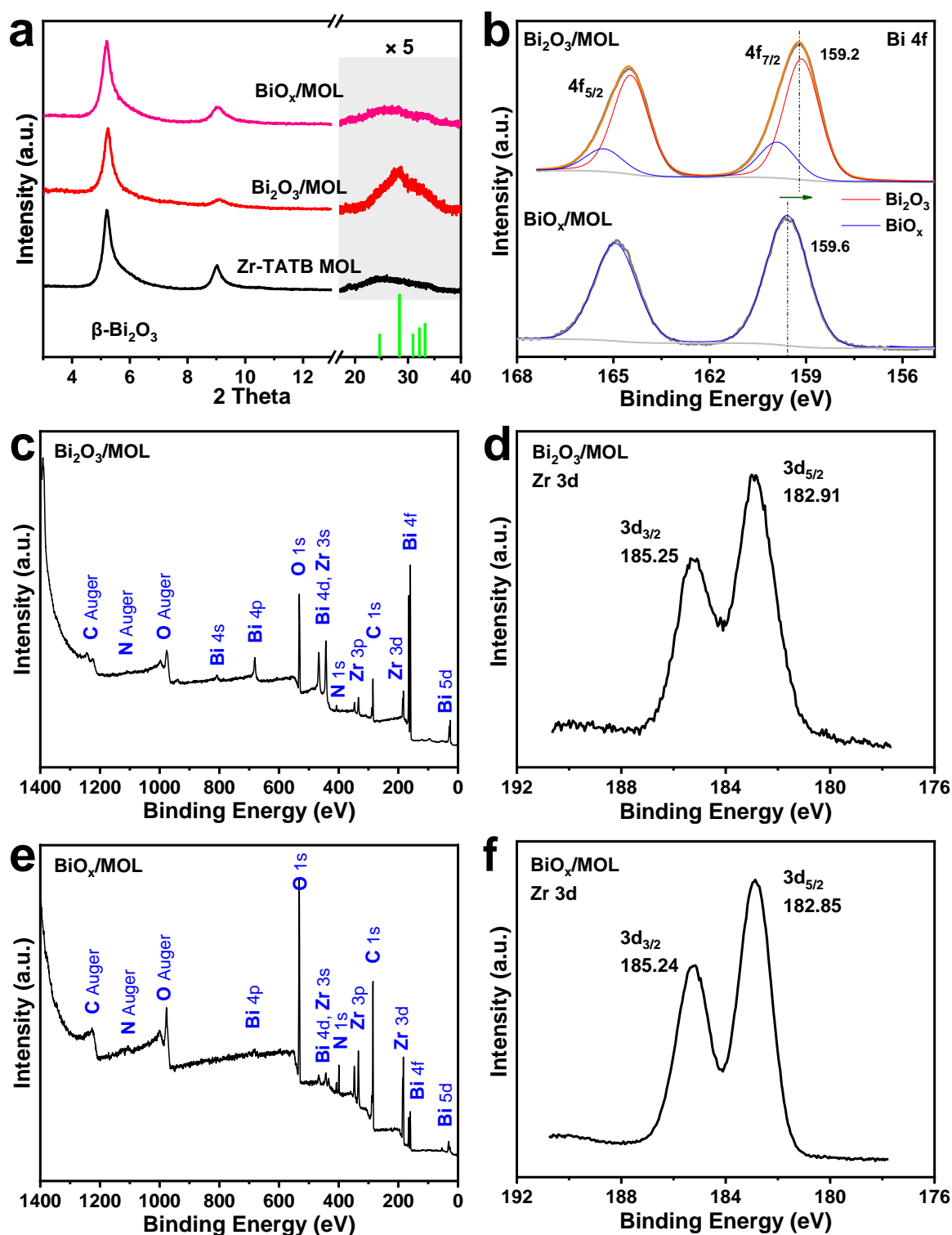


**Figure 5.12** (a) PXRD patterns of the  $\beta$ -Bi<sub>2</sub>O<sub>3</sub> (PDF#18-0244), as-synthesized Zr-TATB MOL, Bi<sub>2</sub>O<sub>3</sub>/MOL and BiO<sub>x</sub>/MOL (b) Bi 4f XPS spectra with peak fittings of Bi<sub>2</sub>O<sub>3</sub>/MOL and BiO<sub>x</sub>/MOL. Full XPS spectra of (c) Bi<sub>2</sub>O<sub>3</sub>/MOL and (e) BiO<sub>x</sub>/MOL. Zr 3d XPS spectra of (d) Bi<sub>2</sub>O<sub>3</sub>/MOL and (f) BiO<sub>x</sub>/MOL.

The difference between BiO<sub>x</sub>/MOL and Bi<sub>2</sub>O<sub>3</sub>/MOL is not only in the morphology. According to the PXRD patterns, BiO<sub>x</sub>/MOL is a non-crystalline structure (Figure 5.12a), which is also verified by the absence of the lattice fringes in HR-TEM. X-ray photoelectron spectroscopy (XPS) examines the chemical state of the elements of the two materials. As for the Bi states, the binding energies of Bi 4f<sub>7/2</sub> are both above 159 eV, which is why the Bi state can be ascribed to be

Bi(III).<sup>[285]</sup> The binding energy of Bi 4f<sub>7/2</sub> in BiO<sub>x</sub>/MOL (159.6 eV) is higher than that of Bi in Bi<sub>2</sub>O<sub>3</sub>/MOL (159.2 eV), indicating an oxidation state being slightly higher than Bi<sub>2</sub>O<sub>3</sub>. This phenomenon can be explained by the ultrafine and amorphous nanoparticles, exhibiting an oxygen-rich structure.<sup>[286]</sup> Considering also the existence of ultrafine nanoparticles in Bi<sub>2</sub>O<sub>3</sub>/MOL (Figure 5.8c,d), we can proceed with peak fitting referring to BiO<sub>x</sub>/MOL, which gives 76.3 % crystalline Bi<sub>2</sub>O<sub>3</sub> nanowires and 23.7 % amorphous BiO<sub>x</sub> nanoparticles (Table 10.4). These are estimated values for qualitative analysis rather than accurate calculations. The full XPS spectra of BiO<sub>x</sub>/MOL and Bi<sub>2</sub>O<sub>3</sub>/MOL are given in Figure 5.12c,e. The absence of the peaks of Bi 6p (1.0 eV) and 6s (10.5 eV), indicates the absence of metallic Bi. Compared with crystalline ZrO<sub>2</sub> (~182.3 eV), the binding energies of Zr 3d<sub>5/2</sub> are significantly higher, which is in accordance with the oxygen-rich structure of the Zr<sub>6</sub>-oxo clusters (Figure 5.1).

The porosity of the Bi<sub>2</sub>O<sub>3</sub>/MOL was examined by N<sub>2</sub> physisorption experiments (Figure 5.13). There is no apparent decrease in the surface area after introducing Bi<sub>2</sub>O<sub>3</sub>. The non-porous characters remain after the post-modifications. For the pore size distribution, the pore size of Bi<sub>2</sub>O<sub>3</sub>/MOL shifts to larger diameters. This observation leads us to speculate that the Bi<sub>2</sub>O<sub>3</sub> nanowires serve as pillars to separate the Zr-TATB MOL layers and prohibit the stacking of the MOLs.

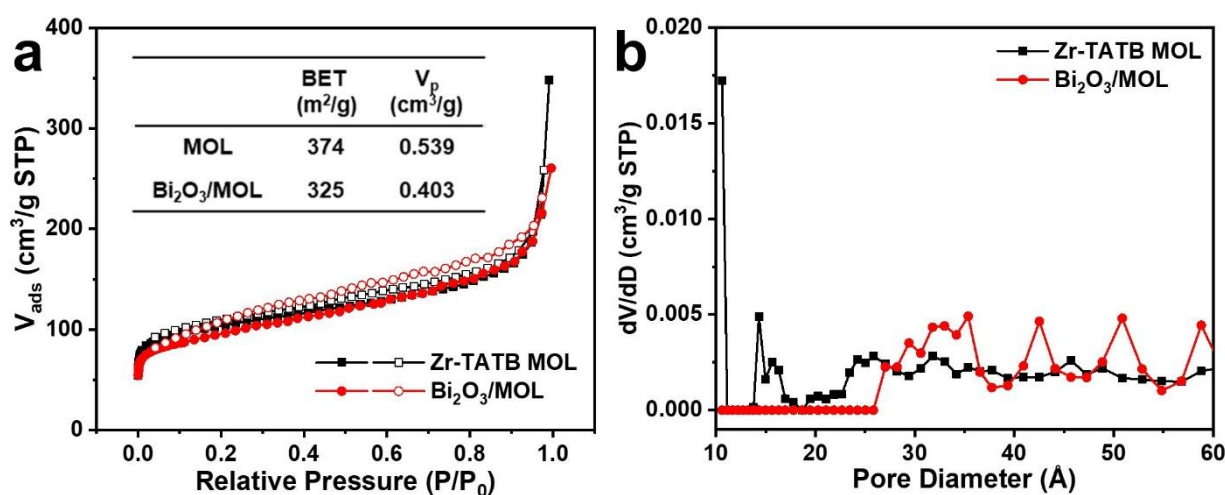


**Figure 5.13** (a) N<sub>2</sub> physisorption isotherms (solid symbols: adsorption curve; open symbols: desorption curve) of Zr-TATB MOL and Bi<sub>2</sub>O<sub>3</sub>/MOL at 77 K (Inserted table: BET surface area and pore volume (V<sub>p</sub>)). (b) DFT pore size distribution of Zr-TATB MOL and Bi<sub>2</sub>O<sub>3</sub>/MOL. The pore size distribution was calculated via DFT by the mode of N<sub>2</sub> at 77 K on silica (cylinder./sphere. pore, NLDFT ads. Model).

### 5.3 Exploring the formation of Bi<sub>2</sub>O<sub>3</sub>/MOL composites

The transformation of BiO<sub>x</sub>/MOL into Bi<sub>2</sub>O<sub>3</sub>/MOL inspired us to investigate the mechanism of the formation of MOL composites more thoroughly. The formation process was investigated by

*ex-situ* TEM measurements (**Figure 5.14**). Samples were taken after certain hydrothermal times. Except for the hydrothermal time, all other parameters were kept the same as Bi<sub>2</sub>O<sub>3</sub>/MOL, described in **Chapter 3.3.2.2**. The sample shown in **Figure 5.14a** was only through a quick ultrasonication upon the mixture of Zr-TATB and Bi precursors in DMF, and no further hydrothermal treatment, which turns out to be no Bi loading. For the synthesis of BiO<sub>x</sub>/MOL, MOL has a much longer reaction time (12 hours), being exposed to the solution of the same Bi precursors. Therefore, the BiO<sub>x</sub>/MOL can be an example to understand the primary modification state before the hydrothermal treatment. Combined with careful discussions in **Chapter 5.1**, we can infer that the starting point is the Bi<sup>3+</sup> post-modification of atomic or cluster-level, schemed in **Figure 5.2**. The reversible coordination of Bi ions to Zr<sub>6</sub>-oxo clusters makes further rearrangement possible, promoted by the solvothermal treatment. Small nanoparticles occurred over the reaction time (**Figure 5.14b**, 0.5 h) and gradually grew into nanowires on the MOL (**Figure 5.14c-e**). The loading gradually increased with time, reaching a maximum after around 12 hours (**Figure 5.14 f**, **Table 10.3**). A visualization of our post-modification strategy is presented in **Figure 5.15**.

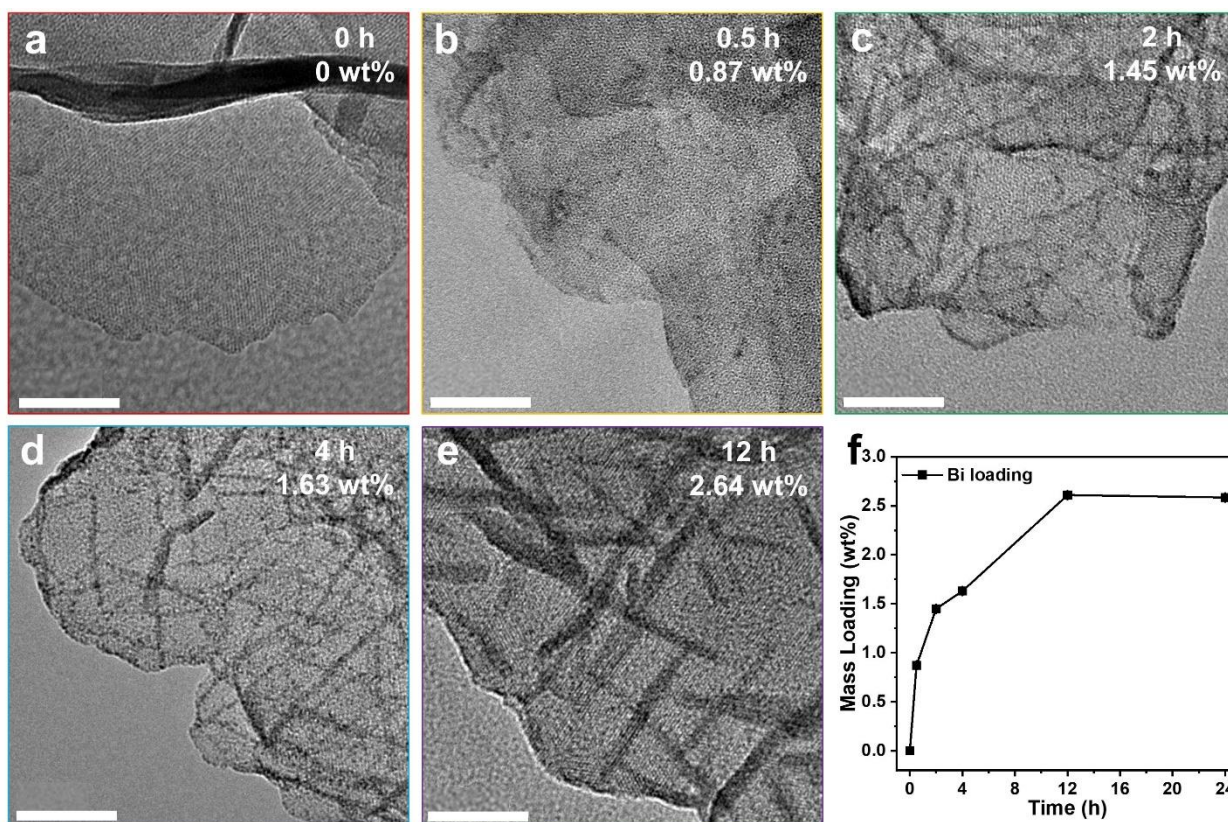


**Figure 5.14** *Ex-situ* TEM images of Bi<sub>2</sub>O<sub>3</sub>/MOL at the different solvothermal times (scale bar: 50 nm). For the *ex-situ* TEM study of the formation of Bi<sub>2</sub>O<sub>3</sub>/MOL, samples were taken after certain synthesis time: (a) 0 h (before solvothermal treatment), (b) 0.5 h, (c) 2 h, (d) 4 h and (e) 12 h. (f) Loading diagram of Bi<sub>2</sub>O<sub>3</sub>/MOL over reaction time.

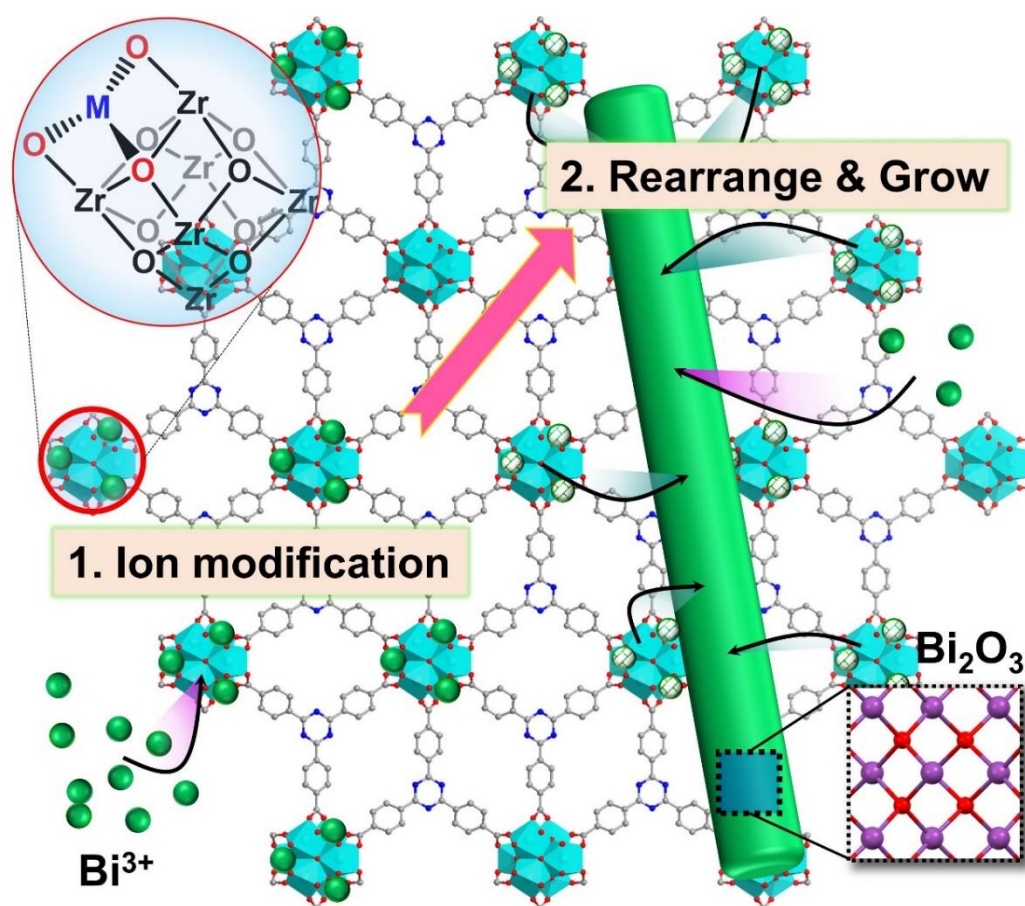


**Figure 5.15** Scheme illustrating the post-modification strategy to construct Bi<sub>2</sub>O<sub>3</sub>/MOL composites. Two steps are proposed: 1. Bi<sup>3+</sup> ion modification on the MOL; 2. The rearrangement of Bi sites occurs and then grows into Bi<sub>2</sub>O<sub>3</sub> nanowires

## 5.4 Synthesis and characterization of reference catalysts

To underline the superiority of MOL-based composites, two reference materials are proposed. One is UiO-66, a typical 3D-MOF, which is also constructed by Zr<sub>6</sub>-oxo clusters and electrically insulating. The other is acetylene black (denoted as AB), widely used as a conductive additive or support in electrochemistry, e.g., batteries and electrocatalysis.

### 5.4.1 Bi<sub>2</sub>O<sub>3</sub>/UiO

UiO-66 is one of the most famous MOFs, widely adopted for versatile applications and commercial availability. It is constructed by the fully coordinated Zr<sub>6</sub>-oxo cluster and a simple linker (BDC), giving a 3D framework of *fcu* topology (**Figure 5.16**). The structural stability in electrocatalysis has been proved,<sup>[209]</sup> which is a commonality for Zr<sub>6</sub>-oxo cluster based MOFs.

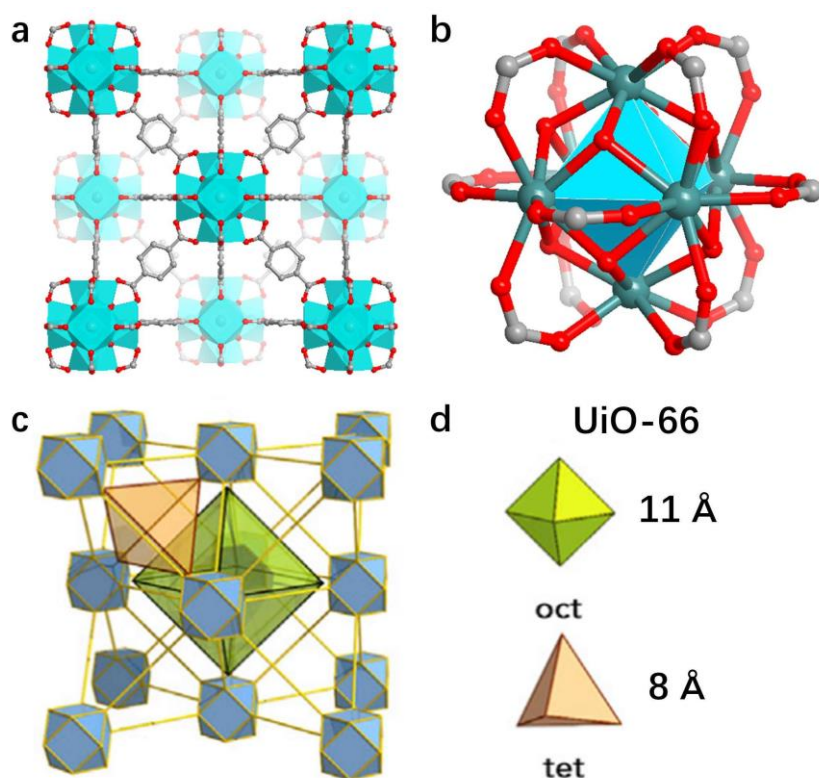


**Figure 5.16** Scheme illustrating the structure of (a) UiO-66 and (b) its Zr<sub>6</sub>-oxo based SBUs. (c) 3D *fcu* topology of the UiO-66<sup>[159]</sup>. (d) Two types of pore cavities in UiO-66.

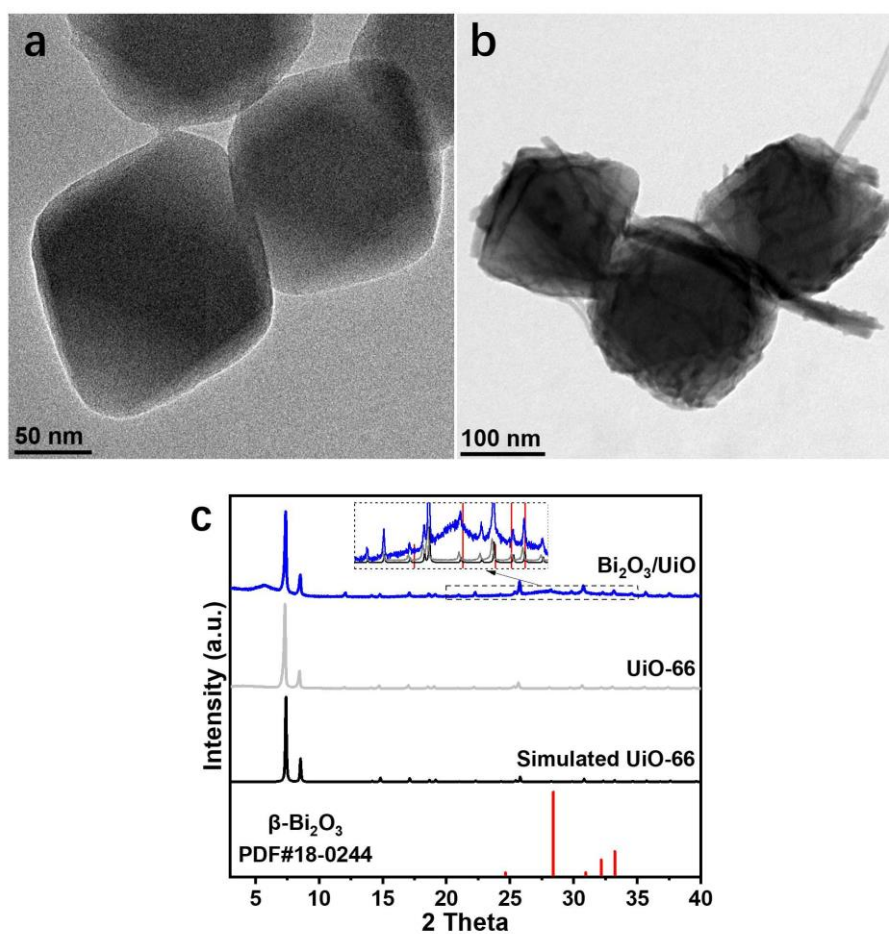


**Figure 5.17** TEM images of (a) UiO-66 and (b) Bi<sub>2</sub>O<sub>3</sub>/UiO. (c) PXRD patterns of the standard β-Bi<sub>2</sub>O<sub>3</sub> (PDF#18-0244), simulated UiO-66, as-synthesized UiO-66, and Bi<sub>2</sub>O<sub>3</sub>/UiO.

The synthesis of UiO-66 was done by modification of a published synthesis protocol (**Chapter 3.3.2.2**).<sup>[287]</sup> TEM and PXRD confirmed its successful synthesis (**Figure 5.17**). As-synthesized UiO-66 exhibits a typical octahedral morphology. The Bi loading was done by a similar method as Bi<sub>2</sub>O<sub>3</sub>/MOL, except the MOL was replaced by UiO-66, denoted as Bi<sub>2</sub>O<sub>3</sub>/UiO. By ICP-AES, the content of Bi is 2.38 wt%. In the TEM images of Bi<sub>2</sub>O<sub>3</sub>/UiO, we can also observe the appearance of the heterogeneous nanowires (**Figure 5.17b**). The crystalline Bi<sub>2</sub>O<sub>3</sub> was found from the PXRD pattern and exhibited a very broad peak at 28° corresponding to β-Bi<sub>2</sub>O<sub>3</sub>. The formation mechanism of the nanowires should be the same as for the Zr-TATB MOL (**Figure 5.15**), for both containing Zr<sub>6</sub>-oxo clusters as SBUs.

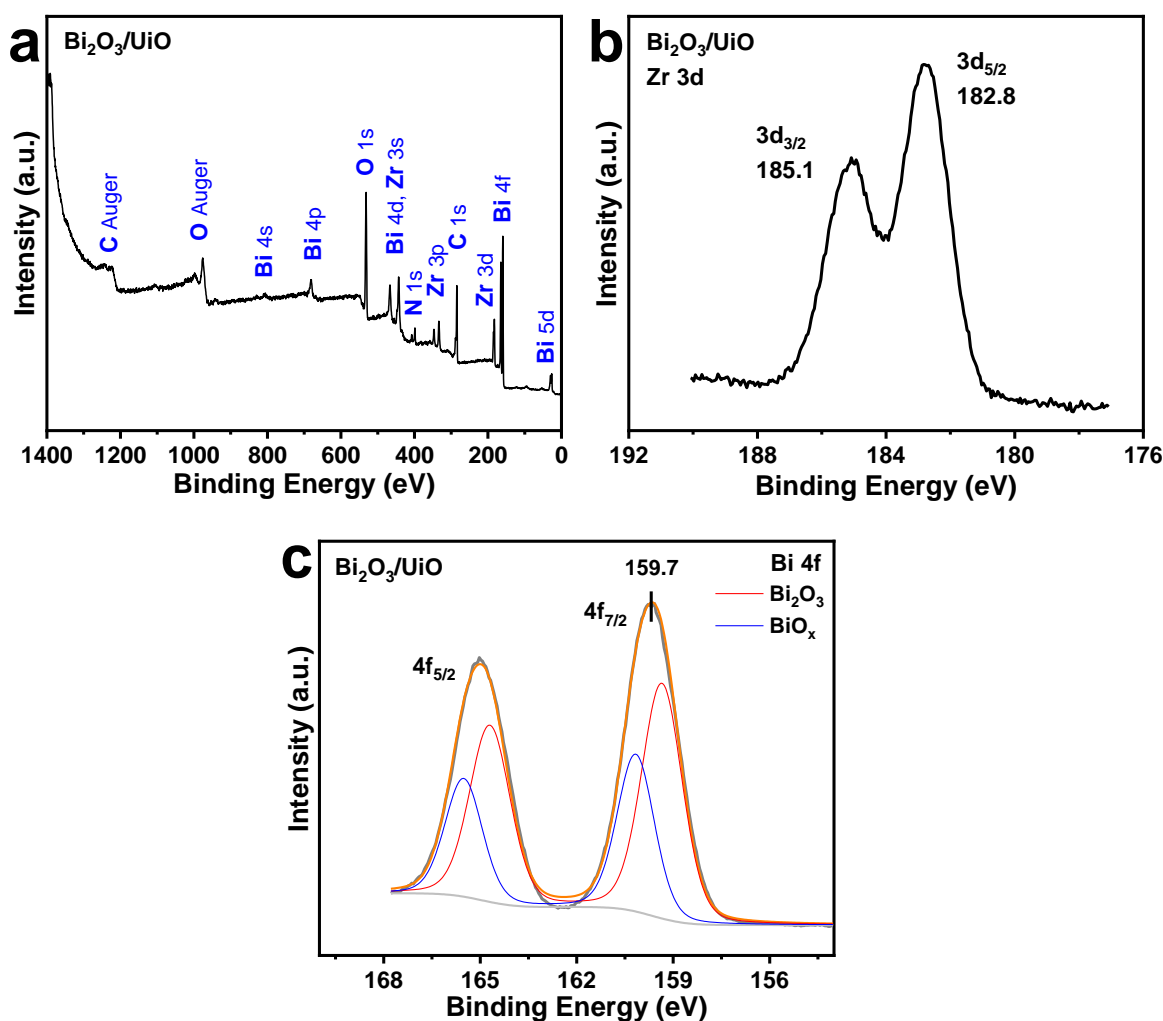


**Figure 5.18** (a) XPS full spectrum, (b) XPS Zr 3d spectrum, and (c) XPS Bi 4f spectrum with peak fittings of the Bi<sub>2</sub>O<sub>3</sub>/UiO.

However, considering the large proportion of the inner surface area (pore size < 2 nm), the growth of the Bi<sub>2</sub>O<sub>3</sub> nanowires can suffer from a steric hindrance. This can be proved by XPS (**Figure 5.18**). The full spectrum confirms the absence of metallic Bi due to the absence of the peaks of Bi 6p (1.0 eV) and 6s (10.5 eV). By the same principle of fitting Bi 4f of Bi<sub>2</sub>O<sub>3</sub>/MOL (**Figure 5.12b**), the Bi 4f XPS spectrum of Bi<sub>2</sub>O<sub>3</sub>/UiO can be fitted by two chemical states (**Table**

10.4), which is crystalline Bi<sub>2</sub>O<sub>3</sub> (61.9%) and amorphous BiO<sub>x</sub> (38.1%) (Figure 5.18c). UiO-66 is less able to form Bi<sub>2</sub>O<sub>3</sub> nanowires (61.9%) than Zr-TATB MOL (76.3%), which could be due to a larger proportion of less accessible inner surface. It needs to be noted that the actual proportion of BiO<sub>x</sub> in Bi<sub>2</sub>O<sub>3</sub>/UiO might be higher than 38.1%, considering the limited detection depth of XPS (< 10 nm). The occupation of inner pore volume by the Bi species can also be verified by N<sub>2</sub> physisorption experiments (Figure 5.19). The absorption of Bi<sub>2</sub>O<sub>3</sub>/UiO decreases significantly in the micropores (relative pressure < 0.1). The occupation of micropores is also verified by comparing the DFT calculated pore size distribution of UiO-66 and Bi<sub>2</sub>O<sub>3</sub>/UiO.

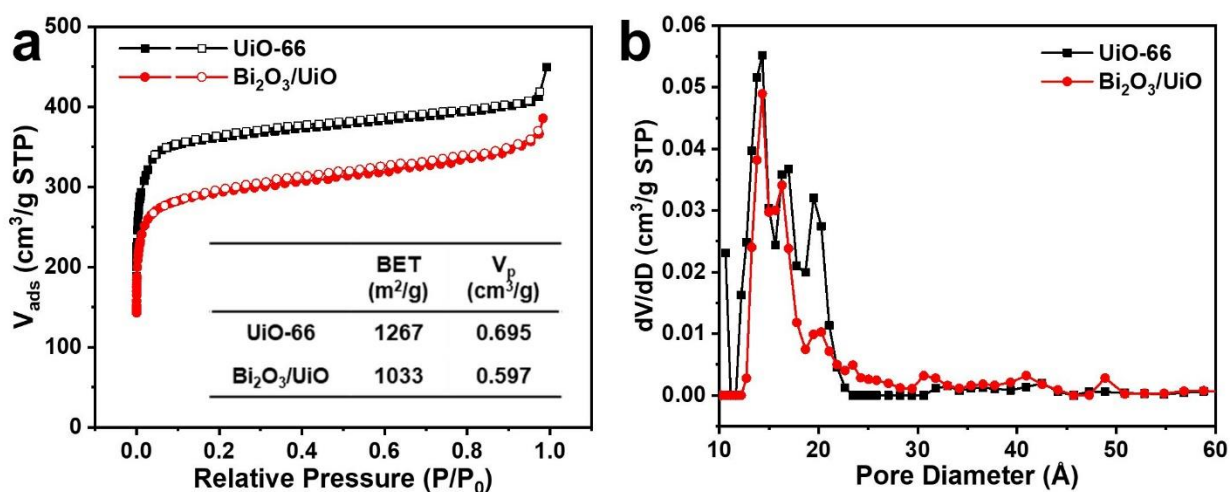


**Figure 5.19** (a) N<sub>2</sub> sorption isotherms (solid symbols: adsorption curve; open symbols: desorption curve) of UiO-66 and Bi<sub>2</sub>O<sub>3</sub>/UiO at 77 K (Inserted table: BET surface area and pore volume (V<sub>p</sub>)). (b) DFT pore size distribution of UiO-66 and Bi<sub>2</sub>O<sub>3</sub>/UiO. DFT calculation mode: N<sub>2</sub> at 77 K on silica (cylindr./sphere. pore, NLDFT ads. Model).

#### 5.4.2 Bi<sub>2</sub>O<sub>3</sub>/AB

Acetylene black is generally made from pyrolysis of acetylene gas, which determines its excellent purity. The AB used in this study is from a commercial supplier (*Alfa Aesar*) without further treatments. The purity is above 99.9% carbon content, specified by Alfa Aesar. Thus, AB lacks apparent anchoring sites (such as -OH, -NH<sub>2</sub>, etc), compared to the MOF samples. Due to contaminations from the atmosphere, we can not precisely analyze the composition of the AB.

Bi<sub>2</sub>O<sub>3</sub>/AB was synthesized by a similar method as Bi<sub>2</sub>O<sub>3</sub>/MOL and Bi<sub>2</sub>O<sub>3</sub>/AB (Chapter 3.3.2.2), with a Bi content of 1.76 wt% (Table 10.3). The morphology of the Bi<sub>2</sub>O<sub>3</sub>/AB was determined by HAADF-STEM (Figure 5.20a,b). A small amount of the Bi-based nanowires can be observed, while a larger proportion are nanoparticles of around 3 nm. The PXRD indicates the formation of the crystalline Bi<sub>2</sub>O<sub>3</sub> (Figure 5.20c). The chemical state of Bi can be measured by XPS (Figure 5.21). The full spectrum confirms the absence of metallic Bi, due to the absence of Bi 6p (1.0 eV) and 6s (10.5 eV). The binding energy of 160 eV can be ascribed to crystalline Bi<sub>2</sub>O<sub>3</sub>. The apparent

higher binding energy can be due to the change in the environment, indicating no strong interactions between the AB and Bi<sub>2</sub>O<sub>3</sub>. In the case of MOF composites, the interaction, simplified as Bi-O-Zr connection, will reduce the oxidation number of the Bi.

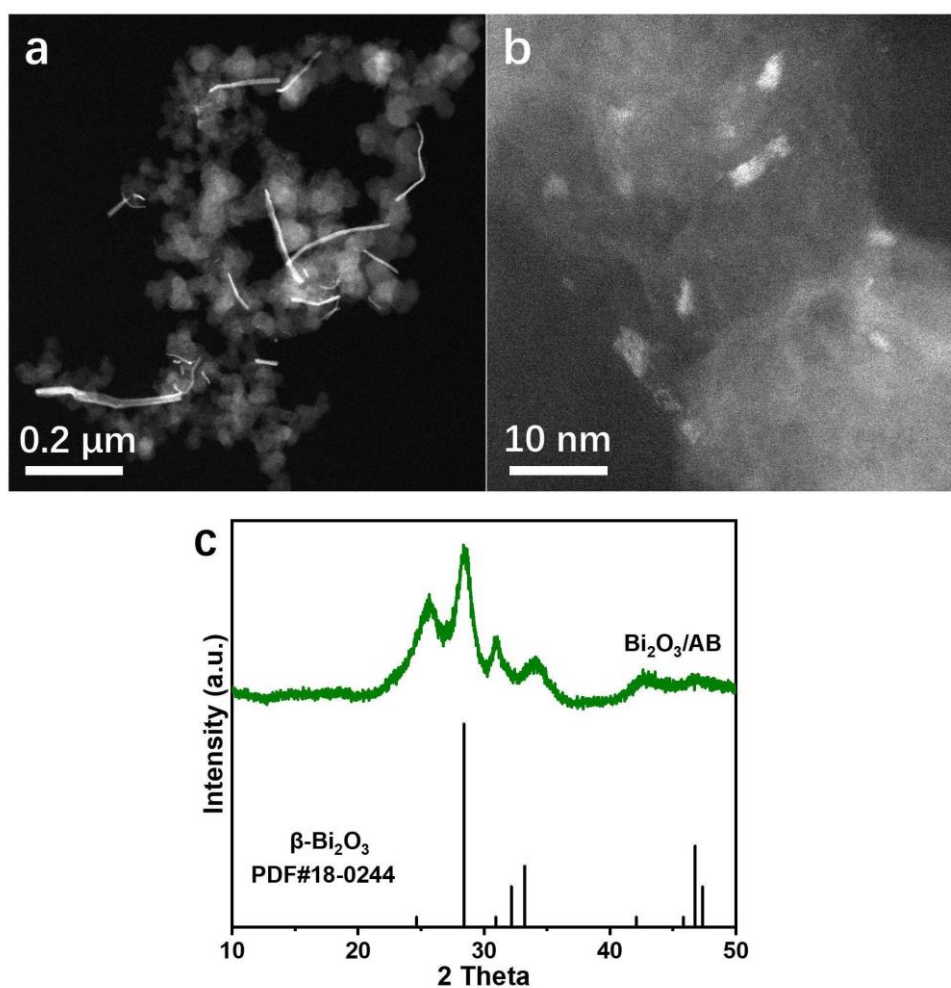


**Figure 5.20** (a,b) HAADF-STEM images of Bi<sub>2</sub>O<sub>3</sub>/AB. The Bi<sub>2</sub>O<sub>3</sub> appears as nanowires and nanoparticles. (c) PXRD patterns of standard  $\beta$ -Bi<sub>2</sub>O<sub>3</sub> (PDF#18-0244) and as-synthesized Bi<sub>2</sub>O<sub>3</sub>/AB.

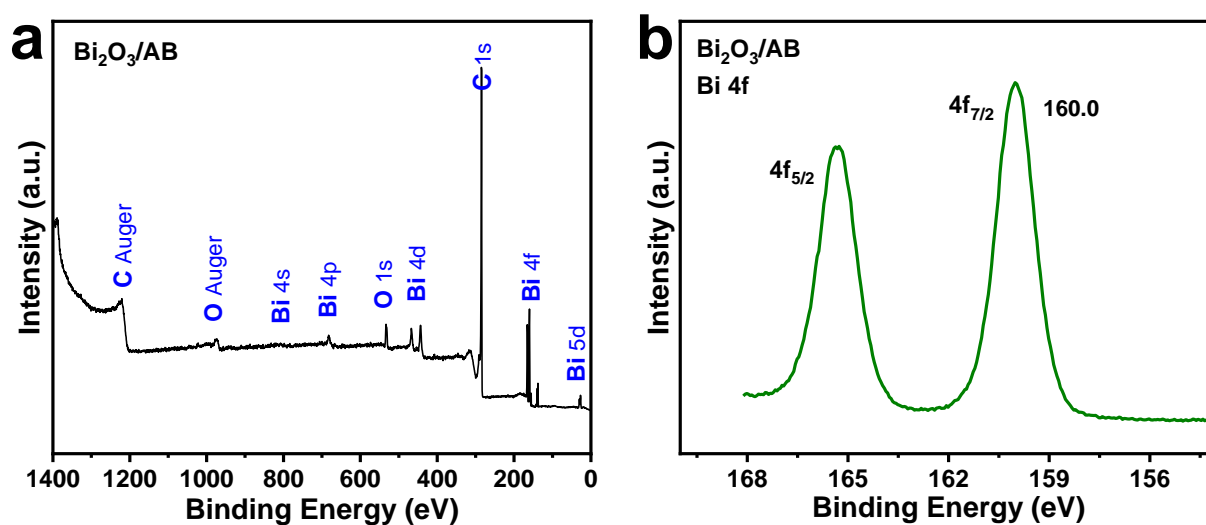


**Figure 5.21** (a) XPS full-spectrum and (b) XPS Bi 4f spectrum of Bi<sub>2</sub>O<sub>3</sub>/AB.

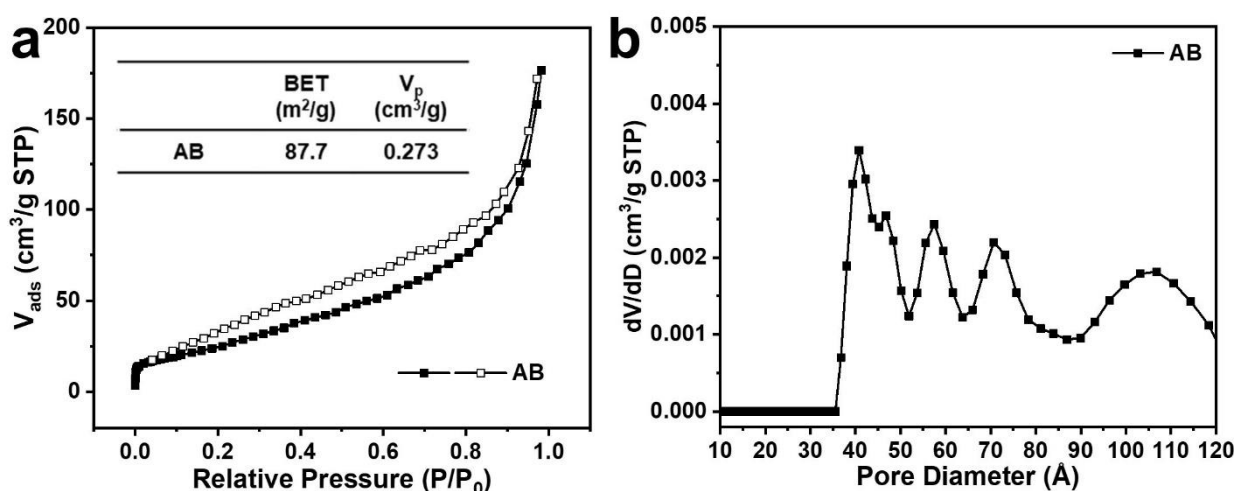


**Figure 5.22** (a) N<sub>2</sub> sorption isotherms (solid symbols: adsorption curve; open symbols: desorption curve) of acetylene black (AB) at 77 K (Inserted table: BET surface area and pore volume (V<sub>p</sub>)). (b) DFT pore size distribution of acetylene black (AB). DFT calculation mode: N<sub>2</sub> at 77 K on carbon (slit/cylinder. pores, QSDFT ads. branch).

The lack of anchoring sites determines the lower loading of Bi on AB (**Table 10.3**). The porosity can be measured from N<sub>2</sub> sorption experiments, originating from the aggregation of AB (**Figure 5.22**). Therefore, we infer that the loading of Bi on AB is based on impregnation effects. Furthermore, partial hydrolysis of Bi<sup>3+</sup> ions can happen by the water residue from solvent or Bi precursors (Bi(NO<sub>3</sub>)<sub>3</sub>·5H<sub>2</sub>O) during the solvothermal treatment, which results in the deposition of Bi species on AB.

## 5.5 Summary of Bi<sub>2</sub>O<sub>3</sub>/MOL composites

Bearing various surface anchoring sites, Zr-TATB MOL exhibits an excellent potential as a composite with various catalytic sites introduced through a post-modification strategy, serving as a versatile catalytic platform. Herein, considering the superior activity of Bi-based active sites in ECR reactions, Bi-loaded MOL composites were constructed as appropriate representatives. As a result, tetragonal Bi<sub>2</sub>O<sub>3</sub> nanowires could be uniformly dispersed on MOLs, after synthetic optimizations. Furthermore, the structure of the Bi species was resolved by advanced electron microscopy techniques. Besides, its structural evolution starting from atomic dispersion of the Bi sites and growing to nanoscale wires, was monitored by ex-situ TEM measurements, which offered an insight into the mechanism of this post-modification strategy.

## 6 | Electrochemical CO<sub>2</sub> Reduction to Formate by Bi/MOL Composites

With the well-characterized Bi-based MOL composites described in **Chapter 5**, ECR reactions were performed to evaluate their performance and examine structure-activity relationships.

### 6.1 Optimization of the H-type cell

The ECR performance of the catalysts was mainly examined by a facile H-type cell, which is generally applied in fundamental investigations of academic research.<sup>[121]</sup> Its advantage is that ECR performance measured at low current densities mainly relies on the amount and type of the active sites. Considering that reaction conditions can be kept constant, the performance depends mostly on the catalyst species.

The scheme of the H-type cell is exhibited in **Figure 3.8**. To guarantee a defined CO<sub>2</sub> supply, two measures are adopted. (1) Acceleration of the CO<sub>2</sub> mass transfer by equipping the cell with a gas recycle system and a magnetic stirrer. (2) Keep at low current densities. Mostly, the current density is kept below 50 mA·cm<sup>-2</sup> when using an H-type cell.<sup>[288]</sup> To avoid the apparent influence of the local CO<sub>2</sub> depletion in the reaction zone, the mass loading of the electrode was reduced to limit the current densities. For our case, we adopted only 0.2 mg·cm<sup>-2</sup>, rather than 1 mg·cm<sup>-2</sup>.

Additionally, there are two further issues that need to be considered and discussed in the next chapters.

#### 6.1.1 Selection of the backing electrode

To provide a large working potential window of the backing electrode, a glassy carbon electrode (GCE) is often used. Glassy carbon offers high hardness, low electrical resistance, smooth surface, and extremely high chemical resistance. In addition, its inert electrochemical surface offers a rather low blind activity in a large potential window. However, due to the flat electrode, the very low backing area of the GCE also leads to a poor apparent current response, which makes it difficult to quantify the products, especially for ECR reactions.

Herein, limited by the accuracy of the applied detection methods, we have to abandon the GCE

and have chosen carbon paper (CP) as the backing electrode. Carbon papers are produced based on proprietary non-woven technologies and composed of many interconnected carbon microfibers. They are also used as gas diffusion layers (GDLs) in fuel cells. Their porous structure allows smooth gas diffusion through the layer. The actual area is much higher than its geometric area. The increased surface area offers more place for depositing the active sites. Besides, hydrophobic treatment (primarily by deposition of PTFE) is commonly applied on two sides of the CP. The hydrophobic treatment is helpful to suppress the HER side reaction from the backing electrode.

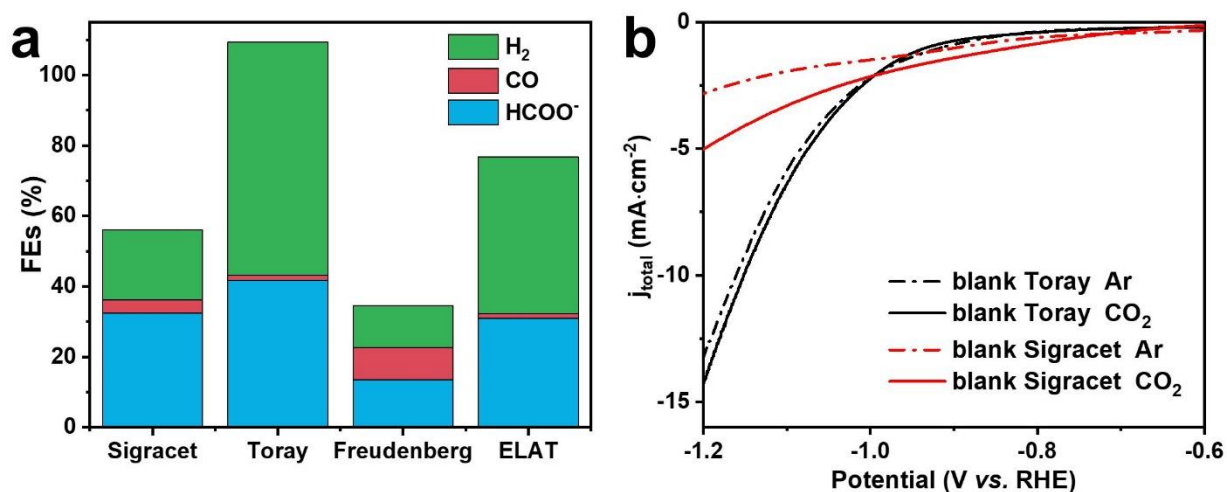


**Figure 6.1** (a) Effect of the different carbon papers as backing electrodes for ECR reactions with SnO<sub>x</sub>/MOL(2) as catalyst. Test condition: Chrono amperometric at -1.37 V vs. RHE. (b) LSV curves over blank Toray (black) and blank Sigracet (red) under Ar/CO<sub>2</sub>.

However, the disadvantage is that the carbon paper is far from being chemically inert during the electrocatalytic tests, which may consume electrons in side reactions and may lead to poor total Faraday efficiency. These unwanted effects are mostly due to impurities and defects of the carbon paper. Considering the quality of the carbon paper can strongly change from supplier to supplier, we can choose proper carbon paper to avoid these unwanted effects. Therefore, we performed simple ECR tests using different carbon papers loaded with the same catalyst (no stirring and gas recycle system in these tests), of which a perfect total Faradaic efficiency and more Faradaic efficiency towards formate would be preferred. The results are plotted in **Figure 6.1a**. The catalyst adopted here was the SnO<sub>x</sub>/MOL(2), which will be described and discussed in **Chapter 7.1.2.1**. The potential of the chrono amperometric was set to be -2.0 V vs. Ag/AgCl (corresponding to -1.37 V vs. RHE), which is nearly the most negative potential applied in ECR reaction in H-type cells for producing formate. From the comparison, Toray carbon paper gave the best total Faradaic efficiency and Faradaic efficiency towards formate. From comparing the LSV curves under CO<sub>2</sub> and Ar, we can also recognize that Toray gave nearly no current response, indicating no ECR activity by bare carbon paper in this potential window (**Figure 6.1b**). In all ECR tests, Toray carbon paper was used by default, unless stated otherwise.

## 6.1.2 Effect of the conductive additive

Even though we adopt 2D MOF composites and use 3D porous carbon paper to get low electrical resistance and provide as much as the contact area between catalyst and electrode. It is nevertheless inevitable that the stacking of the layered structure will block active sites. To eliminate this side effect, certain conductive additives were dispersed together with the catalyst into the ink and cast on the carbon paper. Considering the high purity, acetylene black (AB) was the best choice.

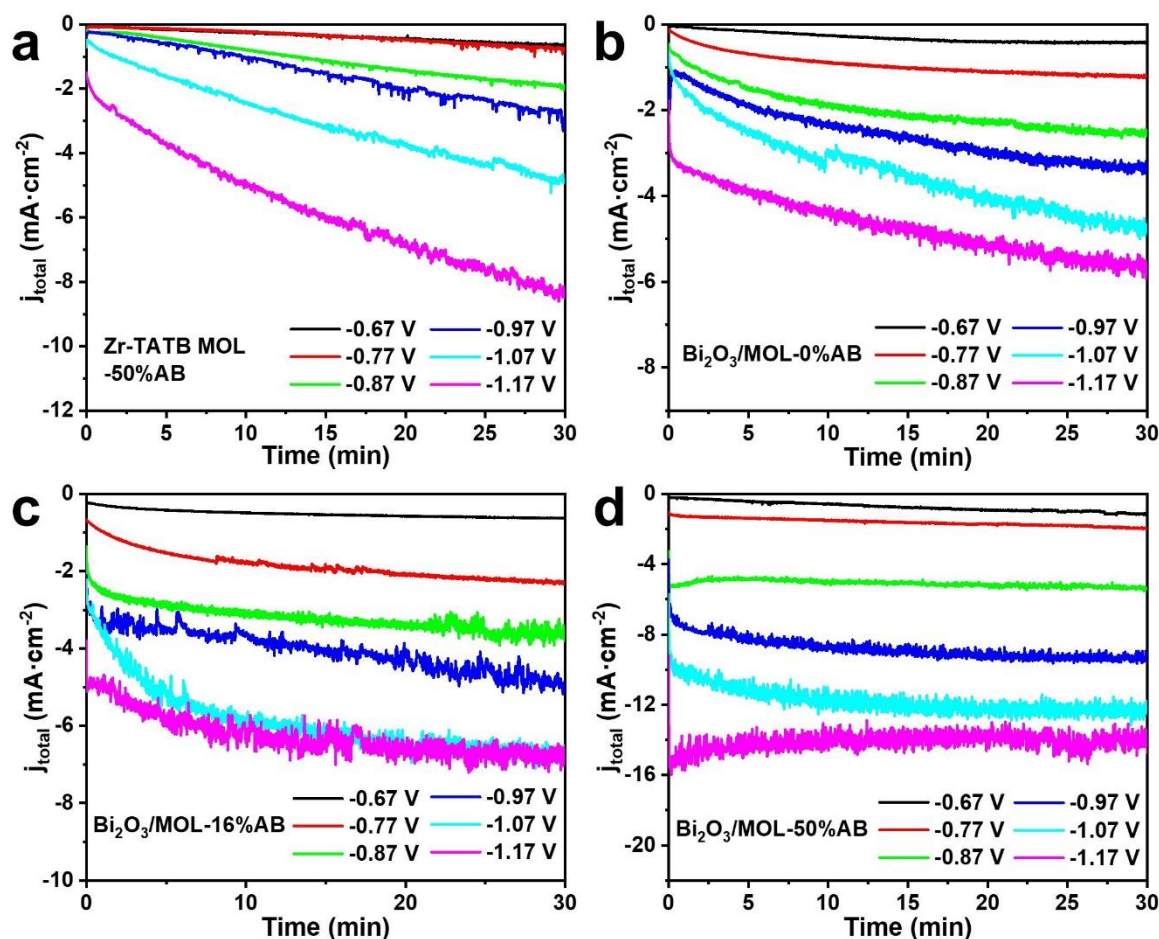


**Figure 6.2** Chrono amperometric I-t plot at different potentials (V vs. RHE) over (a) Zr-TATB MOL with 50% AB as an additive, and (b-d) Bi<sub>2</sub>O<sub>3</sub>/MOL with different content of AB as an additive.

In the followings, the effect of the addition of the AB was investigated (Figure 6.2). The catalyst adopted here was the Bi<sub>2</sub>O<sub>3</sub>/MOL. Before that, the activity of the support Zr-TATB was examined. From the chrono amperometric plot of Zr-TATB (Figure 6.2a), we could recognize that the current response got more negative over time, especially at a more negative potential (such as a range of -0.97 to -1.17 V vs. RHE). From the analysis of the products, we knew that there was no ECR reaction by the Zr-TATB, which met our expectation (Figure 6.3). So the changes in the chrono amperometric I-t plots could be ascribed to the unstable surface state during the tests. One possible explanation could be the hydroxylation of the carbon component (carbon paper or AB), when the active sites for ECR reaction are lacking. The surface was becoming more hydrophilic and

promoted the HER reaction over reaction time. Had active sites been available, which generally serve as electron traps, the hydroxylation of the carbon would have been suppressed. Hereafter, based on tests using Bi<sub>2</sub>O<sub>3</sub>/MOL, we found the addition of AB is beneficial to getting a stable current response (**Figure 6.2b-d**), because AB helps the active sites being supplied by electrons. When the AB content was increased to 50 wt%, which means an equal mass of AB and catalyst, the current responses became stable.

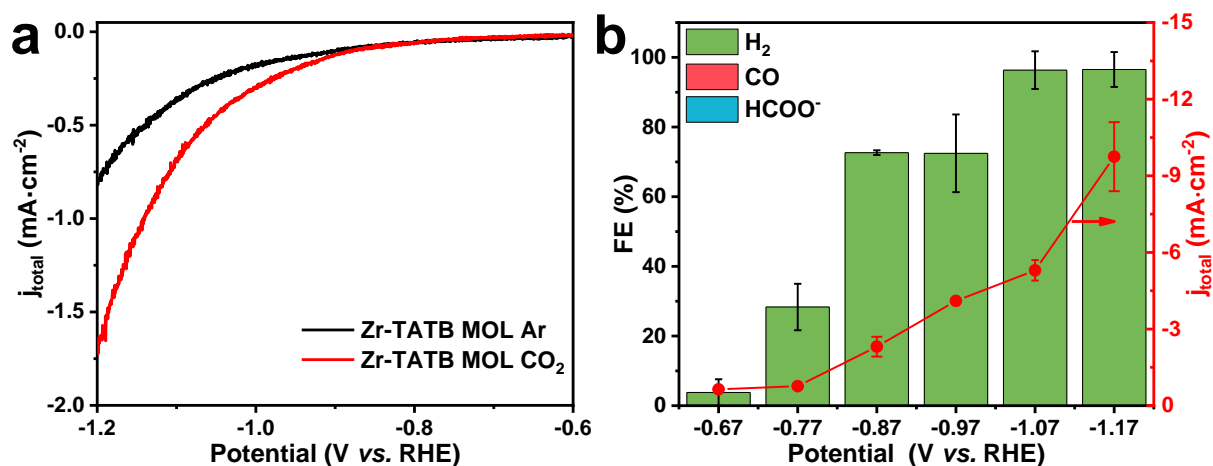


**Figure 6.3** (a) LSV curves under Ar/CO<sub>2</sub>, (b) FEs and current densities of ECR at different potentials over Zr-TATB MOL.

Besides, the ECR performance was also measured and analyzed (**Figure 6.4**). From the LSV curves under Ar and CO<sub>2</sub>, one can deduce that more AB gives a better total current response (**Figure 6.4a**). More AB addition also gives higher formate FEs and less HER (**Figure 6.4b,c**). The exact activities towards formate can be evaluated using the partial current density towards formate related to the geometric area of the electrode or the mass of the Bi, which indicates the significance of the addition of AB (**Figure 6.4d,e**). The exhibition of the apparent TOF(s<sup>-1</sup>) (number of consumed electrons per active site per second) is an established quantity to describe the catalytic activity, which actually gives similar information as the current density related to the mass of the active sites (**Figure 6.4f**).

Even without the addition of AB, the Bi<sub>2</sub>O<sub>3</sub>/MOL still possesses significant activity towards formate. However, FEs and partial current densities towards formate collapsed when applying too negative potentials. This phenomenon indicates that the addition of AB is improving not only the activity but also the stability of the electrode. Hence, the following ECR tests were all conducted with the addition of 50 % AB by default, unless otherwise stated.

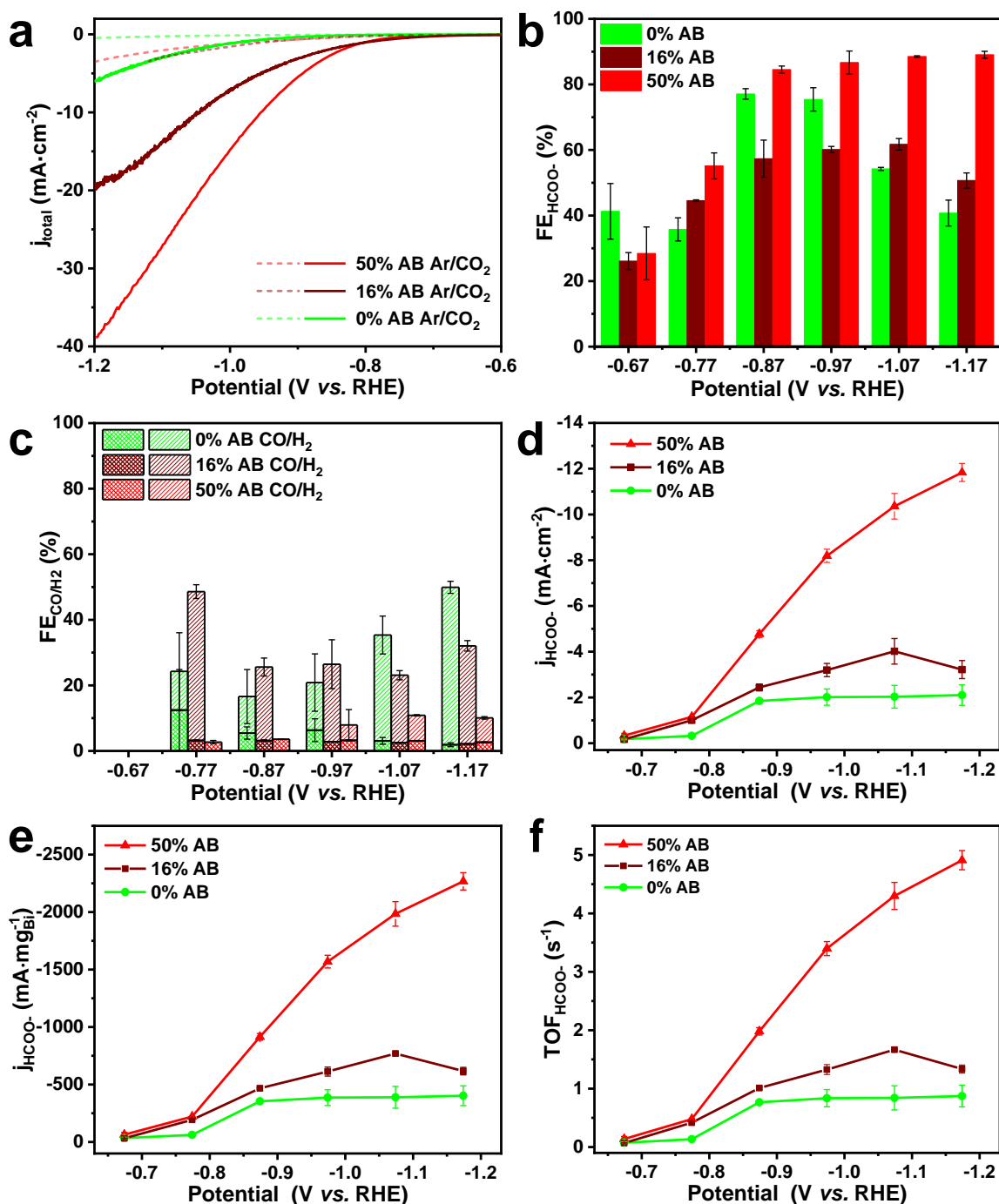


**Figure 6.4** (a) LSV curves under Ar/CO<sub>2</sub>, (b,c) Faradaic efficiencies, (d) formate partial current densities, (e) formate partial current per mg Bi, and (f) TOF (s<sup>-1</sup>) towards 1/2 HCOO<sup>-</sup> at different applied potentials over Bi<sub>2</sub>O<sub>3</sub>/MOL with different AB content (0%, 16%, 50%).

## 6.2 Comparison of the ECR performance of Bi<sub>2</sub>O<sub>3</sub> based composites

To verify the superior performance of MOL-based composites, a typical 3D-MOF (Zr<sub>6</sub>-oxo SBUs based MOF, known as UiO-66) and acetylene black (denoted as AB), as references, were both loaded with Bi by the same method to obtain Bi<sub>2</sub>O<sub>3</sub>/UiO and Bi<sub>2</sub>O<sub>3</sub>/AB, respectively. Besides, further comparative experiments are conducted to understand the superior performance of

Bi<sub>2</sub>O<sub>3</sub>/MOL.

### 6.2.1 ECR performance of Bi<sub>2</sub>O<sub>3</sub>-based composites

The first comparative experiment was conducted with Bi<sub>2</sub>O<sub>3</sub>/MOL, Bi<sub>2</sub>O<sub>3</sub>/UiO, and Bi<sub>2</sub>O<sub>3</sub>/AB. The loading methods were similar, except that different supports of the same mass were substituted (**Chapter 3.3.2.2**). The loading difference of Bi<sub>2</sub>O<sub>3</sub>/MOL (2.61 wt%), Bi<sub>2</sub>O<sub>3</sub>/UiO (2.38 wt%), and Bi<sub>2</sub>O<sub>3</sub>/AB (1.76 wt%) indicates the different loading abilities of supports (**Table 10.3**). The corresponding structural characterizations were already discussed in **Chapter 5**.

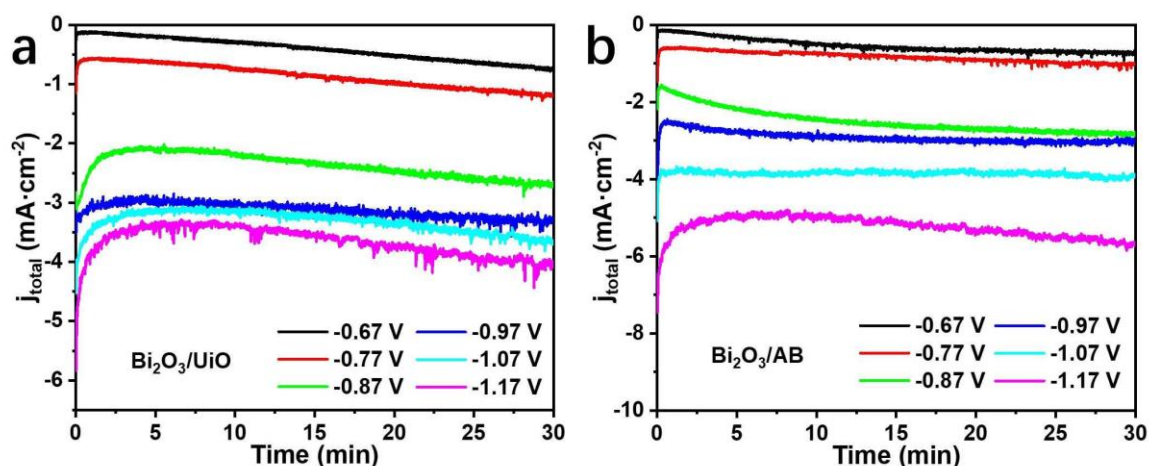


**Figure 6.5** Chrono amperometric I-t plot at different potentials (V vs. RHE) over (a) Bi<sub>2</sub>O<sub>3</sub>/UiO and (b) Bi<sub>2</sub>O<sub>3</sub>/AB.

LSV tests were conducted to evaluate the activity and determine the proper active potential ranges for ECR reaction. Bi<sub>2</sub>O<sub>3</sub>/MOL was found to give the most significant difference by comparing the current responses under Ar and CO<sub>2</sub> atmosphere (**Figure 6.6a**), implying its superior ECR activities. The product-specific activities were examined by chrono amperometric tests (**Figure 6.2d&6.5**) in the H-type cell, in which the loading amount of the catalysts was set to 0.2 mg·cm<sup>-2</sup>. All three catalysts possess apparent activities in the ECR reaction to formate, indicating the general ECR ability of the Bismuth-based active sites. Bi<sub>2</sub>O<sub>3</sub>/MOL exhibits the best performance regarding the FEs and partial current densities (**Figure 6.6b-d**). Bi<sub>2</sub>O<sub>3</sub>/MOL maintains superior formate selectivities of over 85% over a wide potential range from -0.87 V to -1.17 V vs. RHE. Taking the different Bi loadings of the catalysts into account, the currents were normalized by the mass of Bi (**Figure 6.6e**). When depicting the TOF, Bi<sub>2</sub>O<sub>3</sub>/MOL still possesses superior ECR performance (**Figure 6.6f**). To the best of our knowledge, Bi<sub>2</sub>O<sub>3</sub>/MOL exhibits one of the highest formate production amongst MOFs used for direct ECR, highlighting the superiority of constructing MOL composites (**Table 10.5**).

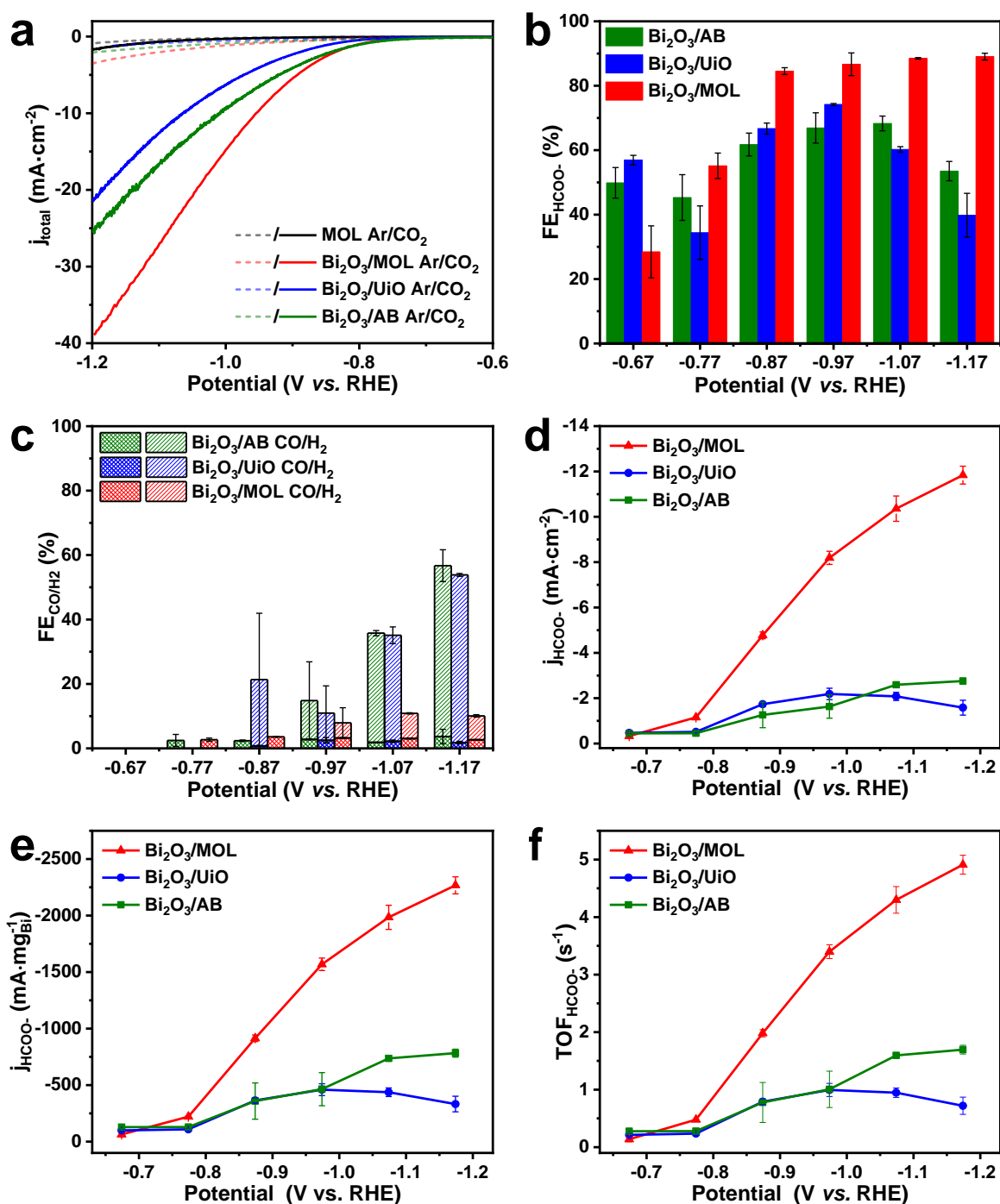


**Figure 6.6** (a) LSV curves under Ar/CO<sub>2</sub>, (b,c) Faradaic efficiencies, (d) formate partial current densities, (e) formate partial current per mg Bi, (f) TOF (s<sup>-1</sup>) towards 1/2 HCOO<sup>-</sup> at different applied potentials over Bi<sub>2</sub>O<sub>3</sub>/MOL, Bi<sub>2</sub>O<sub>3</sub>/UiO and Bi<sub>2</sub>O<sub>3</sub>/AB.

### 6.2.2 Product detections of the ECR reaction

Considering the various products of the ECR reaction, their precise and correct quantification is a prerequisite. For the gas phase, H<sub>2</sub> and CO are the main gas products, determined by the Thermal Conductivity Detector (TCD) of the GC (Figure 6.7a). The principle of TCD is based on the thermal conductivity difference of the gas components. The carrier gas here was Helium. Due to the very similar molar mass of He and H<sub>2</sub>, the TCD detector is not very sensitive to H<sub>2</sub> detection.

N<sub>2</sub> and Ar can also be used as the carrier gas, but are not suitable for detecting CO (one of the leading CO<sub>2</sub> reduction products). To get the complete gas composition by one GC, Helium was selected as the carrier gas, which gives a detection limit of 0.1 % and 100 ppm for H<sub>2</sub> and CO, respectively. Other gas products, such as methane (CH<sub>4</sub>), ethane (C<sub>2</sub>H<sub>6</sub>), and ethylene (C<sub>2</sub>H<sub>4</sub>) are detected by a flame ionization detector (FID) of the GC, with which the detection can reach ppm-level. Most detection of total Faradaic efficiencies from the 100% value can be ascribed to the poor detection of H<sub>2</sub>. Methane (CH<sub>4</sub>), ethane (C<sub>2</sub>H<sub>6</sub>), and ethylene (C<sub>2</sub>H<sub>4</sub>) are mostly invisible from the GC spectra, which indicates their absence or minimal proportion.

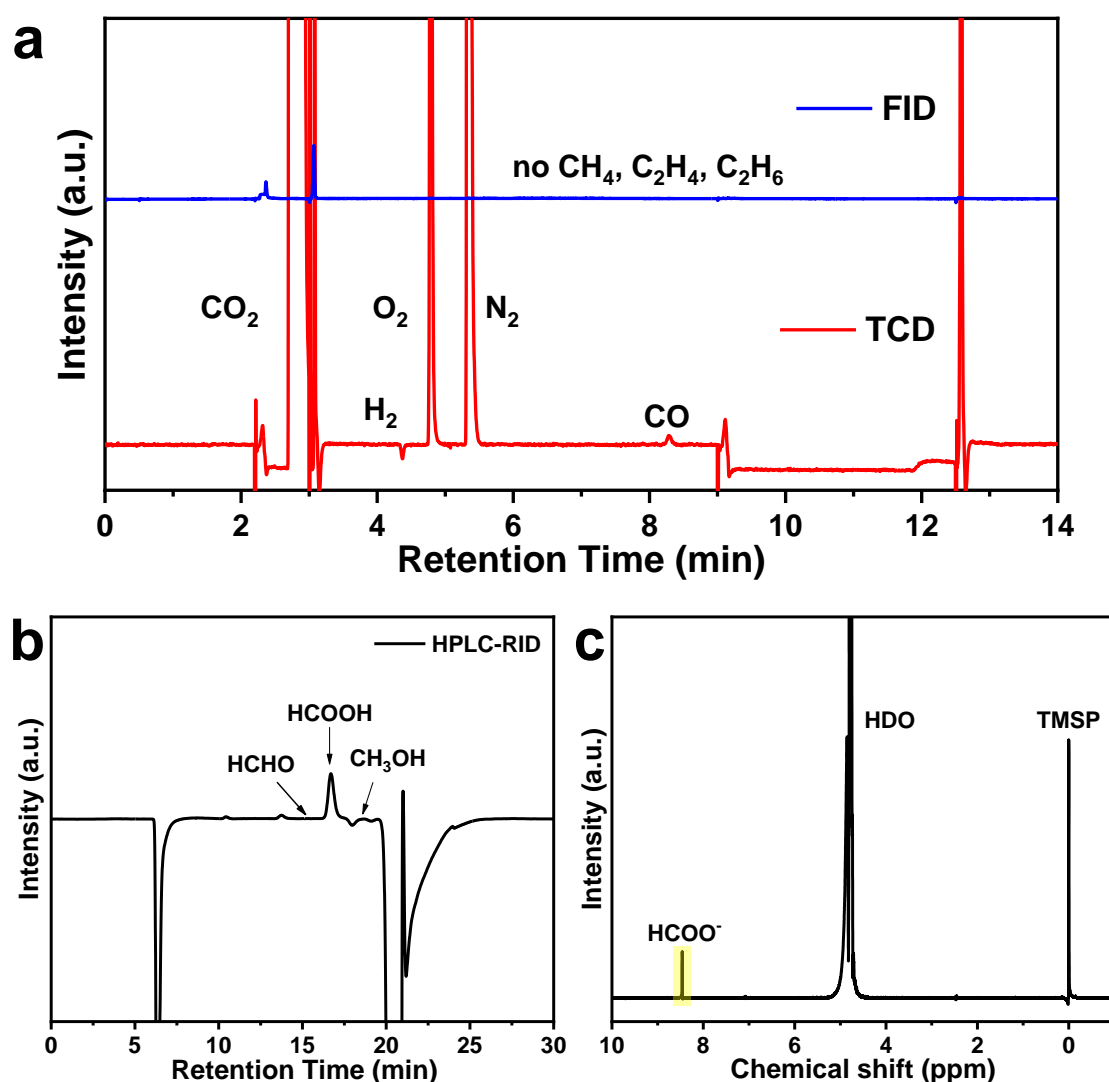


**Figure 6.7** (a) GC analysis of the gas products using TCD detector (red) and FID detector (blue), respectively. (b) HPLC analysis of liquid products using RID detector. (c) <sup>1</sup>H-NMR spectrum of liquid products. TMS was used as an internal standard to quantify the product.

The liquid products are mostly quantified by HPLC, which is capable of detecting formic acid (HCOOH), aldehyde (HCHO), and methanol (MeOH) (Figure 6.7b). The detector is a refractive index detector (RID), based on the refractive index of the analytes in the solvent. The detection limit can reach the ppm level. Other liquid C<sub>2+</sub> products were analyzed by <sup>1</sup>H-NMR with a solvent

suppression method (Figure 6.7c). The corresponding peaks can be identified by literature data.<sup>[285]</sup> In most cases, the formate is the only liquid product detected, while other liquid products are absent or in traces.

### 6.2.3 ECR performance of Bi<sub>2</sub>O<sub>3</sub>-based composites with similar loadings

To exclude the effect of the Bi loadings on the performance, we prepared the Bi<sub>2</sub>O<sub>3</sub>/MOL, Bi<sub>2</sub>O<sub>3</sub>/UiO, and Bi<sub>2</sub>O<sub>3</sub>/AB samples with similar Bi loading (~2.6 wt%) (Table 10.3), by adjusting the addition of the Bi precursors. Firstly, LSV measurements were conducted to evaluate the activity of these composites. For AB composites, increasing the Bi loading from 1.76 wt% to 2.6 wt% increases the current response under CO<sub>2</sub> atmosphere, with a total current being comparable to that of the Bi<sub>2</sub>O<sub>3</sub>/MOL (Figure 6.9a). This enhancement is because of the excellent conductivity of using AB as a support, which conversely allows the conclusion that the Bi<sub>2</sub>O<sub>3</sub> is fully electrically connected. The ECR performances were compared by conducting chrono amperometric tests (Figure 6.8). Bi<sub>2</sub>O<sub>3</sub>/MOL still exhibits the best performance, both in terms of selectivity and partial current density (Figure 6.9). Besides, there is no apparent difference in Faradaic efficiencies compared to the results in Figure 6.6, indicating that the selectivity depends mainly on the nature of the catalyst and not on the Bi<sub>2</sub>O<sub>3</sub> loading.

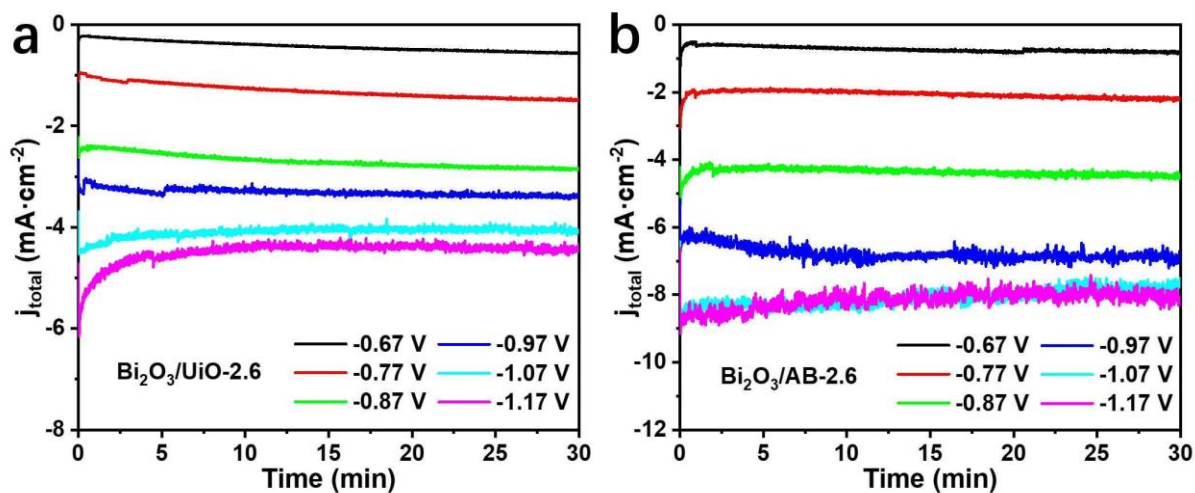


**Figure 6.8** Chrono amperometric I-t plot at different potentials (V vs. RHE) over (a) Bi<sub>2</sub>O<sub>3</sub>/UiO-2.6 and (b) Bi<sub>2</sub>O<sub>3</sub>/AB-2.6. 2.6 are the Bi wt% on the supports.

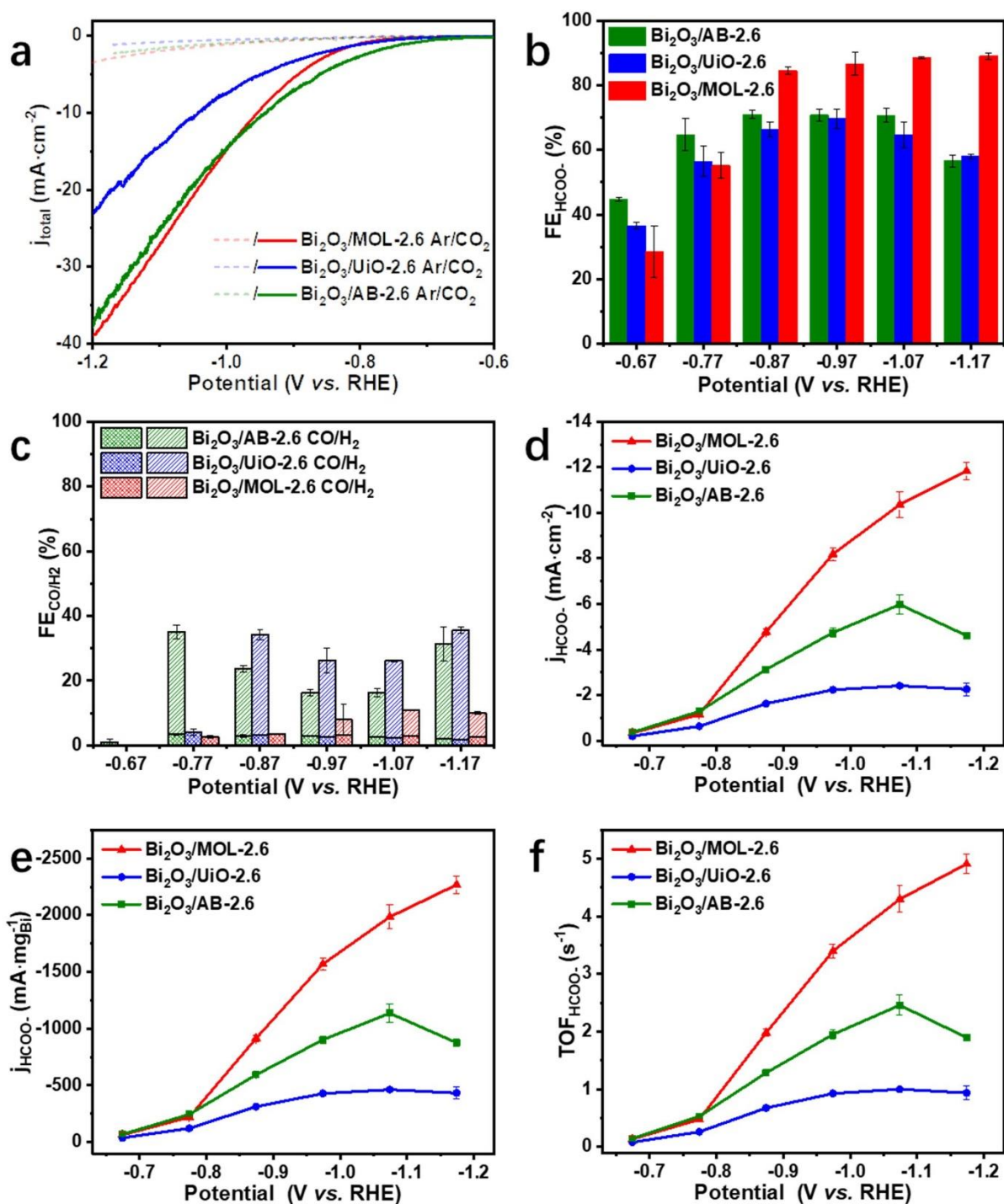


**Figure 6.9** (a) LSV curves under Ar/CO<sub>2</sub>, (b,c) Faradaic efficiencies, (d) formate partial current densities, (e) formate partial current per mg Bi, (f) TOF (s<sup>-1</sup>) towards 1/2 HCOO<sup>-</sup> at different applied potentials over Bi<sub>2</sub>O<sub>3</sub>/MOL-2.6 Bi<sub>2</sub>O<sub>3</sub>/UiO-2.6 and Bi<sub>2</sub>O<sub>3</sub>/AB-2.6. 2.6 means the Bi wt% on the support.

#### 6.2.4 ECR performance of Bi<sub>2</sub>O<sub>3</sub>/MOL with different loadings

The loading effect of the Bi on the MOL was investigated by synthesizing Bi<sub>2</sub>O<sub>3</sub>/MOLs with different loadings by changing the amount of the Bi precursor (**Chapter 3.3.2.2**). The loadings were determined by ICP-AES (**Table 10.3**). The morphologies of these composites were examined by electron microscopy (**Figure 6.10**). At loadings of 3.1 wt% and 1.4 wt%, different amounts of

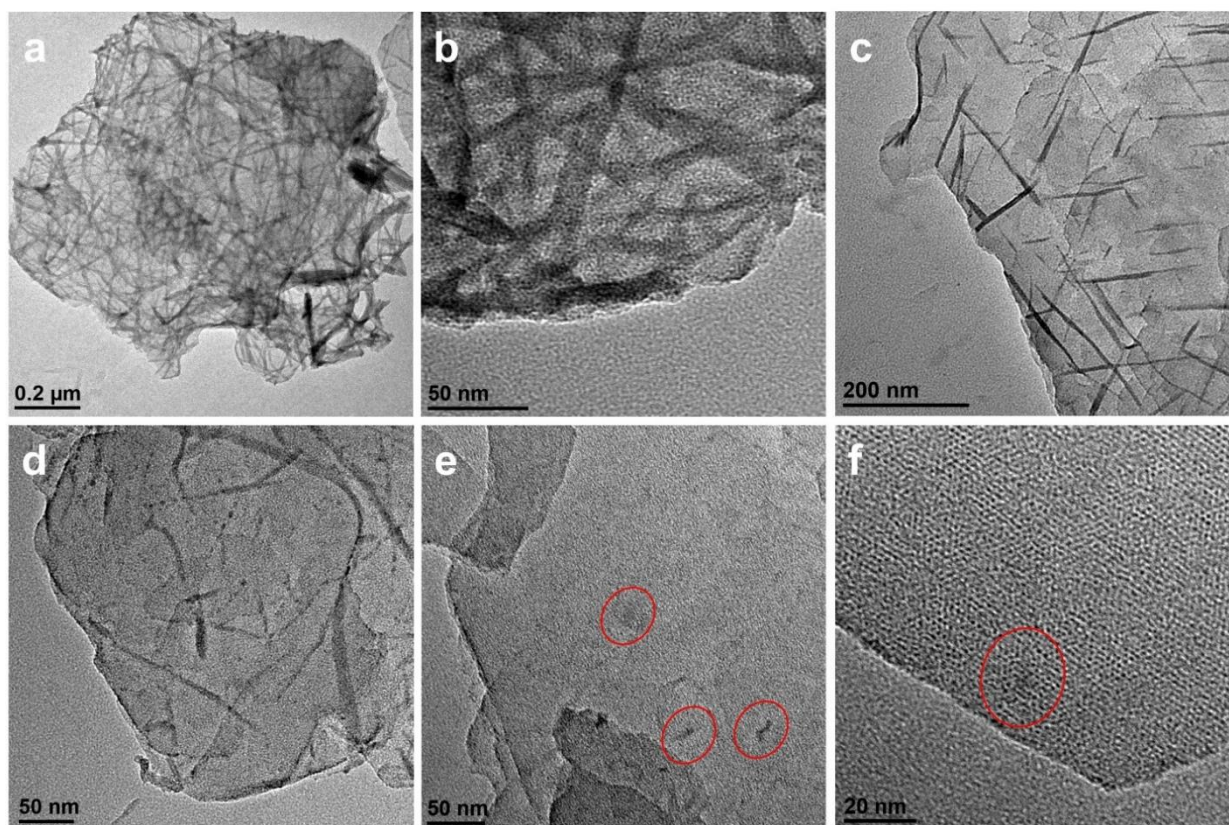


**Figure 6.10** TEM images of (a,b) Bi<sub>2</sub>O<sub>3</sub>/MOL-3.1 (c,d) Bi<sub>2</sub>O<sub>3</sub>/MOL-1.4 (e,f) Bi<sub>2</sub>O<sub>3</sub>/MOL-0.6. Red circles highlight some ultrafine nanoparticles. 3.1, 1.4, and 0.6 are the wt% of Bi on the support.

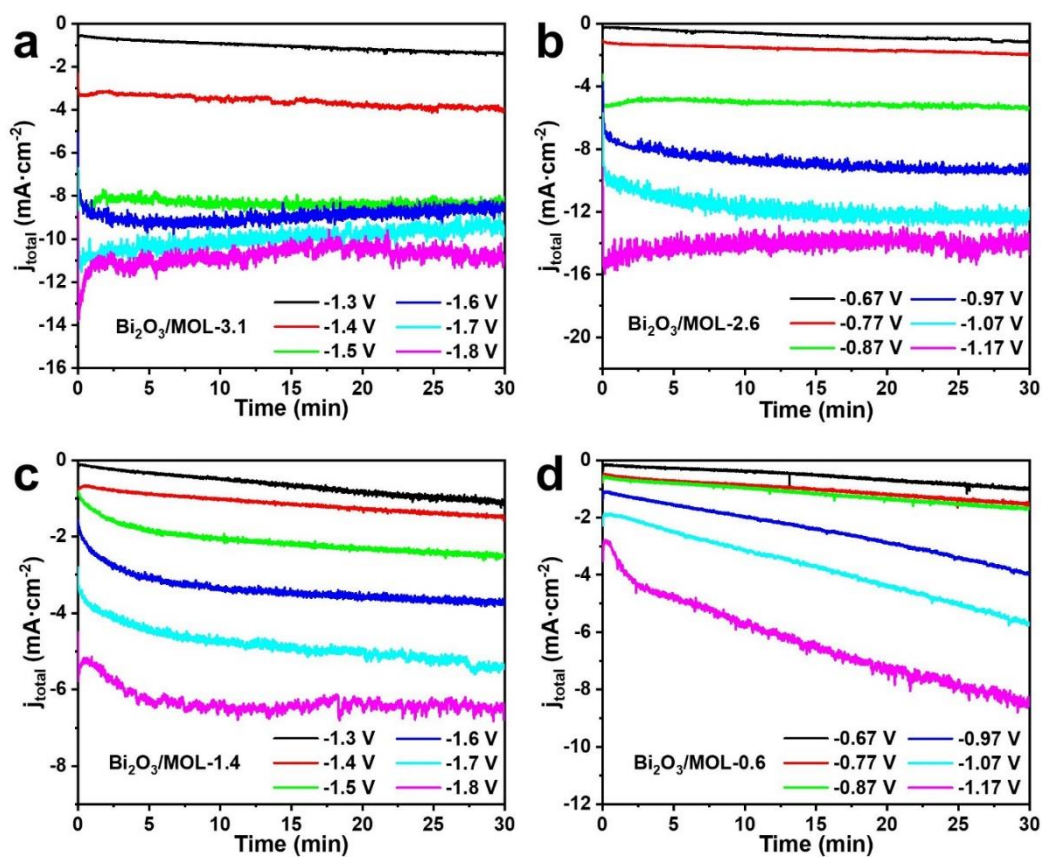


**Figure 6.11** Chrono amperometric I-t plot at different potentials (V vs. RHE) over (a/b) Bi<sub>2</sub>O<sub>3</sub>/MOL-3.1 (b) Bi<sub>2</sub>O<sub>3</sub>/MOL-2.6 (c) Bi<sub>2</sub>O<sub>3</sub>/MOL-1.4 and (d) Bi<sub>2</sub>O<sub>3</sub>/MOL-0.6. 3.1, 2.6, 1.4, and 0.6 are the wt% of Bi on the support.

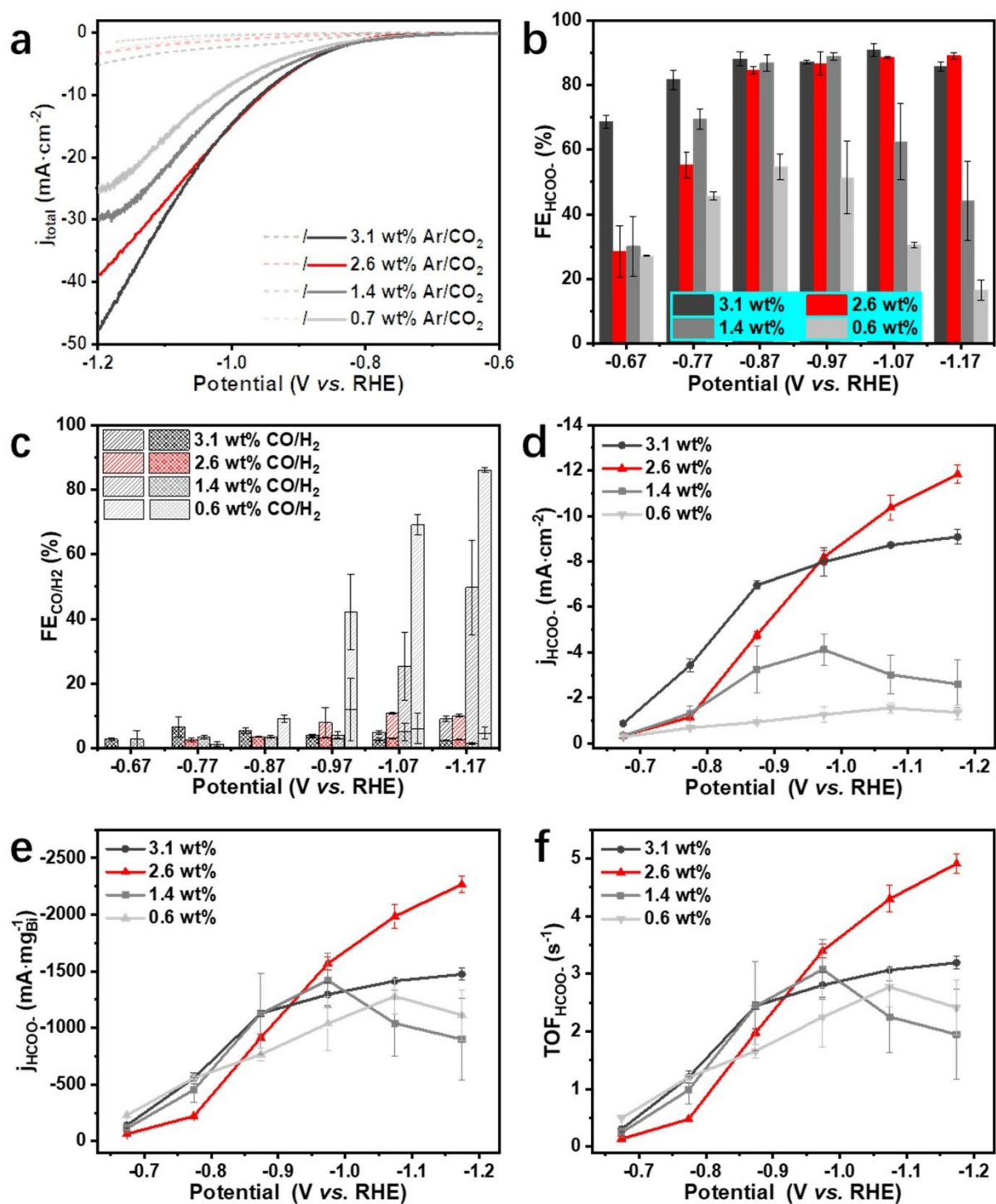


**Figure 6.12** (a) LSV curves under Ar/CO<sub>2</sub>, (b,c) Faradaic efficiencies, (d) formate partial current densities, (e) formate partial current per mg Bi, (f) TOF ( $\text{s}^{-1}$ ) towards 1/2 HCOO<sup>-</sup> at different applied potentials over Bi<sub>2</sub>O<sub>3</sub>/MOL with different Bi content. 3.1, 2.6, 1.4, and 0.6 are the wt% of Bi on the support.

Bi nanowires can be found on the MOL. The diameters of the Bi nanowires didn't show apparent differences, being below 10 nm, no matter of the loadings. For the loading of 0.6 wt%, barely any Bi<sub>2</sub>O<sub>3</sub> nanowires were observed, only some very short wires or nanoparticles. The PXRD patterns indicate the formation of crystalline Bi<sub>2</sub>O<sub>3</sub> (Figure 6.13).

The ECR activities of the Bi<sub>2</sub>O<sub>3</sub>/MOL samples with different loadings were evaluated by LSV measurements (**Figure 6.12a**). It turned out that a higher Bi loading results in a higher current response from LSV plots. The ECR performances were further compared by conducting chrono amperometric tests (**Figure 6.11**). As a result, Bi<sub>2</sub>O<sub>3</sub>/MOL-3.1, Bi<sub>2</sub>O<sub>3</sub>/MOL-2.6, and Bi<sub>2</sub>O<sub>3</sub>/MOL-1.4 all exhibited good faradaic efficiencies (> 85%) at the applied potentials ranging from -0.77 V to -0.97 V *vs.* RHE (**Figure 6.12b**). However, for Bi<sub>2</sub>O<sub>3</sub>/MOL-1.4, its Faradaic efficiencies start to decrease when the potential is below -1.07 V. It might be because of too much side reactions (HER) taking place at the bare MOL or Carbon components (**Figure 6.12c**). This may also be the key point to explain the even worse FEs of Bi<sub>2</sub>O<sub>3</sub>/MOL-0.6.

Looking at the current densities of formate, the loading of 2.6 wt% is the best (**Figure 6.12d-f**). The decrease of the formate current density of the Bi<sub>2</sub>O<sub>3</sub>/MOL-1.4 at higher potential can be explained by an increasing side reaction (HER) at other electrode components, such as carbon. As for the Bi<sub>2</sub>O<sub>3</sub>/MOL-3.1, the very weak increase in activity at too negative potentials can be explained by cluster aggregation of the Bi species due to its dense loading on the surface of the MOL (**Figure 6.10a,b**). As for the Bi<sub>2</sub>O<sub>3</sub>/MOL-0.6, the reason for its poor performance could be side reactions (e.g., HER) and a morphology effect, which seems to be typical for low loadings. The effect of the morphology will be discussed in **Chapter 6.6.3**. Overall, the Bi<sub>2</sub>O<sub>3</sub> loading on the MOL seems to have an optimum, which turns out to be around 2.6 wt%.

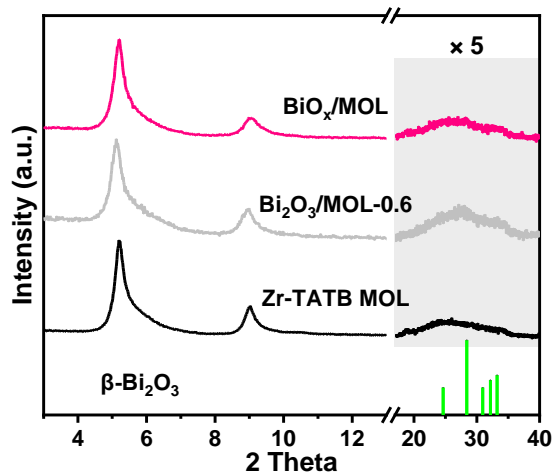


**Figure 6.13** PXRD patterns of standard  $\beta$ -Bi<sub>2</sub>O<sub>3</sub> (PDF#18-0244), as-synthesized Zr-TATB MOL, Bi<sub>2</sub>O<sub>3</sub>/MOL-0.6, and BiO<sub>x</sub>/MOL. 0.6 is the Bi wt% on the support.

### 6.2.5 Comparison of the ECR performance of BiO<sub>x</sub> and Bi<sub>2</sub>O<sub>3</sub>

The effect of hydrothermal treatment was investigated by the reference of BiO<sub>x</sub>/MOL, which is synthesized at room temperature (**Chapter 3.3.2.1**). Bi<sub>2</sub>O<sub>3</sub>/MOL-0.6 was selected for comparison because of the similar loading. The hydrothermal treatment leads to the crystallization of the Bi species, while BiO<sub>x</sub>/MOL presents non-crystalline bismuth species, verified by the PXRD patterns (**Figure 6.13**).

The ECR activity was evaluated by LSV measurements (**Figure 6.15a**). It turns out that a higher crystallinity causes a better current response under a CO<sub>2</sub> atmosphere. The ECR performance was further compared by conducting chrono amperometric tests (**Figure 6.14**). As a result, BiO<sub>x</sub>/MOL possesses better Faradaic efficiencies than Bi<sub>2</sub>O<sub>3</sub>/MOL-0.6 (**Figure 6.15b,c**). However, Bi<sub>2</sub>O<sub>3</sub>/MOL-0.6 exhibits better partial current densities, no matter if related to the geometric area or mass of the Bi. Taking up the precious discussion, bare MOL or carbon paper mainly lead to the HER reaction (**Figure 6.15c**). Overall, we can still infer that crystallinity positively affects ECR performance.

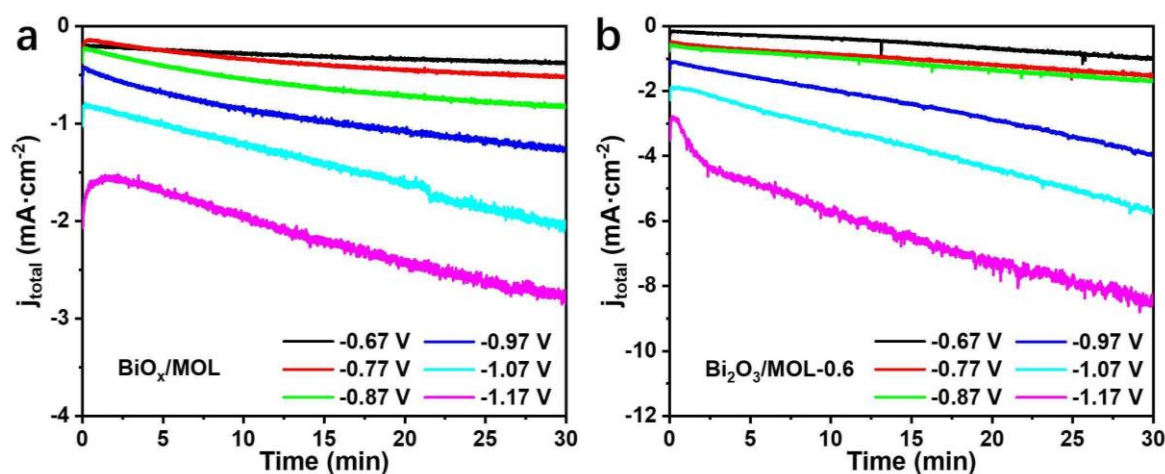


**Figure 6.14** Chrono amperometric I-t plot at different potentials (V vs. RHE) over (a) BiO<sub>x</sub>/MOL and (b) Bi<sub>2</sub>O<sub>3</sub>/MOL-0.6. 0.6 means the Bi wt% on the supports.

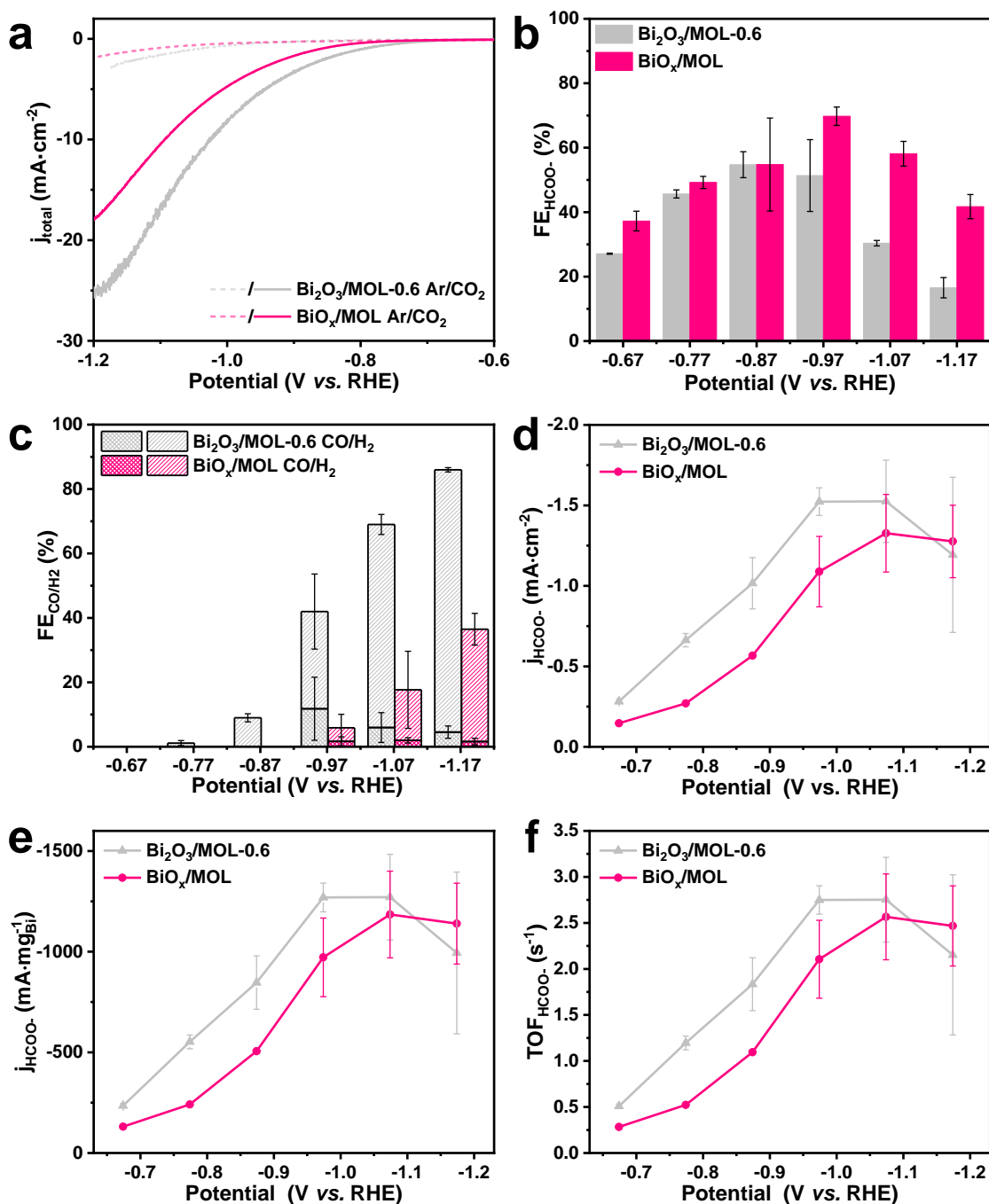


**Figure 6.15** (a) LSV curves under Ar/CO<sub>2</sub>, (b,c) Faradaic efficiencies, (d) formate partial current densities, (e) formate partial current per mg Bi, (f) TOF (s<sup>-1</sup>) towards 1/2 HCOO<sup>-</sup> at different applied potentials over Bi<sub>2</sub>O<sub>3</sub>/MOL-0.6 and BiO<sub>x</sub>/MOL.

### 6.3 Stability test of Bi<sub>2</sub>O<sub>3</sub>/MOL

Stability is one of the key performance indicators for evaluating catalysts parameters. The application requires performance stability, which in turn requires structure stability.

## 6.3.1 Performance stability

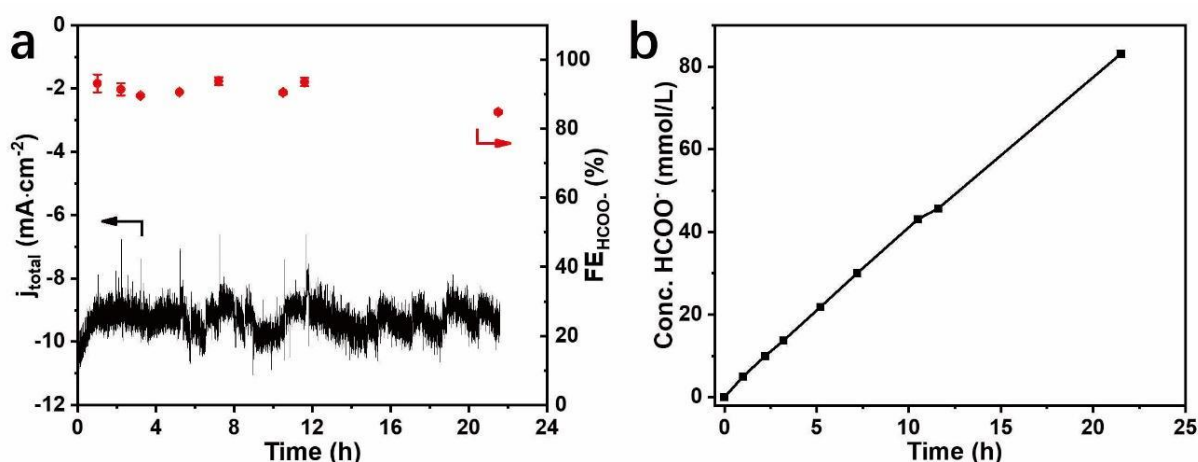


**Figure 6.16** (a) Stability test of Bi<sub>2</sub>O<sub>3</sub>/MOL at -0.97 V vs. RHE. (b) The accumulated concentration of the formate in the cathode chamber.

The stability test was performed in an H-type cell. To guarantee a sufficient supply of the CO<sub>2</sub>, fresh CO<sub>2</sub> gas was continuously bubbled through the electrolyte, which means no gas recycle here. After a certain reaction time, liquid samples were taken to determine the FEs towards HCOO<sup>-</sup>. It turns out that the Bi<sub>2</sub>O<sub>3</sub>/MOL can maintain the performance for at least 20 hours at -0.97 V vs. RHE. The experiment was terminated because of technical problems with the workstation. Until the end of the experiment, the FE remains above 80% (Figure 6.16a). The concentration of formate rises linearly (Figure 6.16b).

## 6.3.2 Structure stability

The morphology of the catalyst after the ECR reaction was investigated by electron microscopy (Figure 6.17). After casting the catalyst on the carbon paper, it is nearly impossible to get it back. Hence, the stability test was conducted using a glassy carbon plate (2.5 × 2.5 cm<sup>2</sup>) as the backing electrode, while all other parameters remained unchanged. The sample for the post-reaction PXRD test was collected by scraping the catalysts off the glassy carbon electrode. These steps were aimed to avoid interference from carbon paper or glassy carbon. The morphology of the MOL layer and the Bi-based nanowires remains intact after the stability test. Owing to the use of Nafion as a binder, the stacking of the layers observed from TEM images is inevitable.

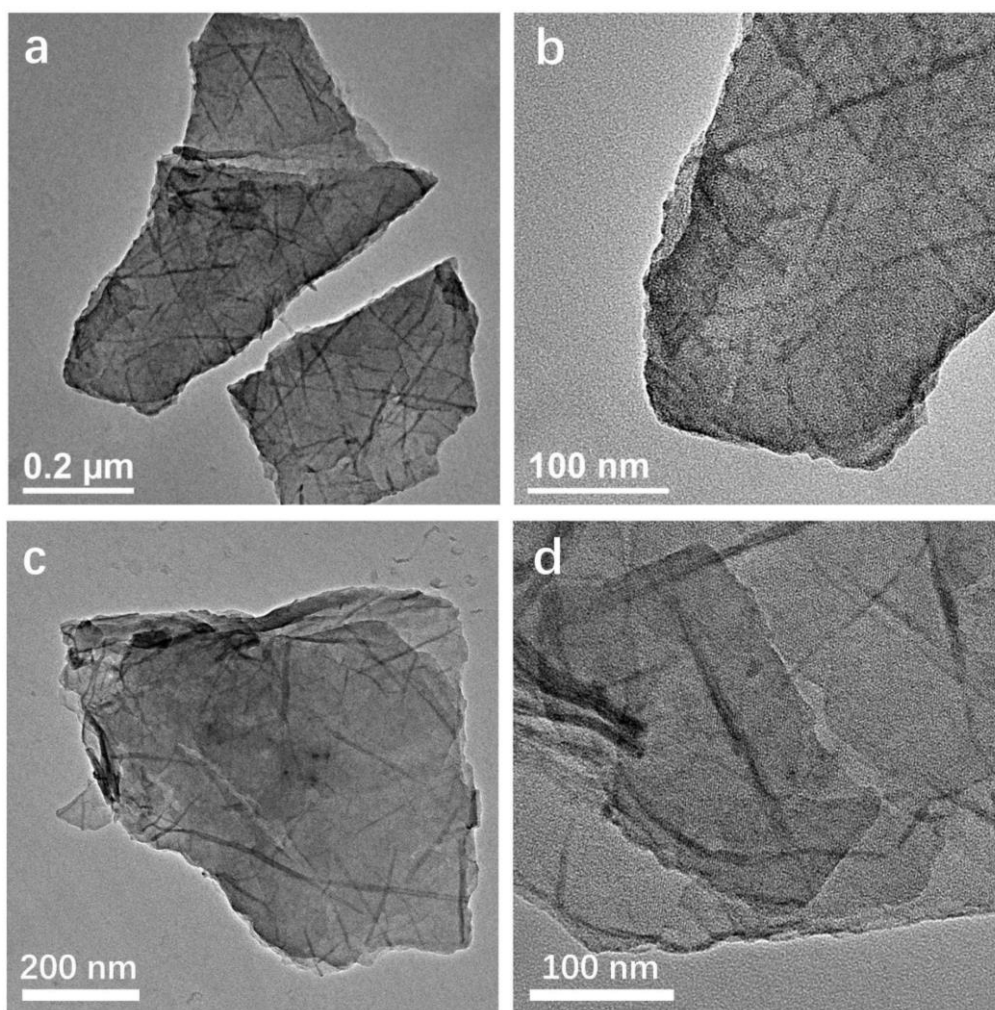


**Figure 6.17** TEM images of Bi<sub>2</sub>O<sub>3</sub>/MOL after (a,b) 15 min test and (c,d) 10 hours test.

Since the TEM can only give relatively localized morphology information of the sample. PXRD was conducted to access the structural stability of Zr-TATB MOL and Bismuth species (**Figure 6.18a**). The peaks of Zr-TATB MOL remain intact after ECR reaction, indicating good structural stability. The appearance of Bi<sub>2</sub>O<sub>2</sub>CO<sub>3</sub> can be ascribed to the reaction of bismuth oxide with bicarbonate from the electrolyte.<sup>[289]</sup> The appearance of metallic Bi comes from the reduction of Bi species.<sup>[126]</sup>

Apart from the assessment of the structural stability by PXRD, the stability of the chemical state was investigated by XPS (**Figure 6.18b-d**). In the full spectrum, no apparent changes can be observed. The binding energies are calibrated by adventitious carbon (C 1s) fitting and Si signal from the Kapton tape. Compared with Bi 4f spectra before and after the test, the overall reduction of Bi species after the test can be clearly observed (**Table 10.4**). The Bi(III) occurred because of the fast oxidation process at the Bi surface once the reaction was terminated.<sup>[126]</sup> The reduction can also be proved by the PXRD post-reaction (**Figure 6.18a**). As for the Zr signal, there is no apparent change in binding energy (Zr 3d<sub>5/2</sub>: 182.6 eV) and peak shape before and after the reaction. Besides, there is no evident signal that can be ascribed to ZrO<sub>2</sub> (Zr 3d<sub>5/2</sub>: ~182.3 eV), which is formed upon

the decomposition of MOL.

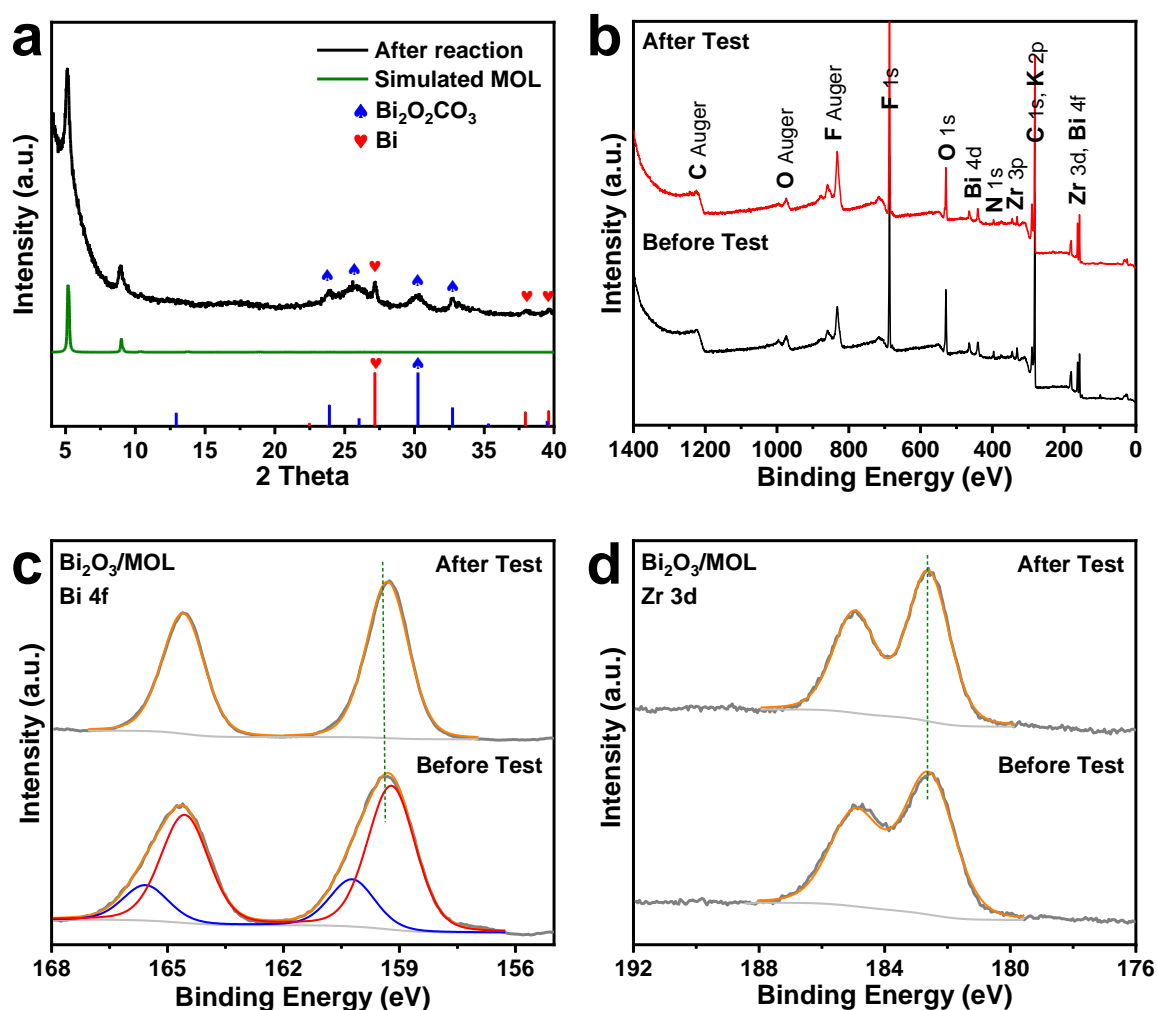


**Figure 6.18** (a) PXRD patterns of standard Bi (PDF#44-1246), Bi<sub>2</sub>O<sub>2</sub>CO<sub>3</sub> (PDF#41-1488), simulated Zr-TATB MOL and Bi<sub>2</sub>O<sub>3</sub>/MOL after a 10-hours test. (b) XPS full spectra (c) XPS Bi 4f spectra and (d) XPS Zr 3d spectra of the Bi<sub>2</sub>O<sub>3</sub>/MOL before and after a 10-hours stability test.

The above experiments prove the good stability of Bi<sub>2</sub>O<sub>3</sub>/MOL, especially the robustness of the Zr-TATB MOL, as was expected.<sup>[209]</sup> It should be noted that too reductive condition still can reduce Zr(IV), which leads to the destruction of the MOL composites.<sup>[290]</sup>

## 6.4 Reasons for the high performance of Bi<sub>2</sub>O<sub>3</sub>/MOL

There is growing attention on using MOFs for electrocatalysis, including 3D-MOFs and layered MOFs. However, the loss of active sites due to electrical conductivity problems of the 3D-MOF was rarely discussed, recognized, and well-presented before. The superior activity of MOL composites can be ascribed to the fully exposed surface area for guest immobilization and electrocatalysis. For lacking *operando* techniques to track the change of the catalyst, we resort to indirect electrochemical methods for investigating its changes during the reaction.

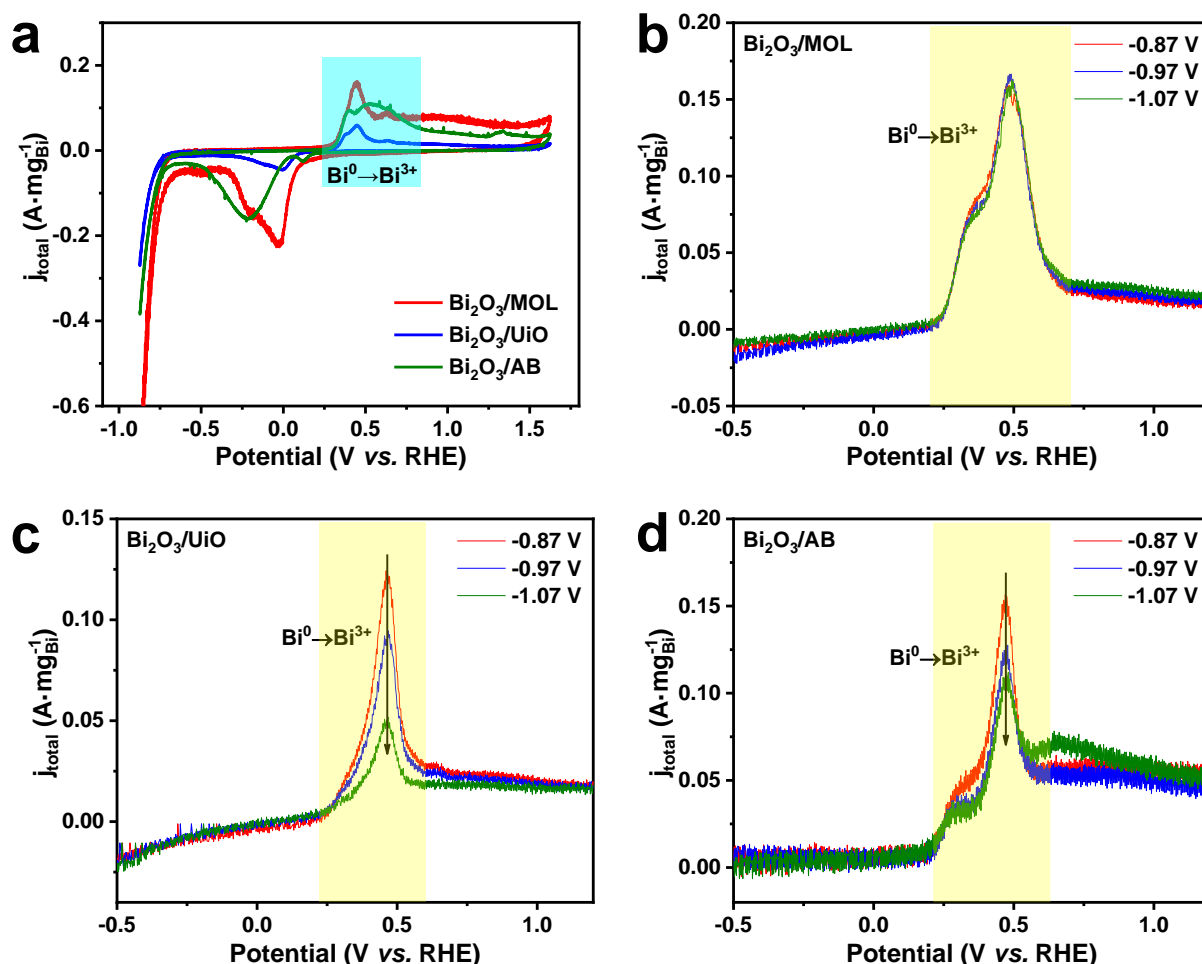


**Figure 6.19** (a) Cyclic voltammetry (CV) plots of fresh Bi<sub>2</sub>O<sub>3</sub>/MOL, Bi<sub>2</sub>O<sub>3</sub>/UiO and Bi<sub>2</sub>O<sub>3</sub>/AB under CO<sub>2</sub> with a scan rate of 50 mV/s. Oxidative LSV plots of (b) Bi<sub>2</sub>O<sub>3</sub>/MOL, (d) Bi<sub>2</sub>O<sub>3</sub>/UiO, and (d) Bi<sub>2</sub>O<sub>3</sub>/AB after chrono amperometric ECR reactions of 30 mins at certain potential (V vs. RHE, 30 min) with a scan rate of 100 mV/s. The current responses were normalized by the mass of Bi.

Firstly, the accessibility of Bi sites was examined for different supports. A considerable amount of Bi sites is buried inside the electrically insulating UiO-66 and is not supplied by electrons, as we discussed and proposed previously (**Chapter 1.3.3**). This part can be proven by oxidative LSV (Bi<sup>0</sup>→Bi<sup>3+</sup>), where electrochemically active Bi will present an oxidative peak and its amount can be roughly quantified by the peak area (**Figure 6.19a**).<sup>[291]</sup> The current responses were normalized to the mass of the loaded Bi, for the convenience of the following comparison. Among these catalysts, Bi<sub>2</sub>O<sub>3</sub>/UiO presented a significantly smaller electrochemically active area than Bi<sub>2</sub>O<sub>3</sub>/MOL and Bi<sub>2</sub>O<sub>3</sub>/AB, indicating the loss of the active sites when loaded inside the electrically insulating 3D-MOFs. On the other hand, Bi<sub>2</sub>O<sub>3</sub>/MOL and Bi<sub>2</sub>O<sub>3</sub>/AB possess similar electrochemical area, indicating the significance of the fully exposed surface area of the MOL.

Secondly, the stabilities of the active sites were examined. It is well recognized that metallic Bi atoms are the active sites for the ECR to formate.<sup>[126]</sup> This process was confirmed by the PXRD and XPS results before and after reaction (**Figure 6.18**). The stabilities of the catalysts after reaction are estimated by the electrochemically active area in oxidative LSV plots. For Bi<sub>2</sub>O<sub>3</sub>/MOL,

the oxidative Bi peak did not show an apparent decrease after chrono amperometric tests at different potentials, indicating its good stability (**Figure 6.19b**). In contrast, Bi<sub>2</sub>O<sub>3</sub>/UiO showed increasingly attenuated peaks, implying deactivation at too negative potentials (**Figure 6.19c**), probably due to an aggregation of Bi sites. Despite having a large conductive area, the moderate decrease in the oxidative peak area for Bi<sub>2</sub>O<sub>3</sub>/AB might be attributed to a limited anchoring strength to prevent aggregation.<sup>[292]</sup>

## 6.5 ECR performance using gas diffusion electrode

To achieve further enhancement of the current density to meet industrial requirements (> 200 mA·cm<sup>-2</sup>), gas diffusion electrodes (GDEs) were applied. As discussed in **Chapter 1.2.2.1**, the advantage of the GDEs is to accelerate the mass transfer of the CO<sub>2</sub> to the active sites.

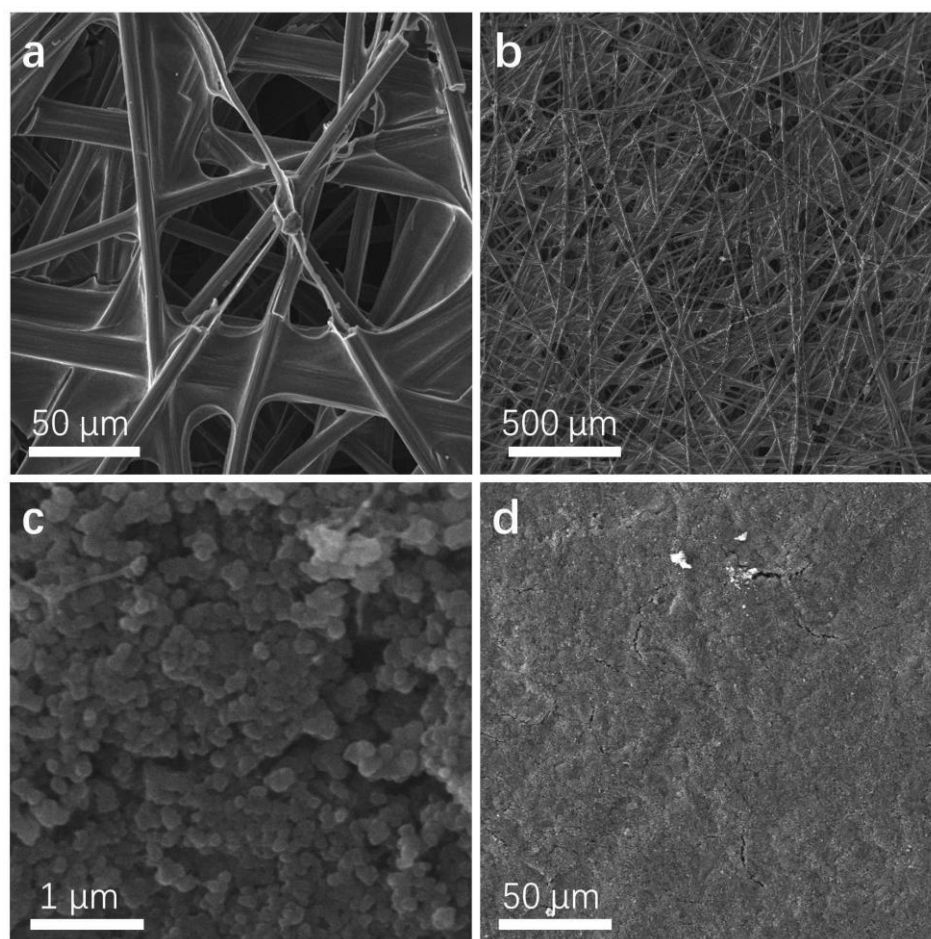


**Figure 6.20** SEM images of (a,b) carbon paper (Sigracet 39BB) and (c,d) home-made GDL.

The experimental set-up has been used in our lab before (**Chapter 3.4.2**).<sup>[19]</sup> The preparation of the GDEs is carried out by drop-casting of a catalyst layer (CL) on a homemade GDL (**Figure 3.9**). We also tried a commercial GDL (Sigracet 39BB) as working electrodes, but the maximum current density reached only a maximum value of 31 mA·cm<sup>-2</sup>. The poor result can be ascribed to a rapid

flooding of the whole working electrode, which became evident after disassembling the cell. This flooding problem can be much improved by using homemade GDLs. Compared with the commercial GDL, the homemade GDL has a higher PTFE content (35 wt%) to reduce the flooding. Besides, the homemade GDL possesses a much narrower gas diffusion channel than the commercial one, which is also beneficial in avoiding flooding (Figure 6.20).

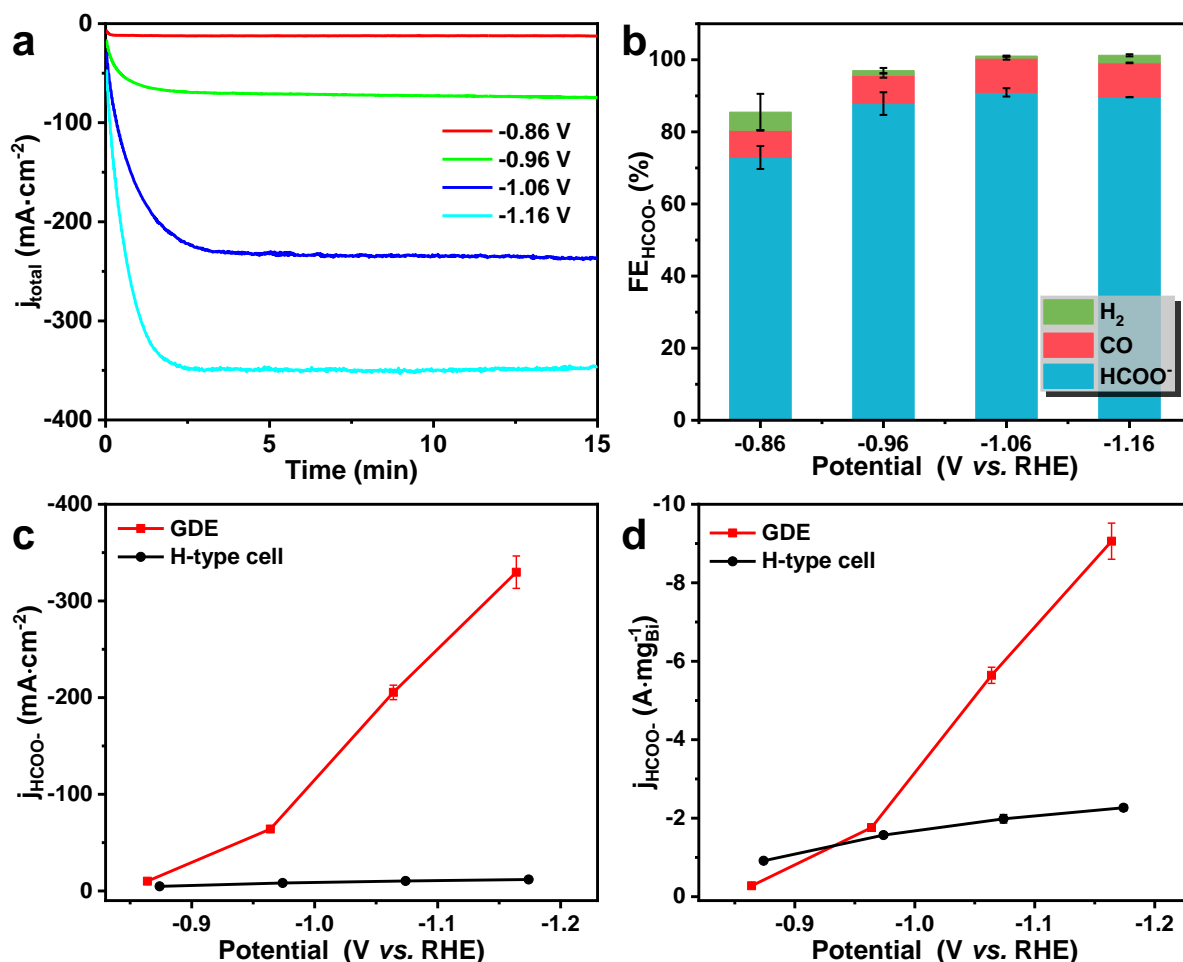


**Figure 6.21** (a) Chrono amperometric I-t plot at different potentials (V vs. RHE) over Bi<sub>2</sub>O<sub>3</sub>/MOL containing gas diffusion electrode (GDE). (b) FEs under different applied potentials over Bi<sub>2</sub>O<sub>3</sub>/MOL by GDE. Comparisons of (c) formate partial current densities and (d) formate partial currents per mg Bi between GDE and H-type cell. The catalyst loading for the GDE test is 1.4 mg·cm<sup>-2</sup>.

Chrono amperometric tests were applied to examine the ECR performance (Figure 6.21). Bi<sub>2</sub>O<sub>3</sub>/MOL can maintain the FEs of over 85% at potentials ranging from -0.96 V to -1.16 V vs. RHE. Strikingly, the partial current density (to formate) can reach 300 mA·cm<sup>-2</sup>. Also, the current per mg Bi by far exceeds the performance of the Bi<sub>2</sub>O<sub>3</sub>/MOL containing carbon paper measured in H-type cells. This enhanced performance is due to the effective CO<sub>2</sub> mass transfer, avoiding the dilemma of local CO<sub>2</sub> depletion in the H-type cell. To the best of our knowledge, this is the first example of achieving an industrially relevant formate production rate by ECR with MOFs-based materials (Table 10.5). However, further applying more negative potentials reduced the FEs and

current density because of the quick flooding of the catalyst layer by increased electro-wetting. Further optimization of the structure of GDE to get even better performance and long-term activity is auspicious and expected.

## 6.6 MOL composites with different bismuth compounds

### 6.6.1 Synthesis strategy of MOL composites with different bismuth compounds

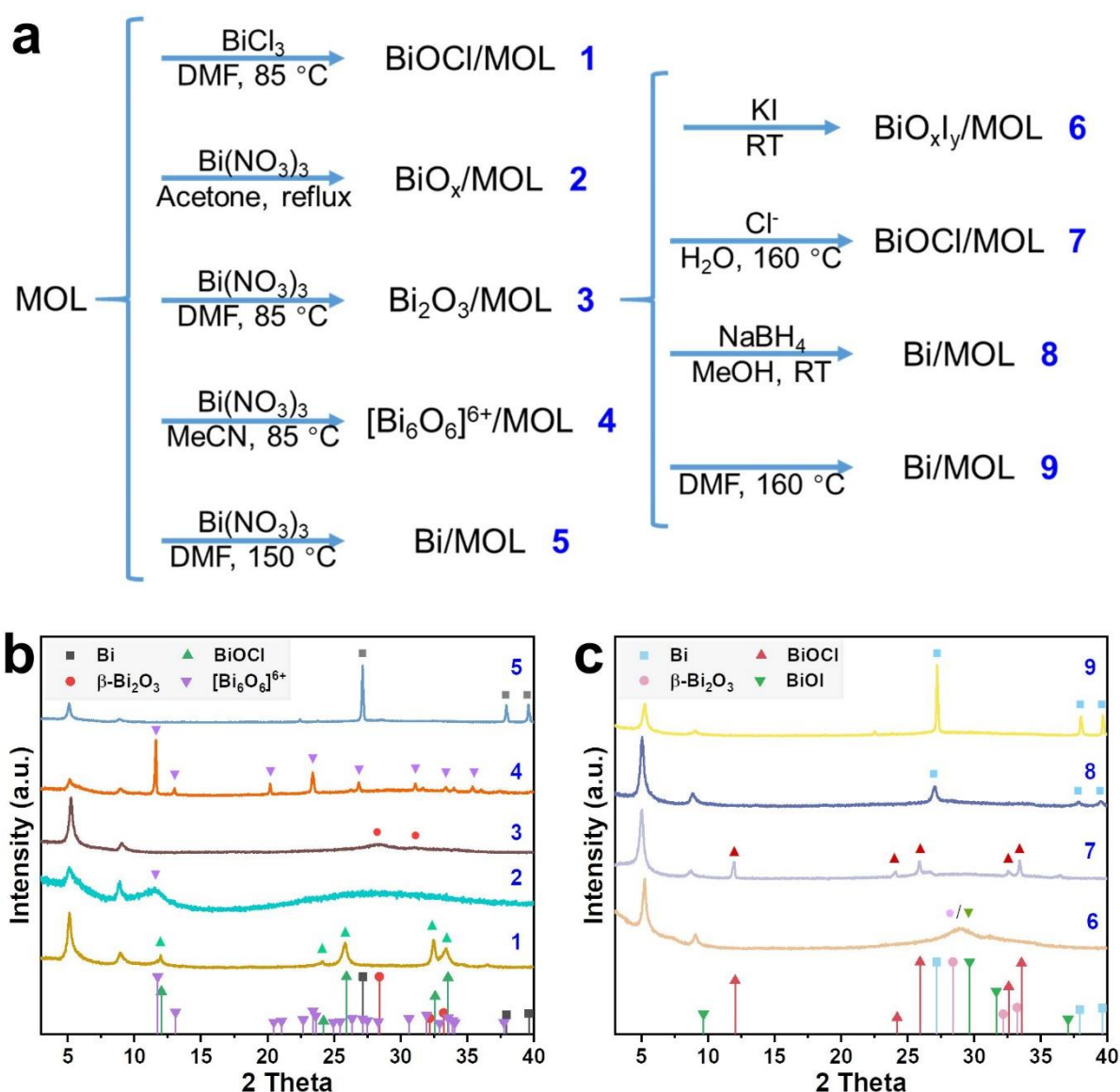


**Figure 6.22** (a) Synthesis scheme of diverse MOL composites bearing different Bi species. (b,c) Corresponding PXRD patterns of the MOL composites after post-modification. Standard: Bi (PDF#44-1246), BiOCl (PDF#73-2060), β-Bi<sub>2</sub>O<sub>3</sub> (PDF#18-0244), BiOI (PDF#10-0445), (Bi<sub>6</sub>O<sub>6</sub>)<sub>2</sub>(NO<sub>3</sub>)<sub>11</sub>(OH)·6H<sub>2</sub>O (COD-1533752).

We tried a lot of methods to load Bi species on the MOL (**Figure 6.22a**). The PXRD can prove the preservation of the crystal structure of the MOL. Since the trivalent Bi ions generally possess

a strong hydrolysis tendency, the successful loading of guest species is most visible by a color change, PXRD, or TEM. Some of these samples will be discussed in the following chapters. Here listed some specific observations: 1. BiCl<sub>3</sub> shows a strong tendency to hydrolyze to BiOCl, which may need a strictly anhydrous solvent. 2. Acetone can cause some damage to the MOL structure at boiling temperature. 3. MeCN can lead to the formation of a series of alkaline nitrates, for example, (Bi<sub>6</sub>O<sub>6</sub>)<sub>2</sub>(NO<sub>3</sub>)<sub>11</sub>(OH)·6H<sub>2</sub>O in [Bi<sub>6</sub>O<sub>6</sub>]<sup>6+</sup>/MOL(4), which is not the case using DMF as a solvent.<sup>[293]</sup> 4. DMF is the most suitable solvent for post-synthetic modification, due to the suppressed hydrolysis and strong solubility of metal precursors. It can also provide a weak reducing effect. 5. The presence of the halogen ion will lead to the formation of BiOX (X=Cl, Br, I).

### 6.6.2 Characterization of BiOCl/MOL(7) and Bi/MOL(8)

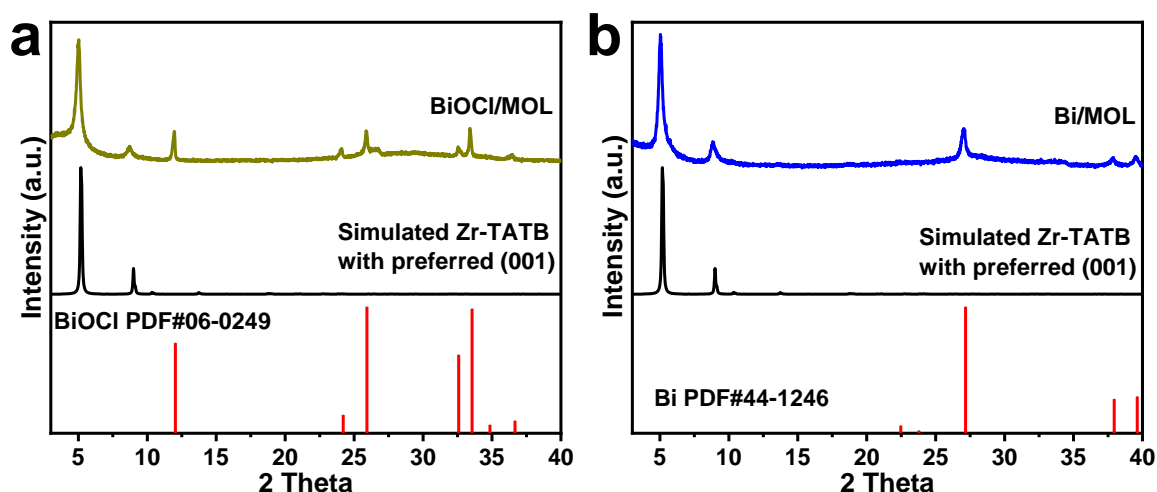


**Figure 6.23** PXRD patterns of (a) BiOCl/MOL(7), simulated Zr-TATB MOL and standard BiOCl (PDF#73-2060); (b) Bi/MOL(8), simulated Zr-TATB MOL and standard metallic Bi (PDF#44-1246).

The most successful examples of Bi-based MOL composites are BiOCl/MOL(7), and Bi/MOL(8), both prepared by post-transformation of Bi<sub>2</sub>O<sub>3</sub>/MOL. The hydrothermal treatment at 160 °C of the Bi<sub>2</sub>O<sub>3</sub>/MOL with the Cl<sup>-</sup> being present leads to BiOCl/MOL(7). The Bi/MOL can be synthesized by reducing the Bi<sub>2</sub>O<sub>3</sub>/MOL with NaBH<sub>4</sub>. The PXRD pattern proves the successful formation of the crystalline BiOCl and metallic Bi, respectively, as well as the preservation of the MOL structure (Figure 6.23). The TEM images characterize their morphologies. As for the BiOCl/MOL(7), small heterogeneous nanoparticles with an average diameter of 3.8 nm can be observed (Figure 6.24). As for the Bi/MOL(8), the Bismuth species is also in the form of nanoparticles with an average diameter of 10.7 nm (Figure 6.25). The MOL lattice can also be observed after the modifications, indicating the rigidity of the MOL structure even after the harsh treatment with NaBH<sub>4</sub> (Figure 6.24 & 6.25).

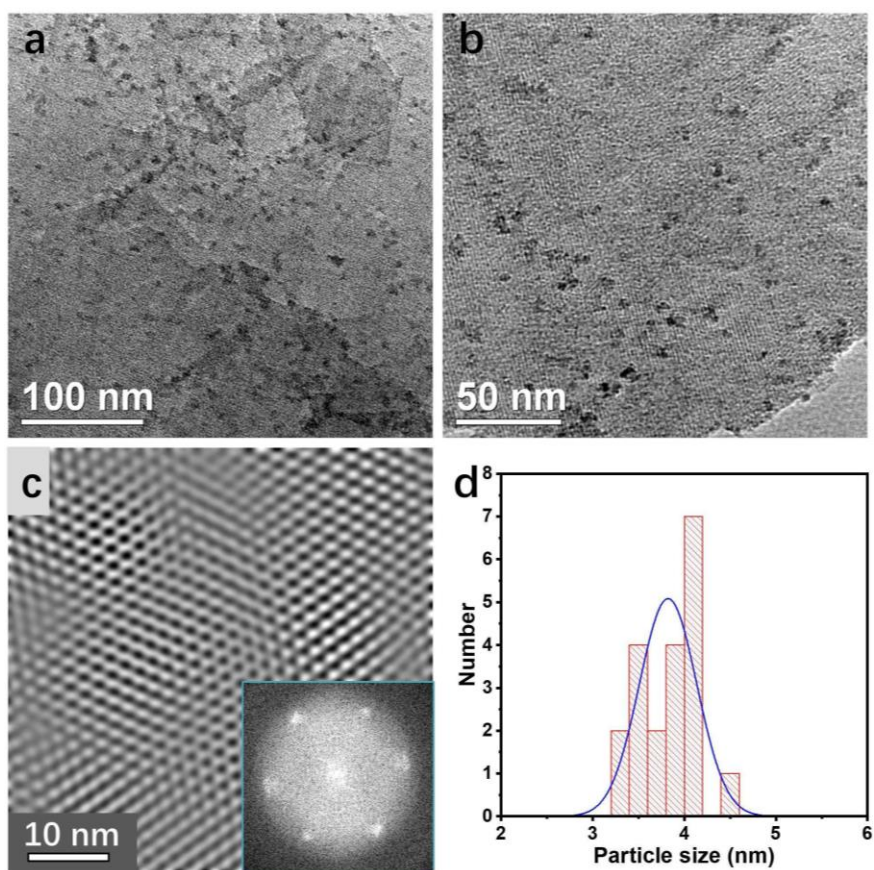


**Figure 6.24** (a,b) TEM images of the BiOCl/MOL. (c) De-noised TEM image of the lattice of the MOL and FFT pattern of (b). (d) Particle size distribution diagram of the BiOCl nanoparticles.

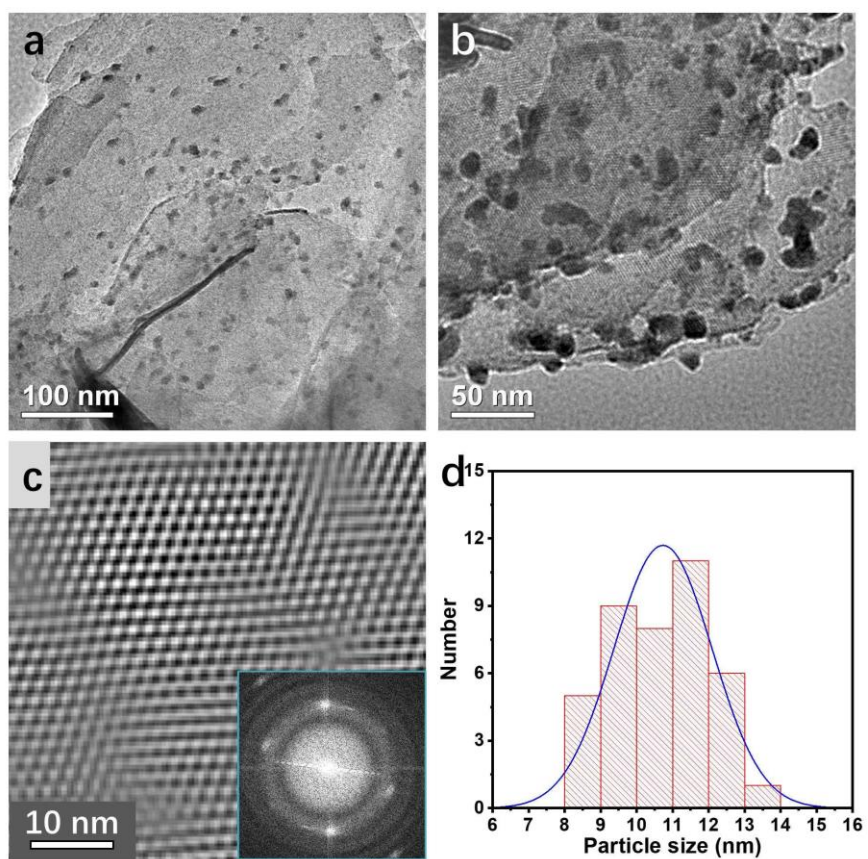


**Figure 6.25** (a,b) TEM images of the Bi/MOL. (c) De-noised TEM image of the lattice of the MOL and FFT pattern of (b). (d) Particle size distribution diagram of the Bi nanoparticles.

## 6.6.3 Comparison of ECR performance of the Bi-based MOL composites

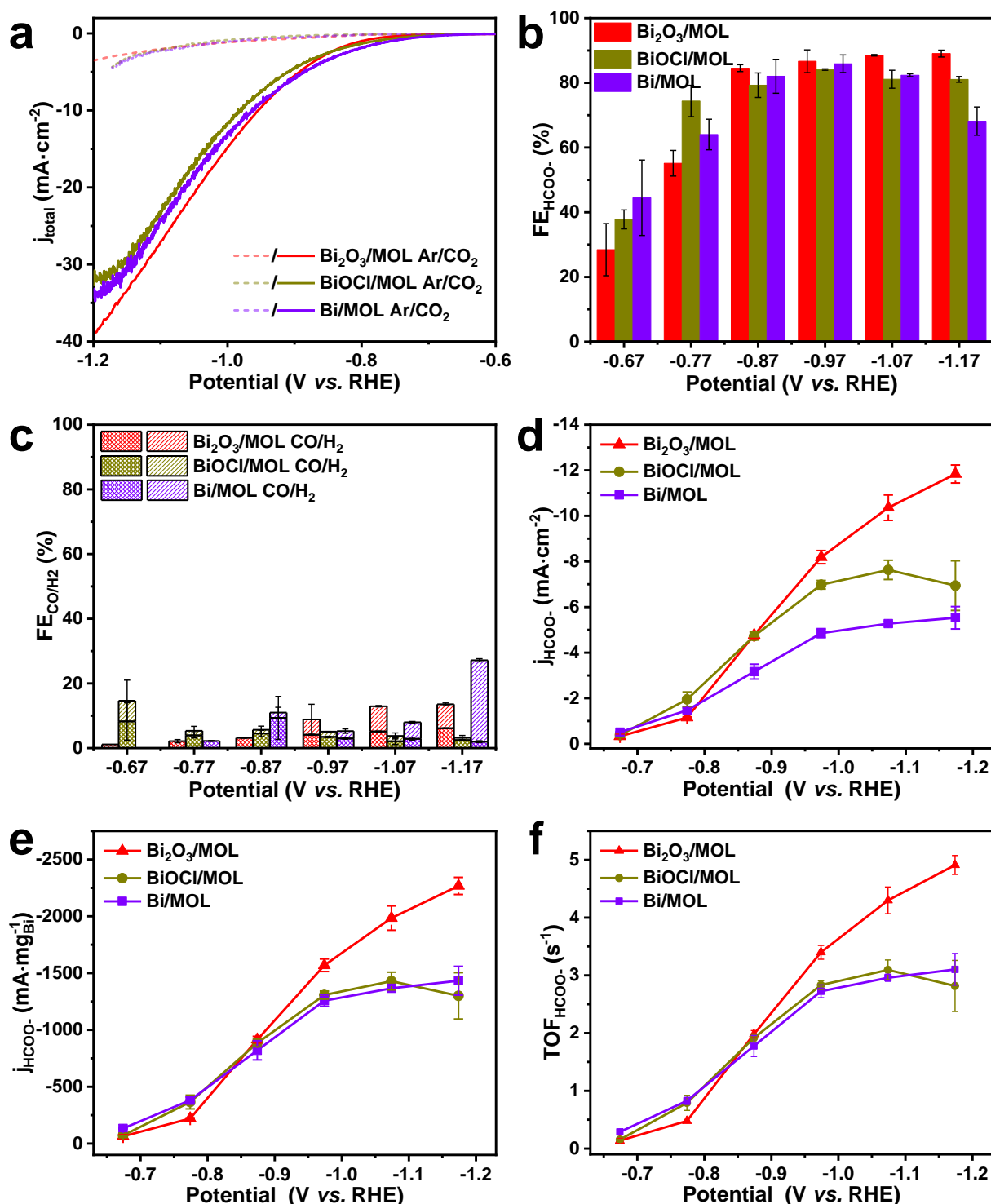


**Figure 6.26** (a) LSV curves under Ar/CO<sub>2</sub>, (b,c) Faradaic efficiencies, (d) formate partial current densities, (e) formate partial current per mg Bi, (f) TOF (s<sup>-1</sup>) towards 1/2 HCOO<sup>-</sup> at different applied potentials over Bi<sub>2</sub>O<sub>3</sub>/MOL, BiOCl/MOL and Bi/MOL.

Considering the different morphology of these Bi species, then it lends itself to proving the impact of the morphology on ECR reaction. Firstly, the ECR activities were investigated by LSV tests under Ar and CO<sub>2</sub> (Figure 6.26a). Bi<sub>2</sub>O<sub>3</sub>/MOL exhibits a slightly higher activity than BiOCl/MOL(7) and Bi/MOL(8). Then, the exact ECR activities were tested by chrono

amperometric tests at different potentials (Figure 6.27). All these three catalysts possess good faradaic efficiencies (> 80%) towards formate in a wide potential range from -0.87 to -1.07 V vs. RHE (Figure 6.26b,c). Bi<sub>2</sub>O<sub>3</sub>/MOL shows a better ECR performance than its counterparts.

Besides, Bi<sub>2</sub>O<sub>3</sub>/MOL also possesses the best partial current density to formate, whether one refers to the geometrical area or the mass of Bi (Figure 6.26d-f). By comparing the results of BiOCl/MOL(7) and Bi/MOL(8), we can conclude that the ECR reaction is not so sensitive to the size of the 0D-nanoparticles, at least when considering the range from 3 to 14 μm. By comparing these three catalysts, we can conclude that the nanowire morphology gives a better ECR performance, which may result from the preferred orientation of the 1D nanoparticles compared to the 0D nanoparticles.

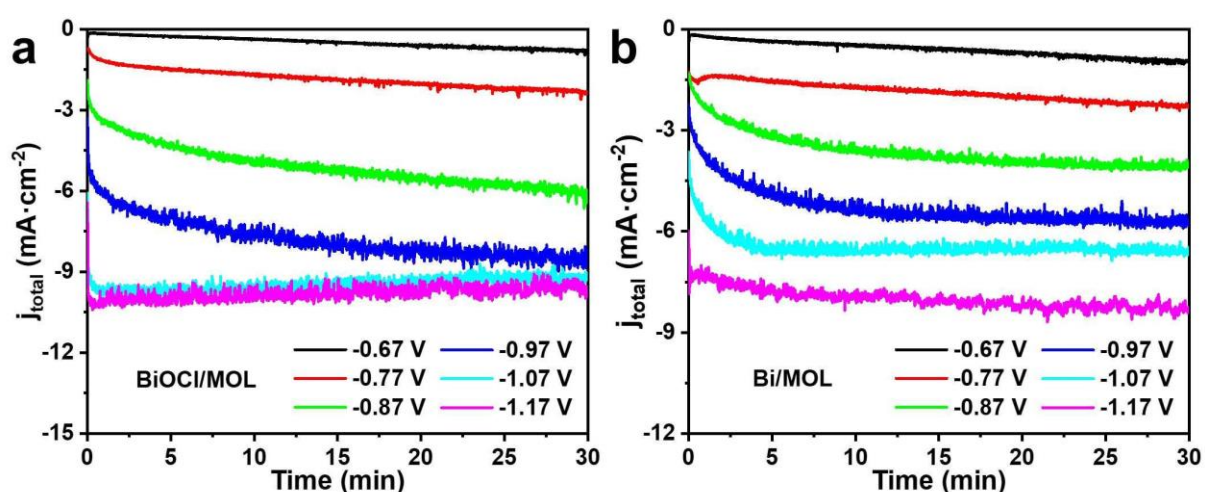


**Figure 6.27** Chrono amperometric I-t plot at different potentials (V vs. RHE) over (a) BiOCl/MOL(7) and (b) Bi/MOL(8).

#### 6.6.4 Other bismuth-based MOL composites

Other Bismuth-based MOL composites will also be briefly discussed, even though they do not have a promising morphology and superior performance.

##### 6.6.4.1 BiOCl/MOL(1)

When using BiCl<sub>3</sub> as the Bi precursor, large irregular particles can be obtained on the MOL (Figure 6.28). The PXRD pattern shows diffraction peaks of crystalline BiOCl (Figure 6.22). Unfortunately, the poor morphology kept us from further ECR tests.

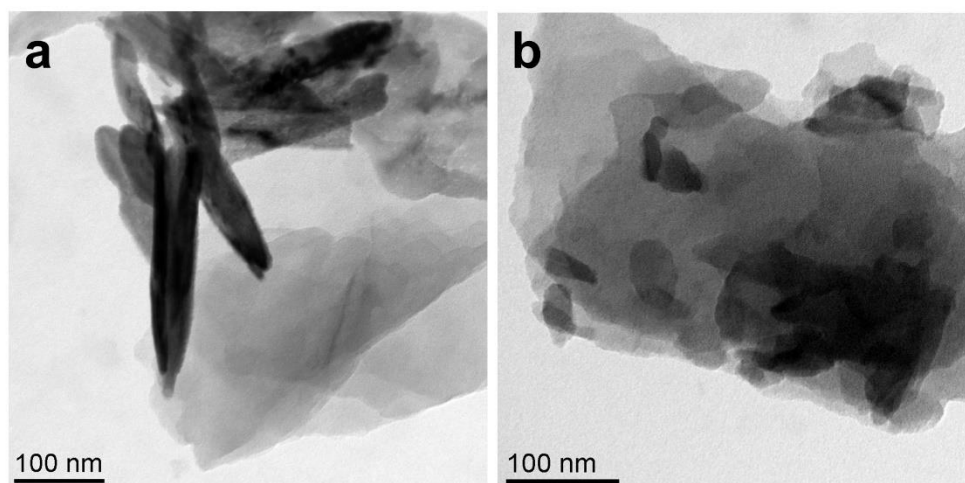


**Figure 6.28** (a,b) TEM images of BiOCl/MOL(1).

#### 6.6.4.2 BiO<sub>x</sub>/MOL(2)

When using acetone as the reaction solvent, some hexagonal nanosheets of over 90 nm thickness can be obtained on the MOL (**Figure 6.29**). For the most part, however, they are not well-shaped and not well-dispersed. The PXRD pattern shows diffraction peaks, which are very close to an alkaline nitrate (**Figure 6.22**). The poor morphology kept us from further ECR tests.

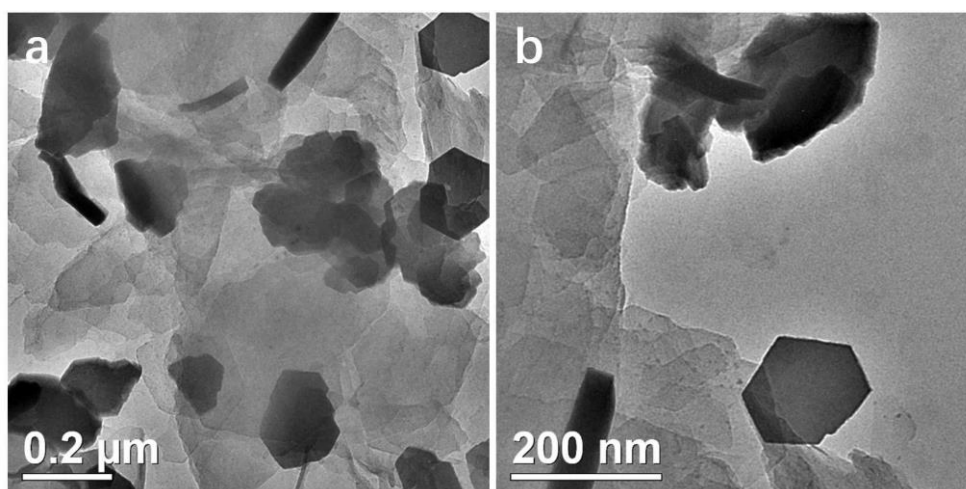


**Figure 6.29** (a,b) TEM images of BiO<sub>x</sub>/MOL(2).

#### 6.6.4.3 [Bi<sub>6</sub>O<sub>6</sub>]<sup>6+</sup>/MOL(4)

When using MeCN as the solvent for metal loading, the diffraction peaks of alkaline nitrate can be clearly distinguished in the PXRD pattern (**Figure 6.22**). The very sharp PXRD reflexes indicate a large crystal size of the compound and/or a huge Bi loading. This shows that the MeCN can not suppress hydrolysis of the Bi precursor during the post-synthetic modification of the MOL. The ECR performance was evaluated by LSV and chrono amperometric tests (**Figure 6.30**). [Bi<sub>6</sub>O<sub>6</sub>]<sup>6+</sup>/MOL(4) exhibited a significant current response under CO<sub>2</sub> compared to under Ar from the LSV test, which suggests a good performance. The chrono amperometric test at -1.17 V vs. RHE gives indications of degradation at the beginning, suggesting a quick structural

transformation over the reaction time. [Bi<sub>6</sub>O<sub>6</sub>]<sup>6+</sup>/MOL(4) can still maintain the FEs of over 80% in the potential ranging from -0.97 V to -1.17 V vs. RHE. Overall, it exhibits good ECR performance, although not better than Bi<sub>2</sub>O<sub>3</sub>/MOL.

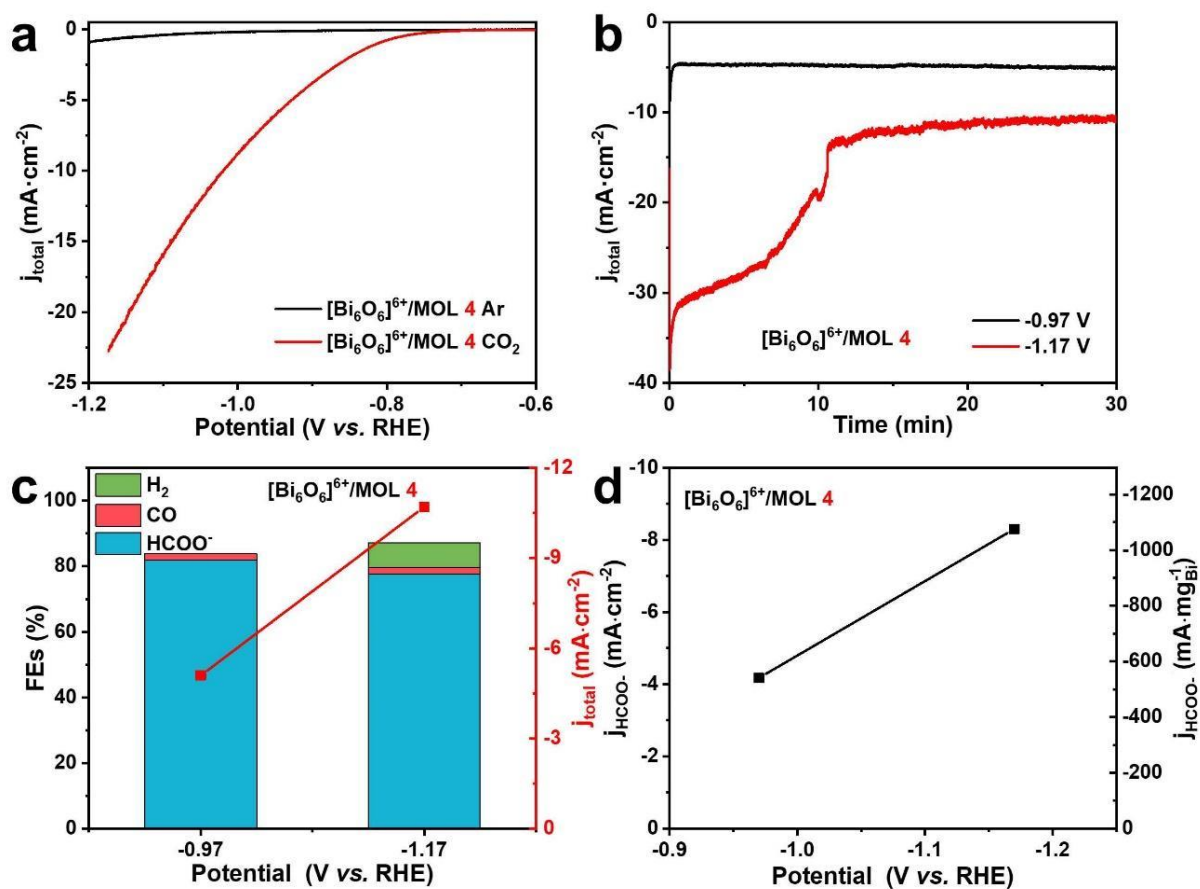


**Figure 6.30** (a) LSV curves under Ar/CO<sub>2</sub>, (b) chrono amperometric I-t plots, (c) Faradaic efficiencies, (d) formate partial current densities/formate partial current per mg Bi at different applied potentials over [Bi<sub>6</sub>O<sub>6</sub>]<sup>6+</sup>/MOL(4).

#### 6.6.4.4 Bi/MOL(5)

Post-modification by solvothermal treatment at a higher temperature led to the formation of metallic Bi on the MOL, arising from the reduction ability of solvent DMF (Figure 6.22). The morphology of the bismuth species was found to be long nanotubes with an outer diameter of around 10 nm on the MOL (Figure 6.31). The activity was examined by LSV tests (Figure 6.32a), which gave even a better current response than Bi<sub>2</sub>O<sub>3</sub>/MOL (Figure 6.6a). However, the actual chrono amperometric tests couldn't confirm a better performance (Figure 6.32b). It only possesses FEs of over 60% at potentials ranging from -0.87 V to -1.07 V vs. RHE (Figure 6.32c). The current densities to formate were also worse than the Bi<sub>2</sub>O<sub>3</sub>/MOL.

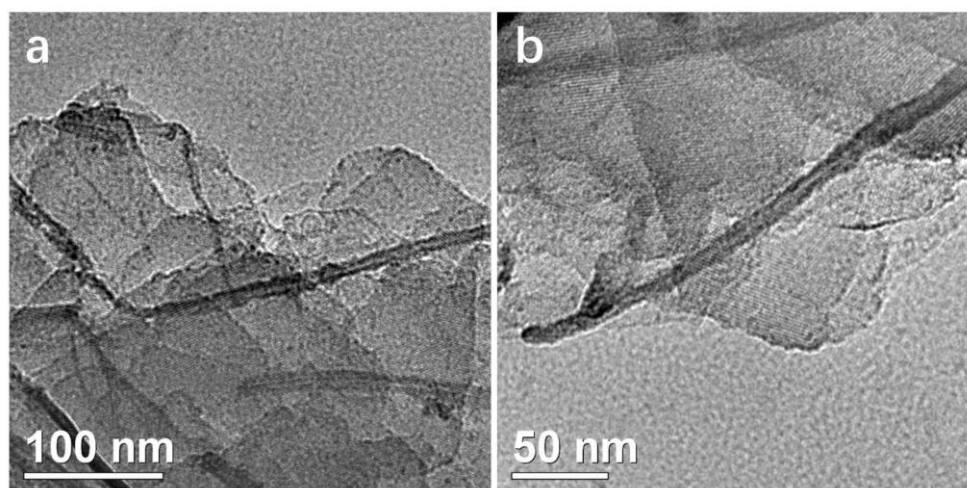


**Figure 6.31** (a,b) TEM images of Bi/MOL(5).

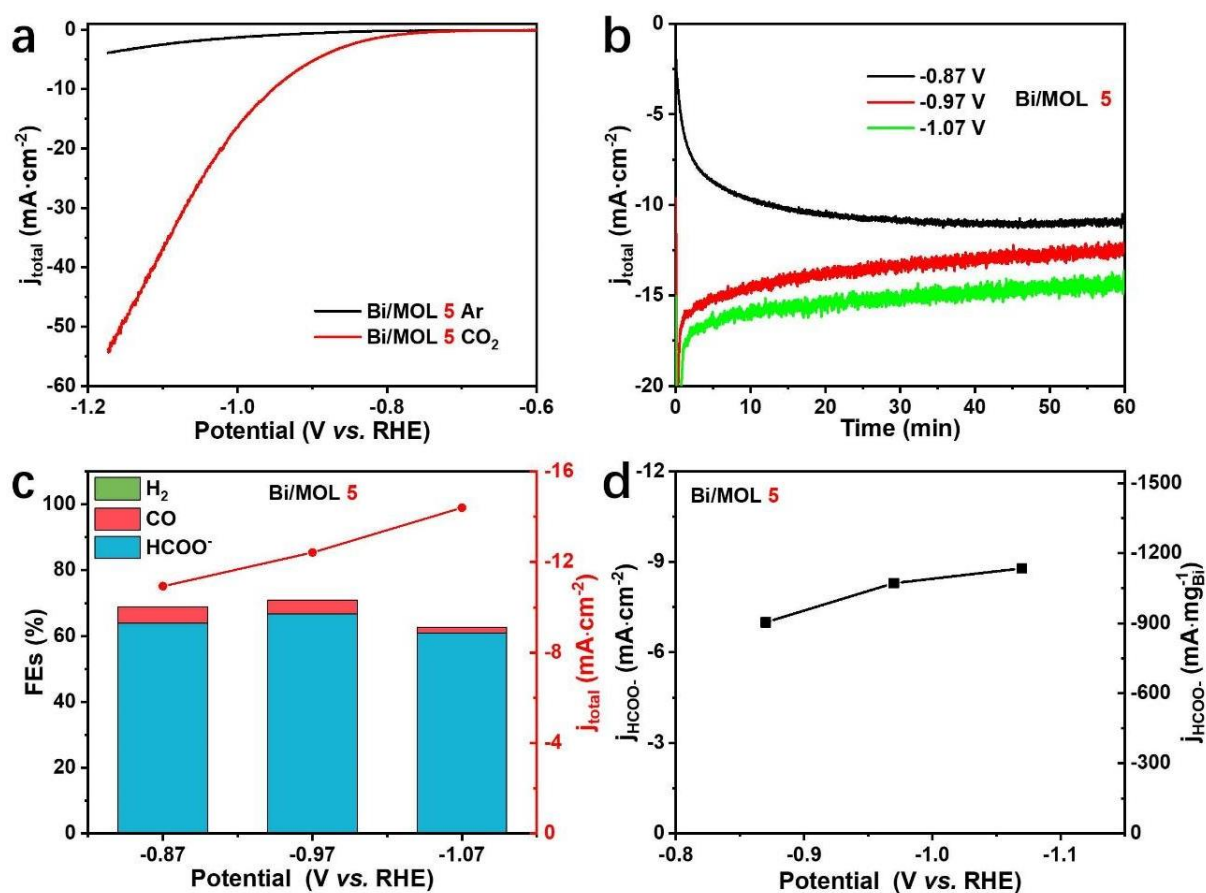


**Figure 6.32** (a) LSV curves under Ar/CO<sub>2</sub>, (b) chrono amperometric I-t plots, (c) Faradaic efficiencies, (d) formate partial current densities/formate partial current per mg Bi at different applied potentials over Bi/MOL(5).

#### 6.6.4.5 BiO<sub>x</sub>I<sub>y</sub>/MOL(6)

The iodide insertion could be verified by the color change (from white to light yellow). However, no crystalline BiOI was formed, as proved by the PXRD diffractions (Figure 6.22). The corresponding composite was denoted as BiO<sub>x</sub>I<sub>y</sub>/MOL(6). The ECR performance was examined by LSV and chrono amperometric tests (Figure 6.33). Overall, a poor ECR performance was found.

The FEs to formate didn't exceed 80% and a deactivation occurred at a higher current (Figure 6.33). The reason can be attributed to the insertion of the iodide into the Bi oxide, even though the actual active site is Bi<sup>0</sup>.

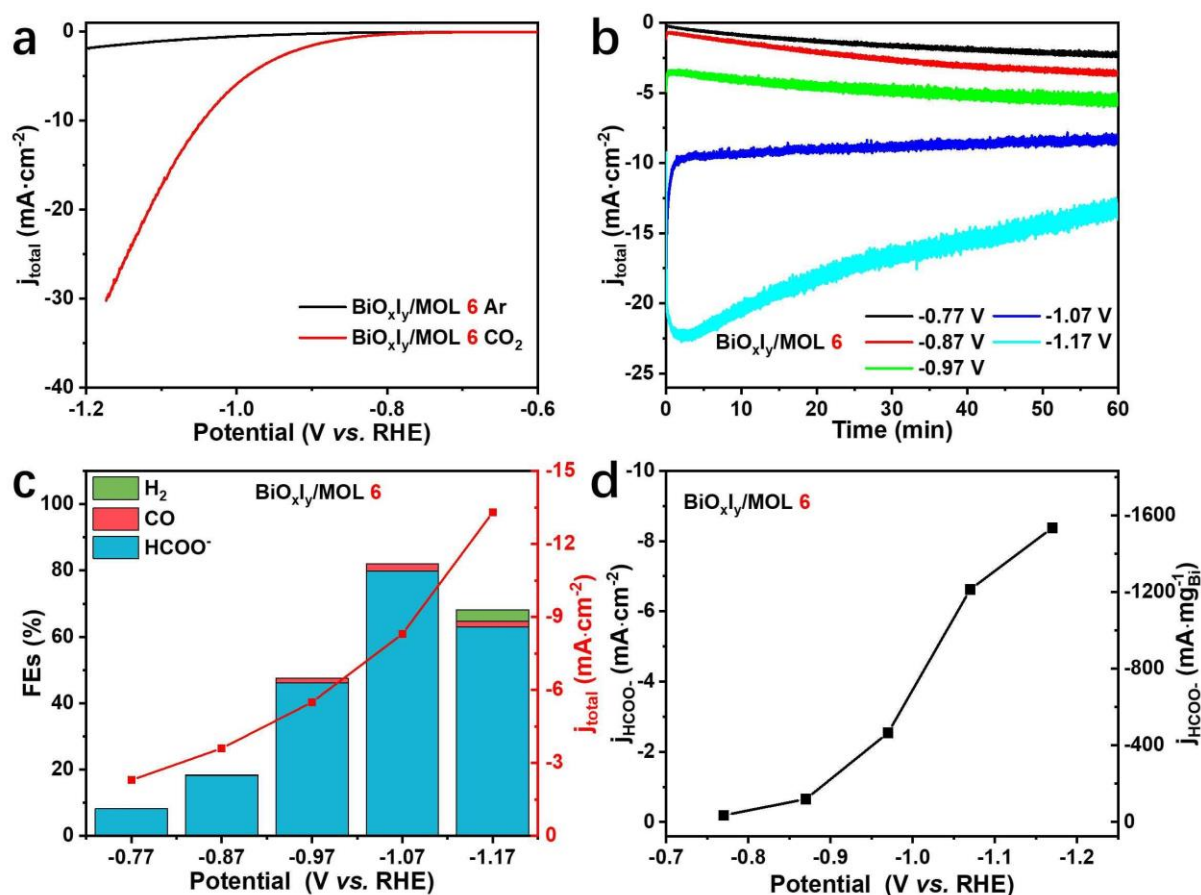


**Figure 6.33** (a) LSV curves under Ar/CO<sub>2</sub>, (b) chrono amperometric I-t plots, (c) Faradaic efficiencies, (d) formate partial current densities/formate partial current per mg Bi at different applied potentials over BiO<sub>x</sub>I<sub>y</sub>/MOL(6).

#### 6.6.4.6 Bi/MOL(9)

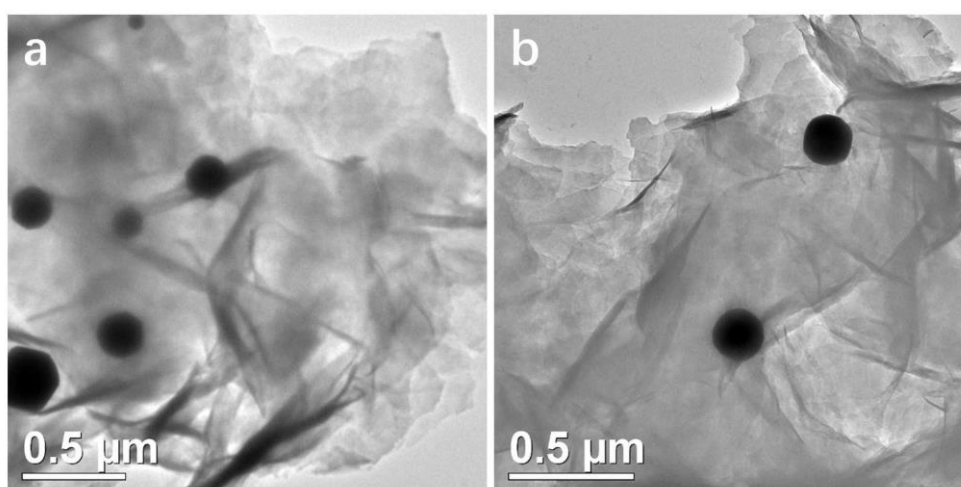


**Figure 6.34** (a,b) TEM images of Bi/MOL(9).

The solvothermal post-treatment of the Bi<sub>2</sub>O<sub>3</sub>/MOL at higher temperatures led to the formation

of the metallic Bi (**Figure 6.22**). The morphology of the bismuth species was investigated by the TEM. The Bi agglomerated into large particles of over 100 nm (**Figure 6.34**). The bad morphology stops us the further ECR tests.

## 6.7 Summary of ECR performance of Bi/MOL

In this chapter, measurements of the ECR performance with a typical H-type cell were reported, which is widely adopted in fundamental research. Besides, the universality of constructing MOL composites with different Bi compounds for ECR reactions was also presented and proved. As a result, it turns out that Bi<sub>2</sub>O<sub>3</sub>/MOL possesses an excellent CO<sub>2</sub> electroreduction activity towards formate, exhibiting a maximum formate current density of 2.3 A·mg<sub>Bi</sub><sup>-1</sup> and Faradaic efficiencies (FEs) of over 85% in a wide potential range from -0.87 to -1.17 V, in contrast with Bi<sub>2</sub>O<sub>3</sub> loaded onto a 3D MOF (Bi<sub>2</sub>O<sub>3</sub>/UiO) or on acetylene black (Bi<sub>2</sub>O<sub>3</sub>/AB). The notable comparison highlights the superiority of MOL composites, bypassing the dilemma of the electrical conductivity issues of the 3D MOF-based electrocatalysts. Furthermore, Bi<sub>2</sub>O<sub>3</sub>/MOL proved to be more stable. Strikingly, further enhancement of the current density towards industrial requirement can be achieved by Bi<sub>2</sub>O<sub>3</sub>/MOL containing gas diffusion electrodes (GDEs), giving a remarkable geometrical formate current density of 330 mA·cm<sup>-2</sup>. Overall, Bi<sub>2</sub>O<sub>3</sub>/MOL exhibits one of the best performances amongst MOFs used for direct ECR (**Table 10.5**), whether measured in an H-type cell or with GDEs. This highlights the superiority of the concept of MOL composites.



## 7 | Electrochemical CO<sub>2</sub> Reduction by Other Metal/MOL Composites

### Metal/MOL Composites

The flexible structure and multivariate nature of the MOFs largely determine the diversity of the MOFs, which allows a rational structure design for versatile applications. In this chapter, the universality of the post-modification strategy was investigated by introducing different guest metal ions.

### 7.1 MOL composites with tin-based active sites

#### 7.1.1 Synthesis strategy of MOL composites of different tin species

Tin-based active sites are also widely investigated to produce formate in ECR reactions for their good activity, high selectivity, non-toxicity, and inexpensive cost. Pure metallic Sn is barely active in ECR reaction. The existence of surface SnO<sub>x</sub> is essential for CO<sub>2</sub> reduction.<sup>[45,124]</sup> Constructing nanosized tin catalysts is a promising strategy to increase the proportion of the surface oxide shell.<sup>[121]</sup>

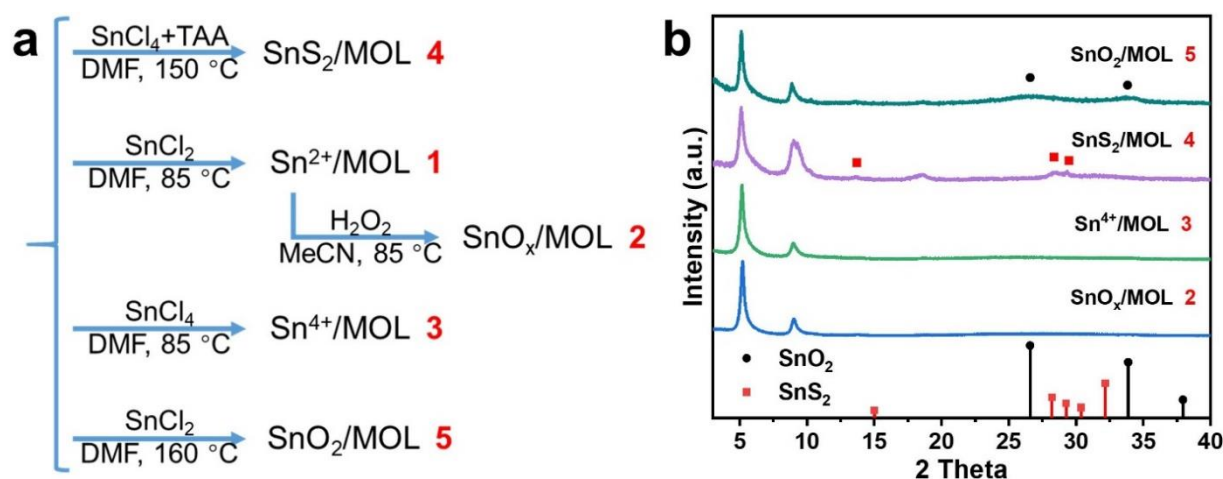


**Figure 7.1** (a) Synthesis scheme of diverse MOL composites with different Sn compounds. (b) Corresponding PXRD patterns of the MOL composites after the post-modifications.

The compounds and morphologies of the tin compounds are not as complex as bismuth species (Chapter 3.3.3.1, Figure 7.1a). The total reduction of tin into metallic Sn<sup>0</sup> is also very different, because it needs harsh conditions. The common Sn precursors can be classified into two types by the valence of Sn: Sn(II) and Sn(IV). Sn(II) possesses strong reduction abilities and is easily

converted into Sn(IV), which can be utilized to form some heterometal doped compounds.<sup>[294]</sup> The retention of the crystal structure of the MOL can be proven by PXRD measurements (**Figure 7.1b**). The corresponding examples will be discussed in the following chapters.

## 7.1.2 Characterizations and ECR performance of tin based MOL composites

### 7.1.2.1 SnO<sub>x</sub>/MOL(2)

Based on the HSAB theory, the Sn<sup>2+</sup> would only form unstable coordination with the MOL. To further stabilize the nano Sn species, a subsequent oxidation treatment by H<sub>2</sub>O<sub>2</sub> can lead to the formation of tin (IV) oxide on the MOL, which we refer to SnO<sub>x</sub>/MOL. Since specific tin compounds could not be identified by the PXRD patterns (**Figure 7.1b**), we use the term “SnO<sub>x</sub>”. The morphology of the SnO<sub>x</sub> can be observed by TEM (**Figure 7.2**). The heterogeneous nanoparticles with an average diameter of 2.5 nm are well dispersed on the MOL, clearly seen due to the contrast difference in the TEM image. Despite the treatment with H<sub>2</sub>O<sub>2</sub>, the lattice structure of the Zr-TATB MOL remains nearly unchanged, verified by PXRD and TEM. The uniform dispersion of the tin species on the MOL can be further confirmed by the TEM-EDX (**Figure 7.3**). The successful synthesis of such small SnO<sub>x</sub> nanoparticles without the need of capping agents stresses the significance of the support effect of the MOL.

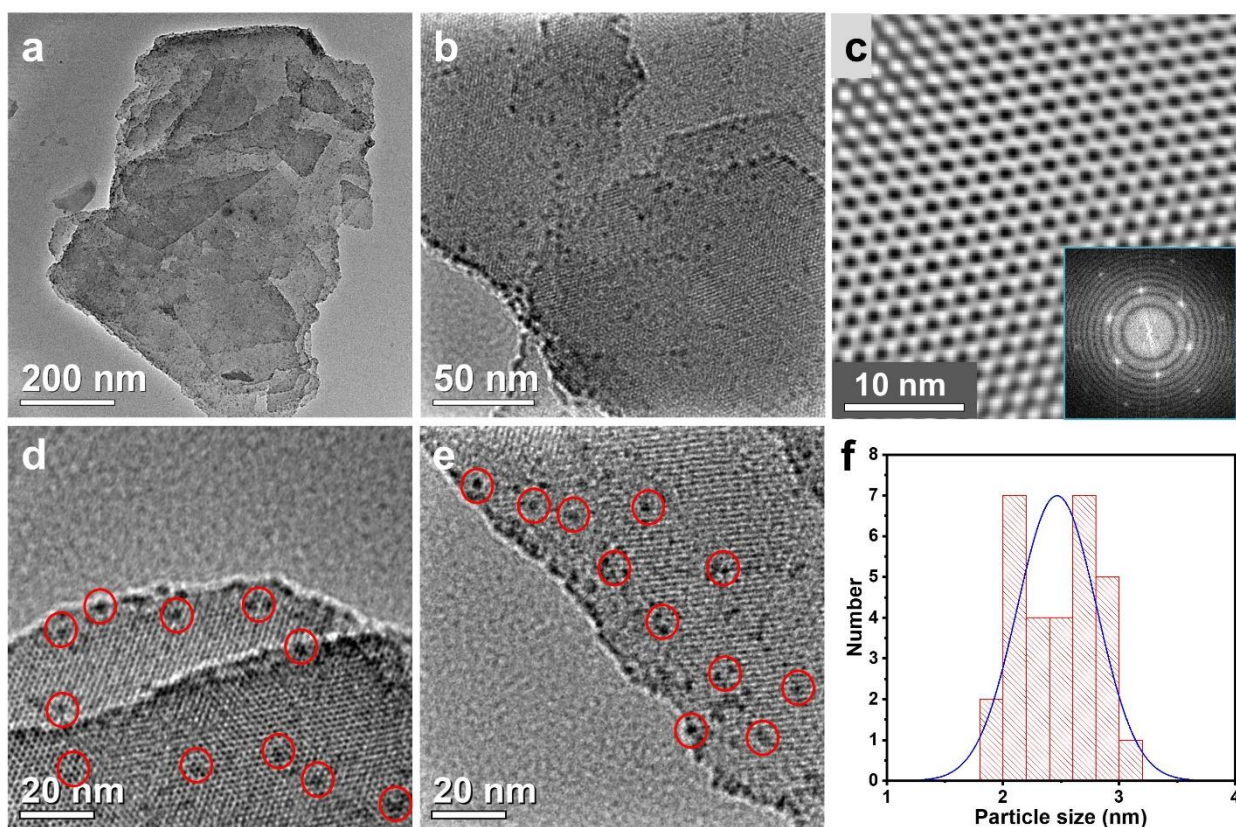


**Figure 7.2** (a,b,d,e) TEM images of SnO<sub>x</sub>/MOL(2). (c) De-noised TEM image of the lattice of the MOL and FFT pattern of (d). (f) Particle size distribution diagram of the SnO<sub>x</sub> nanoparticles.

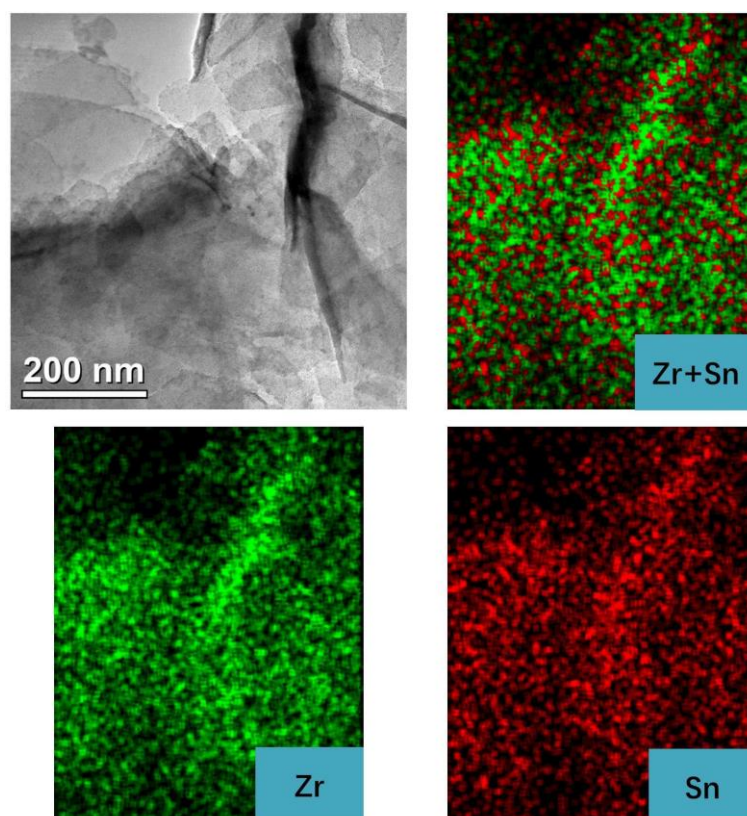


**Figure 7.3** (a) TEM images of SnO<sub>x</sub>/MOL(2) and its corresponding (b,c,d) EDX element maps.

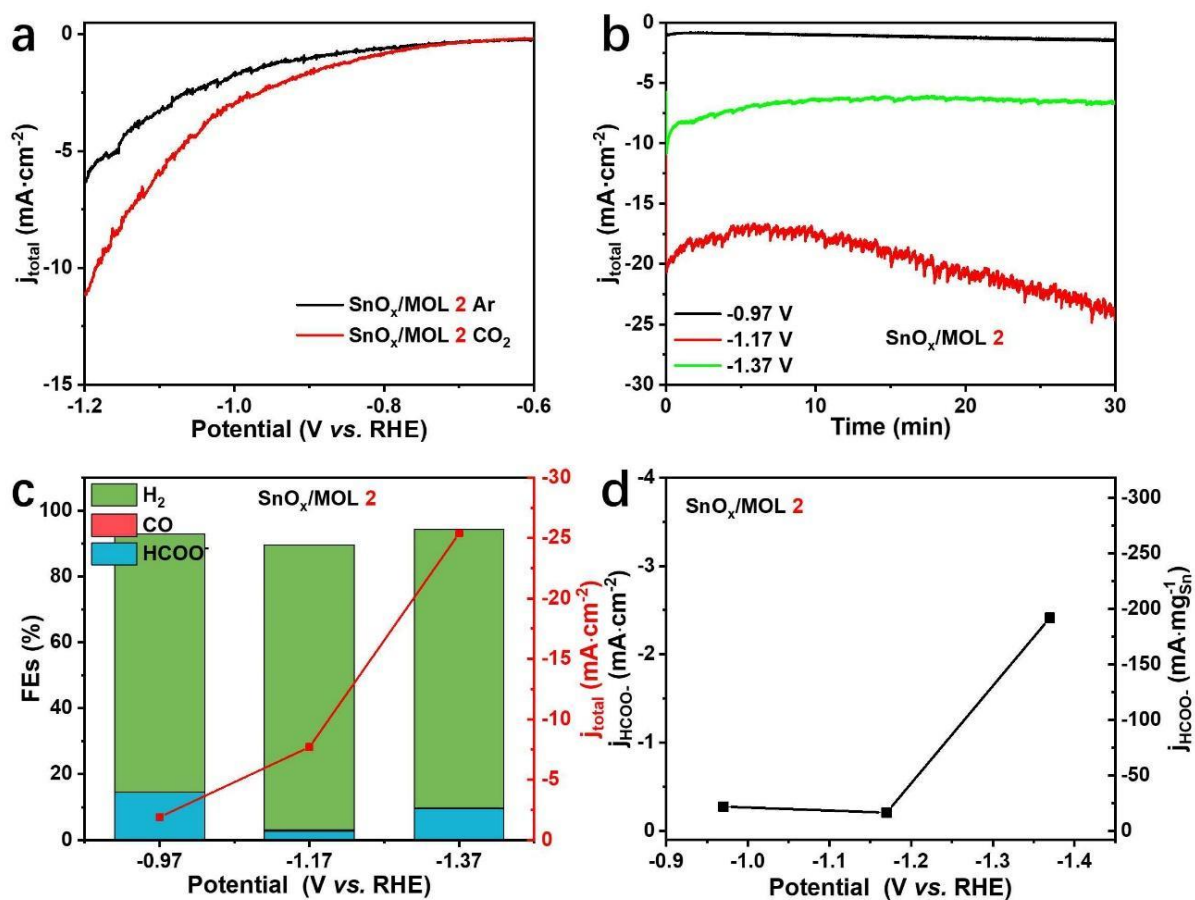


**Figure 7.4** (a) LSV curves under Ar/CO<sub>2</sub>, (b) chrono amperometric I-t plots, (c) Faradaic efficiencies, (d) formate partial current densities/formate partial current per mg Sn at different applied potentials over SnO<sub>x</sub>/MOL(2).

The promising morphology of SnO<sub>x</sub>/MOL(2) prompted us to examine its ECR performance (Figure 7.4). Firstly, the ECR activity was investigated by LSV tests (Figure 7.4a), in which the current difference between under CO<sub>2</sub> and under Ar indicates the activity in ECR reaction. Then, the actual activity was examined by chrono amperometric tests at different potentials. The catalyst only showed minimal activity towards formate, regardless of the faradaic efficiencies or the current density.

### 7.1.2.2 Sn<sup>4+</sup>/MOL(3)

The loading of Zr-TATB MOL with Sn can be directly achieved with Sn<sup>4+</sup>, due to its strong coordination interaction with the oxygenate groups of the Zr-TATB MOL. Once washed with water, the tetra-valent metal ion can undergo quick hydrolysis to form SnO<sub>x</sub> species. We could not resolve the type of the Sn compound in the PXRD pattern, for nearly no diffraction signal from Sn appeared, which could be due to the low amounts and very tiny nanoparticles (Figure 7.1b). However, the morphology of the Sn compounds can be observed in the TEM images (Figure 7.5), based on the contrast difference. The average diameter of these nanoparticles can be measured to 3.2 nm. The retention of the MOL structure can also be confirmed by TEM (Figure 7.5c). The method to get the ultrafine nanoparticle should also be extended to other tetra-valent elements, such as Ti, Ce.

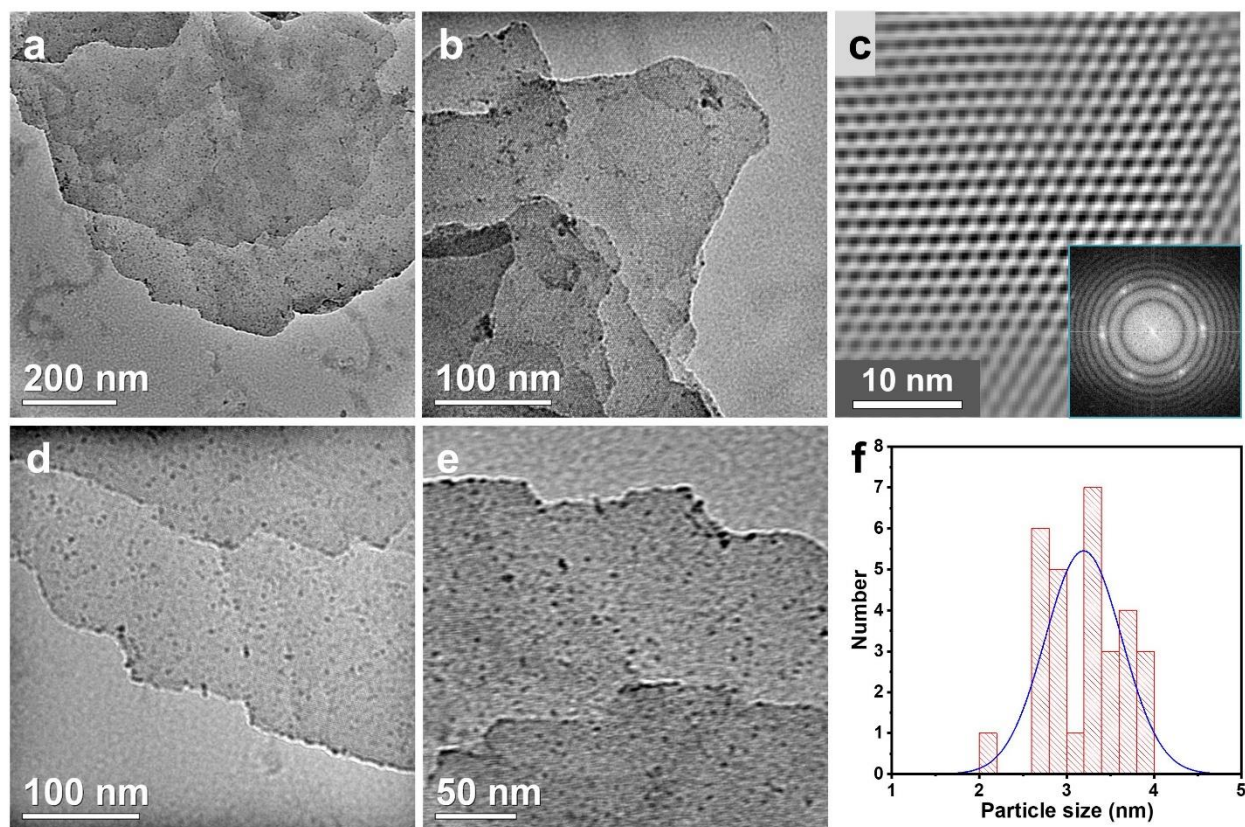


**Figure 7.5** (a-e) TEM images of Sn<sup>4+</sup>/MOL(3). (c) De-noised TEM image of the lattice of the MOL and FFT pattern of (d). (f) Particle size distribution diagram of the SnO<sub>x</sub> nanoparticles.

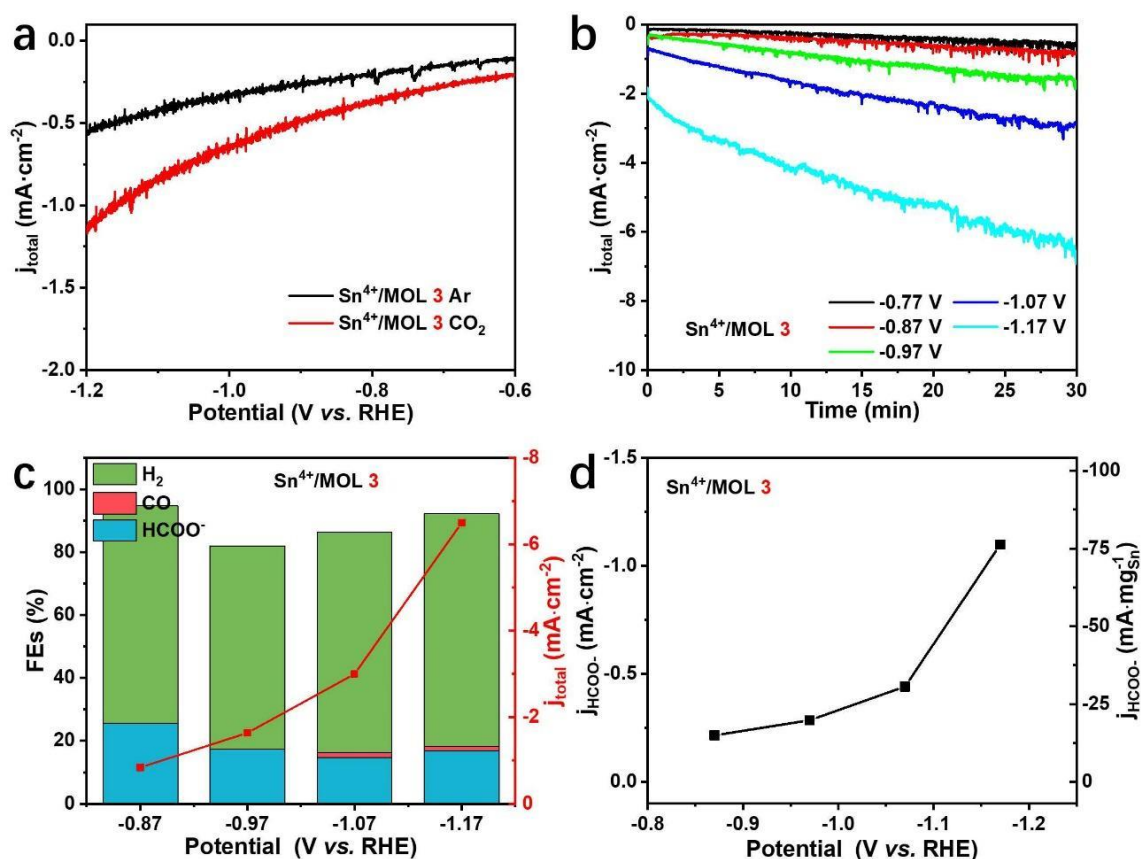


**Figure 7.6** (a) LSV curves under Ar/CO<sub>2</sub>, (b) chrono amperometric I-t plots, (c) Faradaic efficiencies, (d) formate partial current densities/formate partial current per mg Sn at different applied potentials over Sn<sup>4+</sup>/MOL(3).

The ECR performance was examined by LSV and chrono amperometric tests (**Figure 7.6**). The LSV curves show only minor differences between CO<sub>2</sub> and Ar atmospheres. Also, the FEs to formate are low, even though slightly better than SnO<sub>x</sub>/MOL(2). The partial current densities to formate are worse than SnO<sub>x</sub>/MOL(2), whether they are based on the geometrical area or mass of the Sn.

### 7.1.2.3 SnS<sub>2</sub>/MOL(4)

Besides the selectivity to formate, tin-based compounds also open up the possibility of CO, of which a classic example is SnS<sub>2</sub>.<sup>[120]</sup> The solvothermal treatment of a mixture of Zr-TATB MOL, SnCl<sub>4</sub>, and thioacetamide (TAA) in the DMF led to a brown powder, SnS<sub>2</sub>/MOL. The PXRD pattern of the sample is not so well matched with the SnS<sub>2</sub>, but this seems to be the best match (**Figure 7.1**). Furthermore, the Sn:S ratio was determined to 1:2.30 by ICP-AES, which also supports the formation of SnS<sub>2</sub> (**Table 10.3**).

The ECR activity was examined by LSV and chrono amperometric tests (**Figure 7.7**). The LSV curves exhibit apparent current differences between CO<sub>2</sub> and Ar atmosphere, indicating a good activity for the ECR reaction. However, the main product is still formate rather than CO (**Figure 7.7c**). The partial current densities to formate were not that good, similar to the SnO<sub>x</sub>/MOL(2)

related to the current per mg Sn.

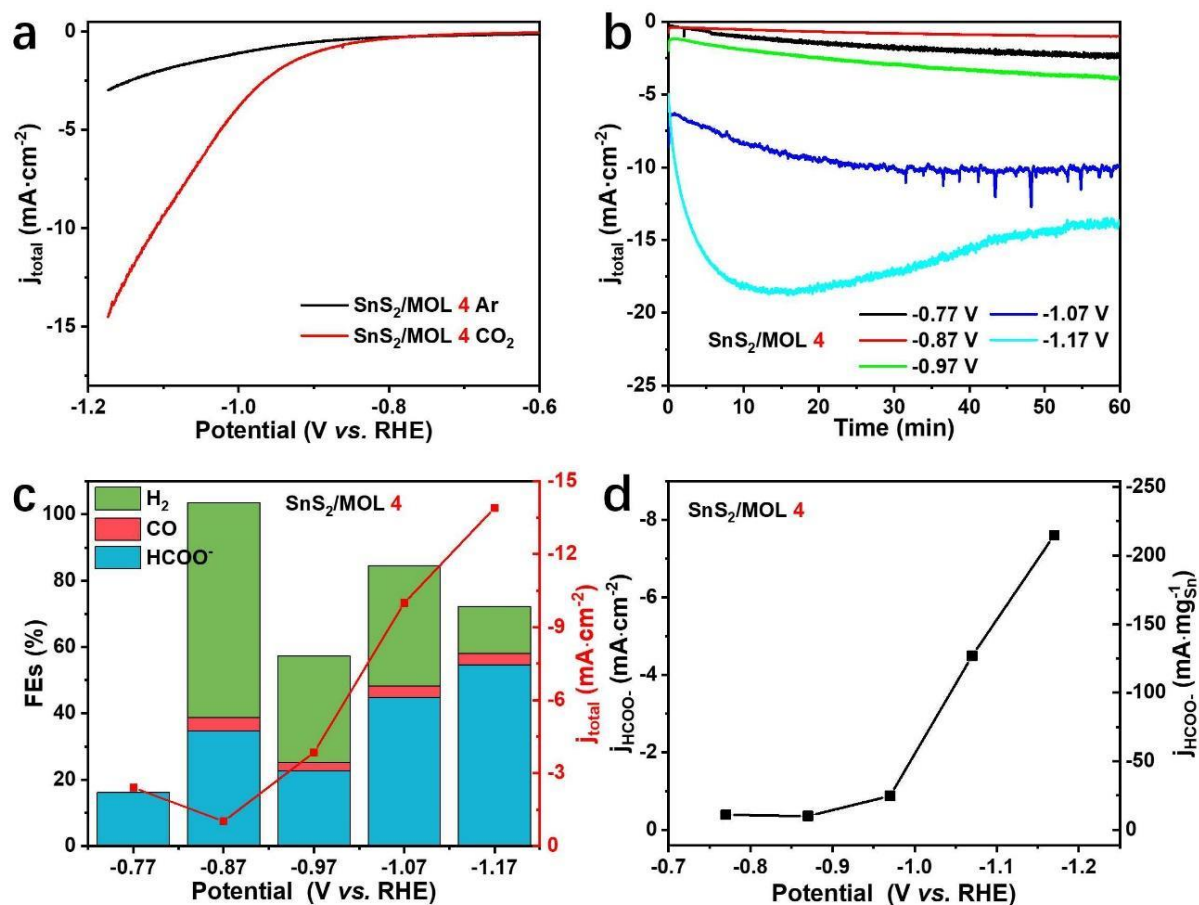


**Figure 7.7** (a) LSV curves under Ar/CO<sub>2</sub>, (b) chrono amperometric I-t plots, (c) Faradaic efficiencies, (d) formate partial current densities/formate partial current per mg Sn at different applied potentials over SnS<sub>2</sub>/MOL(4).

#### 7.1.2.4 SnO<sub>2</sub>/MOL(5)

The poor ECR performance of the above three Sn-based MOL composites encourages us to increase the loading of the Sn. We further increased the temperature of the solvothermal treatment from 85 °C to 160 °C, which led to a higher loading of 18.2 wt% by ICP-AES (Table 10.3). The appearance of additional diffraction peaks in the PXRD pattern proves that the crystal compound is SnO<sub>2</sub> (Figure 7.8). The chemical state can be verified by XPS (Figure 7.8). The absence of the Sn 5s signal (7.0 eV) allows to exclude the existence of metallic Sn. The lack of the Cl 2p signal (199.9 eV) allows to exclude the presence of Cl<sup>-</sup>, which means sufficient hydrolysis of the SnCl<sub>2</sub>. The binding energy of the Sn 3d<sub>5/2</sub> is 486.6 eV, slightly higher than the binding energy of the standard Sn 3d in SnO<sub>2</sub> (486.4 eV) (Figure 7.8c). The slightly higher binding energy can be attributed to the ultrafine particles, verified by TEM (Figure 7.9). Numerous heterogeneous nanoparticles can be found on the MOL based on the contrast difference. The average diameter of the SnO<sub>2</sub> was measured to 4.5 nm. Even at this harsh solvothermal treatment at 160 °C, the lattice structure remained intact, verified by PXRD and TEM (Figure 7.8a & 7.9e).

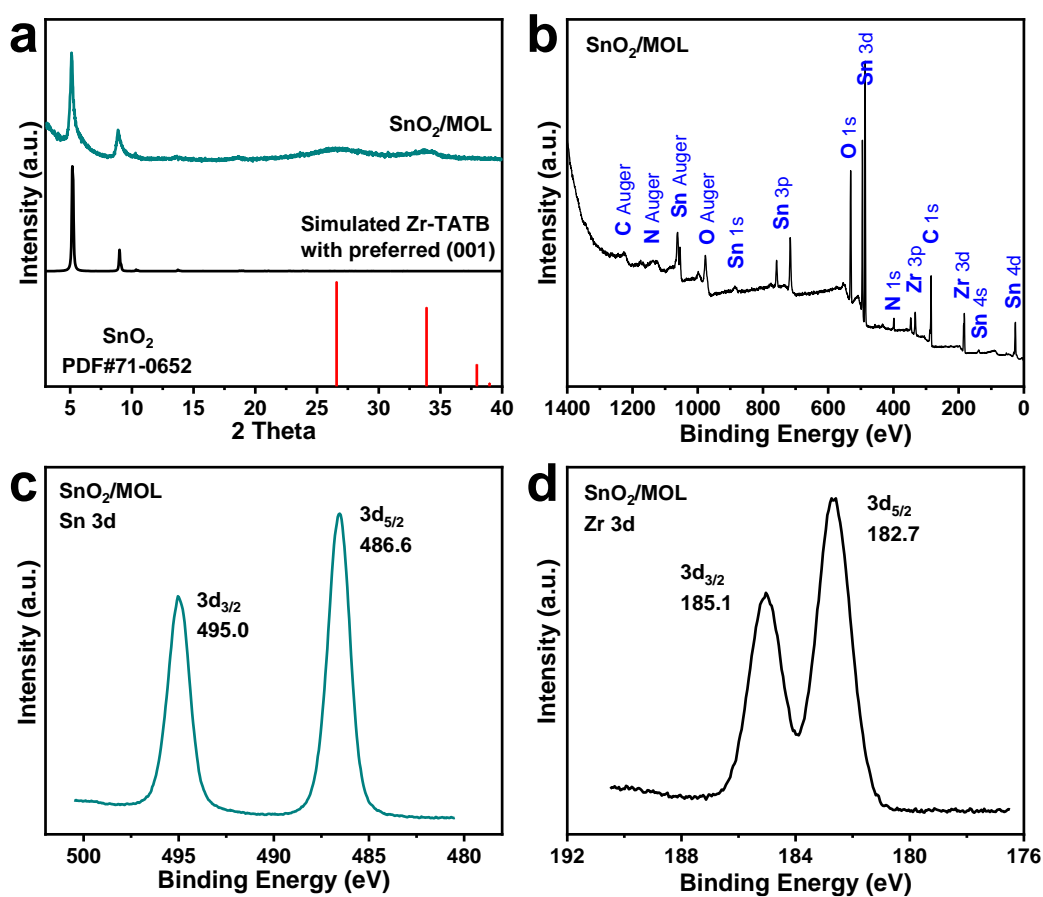


**Figure 7.8** (a) XRD patterns of standard SnO<sub>2</sub> (PDF#71-0652), simulated Zr-TATB MOL, and SnO<sub>2</sub>/MOL(5). (b) XPS full spectrum, (c) XPS Sn 3d spectrum and (d) XPS Zr 3d spectrum of SnO<sub>2</sub>/MOL(5).

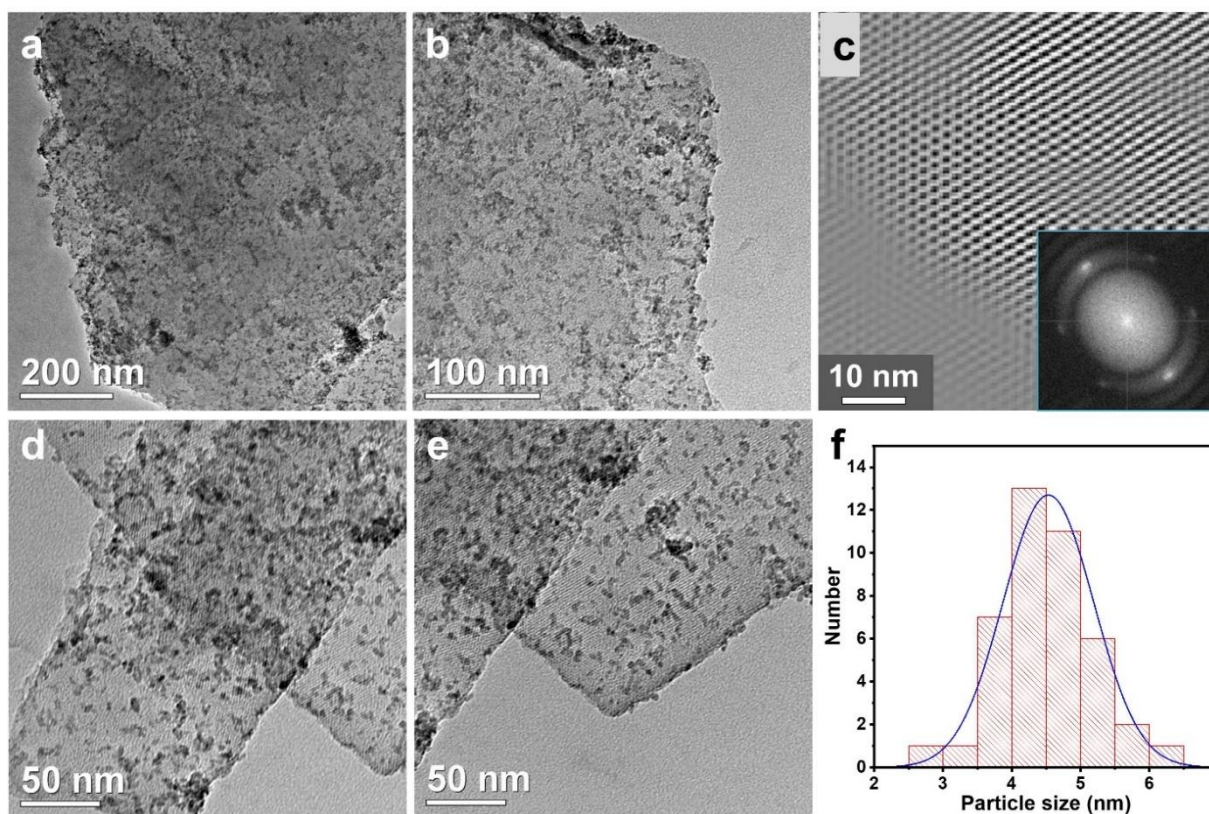


**Figure 7.9** (a-e) TEM images of SnO<sub>2</sub>/MOL(5). (c) De-noised TEM image of the lattice of the MOL and FFT pattern of (e). (f) Particle size distribution diagram of the SnO<sub>2</sub> nanoparticles.

The ECR activity was first investigated by LSV tests under Ar and CO<sub>2</sub> (Figure 7.10a). The apparent current difference between under CO<sub>2</sub> and under Ar indicates its activity in the ECR reaction, even though it is much less active than Bi<sub>2</sub>O<sub>3</sub>/MOL (Figure 6.6a). The actual ECR activities were evaluated by chrono amperometric tests at different potentials (Figure 7.10b). The SnO<sub>2</sub>/MOL can maintain FEs of around 40% towards formate at the potentials ranging from -0.87 V to -1.17 V vs. RHE. The ECR performance is largely similar to that of other Sn oxide based composites (within 200 mA·mg<sub>Sn</sub><sup>-1</sup>) in terms of partial current to formate per mg Sn (Figure 7.10d).

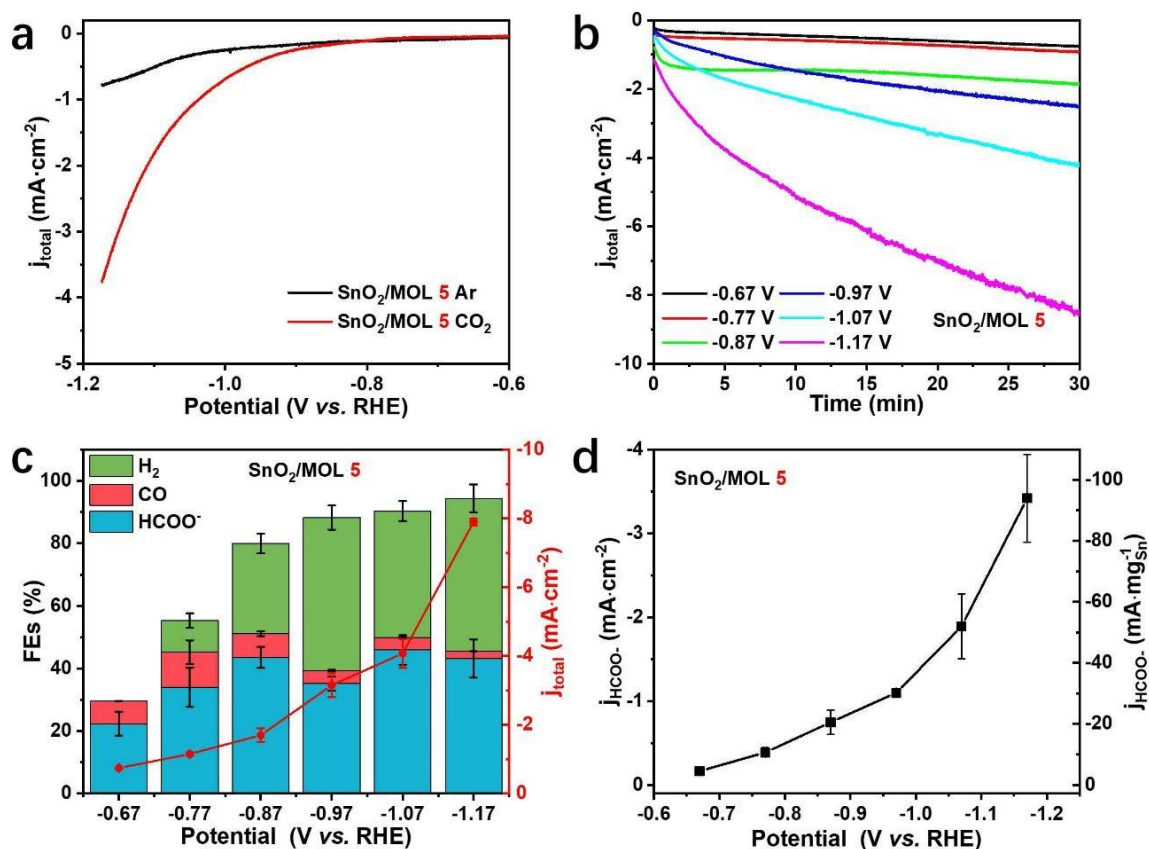


**Figure 7.10** (a) LSV curves under Ar/CO<sub>2</sub>, (b) chrono amperometric I-t plots, (c) Faradaic efficiencies, (d) formate partial current densities/formate partial current per mg Sn at different applied potentials over SnO<sub>2</sub>/MOL(5).

## 7.2 MOL composites with indium-based active sites

### 7.2.1 Synthesis strategy of MOL composites with different Indium species

Besides tin- and bismuth-based active sites, indium-based active sites are also widely investigated to produce formate in ECR reactions. The active sites are also based on redox-active surface oxides or alkaline oxides.<sup>[125]</sup> Constructing nanosized indium oxide could open up new possibilities to increase the proportion of the surface oxide shell.

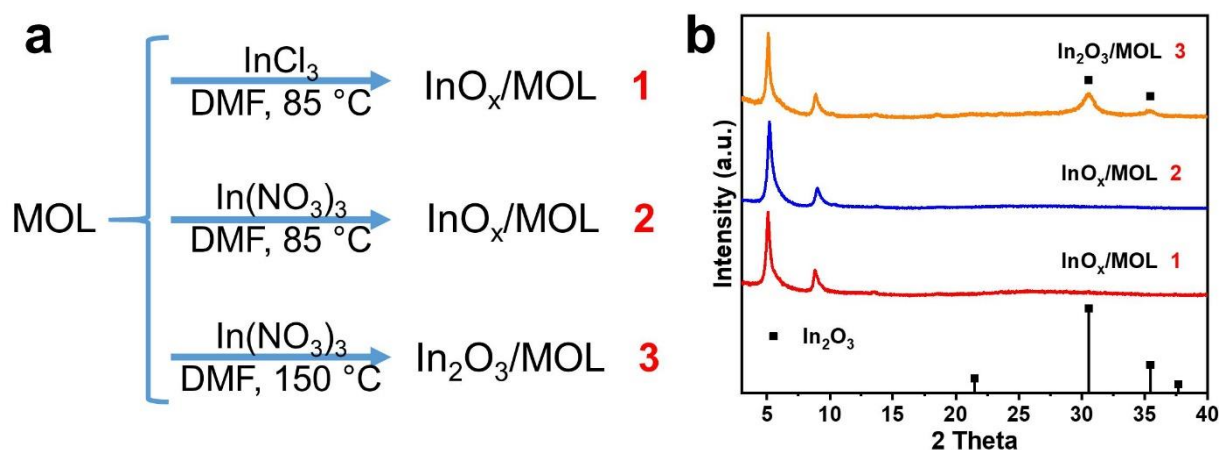


**Figure 7.11** (a) Synthesis scheme of diverse MOL composites with different In species. (b) Corresponding PXRD patterns of the MOL composites after the post-modifications.

The species and morphologies of the Indium compounds are not as complex as bismuth species, similar to Sn (Figure 7.11). The In precursors are mainly one valence state In(III) in  $(\text{NO}_3)_3$ , and  $\text{InCl}_3$  (Chapter 3.3.3.2). The retention of the crystal structure of the MOL can be proven by the PXRD (Figure 7.11b). The exact example will be discussed in the following chapters.

## 7.2.2 Characterizations and ECR performance of indium-based MOL composites

### 7.2.2.1 $\text{InO}_x/\text{MOL}(1)$

$\text{InO}_x/\text{MOL}(1)$  was prepared by the solvothermal treatment of Zr-TATB MOL using  $\text{InCl}_3$  as a precursor. The presence of the indium species is nearly invisible in the PXRD pattern (Figure 7.11b), which can be attributed to the ultrasmall nanoparticles and very low loading. Through ICP-AES, the metal content was measured to be 5.04 wt% (Table 10.3). The actual morphology was characterized by TEM, through which very short nanowires/nanorods and nanoparticles can be distinguished by the contrast difference (Figure 7.12).

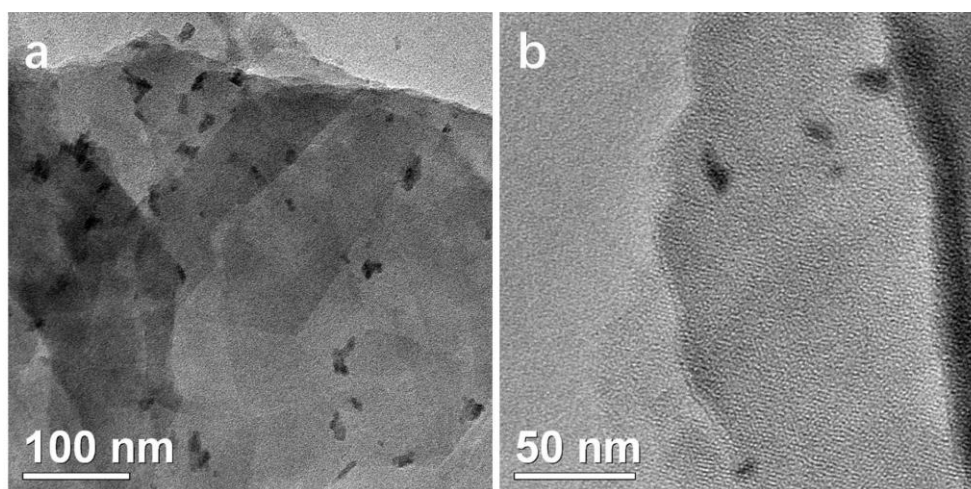


**Figure 7.12** (a,b) TEM images of  $\text{InO}_x/\text{MOL}(1)$ .

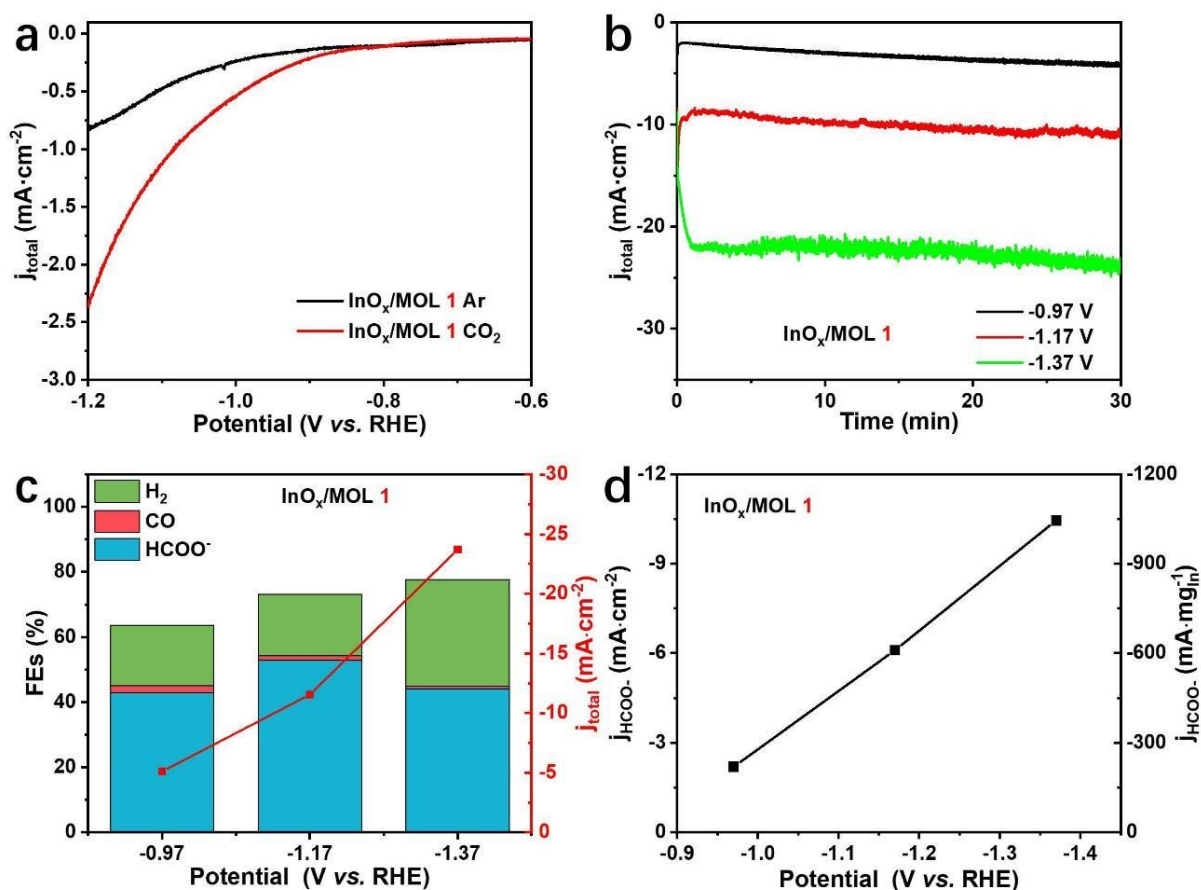


**Figure 7.13** (a) LSV curves under Ar/CO<sub>2</sub>, (b) chrono amperometric I-t plots, (c) Faradaic efficiencies, (d) formate partial current densities/formate partial current per mg In at different applied potentials over InO<sub>x</sub>/MOL(1).

The ECR performance was examined by LSV measurements and chrono amperometric tests (Figure 7.13a). The LSV curves exhibit a significant current difference between under CO<sub>2</sub> and under Ar atmosphere, implying a good activity towards ECR reaction. The chrono amperometric test (Figure 7.13) shows that InO<sub>x</sub>/MOL(1) can maintain FEs towards formate of over 50% in the potential range from -0.97 V to -1.37 V vs. RHE. The partial current density of formate can reach a maximum of 10.45 mA·cm<sup>-2</sup>, corresponding to 1045 mA·mg<sub>In</sub><sup>-1</sup>. Regarding the FEs and current density, this performance was slightly worse than Bi<sub>2</sub>O<sub>3</sub>/MOL, while apparently better than the Sn-based composites.

#### 7.2.2.2 InO<sub>x</sub>/MOL(2)

InO<sub>x</sub>/MOL(2) was prepared by the solvothermal treatment of Zr-TATB MOL using In(NO<sub>3</sub>)<sub>3</sub> as a precursor. The information of the Indium species is nearly invisible from the PXRD (Figure 7.11b), which can be again attributed to the ultrasmall nanoparticles and very low loading. The metal content was measured by ICP-AES to 5.87 wt% (Table 10.3). The actual morphology was characterized by TEM, through which thin nanowires can be observed by the contrast difference (Figure 7.14).

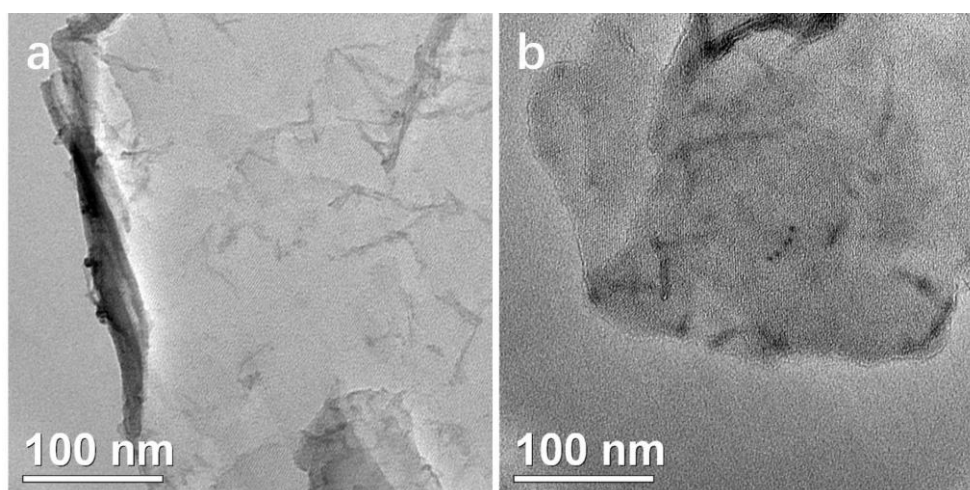


**Figure 7.14** (a,b) TEM images of InO<sub>x</sub>/MOL(2).

The ECR performance was examined by LSV measurements and chrono amperometric tests (Figure 7.15a). The LSV curves exhibit a slight current difference between under CO<sub>2</sub> and under Ar atmospheres, only implying a small activity in ECR reaction. The chrono amperometric test (Figure 7.15) shows that InO<sub>x</sub>/MOL(2) can only reach FEs of around 50% at potentials ranging from -0.87 V to -1.17 V vs. RHE. The partial current density of formate can reach a maximum of 1.93 mA·cm<sup>-2</sup>, corresponding to 164 mA·mg<sub>In</sub><sup>-1</sup>.

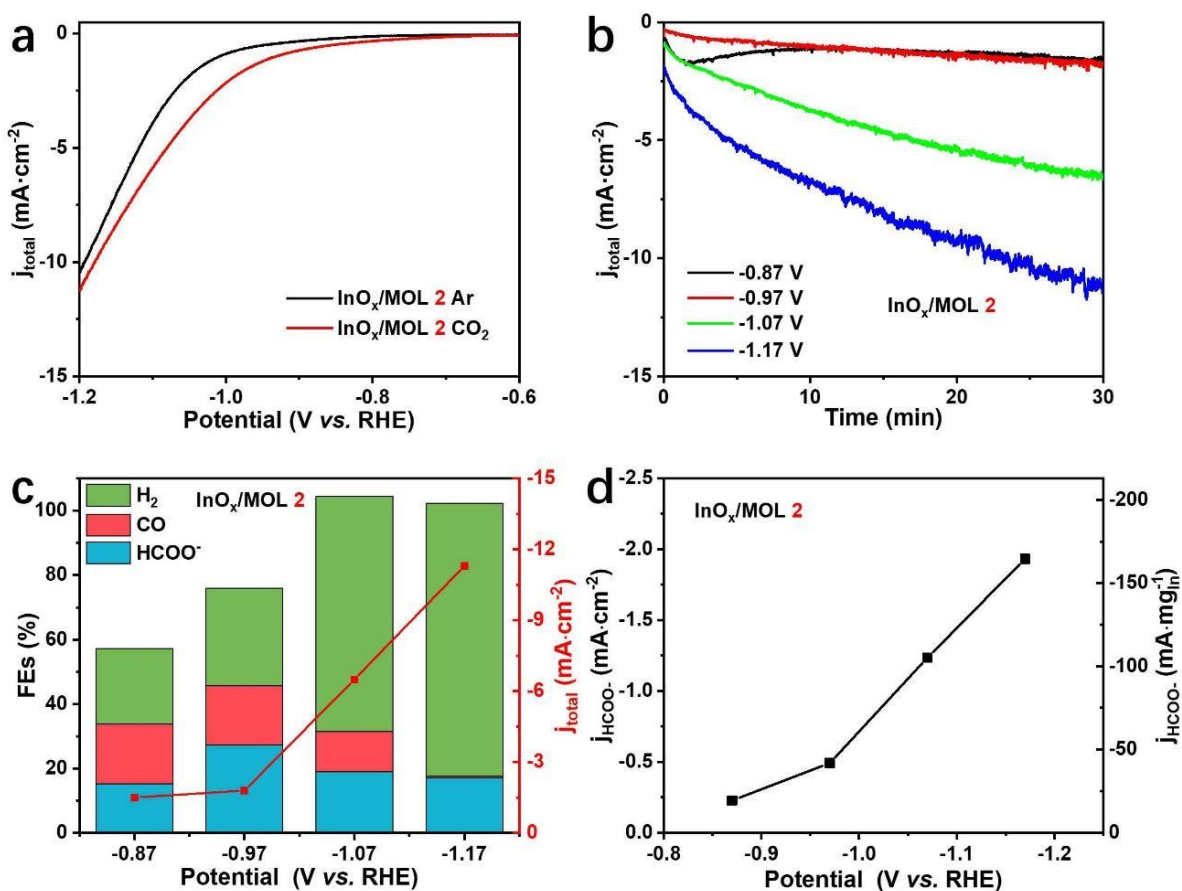


**Figure 7.15** (a) LSV curves under Ar/CO<sub>2</sub>, (b) chrono amperometric I-t plots, (c) Faradaic efficiencies, (d) formate partial current densities/formate partial current per mg In at different applied potentials over InO<sub>x</sub>/MOL(2).

7.2.2.3 In<sub>2</sub>O<sub>3</sub>/MOL(3)

To promote the performance of the In-based composites, we decided to increase the loading by increasing the temperature of the solvothermal treatment of Zr-TATB MOL from 85 °C to 160 °C. The metal content of In<sub>2</sub>O<sub>3</sub>/MOL(3) was determined by ICP-AES to 13.2 wt% (Table 10.3). The presence of the indium species is clearly visible in the PXRD pattern (Figure 7.16b) and can be attributed to the crystalline In<sub>2</sub>O<sub>3</sub>. The chemical state can be verified by XPS (Figure 7.16). The absence of the In 5p signal (~1.0 eV) allows to exclude the existence of the metallic In. The binding energy of the In 3d<sub>5/2</sub> is 444.3 eV, corresponding to In<sub>2</sub>O<sub>3</sub> (Figure 7.16c). The morphology of the indium species was characterized by TEM (Figure 7.17). Tiny nanoparticles with an average diameter of 6.2 nm can be observed, in accordance to the very tiny and broad peaks in the PXRD pattern. These nanoparticles can further aggregate into larger units, having a size of around 30-50 nm. Despite the harsh solvothermal treatment, the lattice structure can be maintained, as verified by PXRD and TEM.

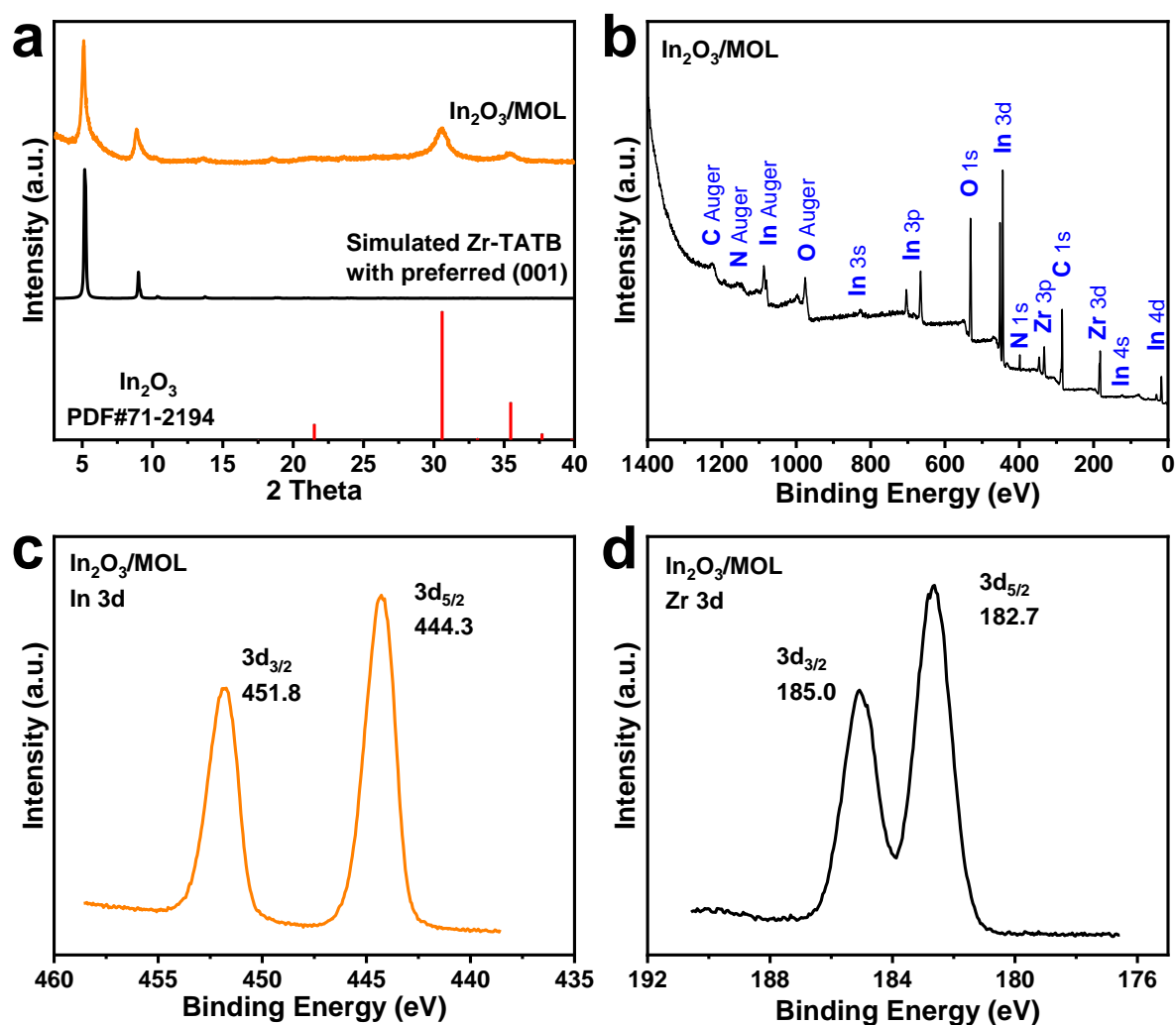


**Figure 7.16** (a) PXRD patterns of standard In<sub>2</sub>O<sub>3</sub> (PDF#71-2194), simulated Zr-TATB MOL, and In<sub>2</sub>O<sub>3</sub>/MOL(3). (b) XPS full spectrum, (c) XPS In 3d spectrum and (d) XPS Zr 3d spectrum of In<sub>2</sub>O<sub>3</sub>/MOL(3).

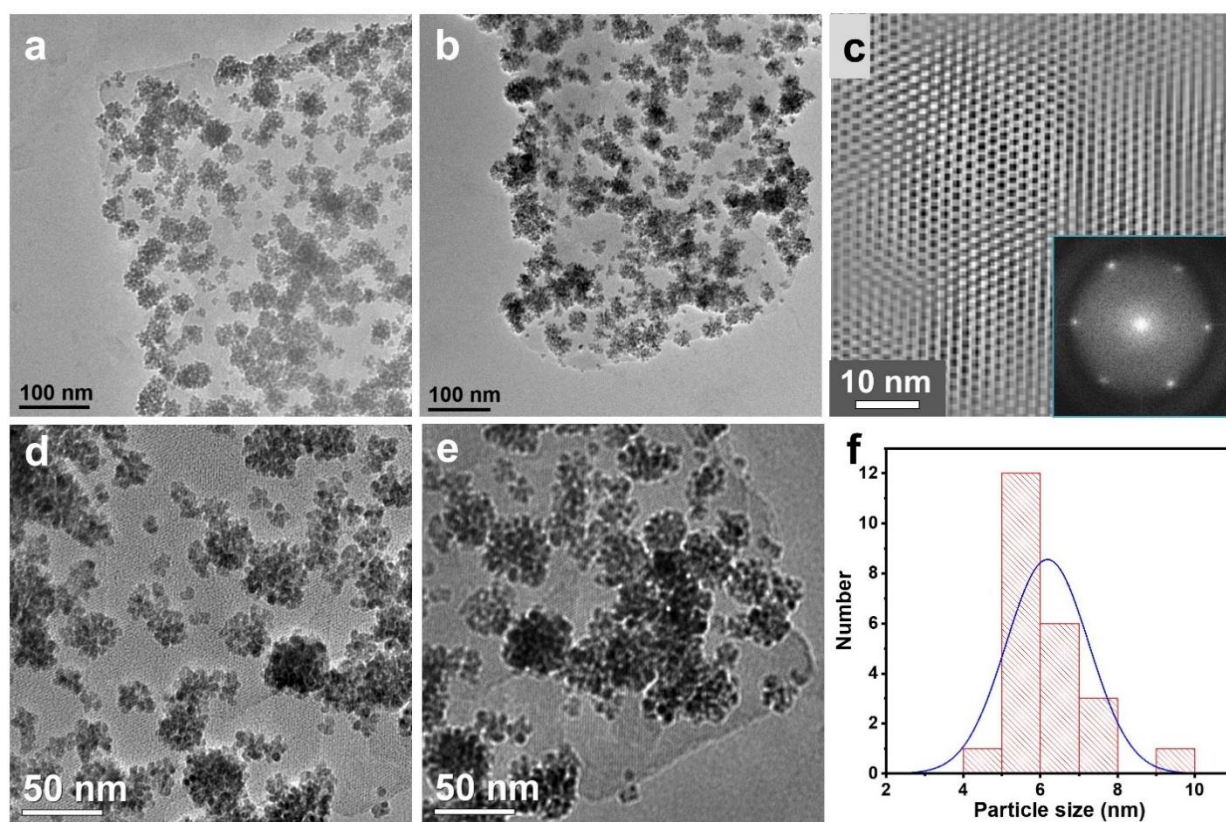


**Figure 7.17** (a-e) TEM images of In<sub>2</sub>O<sub>3</sub>/MOL(3). (c) De-noised TEM image of the lattice of the MOL and FFT pattern of (d). (f) Particle size distribution diagram of the In<sub>2</sub>O<sub>3</sub> nanoparticles.

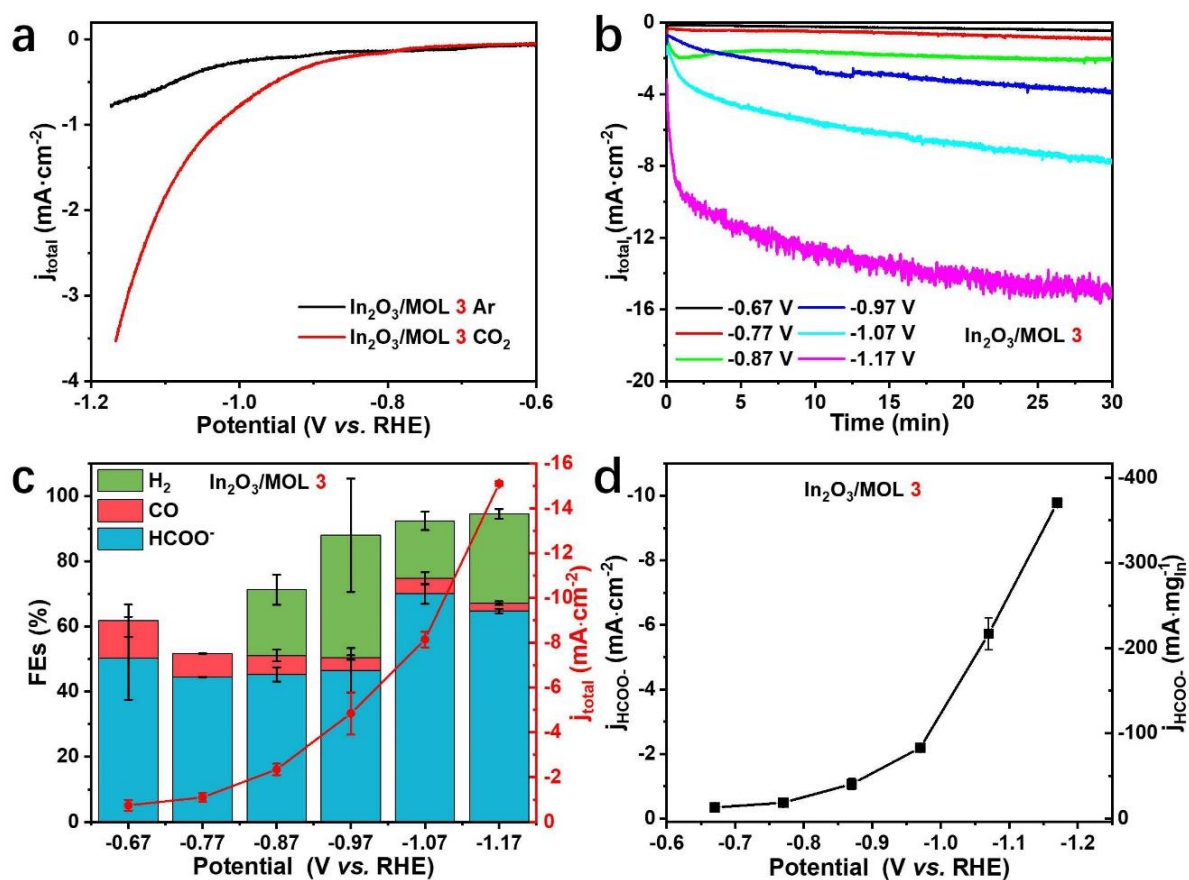


**Figure 7.18** (a) LSV curves under Ar/CO<sub>2</sub>, (b) chrono amperometric I-t plots, (c) Faradaic efficiencies, (d) formate partial current densities/formate partial current per mg In at different applied potentials over In<sub>2</sub>O<sub>3</sub>/MOL(3).

Firstly, the ECR activity was investigated by LSV tests under Ar and CO<sub>2</sub> (Figure 7.18a). The significant difference in current responses under CO<sub>2</sub> and under Ar atmosphere in LSV tests indicates the activity for ECR reaction, even though it is not as large as for the Bi<sub>2</sub>O<sub>3</sub>/MOL (Figure 6.6a). The complete ECR performances were tested by chrono amperometric tests at different potentials (Figure 7.18b). The In<sub>2</sub>O<sub>3</sub>/MOL(3) could maintain FEs towards formate of over 50% at potentials ranging from -0.67 V to -1.17 V vs. RHE. The best faradaic efficiency was 70% at a potential of -1.07 V vs. RHE. The current density of In<sub>2</sub>O<sub>3</sub>/MOL(3) at most reached 9.78 mA·cm<sup>-2</sup>, corresponding to 370 mA·mg<sub>In</sub><sup>-1</sup>. The ECR performance is apparently better than that of Sn-based composites, whereas not better than the performance of Bi-based composites.

## 7.3 MOL composites with other active sites

### 7.3.1 Antimony (Sb)

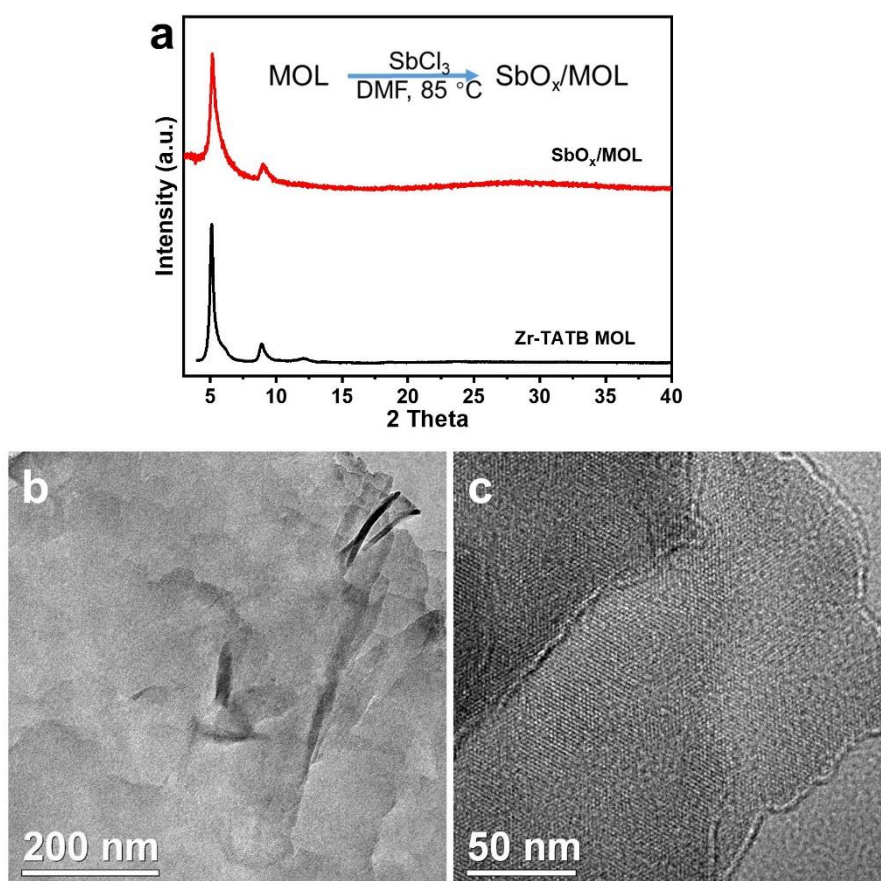


**Figure 7.19** (a) PXRD patterns of Zr-TATB MOL and SbO<sub>x</sub>/MOL. (b,c) TEM images of SbO<sub>x</sub>/MOL

Besides the typical formate catalysts (Sn, In, and Bi), antimony (Sb) is also a well-known active site of formate generation. Antimony was tried to be loaded as Sb<sup>3+</sup> on the Zr-TATB MOL, through solvothermal treatment with SbCl<sub>3</sub> (Chapter 3.3.3.3). The metal content was measured by ICP-

AES to 1.94 wt% (Table 10.3). We could not get further information from the PXRD pattern and TEM image (Figure 7.19), which could be due to the ultrasmall Sb species or even single atoms. Considering the rather mild synthesis environment (no strongly reduction or high alkaline), the state can be speculated to be amorphous SbO<sub>x</sub>. The retention of the MOL structure can be confirmed by the PXRD pattern and TEM image (Figure 7.19).

The ECR performance was examined by LSV measurements and chrono amperometric tests (Figure 7.20a). The LSV curves exhibit apparent current differences between under CO<sub>2</sub> and under Ar atmosphere, implying the possibility of ECR reaction. The chrono amperometric test (Figure 7.20) showed that SbO<sub>x</sub>/MOL is only slightly active for ECR reaction, with the best FE being 11.8 % at -1.27 V vs.RHE. The partial current density of formate only reached values up to 0.4 mA·cm<sup>-2</sup> related to the geometric area, corresponding to 103 mA·mg<sub>Sb</sub><sup>-1</sup>. The poor ECR activity kept us from proving the catalyst any further.

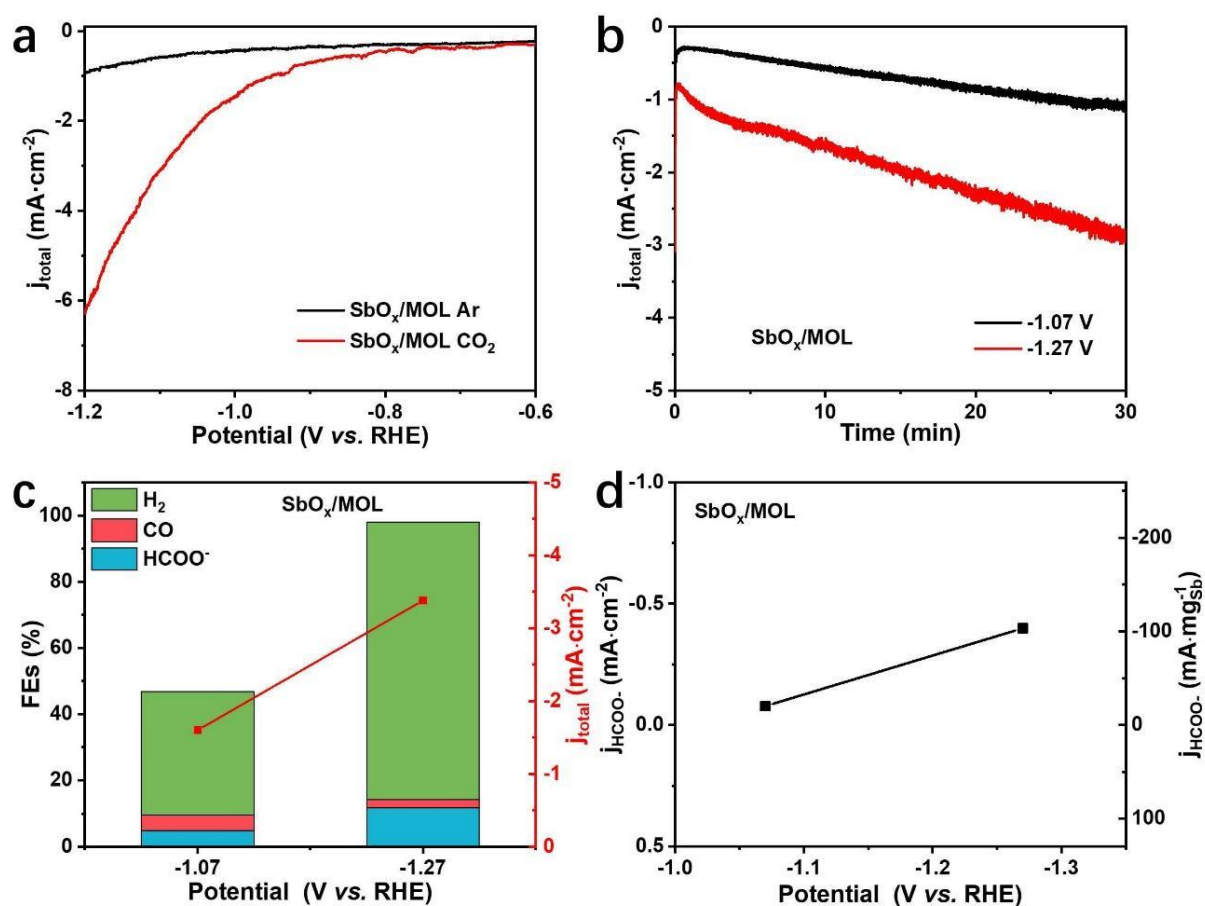


**Figure 7.20** (a) LSV curves under Ar/CO<sub>2</sub>, (b) chrono amperometric I-t plots, (c) Faradaic efficiencies, (d) formate partial current densities/formate partial current per mg Sb at different applied potentials over SbO<sub>x</sub>/MOL.

### 7.3.2 Copper (Cu)

Copper is something special for ECR reaction, because it is the only site that produces C<sub>2+</sub>

products. Cu modification can be obtained by a facile solvothermal treatment of Zr-TATB MOL with Cu(NO<sub>3</sub>)<sub>2</sub>. we considered getting a stable Cu-based composite by reacting with I<sup>-</sup> to form CuI (**Chapter 3.3.3.4**). After the modification, the color of the powder turned from blue to green, which can not be washed away by water. The successful loading can also be confirmed by ICP-AES, giving a Cu content of 6.49 wt% (**Table 10.3**). Unfortunately, we could not resolve the structural state of the Cu species by PXRD and TEM (**Figure 7.21**). The retention of the MOL structure could be confirmed by PXRD and TEM (**Figure 7.21**).

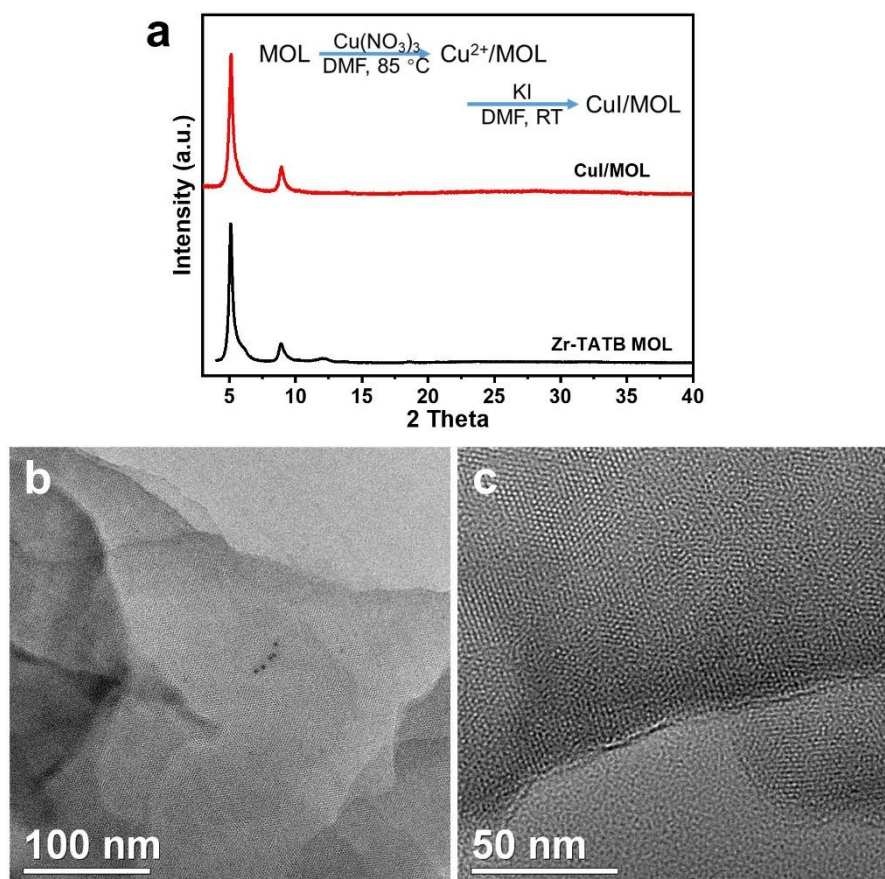


**Figure 7.21** (a) PXRD patterns of Zr-TATB MOL and CuI/MOL. (b,c) TEM images of CuI/MOL. The black dots in the center of the image are the residue from the subjective lens, not from the sample.

The ECR performance was examined by LSV measurements and chrono amperometric tests (**Figure 7.22**). The LSV curves exhibit apparent current differences between CO<sub>2</sub> and Ar atmosphere, implying the possibility of ECR reaction. The chrono amperometric test (**Figure 7.22b-d**) shows that CuI/MOL has a very limited selectivity to formate (18.7 % at -0.87 V vs. RHE) without detecting C<sub>2+</sub> products. The poor total Faradaic efficiency could be due to the very low current response, which is a challenge for product quantification. Limited by the time, no further investigations were carried out. Further optimization could bring out the special role of Cu.

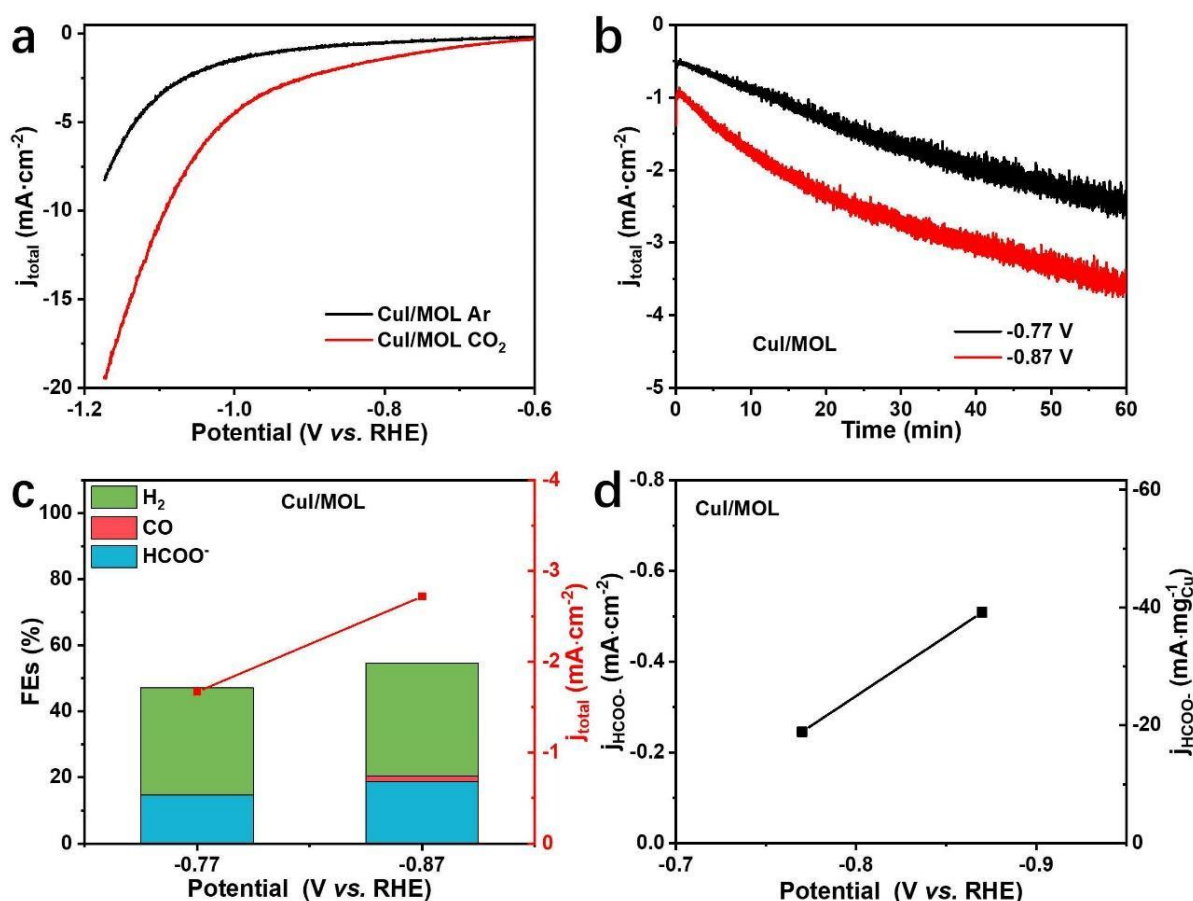


**Figure 7.22** (a) LSV curves under Ar/CO<sub>2</sub>, (b) chrono amperometric I-t plots, (c) Faradaic efficiencies, (d) formate partial current densities/formate partial current per mg Cu at different applied potentials over CuI/MOL.

### 7.3.3 Palladium (Pd)

This post-modification could also achieve loading noble metal sites. Palladium is also an active site to produce CO or formate, which is discussed in the introduction chapter (**Chapter 1.2.3.4**). Considering the oxidizing property of most noble metals, metal ions could be already reduced during the post-modification when using DMF as solvent (**Chapter 3.3.3.5**). The appearance of metallic Pd can be verified by PXRD and TEM (**Figure 7.23**). However, the Pd dispersion is not good, due to an average diameter of 20 nm.

The ECR performance was examined by LSV and chrono amperometric tests (**Figure 7.24**). The LSV curves exhibit a slight current difference between under CO<sub>2</sub> under Ar atmosphere, implying the possibility of ECR reaction. The chrono amperometric test shows CuI/MOL has a very limited selectivity to CO (30.2 % at -1.07 V vs. RHE). The best current density for CO can reach  $1.42 \text{ mA}\cdot\text{cm}^{-2}$ , corresponding to  $65.0 \text{ mA}\cdot\text{mg}_{\text{Pd}}^{-1}$ . This is a good start to further develop Pd/MOL catalyst. However, due to the limited time during my doctorate, the catalyst was not further pursued.

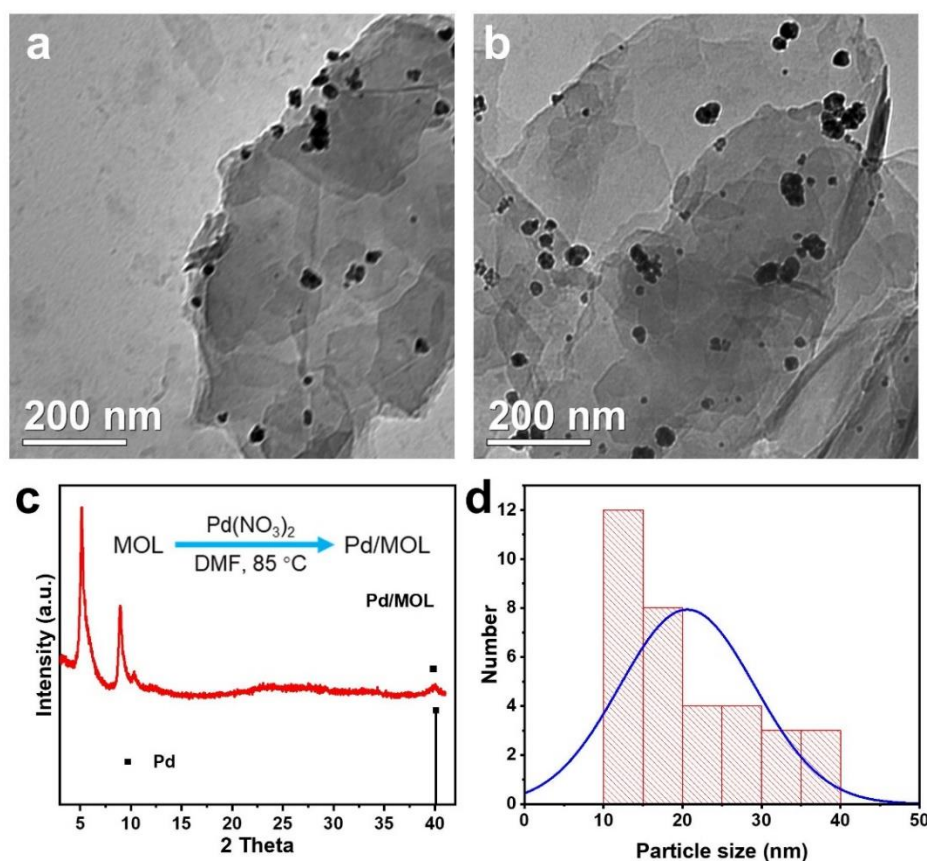


**Figure 7.23** (a,b) TEM images of Pd/MOL. (c) PXRD patterns of the as-synthesized Pd/MOL and standard Pd (PDF#46-1043). (d) Particle size distribution diagram of the Pd nanoparticles.

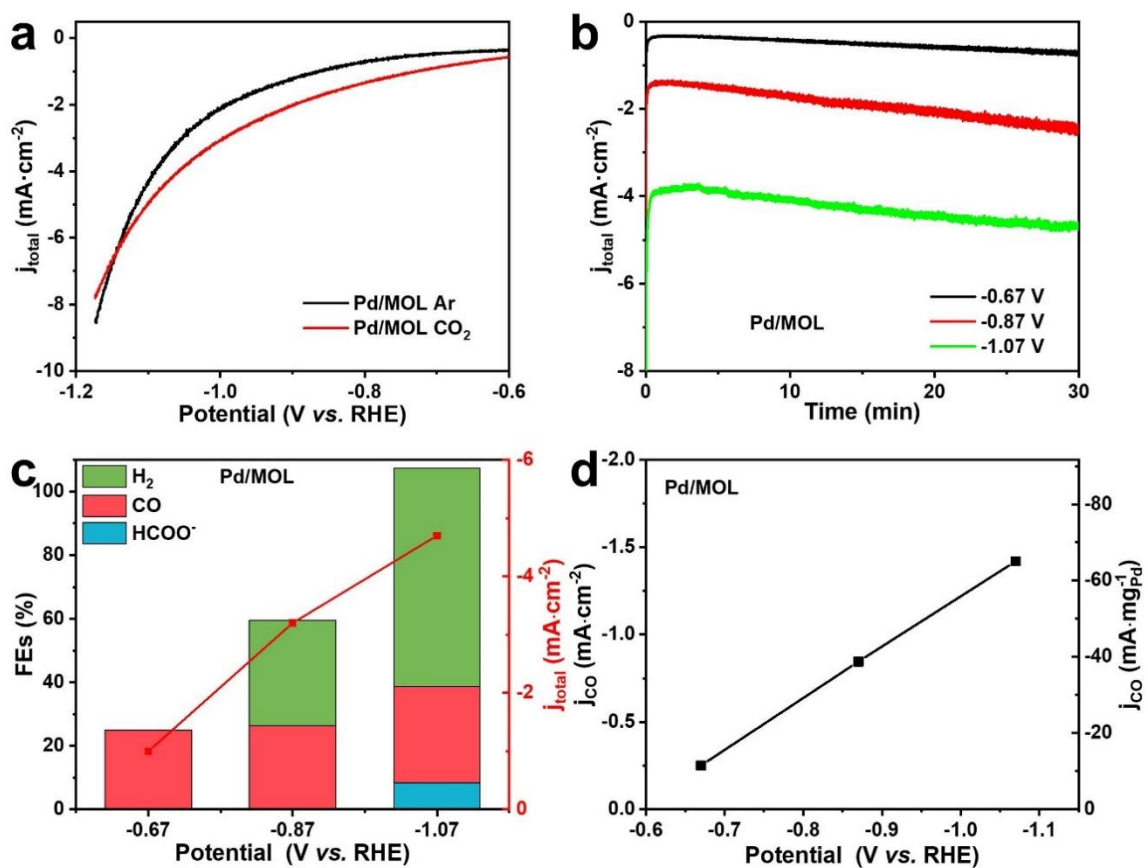


**Figure 7.24** (a) LSV curves under Ar/CO<sub>2</sub>, (b) chrono amperometric I-t plots, (c) Faradaic efficiencies, (d) CO partial current densities/CO partial current per mg Pd at different applied potentials over Pd/MOL.

## 7.4 Comparison of MOLs composites of different active metal sites

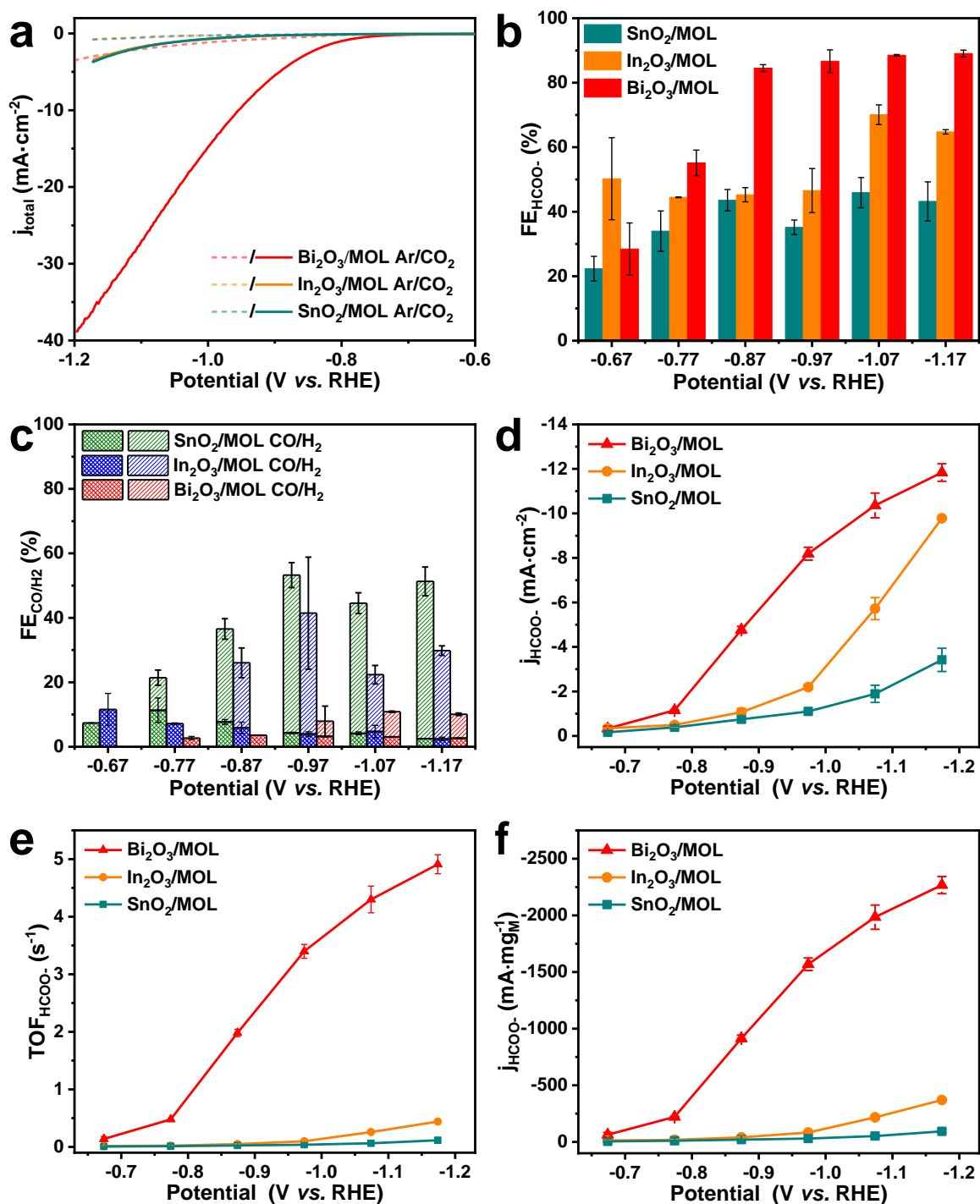


**Figure 7.25** (a) LSV curves under Ar/CO<sub>2</sub>, (b,c) Faradaic efficiencies, (d) formate partial current densities, (e) formate partial current per mg Bi, (f) TOF (s<sup>-1</sup>) towards 1/2 HCOO<sup>-</sup> at different applied potentials over Bi<sub>2</sub>O<sub>3</sub>/MOL(3), In<sub>2</sub>O<sub>3</sub>/MOL(3) and SnO<sub>2</sub>/MOL(5).

Herein, an overall comparison of all the metal/MOLs regarding their ECR performance is given in [Table 10.6](#). Bi, In and Sn based MOL composites exhibited good ECR activities to formate. Generally, Bi/MOL has the best performance, followed by In/MOL, and Sn/MOL being the last one. Specific comparisons of the best Metal/MOL composites are given in [Figure 7.25](#). In a word,

the type of metal species is found to play a key role in determining the ECR activities.

## **7.5 Summary of ECR performance of MOL composites**

In this chapter, we have presented multiple examples to construct MOL composites with different metal species, indicating the high universality of the concept. Generally, ultrafine nanoparticles can be loaded on the MOL without adopting capping agents. The morphology and performance depended strongly on the synthesis method, which inspired us to optimize the synthesis methods to get novel catalysts.

Concerning the ECR performance, we further confirmed the superior performance of bismuth-based composites. The type of the metal species is the key to getting a good formate's ECR performance. Bismuth-based MOL composites gave the best performance towards formate, whether based on the FEs or current response.

The possibilities for getting other ECR products have been demonstrated by choosing corresponding active sites. Therefore, even though this has not been sufficiently optimized to date, it is a promising strategy for further developing MOL-based composites for the ECR reaction.

## 8 | Summary and Outlook

A highly efficient electrocatalytic CO<sub>2</sub> reduction to formate by Bi<sub>2</sub>O<sub>3</sub>/MOL was achieved in this thesis.

A free-standing metal-organic layer (MOL) with a *kgd* lattice was constructed based on Zr<sub>6</sub>-oxo clusters and triazine-based tridentate linkers, the latter being used for the first time for MOL construction. Their good stability and fully exposed surface area, combined with abundant anchoring sites, make MOLs an ideal platform for constructing composites for electrocatalysis. Taking Bi as a representative, uniform Bi<sub>2</sub>O<sub>3</sub> nanowires can be well dispersed onto the MOLs by a facile post-modification strategy. The defined structure and the modification mechanism were elucidated by electron microscopy. Furthermore, a series of MOL composites loaded with diverse guest species was constructed based on this modification principle, highlighting the universality and the superiority of adopting MOLs as 2D templates.

The ECR performances of these MOL composites were systematically investigated. Strikingly, Bi<sub>2</sub>O<sub>3</sub>/MOL possessed a superior ECR performance towards formate in an H-type cell, exhibiting the highest formate partial current density of 2.3 A·mg<sub>Bi</sub><sup>-1</sup>, Faradaic efficiencies towards formate above 85% in a wide potential range between -0.87 and -1.17 V (vs. RHE), and long-term durabilities of over 22 h at -0.97 V (vs. RHE). By comparing 2D-MOL, 3D-MOF (UiO-66) and conductive carbon (acetylene black), the superiority of MOL composites could be demonstrated. To further improve the performance to industrially relevant level, gas diffusion electrodes (GDEs) were used, which opened up an impressive formate current density of over 300 mA·cm<sup>-2</sup>. Whether using carbon paper in the H-type cell or GDEs, Bi<sub>2</sub>O<sub>3</sub>/MOL exhibited the best activities among all MOFs used in ECR reactions, highlighting the superiority and significance of the concept of MOL composites for the ECR reaction. This research demonstrates the great potential of MOL based composites as electrocatalysts and encourages further exploration of highly tunable MOLs for catalytic studies.

Even though significant progress has already been made, the following shortcomings and perspectives must be considered in future work:

1. The support effect of MOL, i.e. its synergistic effect with the guest catalytic sites, has not yet been investigated. Taking Bi<sub>2</sub>O<sub>3</sub>/MOL as an example, high-resolution electron microscopy shows

that the ultras-small  $\text{Bi}_2\text{O}_3$  nanowires may have lattice distortions and are not the typical  $\beta\text{-Bi}_2\text{O}_3$  crystals. Therefore, its effect on the catalytic performance remains unknown. Moreover, it is unclear whether multiple hydroxyl sites of the  $\text{Zr}_6\text{-oxo}$  cluster can synergistically promote the formation and stabilization of intermediates. Theoretical computations could provide clues here.

2. We have not yet achieved control over other ECR products by tuning the MOL composite. For example, optimization of Pd/MOL and Cu/MOL could yield high selectivities towards CO and  $\text{C}_{2+}$  products, respectively.

3. Even better performance can be achieved through optimization of the GDE electrodes, which requires additional engineering considerations.

4. Although we have performed some characterization to determine the stability of the catalyst roughly, there is still a need for possible structural changes of the catalyst, especially the catalytic sites, during the ECR reaction, which requires advanced operando characterization techniques.

## 9 | Reference

- [1] H. Ritchie, M. Roser, Energy Production and Consumption. **2020**, Our World In Data: <https://ourworldindata.org/>.
- [2] BP Statistical Review of World Energy, <http://www.bp.com/>.
- [3] International Energy Agency (IEA), Global Energy Review **2021**, <https://www.iea.org/reports/global-energy-review-2021>.
- [4] Atmospheric CO<sub>2</sub> concentration: 416.71 ppm in Dec. **2021**, <https://www.co2.earth/>.
- [5] H. Ritchie, M. Roser, CO<sub>2</sub> and Greenhouse Gas Emissions. **2020**, Our World In Data: <https://ourworldindata.org/>.
- [6] Supplemental data of Global Carbon Budget **2021**. Global Carbon Project. <https://doi.org/10.18160/gcp-2021>.
- [7] Met Office Hadley Centre observations datasets, <https://www.metoffice.gov.uk/hadobs/hadcrut4/index.html>.
- [8] Intergovernmental Panel on Climate Change (IPCC), IPCC Fifth Assessment Report: Climate Change **2014**, <https://www.ipcc.ch/report/ar5/syr/>.
- [9] Global CCS Institute, 2021 Global Status Report, <https://www.globalccsinstitute.com/resources/global-status-report/>.
- [10] C. Hepburn, E. Adlen, J. Beddington, E. A. Carter, S. Fuss, N. M. Dowell, J. C. Minx, P. Smith, C. K. Williams, *Nature* **2019**, *575*, 87-97.
- [11] M. Mikkelsen, M. Jørgensen, F. C. Krebs, *Energy Environ. Sci.* **2010**, *3*, 43-81.
- [12] R. Wiser, K. Jenni, J. Seel, E. Baker, M. Hand, E. Lantz, A. Smith, *Nat Energy* **2016**, *1*, 16135
- [13] M. Victoria, N. Haegel, I. M. Peters, R. Sinton, A. Jäger-Waldau, C. Del Cañizo, C. Breyer, M. Stocks, A. Blakers, I. Kaizuka, K. Komoto, A. Smets, *Joule* **2021**, *5*, 1041-1056.
- [14] G. Glenk, S. Reichelstein, *Nat Energy* **2019**, *4*, 216-222.
- [15] R. G. Grim, Z. Huang, M. T. Guarnieri, J. R. Ferrell III, L. Tao, J. A. Schaidle, *Energy Environ. Sci.* **2020**, *13*, 472-494.
- [16] J. M. Spurgeon, B. Kumar, *Energy Environ. Sci.* **2018**, *11*, 1536-1551
- [17] C. Chen, J. F. K. Kotyk, S. W. Sheehan, *Chem* **2018**, *4*, 2571-2586.
- [18] A. Somoza-Tornos, O. J. Guerra, A. M. Crow, W. A. Smith, B.-M. Hodge, *iScience* **2021**, *24*, 102813.
- [19] A. Löwe, M. Schmidt, F. Bienen, D. Kopljar, N. Wagner, E. Klemm, *ACS Sustainable Chem. Eng.* **2021**, *9*, 4213-4223.
- [20] M. F. Philips, G.-J. M. Gruter, M. T. M. Koper, K. J. P. Schouten, *ACS Sustainable Chem. Eng.* **2020**, *8*, 15430-15444.
- [21] R. I. Masel, Z. Liu, H. Yang, J. J. Kaczur, D. Carrillo, S. Ren, D. Salvatore, C. P. Berlinguette, *Nat. Nanotechnol.* **2021**, *16*, 118-128.
- [22] L. V. Haynes, D. T. Sawyer, *Anal. Chem.* **1967**, *39*, 332-338.
- [23] S. Meshitsuka, M. Ichikawa, K. Tamaru, *J. Chem. Soc. Chem. Commun.* **1974**, 158-159.
- [24] Y. Hori, K. Kikuchi, S. Suzuki, *Chem. Lett.* **1985**, *14*, 1695-1698.
- [25] Y. Hori, H. Wakebe, T. Tsukamoto, O. Koga, *Electrochim. Acta* **1994**, *39*, 1833-1839.

- [26] T. Yamamoto, D. A. Tryk, A. Fujishima, H. Ohata, *Electrochim. Acta* **2002**, *47*, 3327-3334.
- [27] R. Hinogami, S. Yotsuhashi, M. Deguchi, Y. Zenitani, H. Hashiba, Y. Yamada, *ECS Electrochem. Lett.* **2012**, *1*, H17-H19
- [28] B. Kumar, M. Asadi, D. Pisasale, S. Sinha-Ray, B. A. Rosen, R. Haasch, J. Abiade, A. L. Yarin, A. Salehi-Khojin, *Nat. Commun.* **2013**, *4*, 2819.
- [29] S. Shironita, K. Karasuda, K. Sato, M. Umed, *J. Power Sources* **2013**, *240*, 404-410.
- [30] M. Asadi, B. Kumar, A. Behranginia, B. A. Rosen, A. Baskin, N. Reppin, D. Pisasale, P. Phillips, W. Zhu, R. Haasch, R. F. Klie, P. Král, J. Abiade, A. Salehi-Khojin, *Nat. Commun.* **2014**, *5*, 4470.
- [31] S. Lin, C. S. Diercks, Y. B. Zhang, N. Kornienko, E. M. Nichols, Y. Zhao, A. R. Paris, D. Kim, P. Yang, O. M. Yaghi, C. J. Chang, *Science* **2015**, *349*, 1208-1213.
- [32] C. Zhao, X. Dai, T. Yao, W. Chen, X. Wang, J. Wang, J. Yang, S. Wei, Y. Wu, Y. Li, *J. Am. Chem. Soc.* **2017**, *139*, 8078-8081.
- [33] S. Verma, S. Lu, P. J. Kenis, *Nat. Energy* **2019**, *4*, 466-474.
- [34] A. Paparom, J. Okura, *Coord. Chem. Rev.* **2017**, *334*, 136-149.
- [35] Y. Y. Birdja, E. Pérez-Gallent, M. C. Figueiredo, A. J. Göttle, F. Calle-Vallejo, M. T. M. Koper, *Nat Energy* **2019**, *4*, 732-745.
- [36] L. Zhang, Z.-J. Zhao, J. Gong, *Angew. Chem. Int. Ed.* **2017**, *56*, 11326-11353.
- [37] S. Jin, Z. Hao, K. Zhang, Z. Yan, J. Chen, *Angew. Chem. Int. Ed.* **2021**, *60*, 20627-20648.
- [38] W. Zhang, Y. Hu, L. Ma, G. Zhu, Y. Wang, X. Xue, R. Chen, S. Yang, Z. Jin. *Adv. Sci.* **2017**, 1700275.
- [39] D. D. Zhu, J. L. Liu, S. Z. Qiao, *Adv. Mater.* **2016**, *28*, 3423-3452.
- [40] J. R. Rumble, J. Rumble, CRC Handbook of Chemistry and Physics, 98th ed.; CRC Press LLC, **2017**.
- [41] R. Kas, K. Yang, D. Bohra, R. Kortlever, T. Burdyny, W. A. Smith, *Chem. Sci.* **2020**, *11*, 1738-1749.
- [42] G. O. Larrazábal, A. J. Martín, J. Pérez-Ramírez, *J. Phys. Chem. Lett.* **2017**, *8*, 3933-3944.
- [43] O. A. Baturina, Q. Lu, M. A. Padilla, L. Xin, W. Li, A. Serov, K. Artyushkova, P. Atanassov, F. Xu, A. Epshteyn, T. Brintlinger, M. Schuette, G. E. Collins, *ACS Catal.* **2014**, *4*, 3682-3695.
- [44] E. Gileadi, *Electrode Kinetics for Chemists, Engineers, and Materials Scientists*; Wiley-VCH: New York, **1993**.
- [45] Y. Chen, M. W. Kanan, *J. Am. Chem. Soc.* **2012**, *134*, 1986-1989.
- [46] S. Gao, Y. Lin, X. Jiao, Y. Sun, Q. Luo, W. Zhang, D. Li, J. Yang, Y. Xie, *Nature* **2016**, *529*, 68-71.
- [47] S. Komatsu, T. Yanagihara, Y. Hiraga, M. Tanaka, A. Kunugi, *Denki Kagaku oyobi Kogyo Butsuri Kagaku* **1995**, *63*, 217-224.
- [48] A. Bagger, W. Ju, A. S. Varela, P. Strasser, J. Rossmeisl, *ChemPhysChem* **2017**, *18*, 3266-3273.
- [49] H. Rabiee, L. Ge, X. Zhang, S. Hu, M. Li, Z. Yuan, *Energy Environ. Sci.* **2021**, *14*, 1959-2008.
- [50] D. Ma, T. Jin, K. Xie, H. Huang, *J. Mater. Chem. A* **2021**, *9*, 20897-20918.
- [51] T. N. Nguyen, C.-T. Dink, *Chem. Soc. Rev.* **2020**, *49*, 7488-7504.
- [52] N. T. Nesbitt, T. Burdyny, H. Simonson, D. Salvatore, D. Bohra, R. Kas, W. A. Smith, *ACS Catal.* **2020**, *10*, 14093-14106.
- [53] F. P. García de Arquer, C. T. Dinh, A. Ozden, J. Wicks, C. McCallum, A. R. Kirmani, D. H. Nam, C. Gabardo, A. Seifitokaldani, X. Wang, Y. C. Li, F. Li, J. Edwards, L. J. Richter, S. J. Thorpe, D. Sinton, E. H. Sargent, *Science* **2020**, *367*, 661-666.
- [54] J. E. Huang, F. Li, A. Ozden, A. Sedighian Rasouli, F. P. Garcia de Arquer, S. Liu, S. Zhang, M. Luo, X. Wang, Y. Lum, Y. Xu, K. Bertens, R. K. Miao, C. T. Dinh, D. Sinton, E. H. Sargent, *Science* **2021**, *372*, 1074-1078.
- [55] C. Chen, Y. Li, P. Yang, *Chem* **2021**, *5*, 737-742.

- [56] J. A. Rabinowitz, M. W. Kanan, *Nat. Commun.* **2020**, *11*, 5231.
- [57] Y. C. Tan, K. B. Lee, H. Song, J. Oh, *Joule* **2020**, *4*, 1104-1120.
- [58] L. Ge, H. Rabiee, M. Li, S. Subramanian, Y. Zheng, J. H. Lee, T. Burdyny, H. Wang, *Chem* **2021**, Doi: 10.1016/j.chempr.2021.12.002.
- [59] L. Li, A. Ozden, S. Guo, F. P. García de Arquer, C. Wang, M. Zhang, J. Zhang, H. Jiang, W. Wang, H. Dong, D. Sinton, E. H. Sargent, M. Zhong, *Nat. Commun.* **2021**, *12*, 5223.
- [60] R. K. Miao, Y. Xu, A. Ozden, A. Robb, C. P. O'Brien, C. M. Gabardo, G. Lee, J. P. Edwards, J. E. Huang, M. Fan, X. Wang, S. Liu, Y. Yan, E. H. Sargent, D. Sinton, *Joule* **2021**, *5*, 2742-2753.
- [61] D. Bohra, J. H. Chaudhry, T. Burdyny, E. A. Pidko, W. A. Smith, *Energy Environ. Sci.* **2019**, *12*, 3380-3389.
- [62] S. Zhu, B. Jiang, W.-B. Cai, M. Shao, *J. Am. Chem. Soc.* **2017**, *139*, 15664-15667.
- [63] C.-T. Dinh, T. Burdyny, M. G. Kibria, A. Seifitokaldani, C. M. Gabardo, F. P. G. de Arquer, A. Kiani, J. P. Edwards, P. De Luna, O. S. Bushuyev, C. Zou, R. Quintero-Bermudez, Y. Pang, D. Sinton, E. H. Sargent, *Science* **2018**, *360*, 783-787.
- [64] E. R. Cofell, U. O. Nwabara, S. S. Bhargava, D. E. Henckel, P. J. A. Kenis, *ACS Appl. Mater. Interfaces* **2021**, *13*, 15132-15142.
- [65] M. Obkopp, A. Löwe, C. M. S. Lobo, S. Baranyai, T. Khoza, M. Auinger, E. Klemm, *J. CO<sub>2</sub> Util.* **2022**, *56*, 101823.
- [66] A. Murata, Y. Hori, *Bull. Chem. Soc. Jpn.* **1991**, *64*, 123-127.
- [67] J. Resasco, L. D. Chen, E. Clark, C. Tsai, C. Hahn, T. F. Jaramillo, K. Chan, A. T. Bell, *J. Am. Chem. Soc.* **2017**, *139*, 11277-11287.
- [68] M. R. Singh, Y. Kwon, Y. Lum, J. W. Ager, III, A. T. Bell, *J. Am. Chem. Soc.* **2016**, *138*, 39, 13006-13012.
- [69] K. Elouarzaki, V. Kannan, V. Jose, H. S. Sabharwal, J.-M. Lee, *Adv. Energy Mater.* **2019**, *9*, 1900090.
- [70] M. König, J. Vaes, E. Klemm, D Pant, *iScience* **2019**, *19*, 135-160.
- [71] M. Alvarez-Guerra, J. Albo, E. Alvarez-Guerra, A. Irabien, *Energy Environ. Sci.* **2015**, *8*, 2574-2599.
- [72] J. Medina-Ramos, R. C. Pupillo, T. P. Keane, J. L. DiMeglio, J. Rosenthal, *J. Am. Chem. Soc.* **2015**, *137*, 5021-5027
- [73] F. Chang, G. Zhan, Z. Wu, Y. Duan, S. Shi, S. Zeng, X. Zhang, S. Zhang, *ACS Sustainable Chem. Eng.* **2021**, *9*, 9045-9052
- [74] A. Löwe, C. Rieg, T. Hierlemann, N. Salas, D. Kopljar, N. Wagner, E. Klemm, *ChemElectroChem* **2019**, *6*, 4497-4506.
- [75] T. Mizuno, K. Ohta, A. Sasaki, T. Akai, M. Hirano, A. Kawabe, *Energy Sources* **1995**, *17*, 503-508.
- [76] M. Todoroki, K. Hara, A. Kudo, T. Sakata, *J. Electroanal. Chem.* **1995**, *394*, 199
- [77] X. Zhao, L. Du, B. You, Y. Sun, *Catal. Sci. Technol.* **2020**, *10*, 2711-2720.
- [78] C. Chen, X. Zhu, X. Wen, Y. Zhou, L. Zhou, H. Li, L. Tao, Q. Li, S. Du, T. Liu, D. Yan, C. Xie, Y. Zou, Y. Wang, R. Chen, J. Huo, Y. Li, J. Cheng, H. Su, X. Zhao, W. Cheng, Q. Liu, H. Lin, J. Luo, J. Chen, M. Dong, K. Cheng, C. Li, S. Wang, *Nat. Chem.* **2020**, *12*, 717-724.
- [79] Y. Feng, H. Yang, Y. Zhang, X. Huang, L. Li, T. Cheng, Q. Shao, *Nano Lett.* **2020**, *20*, 8282-8289.
- [80] O. Yishai, S. N Lindner, J. G. de la Cruz, H. Tenenboim, A. Bar-Even, *Curr. Opin. Chem. Biol.* **2016**, *35*, 1-9.
- [81] T. Haas, R. Krause, R. Weber, M. Demler, G. Schmid, *Nat. Catal.* **2018**, *1*, 32.
- [82] T. Li, Y. Cao, J. He, C. P. Berlinguette, *ACS Cent. Sci.* **2017**, *3*, 778.
- [83] S. Choi, M. Balamurugan, K.-G. Lee, K. H. Cho, S. Park, H. Seo, K. T. Nam, *J. Phys. Chem. Lett.*

2020, 11, 2941-2948.

- [84] A. S. Varela, W. Ju, P. Strasser, *Adv. Energy Mater.* **2018**, 8, 1703614.
- [85] Y. Wang, P. Han, X. Lv, L. Zhang, G. Zheng, *Joule* **2018**, 2, 2551-2582.
- [86] A. Vasileff, C. Xu, Y. Jiao, Y. Zheng, S.-Z. Qiao, *Chem* **2018**, 4, 1-23.
- [87] W. Yang, K. Dastafkan, C. Jia, C. Zhao, *Adv. Mater. Technol.* **2018**, 3, 1700377.
- [88] Z. Sun, T. Ma, H. Tao, Q. Fan, B. Han, *Chem* **2017**, 3, 560-587.
- [89] A. S. Hall, Y. Yoon, A. Wuttig, Y. Surendranath, *J. Am. Chem. Soc.* **2015**, 137, 14834-14837.
- [90] N. W. Kinzel, C. Werlé, W. Leitner, *Angew. Chem. Int. Ed.* **2021**, 60, 11628-11686.
- [91] Y. Wu, Y. Liang, H. Wang, *Acc. Chem. Res.* **2021**, 54, 3149-3159.
- [92] L. Sun, V. Reddu, A. C. Fisher, X. Wang, *Energy Environ. Sci.* **2020**, 13, 374-403.
- [93] J. Wu, T. Sharifi, Y. Gao, T. Zhang, P. M. Ajayan, *Adv. Mater.* **2019**, 31, 1804257.
- [94] X. Duan, J. Xu, Z. Wei, J. Ma, S. Guo, S. Wang, H. Liu, S. Dou, *Adv. Mater.* **2017**, 29, 1701784.
- [95] Y. Zhu, X. Yang, C. Peng, C. Priest, Y. Mei, G. Wu, *Small* **2021**, 17, 2005148.
- [96] J. Wu, M. Liu, P. P. Sharma, R. M. Yadav, L. Ma, Y. Yang, X. Zou, X. D. Zhou, R. Vajtai, B. I. Yakobson, J. Lou, P. M. Ajayan, *Nano Lett.* **2016**, 16, 466-470.
- [97] X. Cui, Z. Pan, L. Zhang, H. Peng, G. Zheng, *Adv. Energy Mater.* **2017**, 7, 1701456.
- [98] R. Daiyan, X. Tan, R. Chen, W. H. Saputera, H. A. Tahini, E. Lovell, Y. H. Ng, S. C. Smith, L. Dai, X. Lu, R. Amal, *ACS Energy Lett.* **2018**, 3, 2292-2298.
- [99] N. Sreekanth, M. A. Nazrulla, T. V. Vineesh, K. Sailaja, K. L. Phani, *Chem. Commun.* **2015**, 51, 16061-16064.
- [100] Y. Liu, Y. Zhang, K. Chen, X. Quan, X. Fan, Y. Su, S. Chen, H. Zhao, Y. Zhang, H. Yu, M. R. Hoffmann, *Angew. Chem. Int. Ed.* **2017**, 56, 15607-15611
- [101] H. Yang, Y. Wu, Q. Lin, L. Fan, X. Chai, Q. Zhang, J. Liu, C. He, Z. Lin, *Angew. Chem. Int. Ed.* **2018**, 57, 15476-15480.
- [102] A. Wang, J. Li, T. Zhang, *Nat. Rev. Chem.* **2018**, 2, 65-81.
- [103] A. S. Varela, W. Ju, A. Bagger, P. Franco, J. Rossmeisl, P. Strasser, *ACS Catal.* **2019**, 9, 7270-7284.
- [104] W. Ju, A. Bagger, G.-P. Hao, A. S. Varela, I. Sinev, V. Bon, B. R. Cuenya, S. Kaskel, J. Rossmeisl, P. Strasser. *Nat. Commun.* **2017**, 8, 944.
- [105] L. Jiao, W. Yang, G. Wan, R. Zhang, X. Zheng, H. Zhou, S.-H. Yu, H.-L. Jiang, *Angew. Chem. Int. Ed.* **2020**, 59, 20589-20595.
- [106] J. Gu, C.-S. Hsu, L. Bai, H. M. Chen, X. Hu, *Science* **2019**, 364, 1091-1094
- [107] H. B. Yang, S.-F. Hung, S. Liu, K. Yuan, S. Miao, L. Zhang, X. Huang, H.-Y. Wang, W. Cai, R. Chen, J. Gao, X. Yang, W. Chen, Y. Huang, H. M. Chen, C. M. Li, T. Zhang, B. Liu, *Nat. Energy* **2018**, 3, 140-147.
- [108] M. G. Kibria, J. P. Edwards, C. M. Gabardo, C. T. Dinh, A. Seifitokaldani, D. Sinton, E. H. Sargent, *Adv. Mater.* **2019**, 31, 1807166.
- [109] D. Gao, H. Zhou, F. Cai, J. Wang, G. Wang, X. Bao, *ACS Catal.* **2018**, 8, 1510-1519.
- [110] H. Mistry, R. Reske, Z. Zeng, Z.-J. Zhao, J. Greeley, P. Strasser, B. R. Cuenya, *J. Am. Chem. Soc.* **2014**, 136, 16473-16476.
- [111] D. Gao, H. Zhou, J. Wang, S. Miao, F. Yang, G. Wang, J. Wang, X. Bao, *J. Am. Chem. Soc.* **2015**, 137, 4288-4291.
- [112] C. Kim, H. S. Jeon, T. Eom, M. S. Jee, H. Kim, C. M. Friend, B. K. Min, Y. J. Hwang, *J. Am. Chem. Soc.* **2015**, 137, 13844-13850.

- [113] W. Zhu, R. Michalsky, Ö. Metin, H. Lv, S. Guo, C. J. Wright, X. Sun, A. A. Peterson, S. Sun, *J. Am. Chem. Soc.* **2013**, *135*, 16833-16836.
- [114] S. Zhu, Q. Wang, X. Qin, M. Gu, R. Tao, B. P. Lee, L. Zhang, Y. Yao, T. Li, M. Shao, *Adv. Energy Mater.* **2018**, *8*, 1802238.
- [115] H. Mistry, Y.-W. Choi, A. Bagger, F. Scholten, C. S. Bonifacio, I. Sinev, N. J. Divins, I. Zegkinoglou, H. S. Jeon, K. Kisslinger, E. A. Stach, J. C. Yang, J. Rossmeisl, B. Roldan Cuenya, *Angew. Chem. Int. Ed.* **2017**, *56*, 11394-11398.
- [116] Z. Cao, D. Kim, D. Hong, Y. Yu, J. Xu, S. Lin, X. Wen, E. M. Nichols, K. Jeong, J. A. Reimer, P. Yang, C. J. Chang, *J. Am. Chem. Soc.* **2016**, *138*, 8120-8125.
- [117] D. L. T. M. Nguyen, S. Jee, D. H. Won, H. Jung, H. S. Oh, B. K. Min, Y. J. Hwang, *ACS Sustainable Chem. Eng.* **2017**, *5*, 11377-11386.
- [118] H. S. Jeon, I. Sinev, F. Scholten, N. J. Divins, I. Zegkinoglou, L. Pielsticker, B. R. Cuenya, *J. Am. Chem. Soc.* **2018**, *140*, 9383-9386.
- [119] Y. Wu, P. Zhai, S. Cao, Z. Li, B. Zhang, Y. Zhang, X. Nie, L. Sun, J. Hou, *Adv. Energy Mater.* **2020**, *10*, 2002499.
- [120] J. Xu, S. Lai, M. Hu, S. Ge, R. Xie, F. Li, D. Hua, H. Xu, H. Zhou, R. Wu, J. Fu, Y. Qiu, J. He, C. Li, H. Liu, Y. Liu, J. Sun, X. Liu, J. Luo, *Small Methods* **2020**, *4*, 2000567.
- [121] Z. Yang, F. E. Oropeza, and K. H. L. Zhang, *APL Mater.* **2020**, *8*, 060901.
- [122] K. Van Daele, B. De Mot, M. Pupo, N. Daems, D. Pant, R. Kortlever, T. Breugelmans, *ACS Energy Lett.* **2021**, *6*, 4317-4327.
- [123] Y. Guan, M. Liu, X. Rao, Y. Liu, J. Zhang, *J. Mater. Chem. A* **2021**, *9*, 13770-13803.
- [124] A. Dutta, A. Kuzume, V. Kaliginedi, M. Rahaman, I. Sinev, M. Ahmadi, B. R. Cuenya, S. Vesztergom, P. Broekmann, *Nano Energy* **2018**, *53*, 828-840.
- [125] J. L. White, A. B. Bocarsly, *J. Electrochem. Soc.* **2016**, *163*, H410-H416.
- [126] A. Dutta, I. Z. Montiel, K. Kiran, A. Rieder, V. Grozovski, L. Gut, P. A. Broekmann, *ACS Catal.* **2021**, *11*, 4988-5003.
- [127] S. Gao, X. Jiao, Z. Sun, W. Zhang, Y. Sun, C. Wang, Q. Hu, X. Zu, F. Yang, S. Yang, L. Liang, J. Wu, Y. Xie, *Angew. Chem. Int. Ed.* **2016**, *55*, 698-702.
- [128] M. Rahaman, A. Dutta, P. Broekmann, *ChemSusChem* **2017**, *10*, 1733-1741.
- [129] X. Min, M. W. Kanan, *J. Am. Chem. Soc.* **2015**, *137*, 4701-4708.
- [130] C. W. Li, J. Ciston, M. W. Kanan, *Nature* **2014**, *508*, 504-507.
- [131] D. Gao, R. M. Arán-Ais, H. S. Jeon, B. R. Cuenya, *Nat. Catal.* **2019**, *2*, 198-210.
- [132] A. Verdager-Casadevall, C. W. Li, T. P. Johansson, S. B. Scott, J. T. McKeown, M. Kumar, I. E. L. Stephens, M. W. Kanan, I. Chorkendorff, *J. Am. Chem. Soc.* **2015**, *137*, 9808-9811.
- [133] J. Wang, H.-Y. Tan, Y. Zhu, H. Chu, H. M. Chen, *Angew. Chem. Int. Ed.* **2021**, *60*, 17254-17267.
- [134] P. De Luna, R. Quintero-Bermudez, C.-T. Dinh, M. B. Ross, O. S. Bushuyev, P. Todorović, T. Regier, S. O. Kelley, P. Yang, E. H. Sargent, *Nat. Catal.* **2018**, *1*, 103-110.
- [135] H. Mistry, A. S. Varela, C. S. Bonifacio, I. Zegkinoglou, I. Sinev, Y.-W. Choi, K. Kisslinger, E. A. Stach, J. C. Yang, P. Strasser, B. R. Cuenya, *Nat. Commun.* **2016**, *7*, 12123.
- [136] A. Vasileff, C. Xu, Y. Jiao, Y. Zheng, S. Z. Qiao, *Chem* **2018**, *4*, 1809-1831.
- [137] T. T. H. Hoang, S. Verma, S. Ma, T. T. Fister, J. Timoshenko, A. I. Frenkel, P. J. A. Kenis, A. A. Gewirth, *J. Am. Chem. Soc.* **2018**, *140*, 5791-5797.
- [138] S. Ma, M. Sadakiyo, M. Heima, R. Luo, R. T. Haasch, J. I. Gold, M. Yamauchi, P. J. A. Kenis, *J. Am. Chem. Soc.* **2017**, *139*, 47-50.

- [139] D. Ren, B. S.-H. Ang, B. S. Yeo, *ACS Catal.* **2016**, *6*, 8239-8247.
- [140] O. M. Yaghi, G. Li, H. Li, *Nature* **1995**, *378*, 703-705.
- [141] H. Furukawa, K. E. Cordova, M. O’Keeffe, O. M. Yaghi, *Science* **2013**, *341*, 1230444.
- [142] O. M. Yaghi, M. J. Kalmutzki, C. S. Diercks, Introduction to Reticular Chemistry: Metal-Organic Frameworks and Covalent Organic Frameworks. Wiley-VCH, Weinheim, **2019**.
- [143] H.-C. Zhou, S. Kitagawa, *Chem. Soc. Rev.* **2014**, *43*, 5415-5418.
- [144] R. Freund, S. Canossa, S. M. Cohen, W. Yan, H. Deng, V. Guillerm, M. Eddaoudi, D. G. Madden, D. Fairen-Jimenez, H. Lyu, L. K. Macreadie, Z. Ji, Y. Zhang, B. Wang, F. Haase, C. Woll, O. Zaremba, J. Andreo, S. Wuttke, C. S. Diercks, *Angew. Chem., Int. Ed.* **2021**, *60*, 23946-23974.
- [145] CSD MOF Collection. <https://www.ccdc.cam.ac.uk/Community/csd-community/csd-mof-collection/>.
- [146] B. Li, H.-M. Wen, Y. Cui, W. Zhou, G. Qian, B. Chen, *Adv. Mater.* **2016**, *28*, 8819-8860.
- [147] Q. Yang, Q. Xu, H.-L. Jiang, *Chem. Soc. Rev.* **2017**, *46*, 4774-4808.
- [148] A. Kirchon, L. Feng, H. F. Drake, E. A. Joseph, H.-C. Zhou, *Chem. Soc. Rev.* **2018**, *47*, 8611-8638.
- [149] L. Jiao, J. Wang, H.-L. Jiang, *Acc. Mater. Res.* **2021**, *2*, 327-339.
- [150] M. J. Van Vleet, T. Weng, X. Li, J. R. Schmidt, *Chem. Rev.* **2018**, *118*, 3681-3721.
- [151] M. Filez, C. Caratelli, M. Rivera-Torrente, F. Muniz-Miranda, M. Hoek, M. Altelaar, A. J. R. Heck, V. Van Speybroeck, B. M. Weckhuysen, *Cell Rep. Phys. Sci.* **2021**, *2*, 100680.
- [152] W. L. Teo, W. Zhou, C. Qian, Y. Zhao, *Mater Today.* **2021**, *47*, 170-186.
- [153] C. Wang, X. Liu, N. K. Demir, J. P. Chen, K. Li, *Chem. Soc. Rev.* **2016**, *45*, 5107-5134.
- [154] S. Yuan, L. Feng, K. Wang, J. Pang, M. Bosch, C. Lollar, Y. Sun, J. Qin, X. Yang, P. Zhang, Q. Wang, L. Zou, Y. Zhang, L. Zhang, Y. Fang, J. Li, H. C. Zhou, *Adv. Mater.* **2018**, *30*, 1704303.
- [155] S. S. Kaye, A. Dailly, O. M. Yaghi, J. R. Long, *J. Am. Chem. Soc.* **2007**, *129*, 14176-14177.
- [156] S. Wang, T. Kitao, N. Guillou, M. Wahiduzzaman, C. Martineau-Corcus, F. Nouar, A. Tissot, L. Binet, N. Ramsahye, S. Devautour-Vinot, S. Kitagawa, S. Seki, Y. Tsutsui, V. Briois, N. Steunou, G. Maurin, T. Uemura, C. Serre, *Nat. Commun.* **2018**, *9*, 1660.
- [157] Y.-B. Huang, J. Liang, X.-S. Wang, R. Cao, *Chem. Soc. Rev.* **2017**, *46*, 126-157.
- [158] M. Eddaoudi, J. Kim, N. Rosi, D. Vodak, J. Wachter, M. O’Keeffe, O. M. Yaghi, *Science* **2002**, *295*, 469-472.
- [159] P. M. Bhatt, V. Guillerm, S. J. Datta, A. Shkurenko, M. Eddaoudi, *Chem* **2020**, *6*, 1613-1633.
- [160] Reticular Chemistry Structure Resource (RCSR). <http://rcsr.anu.edu.au/>.
- [161] K. K. Tanabe, S. M. Cohen, *Chem. Soc. Rev.* **2011**, *40*, 498-519.
- [162] T. Islamoglu, S. Goswami, Z. Li, A. J. Howarth, O. K. Farha, J. T. Hupp, *Acc. Chem. Res.* **2017**, *50*, 805-813.
- [163] Q.-G. Zhai, X. Bu, X. Zhao, D.-S. Li, P. Feng, *Acc. Chem. Res.* **2017**, *50*, 407-417.
- [164] Y. Xu, Q. Li, H. Xue, H. Pang, *Coord. Chem. Rev.* **2018**, *376*, 292-318.
- [165] S. Dou, X. Li, X. Wang, *ACS Materials Lett.* **2020**, *2*, 1251-1267.
- [166] T. Zhan, Y. Zou, Y. Yang, X. Ma, Z. Zhang, S. Xiang, *ChemCatChem* **2022**, DOI: 10.1002/cctc.202101453.
- [167] D.-H. Nam, P. De Luna, A. Rosas-Hernández, A. Thevenon, F. Li, T. Agapie, J. C. Peters, O. Shekhah, M. Eddaoudi, E. H. Sargent, *Nat. Mater.* **2020**, *19*, 266-276.
- [168] D. Zhu, M. Qiao, J. Liu, T. Tao, C. Guo, *J. Mater. Chem. A* **2020**, *8*, 8143-8170.
- [169] Web of Science, <https://www.webofscience.com/>.
- [170] X. F. Lu, Y. Fang, D. Luan, X. W. Lou, *Nano Lett.* **2021**, *21*, 1555-1565.

- [171] P. Deng, F. Yang, Z. Wang, S. Chen, Y. Zhou, S. Zaman, B. Y. Xia, *Angew. Chem. Int. Ed.* **2020**, *59*, 10807-10813.
- [172] Q. Zhu, X. Sun, D. Yang, J. Ma, X. Kang, L. Zheng, J. Zhang, Z. Wu, B. Han, *Nat. Commun.* **2019**, *10*, 3851.
- [173] J. Jiang, P. Jiang, D. Wang, Y. Li, *Nanoscale* **2020**, *12*, 20580-20589.
- [174] C. Cao, D.-D. Ma, J.-F. Gu, X. Xie, G. Zeng, X. Li, S.-G. Han, Q.-L. Zhu, X.-T. Wu, Q. Xu, *Angew. Chem. Int. Ed.* **2020**, *59*, 15014-15020.
- [175] D. Yao, C. Tang, A. Vasileff, X. Zhi, Y. Jiao, S.-Z. Qiao, *Angew. Chem. Int. Ed.* **2021**, *60*, 18178-18184.
- [176] W. Zheng, L.Y. S. Lee, *ACS Energy Lett.* **2021**, *6*, 2838-2843.
- [177] N. Kornienko, Y. B. Zhao, C. S. Kley, C. H. Zhu, D. Kim, S. Lin, C. J. Chang, O. M. Yaghi, P. D. Yang, *J. Am. Chem. Soc.* **2015**, *137*, 14129-14135.
- [178] C.-W. Kung, C. O. Audu, A. W. Peters, H. Noh, O. K. Farha, J. T. Hupp, *ACS Energy Lett.* **2017**, *2*, 2394-2401.
- [179] Y. Guo, H. Yang, X. Zhou, K. Liu, C. Zhang, Z. Zhou, C. Wang, W. Lin *J. Mater. Chem. A* **2017**, *5*, 24867-24873.
- [180] J. Albo, D. Vallejo, G. Beobide, O. Castillo, P. Castaño, A. Irabien, *ChemSusChem* **2017**, *10*, 1100-1109.
- [181] Y. Wang, P. Hou, Z. Wang, P. Kang, *ChemPhysChem* **2017**, *18*, 3142-3147.
- [182] X. Jiang, H. Wu, S. Chang, R. Si, S. Miao, W. Huang, Y. Li, G. Wang, X. Bao, *J. Mater. Chem. A* **2017**, *5*, 19371-19377.
- [183] Y.-R. Wang, Q. Huang, C.-T. He, Y. Chen, J. Liu, F.-C. Shen, Y.-Q. Lan, *Nat. Commun.* **2018**, *9*, 4466.
- [184] M. Perfecto-Irigaray, J. Albo, G. Beobide, O. Castillo, A. Irabien S. Pérez-Yáñez, *RSC Adv.* **2018**, *8*, 21092-21099.
- [185] C. Chen, D. Yan, X. Luo, W. Gao, G. Huang, Z. Han, Y. Zeng, Z. Zhu, *ACS Appl. Energy Mater.* **2018**, *1*, 4662-4671.
- [186] X. Jiang, H. Li, J. Xiao, D. Gao, R. Si, F. Yang, Y. Li, G. Wang, X. Bao, *Nano Energy* **2018**, *52*, 345-350.
- [187] X. Tan, C. Yu, C. Zhao, H. Huang, X. Yao, X. Han, W. Guo, S. Cui, H. Huang, J. Qiu, *ACS Appl. Mater. Interfaces* **2019**, *11*, 9904-9910.
- [188] J. Albo, M. Perfecto-Irigaray, G. Beobide, A. Irabien, *J. CO2 Util.* **2019**, *33*, 157-165.
- [189] F. Yang, A. Chen, P. L. Deng, Y. Zhou, Z. Shahid, H. Liu, B. Y. Xia, *Chem. Sci.* **2019**, *10*, 7975-7981.
- [190] R. Matheu, E. Gutierrez-Puebla, M. Á. Monge, C. S. Diercks, J. Kang, M. S. Prévot, X. Pei, N. Hanikel, B. Zhang, P. Yang, O. M. Yaghi, *J. Am. Chem. Soc.* **2019**, *141*, 17081-17085.
- [191] Y. Guo, W. Shi, H. Yang, Q. He, Z. Zeng, J.-Y. Ye, X. He, R. Huang, C. Wang, W. Lin, *J. Am. Chem. Soc.* **2019**, *141*, 17875-17883.
- [192] S. Dou, J. Song, S. Xi, Y. Du, J. Wang, Z.-F. Huang, Z. J. Xu, X. Wang, *Angew. Chem., Int. Ed.* **2019**, *58*, 4041-4045.
- [193] J.-X. Wu, W.-W. Yuan, M. Xu, Z.-Y. Gu, *Chem. Commun.* **2019**, *55*, 11634-11637.
- [194] Y. T. Guntern, J. R. Pankhurst, J. Vávra, M. Mensi, V. Mantella, P. Schouwink, R. Buonsanti, *Angew. Chem., Int. Ed.* **2019**, *58*, 12632-12639.
- [195] J. Han, P. An, S. Liu, X. Zhang, D. Wang, Y. Yuan, J. Guo, X. Qiu, K. Hou, L. Shi, Y. Zhang, S. Zhao, C. Long, Z. Tang, *Angew. Chem. Int. Ed.* **2019**, *58*, 12711-12716.

- [196] D. Yang, H. Yu, T. He, S. Zuo, X. Liu, H. Yang, B. Ni, H. Li, L. Gu, D. Wang, X. Wang, *Nat. Commun.* **2019**, *10*, 3844.
- [197] Z. Xin, Y.-R. Wang, Y. Chen, W.-L. Li, L.-Z. Dong, Y.-Q. Lan, *Nano Energy* **2020**, *67*, 104233.
- [198] X.-D. Zhang, S.-Z. Hou, J.-X. Wu, Z.-Y. Gu, *Chem.-Eur. J.* **2020**, *26*, 1604-1611.
- [199] S.-H. Hou, X.-D. Zhang, W.-W. Yuan, Y.-X. Li, Z.-Y. Gu, *Inorg. Chem.* **2020**, *59*, 11298-11304.
- [200] H. Zhong, M. Ghorbani-asl, K. H. Ly, J. Zhang, J. Ge, M. Wang, Z. Liao, D. Makarov, E. Zschech, E. Brunner, I. M. Weidinger, J. Zhang, A. V. Krasheninnikov, S. Kaskel, R. Dong, X. Feng, *Nat. Commun.* **2020**, *11*, 1409.
- [201] X. Zhang, Y. Zhang, Q. Li, X. Zhou, Q. Li, J. Yi, Y. Liu, J. Zhang, *J. Mater. Chem. A* **2020**, *8*, 9776-9787.
- [202] Tian Wen, M. Liu, S. Chen, Q. Li, Y. Du, T. Zhou, C. Ritchie, J. Zhang, *Small* **2020**, *16*, 1907669.
- [203] D. Yang, S. Zuo, H. Yang, Y. Zhou, X. Wang, *Angew. Chem. Int. Ed.* **2020**, *59*, 18954-18959.
- [204] M.-J. Liu, S.-M. Cao, B.-Q. Feng, B.-X. Dong, Y.-X. Ding, Q.-H. Zheng, Y.-L. Teng, Z.-W. Li, W.-L. Liu, Li-Gang Feng, *Dalton Trans.* **2020**, *49*, 14995-15001.
- [205] W. Gong, W. Chen, G. Li, X. Dong, Y. Song, W. Wei, Y. Sun, *ChemSusChem* **2020**, *13*, 4035-4040.
- [206] E.-X. Chen, J. Yang, M. Qiu, X. Wang, Y.-F. Zhang, Y.-J. Guo, S.-L. Huang, Y.-Y. Sun, J. Zhang, Y. Hou, Q. Lin, *ACS Appl. Mater. Interfaces* **2020**, *12*, 52588-52594.
- [207] Y. Zhou, L. Zheng, D. Yang, H. Yang, Q. Lu, Q. Zhang, L. Gu, X. Wang, *Small Methods* **2021**, *5*, 2000991.
- [208] Q. Huan, Q. Niu, N.-N. Ma, L.-Z. Dong, S.-L. Li, D.-S. Li, Y.-P. Cai, Y. -Q. Lan, *Chem. Commun.* **2020**, *56*, 14817-14820.
- [209] D. Nam, O. Shekhah, G. Lee, A. Mallick, H. Jiang, F. Li, B. Chen, J. Wicks, M. Eddaoudi, E. H. Sargent, *J. Am. Chem. Soc.* **2020**, *142*, 21513-21521.
- [210] J.-D. Yi, R. Xie, Z.-L. Xie, G.-L. Chai, T.-F. Liu, R.-P. Chen, Y.-B. Huang, R. Cao, *Angew. Chem., Int. Ed.* **2020**, *59*, 23641-23648.
- [211] Y. Guo, Y. Wang, Y. Shen, Z. Cai, Z. Li, J. Liu, J. Chen, C. Xiao, H. Liu, W. Lin, C. Wang, *J. Am. Chem. Soc.* **2020**, *142*, 21493-21501.
- [212] Z. Meng, J. Luo, W. Li, K. A Mirica, *J. Am. Chem. Soc.* **2020**, *142*, 21656-21669.
- [213] X.-D. Zhang, L.-R. Huang, J.-X. Wu, Z.-Y. Gu, *Chem. Commun.* **2021**, *57*, 5191-5194.
- [214] L. Zhang, X.-X. Li, Z.-L. Lang, Y. Liu, J. Liu, L. Yuan, W.-Y. Lu, Y.-S. Xia, L.-Z. Dong, D.-Q. Yuan, Y.-Q. Lan, *J. Am. Chem. Soc.* **2021**, *143*, 3808-3816.
- [215] S. Mukhopadhyay, R. Shimoni, I. Liberman, R. Ifraemov, I. Rozenberg, I. Hod, *Angew. Chem. Int. Ed.* **2021**, *60*, 13423-13429.
- [216] J. Liu, D. Yang, Y. Zhou, G. Zhang, G. Xing, Y. Liu, Y. Ma, O. Terasaki, S. Yang, L. Chen, *Angew. Chem. Int. Ed.* **2021**, *60*, 14473-14479.
- [217] X.-F. Qiu, H.-L. Zhu, J.-R. Huang, P.-Q. Liao, X.-M. Chen, *J. Am. Chem. Soc.* **2021**, *143*, 7242-7246.
- [218] Y. Liu, S. Li, L. Dai, J. Li, J. Lv, Z. Zhu, A. Yin, P. Li, B. Wang, *Angew. Chem. Int. Ed.* **2021**, *60*, 16409-16415.
- [219] P. Shao, W. Zhou, Q.-L. Hong, L. Yi, L. Zheng, W. Wang, H.-X. Zhang, H. Zhang, J. Zhang, *Angew. Chem. Int. Ed.* **2021**, *60*, 16687-16692.
- [220] J.-D. Yi, D.-H. Si, R. Xie, Q. Yin, M.-D. Zhang, Q. Wu, G.-L. Chai, Y.-B. Huang, R. Cao, *Angew. Chem. Int. Ed.* **2021**, *60*, 17108-17114.
- [221] M.-L. Sun, Y.-R. Wang, W.-W. He, R.-L. Zhong, Q.-Z. Liu, S. Xu, J.-M. Xu, X.-L. Han, X. Ge, S.-L. Li, Y.-Q. Lan, A. M Al-Enizi, A. Nafady, S. Ma, *Small* **2021**, *17*, 2100762.

- [222] Y. Zhou, L. Zheng, D. Yang, H. Yang, X. Wang, *Adv. Mater.* **2021**, *33*, 2101886.
- [223] Z.-H. Zhu, B.-H. Zhao, S.-L. Hou, X.-L. Jiang, Z.-L. Liang, B. Zhang, B. Zhao, *Angew. Chem. Int. Ed.* **2021**, *60*, 23394-23404.
- [224] Y. Zhou, S. Liu, Y. Gu, G.-H. Wen, J. Ma, J.-L. Zuo, M. Ding, *J. Am. Chem. Soc.* **2021**, *143*, 14071-14076.
- [225] Z.-H. Zhao, K. Zheng, N.-Y. Huang, H.-L. Zhu, J.-R. Huang, P.-Q. Liao, X.-M. Chen, *Chem. Commun.* **2021**, *57*, 12764-12767.
- [226] S. Chen, W.-H. Li, W. Jiang, J. Yang, J. Zhu, L. Wang, H. Ou, Z. Zhuang, M. Chen, X. Sun, D. Wang, Y. Li, *Angew. Chem. Int. Ed.* **2022**, e202114450.
- [227] S. Frank, E. S. Grape, E. D. Bøjesen, R. Larsen, P. Lamagni, J. Catalano, A. K. Inge, N. Lock, *J. Mater. Chem. A* **2021**, *9*, 26298-26310.
- [228] D. Yang, S. Zuo, H. Yang, Y. Zhou, Q. Lu, X. Wang, *Adv. Mater.* **2021**, *34*, 2107293.
- [229] Z. Liang, H.-Y. Wang, H. Zheng, W. Zhang, R. Cao, *Chem. Soc. Rev.* **2021**, *50*, 2540-2581.
- [230] L. Sun, M. G. Campbell, M. Dincă, *Angew. Chem. Int. Ed.* **2016**, *55*, 3566-3579.
- [231] M. Yu, R. Dong, X. Feng, *J. Am. Chem. Soc.* **2020**, *142*, 12903-12915.
- [232] F. Leng, H. Liu, M. Ding, Q.-P. Lin, H.-L. Jiang, *ACS Catal.* **2018**, *8*, 4583-4590.
- [233] C. F. Wen, M. Zhou, P. F. Liu, Y. Liu, X. Wu, F. Mao, S. Dai, B. Xu, X. L. Wang, Z. Jiang, P. Hu, S. Yang, H. F. Wang, H. G. Yang, *Angew. Chem. Int. Ed.* **2022**, *61*, e202111700.
- [234] S. Hasegawa, S. Horike, R. Matsuda, S. Furukawa, K. Mochizuki, Y. Kinoshita, S. Kitagawa, *J. Am. Chem. Soc.* **2007**, *129*, 2607-2614.
- [235] X. Ma, H. Liu, W. Yang, G. Mao, L. Zheng, H.-L. Jiang, *J. Am. Chem. Soc.* **2021**, *143*, 12220-12229.
- [236] K. P. Kuhl, E. R. Cave, D. N. Abram, T. F. Jaramillo, *Energy Environ. Sci.* **2012**, *5*, 7050-7059.
- [237] D. Feng, K. Wang, J. Su, T.-F. Liu, J. Park, Z. Wei, M. Bosch, A. Yakovenko, X. Zou, H.-C. Zhou, *Angew. Chem. Int. Ed.* **2015**, *54*, 149-154.
- [238] D. Feng, Z.-Y. Gu, J.-R. Li, H.-L. Jiang, Z. Wei, H.-C. Zhou, *Angew. Chem. Int. Ed.* **2012**, *51*, 10307-10310.
- [239] A. Fateeva, P. A. Chater, C. P. Ireland, A. A. Tahir, Y. Z. Khimyak, P. V. Wiper, J. R. Darwent, M. J. Rosseinsky, *Angew. Chem. Int. Ed.* **2012**, *51*, 7440-7444.
- [240] Z. Wu, Q. Zhuo, T. Sun, Z. Wang, *J. Appl. Polym. Sci.* **2015**, *132*, 41409.
- [241] C. Chen, B. Zhang, J. Zhong, Z. Cheng, *J. Mater. Chem. A* **2017**, *5*, 21955-21964.
- [242] S. Chatterjee, C. Griego, J. L. Hart, Y. Li, M. L. Taheri, J. Keith, J. D. Snyder, *ACS Catal.* **2019**, *9*, 5290-5301.
- [243] Y. Zhao, L. Zheng, D. Jiang, W. Xia, X. Xu, Y. Yamauchi, J. Ge, J. Tang, *Small* **2021**, *17*, 2006590.
- [244] O. M. Yaghi, Reticular Chemistry in All Dimensions. *ACS Cent. Sci.* **2019**, *5*, 1295-1300.
- [245] Y. Ding, Y.-P. Chen, X. Zhang, L. Chen, Z. Dong, H.-L. Jiang, H. Xu, H.-C. Zhou, *J. Am. Chem. Soc.* **2017**, *139*, 9136-9139.
- [246] M. Zhao, Y. Wang, Q. Ma, Y. Huang, X. Zhang, J. Ping, Z. Zhang, Q. Lu, Y. Yu, H. Xu, Y. Zhao, H. Zhang, *Adv. Mater.* **2015**, *27*, 7372-7378.
- [247] T. Kambe, R. Sakamoto, K. Hoshiko, K. Takada, M. Miyachi, J.-H. Ryu, S. Sasaki, J. Kim, K. Nakazato, M. Takata, H. Nishihara, *J. Am. Chem. Soc.* **2013**, *135*, 2462-2465.
- [248] L. Zhuang, L. Ge, H. Liu, Z. Jiang, Y. Jia, Z. Li, D. Yang, R. K. Hocking, M. Li, L. Zhang, X. Wang, X. Yao, Z. Zhu, *Angew. Chem., Int. Ed.* **2019**, *58*, 13565-13572.
- [249] Y. Zhao, N. Kornienko, Z. Liu, C. Zhu, S. Asahina, T.-R. Kuo, W. Bao, C. Xie, A. Hexemer, O. Terasaki, P. Yang, O. M. Yaghi, *J. Am. Chem. Soc.* **2015**, *137*, 2199-2202.

- [250] S. S. Y. Chui, S. M.-F. Lo, J. P. H. Charmant, A. G. Orpen, I. D. Williams, *Science* **1999**, 283, 1148-1150.
- [251] K. Tan, N. Nijem, P. Canepa, Q. Gong, J. Li, T. Thonhauser, Y. J. Chabal, *Chem. Mater.* **2012**, 24, 3153-3167.
- [252] S. Zhao, Y. Wang, J. Dong, C.-T. He, H. Yin, P. An, K. Zhao, X. Zhang, C. Gao, L. Zhang, J. Lv, J. Wang, J. Zhang, A. M. Khattak, N. A. Khan, Z. Wei, J. Zhang, S. Liu, H. Zhao, Z. Tang, *Nat. Energy* **2016**, 1, 16184.
- [253] Y. Bai, Y. Dou, L. H. Xie, W. Rutledge, J. R. Li, H. C. Zhou, *Chem. Soc. Rev.* **2016**, 45, 2327-2367.
- [254] S. Leubner, H. Zhao, N. V. Velthoven, M. Henrion, H. Reinsch, D. E. De Vos, U. Kolb, N. Stock, *Angew. Chem. Int. Ed.* **2019**, 58, 10995-11000.
- [255] M. J. Cliffe, E. Castillo-Martinez, Y. Wu, J. Lee, A. C. Forse, F. C. N. Firth, P. Z. Moghadam, D. Fairen-Jimenez, M. W. Gaultois, J. A. Hill, O. V. Magdysyuk, B. Slater, A. L. Goodwin, C. P. Grey, *J. Am. Chem. Soc.* **2017**, 139, 5397-5404.
- [256] A. Cadiou, L. S. Xie, N. Kolobov, A. Shkurenko, M. Qureshi, M. R. Tchalala, S. S. Park, A. Bavykina, M. Eddaoudi, M. Dincă, C. H. Hendon, J. Gascon, *Chem. Mater.* **2020**, 32, 97-104.
- [257] X. Hu, P. Chen, C. Zhang, Z. Wang, C. Wang, *Chem. Commun.* **2019**, 55, 9657-9660.
- [258] N. Panagiotou, I. Liatsou, A. Pournara, G. K. Angeli, R. M. Giappa, E. Tylianakis, M. J. Manos, G. E. Froudakis, P. N. Trikalitis, I. Pashalidis, A. J. Tasiopoulos, *J. Mater. Chem. A* **2020**, 8, 1849-1857.
- [259] T. He, B. Ni, S. Zhang, Y. Gong, H. Wang, L. Gu, J. Zhuang, W. Hu, X. Wang, *Small* **2018**, 14, 1703929.
- [260] J. Ma, A. G. Wong-Foy, A. J. Matzger, *Inorg. Chem.* **2015**, 54, 4591-4593.
- [261] L. Cao, Z. Lin, F. Peng, W. Wang, R. Huang, C. Wang, J. Yan, J. Liang, Z. Zhang, T. Zhang, L. Long, J. Sun, W. Lin, *Angew. Chem. Int. Ed.* **2016**, 55, 4962-4966.
- [262] L. Cao, Z. Lin, W. Shi, Z. Wang, C. Zhang, X. Hu, C. Wang, W. Lin, *J. Am. Chem. Soc.* **2017**, 139, 7020-7029.
- [263] G. Lan, K. Ni, R. Xu, K. Lu, Z. Lin, C. Chan, W. Lin, *Angew. Chem. Int. Ed.* **2017**, 56, 12102-12106.
- [264] X.-N. Zou, D. Zhang, T.-X. Luan, Q. Li, L. Li, P.-Z. Li, Y. Zhao, *ACS Appl. Mater. Interfaces* **2021**, 13, 20137-20144.
- [265] R. Wang, Z. Wang, Y. Xu, F. Dai, L. Zhang, D. Sun, *Inorg. Chem.* **2014**, 53, 7086-7088.
- [266] G. C. Shearer, S. Chavan, J. Ethiraj, J. G. Vitillo, S. Svelle, U. Olsbye, C. Lamberti, S. Bordiga, K. P. Lillerud, *Chem. Mater.* **2014**, 26, 4068-4071.
- [267] Z. Kang, Y. Peng, Y. Qian, D. Yuan, M. A. Addicoat, T. Heine, Z. Hu, L. Tee, Z. Guo, D. Zhao, *Chem. Mater.* **2016**, 28, 1277-1285.
- [268] Z. R. Tao, J. X. Wu, Y. J. Zhao, M. Xu, W. Q. Tang, Q. H. Zhang, L. Gu, D. H. Liu, Z. Y. Gu, *Nat. Commun.* **2019**, 10, 2911.
- [269] Y. Li, K. Wang, W. Zhou, Y. Li, R. Vila, W. Huang, H. Wang, G. Chen, G.-H. Wu, Y. Tsao, H. Wang, R. Sinclair, W. Chiu, Y. Cui, *Matter* **2019**, 1, 428.
- [270] Y. Song, Y. Pi, X. Feng, K. Ni, Z. Xu, J. S. Chen, Z. Li, W. Lin, *J. Am. Chem. Soc.* **2020**, 142, 6866-6871.
- [271] F. Drache, V. Bon, I. Senkowska, C. Marschelke, A. Synytska, S. Kaskel, *Inorg. Chem.* **2016**, 55, 7206-7213.
- [272] Y. Zhao, N. Kornienko, Z. Liu, C. Zhu, S. Asahina, T.-R. Kuo, W. Bao, C. Xie, A. Hexemer, O. Terasaki, P. Yang, O. M. Yaghi, *J. Am. Chem. Soc.* **2015**, 137, 2199-2202.
- [273] A. J. Göttle, M. T. M. Koper, *J. Am. Chem. Soc.* **2018**, 140, 4826-4834.
- [274] Q. Zhang, M. Jian, P. Zhao, C. Hu, J. Qu, X. Li, J. Hu, R. Liu, X. Zhang, *Nanoscale* **2020**, 12, 6012-176

- 6019.
- [275] Q. Wu, C. Zhang, K. Sun, H.-L. Jiang, *Acta Chim. Sinica* **2020**, *78*, 688-694.
- [276] F. Luo, Y.-X. Che, J.-m. Zheng, *Cryst. Growth Des.* **2009**, *9*, 1066-1071.
- [277] G. C. Shearer, S. Chavan, S. Bordiga, S. Svelle, U. Olsbye, K. P. Lillerud, *Chem. Mater.* **2016**, *28*, 3749-3761.
- [278] K. Tan, H. Pandey, H. Wang, E. Velasco, K. Wang, H. Zhou, J. Li, T. Thonhauser, *J. Am. Chem. Soc.* **2021**, *143*, 6328-6332.
- [279] K. Manna, P. Ji, Z. Lin, F. X. Greene, A. Urban, N. C. Thacker, W. Lin, *Nat. Commun.* **2016**, *7*, 12610.
- [280] M. L. Ramos, L. L. G. Justino, A. Branco, C. M. G. Duarte, P. E. Abreu, S. M. Fonseca, H. D. Burrows, *Dalton Trans.* **2011**, *40*, 11732-11741.
- [281] C. Xu, Y. Pan, G. Wan, H. Liu, L. Wang, H. Zhou, S.-H. Yu, H.-L. Jiang, *J. Am. Chem. Soc.* **2019**, *141*, 19110-19117.
- [282] Q. Gong, P. Ding, M. Xu, X. Zhu, M. Wang, J. Deng, Q. Ma, N. Han, Y. Zhu, J. Lu, *Nat. Commun.* **2019**, *10*, 2807.
- [283] X. Gou, R. Li, G. X. Wang, Z. Chen, D. Wexler, *Nanotechnology* **2009**, *20*, 495501.
- [284] Crystallography Open Database, <https://www.crystallography.net/cod/>.
- [285] NIST X-ray Photoelectron Spectroscopy Database, <http://dx.doi.org/10.18434/T4T88K>.
- [286] Y. Yang, L. Xing, W. Ren, D. Zhao, S. Jian, C. Cao, C. Wang, Y. Tian, X. Yu, X. Li, *Ind. Eng. Chem. Res.* **2019**, *58*, 22006-22014.
- [287] J. H. Cavka, S. Jakobsen, U. Olsbye, N. Guillou, C. Lamberti, S. Bordiga, K. P. Lillerud, *J. Am. Chem. Soc.* **2008**, *130*, 13850-13851.
- [288] W. Ma, S. Xie, X.-G. Zhang, F. Sun, J. Kang, Z. Jiang, Q. Zhang, D.-Y. Wu, Y. Wang, *Nat. Commun.* **2019**, *10*, 892.
- [289] Y. Zhou, P. Yan, J. Jia, S. Zhang, X. Zheng, L. Zhang, B. Zhang, J. Chen, W. Hao, G. Chen, Q. Xu, B. Han, *J. Mater. Chem. A* **2020**, *8*, 13320-13327.
- [290] Z. Wang, A. Bilegsaikhan, R. T. Jerozal, T. A. Pitt, P. J. Milner, *ACS Appl. Mater. Interfaces* **2021**, *13*, 17517-17531.
- [291] A. C. Lazanas, K. Tsirka, A. S. Paipetis, M. I. Prodromidis, *Electrochim. Acta* **2020**, *336*, 135726.
- [292] W. Zhang, S. Yang, M. Jiang, Y. Hu, C. Hu, X. Zhang, Z. Jin, *Nano Lett.* **2021**, *21*, 2650-2657.
- [293] N. Henry, M. Evain, P. Deniard, S. Jobic, O. Mentre, F. Abraham, *J. Solid State Chem.* **2003**, *176*, 127-136.
- [294] J. Sui, H. Liu, S. Hu, K. Sun, G. Wan, H. Zhou, X. Zheng, H.-L. Jiang, *Adv. Mater.* **2021**, *34*, 2109203.



## 10 | Appendix

### 10.1 Lists of chemicals and characterization instructions

**Table 10.1** List of chemical resources.

Chemicals	Purity	Abbr.	Supplier
<b>General Chemicals</b>			
Deionized water	-	DI-H <sub>2</sub> O	In-house made
Double-distilled water	-	DD-H <sub>2</sub> O	
HPLC water	HPLC grade	HPLC-H <sub>2</sub> O	Carl Roth
HPLC Sulfuric acid	98%	H <sub>2</sub> SO <sub>4</sub>	Sigma Aldrich
Perchloric acid	70%	HClO <sub>4</sub>	
Hydrofluoric Acid	40%	HF	
Dimethylformamide	p.a.	DMF	
Deuterated water	99.9 at% D	D <sub>2</sub> O	
Deuterated water (TMSP) <sup>[a]</sup>	99.9 at% D	D <sub>2</sub> O	
Methylsulfonylmethane	98%	DMSO <sub>2</sub>	
Hydrochloric acid	35-37%	HCl	
Sulfuric acid	98%	H <sub>2</sub> SO <sub>4</sub>	
Nitric acid	65%	HNO <sub>3</sub>	
Acetone	p.a.	-	
Ethanol	p.a.	EtOH	
Methanol	p.a.	MeOH	
isopropanol	p.a.	i-PrOH	
Acetonitrile	p.a.	MeCN	
Deuterated dimethyl sulfoxide	99.8 at% D	DMSO-d <sub>6</sub>	Eurisotop
Deuterated chloroform	99.8 at% D	CDCl <sub>3</sub>	
<b>Gas Supply</b>			

Nitrogen	5.0	N <sub>2</sub>	Westfalen AG
Argon	5.0	Ar	
Helium	4.6	He	
Carbon dioxide	4.5	CO <sub>2</sub>	
Standard gas bottles	-	H <sub>2</sub> /CO/N <sub>2</sub> /CO <sub>2</sub>	
<b>Linkers Synthesis</b>			
Anhydrous Aluminum(III) Chloride	p.a.	AlCl <sub>3</sub>	In-house chemical store
Ethyl acetate	p.a.	EA	
Chloroform	p.a.	CHCl <sub>3</sub>	
Toluene	p.a.	-	
Chromium(VI) oxide	p.a.	CrO <sub>3</sub>	
Acetic anhydride	p.a.	Ac <sub>2</sub> O	
Tetrahydrofuran	p.a.	THF	
Pyrrole	99%	-	Sigma Aldrich
Propionic acid	99%	-	
Cyanuric chloride	98%	C <sub>3</sub> N <sub>3</sub> Cl <sub>3</sub>	TCI
Methyl <i>p</i> -formylbenzoate	98%	-	
<b>Catalysts Synthesis</b>			
Acetic acid	99.7%	HOAc	Sigma Aldrich
4,4',4''-s-Triazine-2,4,6-triyl-tribenzoic acid	95%	H <sub>3</sub> TATB	
Hydrogen peroxide	30 wt%	H <sub>2</sub> O <sub>2</sub>	
Triethylamine	99%	-	
2-Aminoterephthalic Acid	99%	ATA	
Bismuth(III) chloride	98%	BiCl <sub>3</sub>	
Aluminum(III) chloride hexahydrate	99%	AlCl <sub>3</sub> ·6H <sub>2</sub> O	
Aluminum(III) nitrate nonahydrate	98%	Al(NO <sub>3</sub> ) <sub>3</sub> ·9H <sub>2</sub> O	
Palladium(II) nitrate hydrate	p.a.	Pd(NO <sub>3</sub> ) <sub>2</sub>	
Silver nitrate	p.a.	AgNO <sub>3</sub>	
Urea	99.5%	-	
Bismuth(III) nitrate pentahydrate	98%	Bi(NO <sub>3</sub> ) <sub>3</sub> ·5H <sub>2</sub> O	

Tin(II) chloride dihydrate	99.99%	$\text{SnCl}_2 \cdot 2\text{H}_2\text{O}$	Alfa Aesar
Antimony(III) chloride	99%	$\text{SbCl}_3$	
Potassium iodide	99.4%	KI	
Zirconium dichloride oxide hydrate	99.9%	$\text{ZrOCl}_2 \cdot 8\text{H}_2\text{O}$	
Indium(III) nitrate hydrate	99.99%	$\text{In}(\text{NO}_3)_3 \cdot x\text{H}_2\text{O}$	
Indium(III) chloride	99.99%	$\text{InCl}_3$	
Zirconium(IV) chloride	98%	$\text{ZrCl}_4$	ACROS
1,4-benzene dicarboxylic acid	98%	BDC	
Tin(IV) chloride pentahydrate	98%	$\text{SnCl}_4 \cdot 5\text{H}_2\text{O}$	
Thioacetamide	99%	TAA	
Copper(II) nitrate trihydrate	p.a.	$\text{Cu}(\text{NO}_3)_2 \cdot 3\text{H}_2\text{O}$	In-house chemical store
<b>Electrocatalysis</b>			
Potassium bicarbonate	p.a.	$\text{KHCO}_3$	Carl Roth
Potassium Chloride	p.a.	KCl	
Potassium formate	$\geq 98\%$	HCOOK	
Potassium hydroxide	p.a.	KOH	
Nafion Perfluorinated resin solution	5 wt%	Nafion	Sigma Aldrich
Acetylene black	99.9%	AB	Alfa Aesar
Polytetrafluoroethylene powder	-	PTFE	Dyneon
Sigracet 39BB	-	-	Ion power
Toray (TGP-H-060)	-	-	FuelCellsEtc
Freudenberg H23C2	-	-	
Hydrophilic ELAT	-	-	
Nafion 117 membrane	-	-	DuPont

[a]  $\text{D}_2\text{O}$  contains 0.05 wt. % 3-(trimethylsilyl)propionic-2,2,3,3-*d*4 acid, sodium salt (TMSP).

**Table 10.2** List of instruments.

<b>Characterizations</b>	<b>Abbr.</b>	<b>Instruments</b>
Inductively Coupled Plasma Atomic Emission Spectroscopy	ICP-AES	Varian Vista-MPX
Powder X-ray Diffraction	PXRD	BrukerD8 Advance
Thermogravimetric analysis	TGA	Setaram Thermogravimetric Analyzer Setsys TG-16/18
Nitrogen Physisorption	-	Quantachrome Autosorb 3b
Nuclear Magnetic Resonance	NMR	Bruker Advance 300
Scanning Electron Microscopy	SEM	TESCAN VEGA3 XM
Field Emission Scanning Electron Microscopy	FE-SEM	Zeiss Supra 40
Atomic Force Microscopy	AFM	Bruker Multi-mode 8 Atomic Force Microscope
High-Performance Liquid Chromatography	HPLC	Agilent 1260 Infinity
Gas Chromatography	GC	Agilent 7890A
X-ray photoelectron spectroscopy	XPS	Kratos Axis Ultra
Transmission Electron Microscopy	TEM	Philips CM-200 FEG TEM
High-Resolution Transmission Electron Microscopy	HR-TEM	JEOL ARM200F TEM
Scanning Transmission Electron microscope	STEM	
Electron Energy Loss Spectroscopy	EELS	

## 10.2 ICP results

**Table 10.3** ICP-AES results of MOL composites.

Catalyst	Loading (wt%) <sup>[a]</sup>
BiO <sub>x</sub> /MOL	Bi: 0.56 ± 0.00
Bi <sub>2</sub> O <sub>3</sub> /MOL	Bi: 2.61 ± 0.03
Bi <sub>2</sub> O <sub>3</sub> /MOL-2.6	
Bi <sub>2</sub> O <sub>3</sub> /MOL (12 h)	
Bi <sub>2</sub> O <sub>3</sub> /MOL(3)	
Bi <sub>2</sub> O <sub>3</sub> /MOL (0.5 h)	Bi: 0.87 ± 0.00
Bi <sub>2</sub> O <sub>3</sub> /MOL 2 h	Bi: 1.45 ± 0.01
Bi <sub>2</sub> O <sub>3</sub> /MOL 5 h	Bi: 1.63 ± 0.02
Bi <sub>2</sub> O <sub>3</sub> /MOL 24 h	Bi: 2.59 ± 0.00
Bi <sub>2</sub> O <sub>3</sub> /UiO	Bi: 2.38 ± 0.01
Bi <sub>2</sub> O <sub>3</sub> /UiO-2.6	Bi: 2.60 ± 0.01
Bi <sub>2</sub> O <sub>3</sub> /AB	Bi: 1.76 ± 0.02
Bi <sub>2</sub> O <sub>3</sub> /AB-2.6	Bi: 2.63 ± 0.01
Bi <sub>2</sub> O <sub>3</sub> /MOL-0.6	Bi: 0.61 ± 0.01
Bi <sub>2</sub> O <sub>3</sub> /MOL-1.4	Bi: 1.45 ± 0.00
Bi <sub>2</sub> O <sub>3</sub> /MOL-3.1	Bi: 3.08 ± 0.01
BiO <sub>x</sub> /MOL(2)	Bi: 4.10 ± 0.00

[Bi <sub>6</sub> O <sub>6</sub> ] <sup>6+</sup> /MOL(4)	Bi: 3.86 ± 0.05
Bi/MOL(5)	Bi: 3.87 ± 0.00
BiO <sub>x</sub> I <sub>y</sub> /MOL(6)	Bi: 2.73 ± 0.02
BiOCl/MOL(7)	Bi: 2.67 ± 0.01
Bi/MOL(8)	Bi: 1.93 ± 0.01
SnO <sub>x</sub> /MOL(2)	Sn: 6.29 ± 0.00
Sn <sup>4+</sup> /MOL(3)	Sn: 7.10 ± 0.00
SnS <sub>2</sub> /MOL(4) <sup>[b]</sup>	Sn: 17.71 ± 0.01
	S: 11.04 ± 0.20
SnO <sub>2</sub> /MOL(5)	Sn: 18.20 ± 0.06
InO <sub>x</sub> /MOL(1)	In: 5.04 ± 0.01
InO <sub>x</sub> /MOL(2)	In: 5.87 ± 0.01
In <sub>2</sub> O <sub>3</sub> /MOL(3)	In: 13.20 ± 0.05
SbO <sub>x</sub> /MOL	Sb: 1.94 ± 0.02
CuI/MOL	Cu: 6.49 ± 0.01
Pd/MOL	Pd: 10.91 ± 0.10

[a] Error margins were determined by repeated ICP measurements. [b] Its atomic ratio of S:Sn is calculated to be 2.31:1.

### 10.3 XPS results

**Table 10.4** Summary of XPS fitting results.<sup>[a]</sup>

Samples	Peaks	Fitting State	B. E. <sup>[b]</sup> (eV)	FWHM <sup>[c]</sup> (eV)	Area %
Bi <sub>2</sub> O <sub>3</sub> /MOL	Bi 4f <sub>7/2</sub>	Bi <sub>2</sub> O <sub>3</sub>	159.1	1.30	76.3%
		Bi(III)O <sub>x</sub>	159.9	1.37	23.7%
BiO <sub>x</sub> /MOL	Bi 4f <sub>7/2</sub>	Bi(III)O <sub>x</sub>	159.6	1.56	100%
Bi <sub>2</sub> O <sub>3</sub> /UiO <sup>[d]</sup>	Bi 4f <sub>7/2</sub>	Bi <sub>2</sub> O <sub>3</sub>	159.3	1.48	61.9%
		Bi(III)O <sub>x</sub>	160.2	1.36	38.1%
Bi <sub>2</sub> O <sub>3</sub> /AB	Bi 4f <sub>7/2</sub>	Bi <sub>2</sub> O <sub>3</sub>	160.0	1.29	100%
Bi <sub>2</sub> O <sub>3</sub> /MOL before test	Bi 4f <sub>7/2</sub>	Bi <sub>2</sub> O <sub>3</sub>	159.2	1.46	76.5%
		Bi(III)O <sub>x</sub>	160.2	1.37	23.5%
	Zr 3d <sub>5/2</sub>	Zr(IV)	182.6	1.88	100%
Bi <sub>2</sub> O <sub>3</sub> /MOL after test	Bi 4f <sub>7/2</sub>	Bi(III)	159.3	1.28	100%
	Zr 3d <sub>5/2</sub>	Zr(IV)	182.6	1.59	100%

[a] The fitting of the XPS spectra were performed by XPSPEAK with a Shirley-type background. The area ratio of Bi 4f<sub>7/2</sub> and Bi 4f<sub>5/2</sub> was fixed to 4:3 during the fitting process. [b] B.E.: Binding Energy. [c] FWHM: the full width at half maximum. [d] Considering the limited detection depth of XPS, the actual proportion of Bi(III)O<sub>x</sub> in Bi<sub>2</sub>O<sub>3</sub>/UiO would be apparently higher than 38.1%. The formation of Bi<sub>2</sub>O<sub>3</sub> nanowires would be subject to steric hindrance in the inner pores.

## 10.4 Summary and comparison of ECR reactions by MOFs

**Table 10.5** Summary of MOFs/MOF composites used in ECR to formate.

Catalyst	Current Density <sup>[a]</sup>		TOF <sup>[c]</sup> (h <sup>-1</sup> )	FE (%)	Potential (V vs. RHE)	Stab. (h)	Ref.
	by area (mA·cm <sup>-2</sup> )	by mass <sup>[b]</sup> (mA·mg <sup>-1</sup> )					
CR-MOF	1.1	1.11	7.4	30	-1.19	2.2	[27]
Cu/NU-1000	0.3	-	-	28	-0.82	0.5	[178]
CAU-17	8.2	8.20	136	41	-0.32	5	[188]
HNTM-Cu <sup>[d]</sup>	2.2	2.18	3520	77	-0.7	-	[196]
In-BDC	12.1	12.1	4500	>80	-0.42 to -0.77	21	[199]
Bi-BTC	10.7	-	-	>80	-0.76 to -1.06	12	[201]
Cu-TCPP(Cu)	1.7	3.40	50	80.9	-0.7	5	[203]
Sn/ZIF-8	20	20.0	14750	74	-1.1	-	[205]
MOF-ns-Cu <sup>[d]</sup>	2.0	3.98	334	83	-0.6	12	[207]
C@In(BCP)	6.9	6.9	158	90.1	-0.84	20	[223]
In-MOF-[NiS <sub>4</sub> ]	36.0	36.0	1174	89.6	-1.3	12	[224]
Su-100	7.2	72	1645	90.0	-0.97	0.5	[227]
Bi <sub>2</sub> O <sub>3</sub> /MOL <sup>[e]</sup>	11.8	59.18	17676	>85	-0.87 to -1.17	22	This work
	329.8	235.6	70360	>85	-0.96 to -1.16	-	
In <sub>2</sub> O <sub>3</sub> /MOL	9.8	48.91	1587	70	-1.07	-	
SnO <sub>2</sub> /MOL	3.4	17.09	416	45	-1.07	-	
BiOCl/MOL	7.6	38.15	11141	>80	-0.87 to -1.17	-	
Bi/MOL	5.5	27.65	11172	>80	-0.87 to -1.07	-	

[a] Partial current density to formate at the potential of the FE<sub>max</sub>. [b] The current responses are normalized by the mass of the catalyst, not mass of active sites. [c] Turnover frequency was calculated by 1/2 HCOO<sup>-</sup> (number of electrons) per metal site, divided by reaction time (h). [d] Light promoted ECR. [e] Activities obtained using the H-type cell and GDE, respectively.

**Table 10.6** Summary and comparison of Metal/MOL composites used in ECR reactions by the H-type cell.

Catalyst	Metal Loading (wt%)	Current Density <sup>[a]</sup>			FE (%)	Potential (V vs. RHE)
		by area (mA·cm <sup>-2</sup> )	by mass <sup>[b]</sup> (mA·mg <sup>-1</sup> )	by mass(M) <sup>[c]</sup> (mA·mg <sub>M</sub> <sup>-1</sup> )		
Bi <sub>2</sub> O <sub>3</sub> /MOL(3)	2.61	10.35	51.75	1983	88.5	-1.07
[Bi <sub>6</sub> O <sub>6</sub> ] <sup>6+</sup> /MOL(4)	3.86	8.3	41.5	1075	77.6	-1.17
Bi/MOL(5)	3.87	8.78	43.9	1134	61	-1.07
BiO <sub>x</sub> I <sub>y</sub> /MOL(6)	2.73	6.62	33.1	1212	79.8	-1.07
BiOCl/MOL(7)	2.67	7.63	38.15	1429	81.1	-1.07
Bi/MOL(8)	1.93	5.27	26.35	1365	82.4	-1.07
SnO <sub>x</sub> /MOL(2)	6.29	2.41	12.05	191.6	9.5	-1.37
Sn <sup>4+</sup> /MOL(3)	7.1	1.1	5.5	77.5	16.9	-1.17
SnS <sub>2</sub> /MOL(4)	17.71	7.6	38	214.6	54.7	-1.17
SnO <sub>2</sub> /MOL(5)	18.2	3.42	17.1	94.0	43.2	-1.17
InO <sub>x</sub> /MOL(1)	5.04	6.1	30.5	605.2	52.8	-1.17
InO <sub>x</sub> /MOL(2)	5.87	1.93	9.65	164.4	17.1	-1.17
In <sub>2</sub> O <sub>3</sub> /MOL(3)	13.2	9.78	48.9	370.4	64.76	-1.17
SbO <sub>x</sub> /MOL	1.94	0.399	1.995	102.8	11.8	-1.27
CuI/MOL	6.49	0.51	2.55	39.3	18.7	-0.87
Pd/MOL <sup>[d]</sup>	10.91	1.42	7.1	65.1	30.2	-1.07

[a] Partial current density to formate at the certain potential. [b] The current responses are normalized by the mass of the catalyst. [c] The current responses are normalized by the mass of the active metals. [d] ECR to CO.

## 10.5 Nomenclature

### 10.5.1 Symbols

**Table 10.7** List of symbols.

m	Meter	K	Kelvins
L	Liter	mol	mole
at%	atomic percent	V	Voltage
wt%	weight percent	A	Ampere
M	mol/L	j	Current density
h	Hour	C	Coulomb
min	Minute	I	Current
s	Second	g	gram
eV	Electron volt	Z	Atomic number
°C	Centigrade		

### 10.5.2 Abbreviations

**Table 10.8** List of abbreviations.

2D	2 Dimensional	BET	Brunauer-Emmett-Teller
AB	Acetylene Black	BTB	benzene-1,3,5-tribenzoate
ABS	Acrylonitrile Butadiene Styrene	BPDC	biphenyl-4,4'-dicarboxylate
ACM	Advanced Catalytic Materials	CC	Current Collector
AEM	Anion Exchange Membrane	CCDC	Cambridge Crystallographic Data Centre
AFM	Atomic Force Microscopy	CCUS	Carbon capture, utilization and storage
ALD	Atomic Layer Deposition	CE	Counter Electrode
ATA	2-Aminoterephthalic Acid	CEM	Cation Exchange Membrane
bcc	body-centred cubic	CIPH	Catalyst:Ionomer Planar Heterojunction
BDC	1,4-benzene dicarboxylic acid	CL	Catalyst Layer
B.E.	Binding Energy	CN	Coordination Number

COD	Crystallography Open Database		Microscopy
CVD	Chemical Vapor Deposition	HSAB	Hard-Soft Acid-Base
CO <sub>2</sub> -EOR	CO <sub>2</sub> Enhanced Oil Recovery	hxl	hexagonal lattice
COF	Covalent Organic Framework	ICP-AES	Inductively Coupled Plasma Atomic Emission Spectroscopy
CO <sub>2</sub> RR	CO <sub>2</sub> reduction reaction	IEA	International Energy Agency
CSD	Cambridge Structural Database	IHP	Inner Helmholtz plane
DLC	Double-Layer Capacitance	<i>kgd</i>	kagome dual
DFT	Density Functional Theory	LDH	Layered Double Hydroxides
ECR	Electrocatalytic CO <sub>2</sub> reduction	LUMO	Lowest Unoccupied Molecular Orbital
ECSA	Electrochemical Surface Area	LSV	Linear Sweep Voltammetry
EDL	Electrochemical double layer	MEA	Membrane Electrode Assembly
EDX	Energy Dispersive X-Ray Analysis	MFC	Mass Flow Controller
EE	Energy Efficiency	MFM	Mass Flow Meter
EELS	Electron Energy Loss Spectroscopy	MOF	Metal-Organic Framework
fcc	face-centred cubic	MOL	Metal-Organic Layer
FE-SEM	Field Emission Scanning Electron Microscopy	MPL	Microporous Layer
FID	Flame Ionization Detector	MWCNT	Multi-Walled Carbon Nanotube
FWHM	full width at half maximum	NC	Nitrogen-doped Carbon
GC	Gas Chromatography	NMR	Nuclear Magnetic Resonance
GDE	Gas Diffusion Electrode	NS	Nanosheet
GDL	Gas Diffusion Layer	NU	Northwest University
GHG	Greenhouse Gas	OD	Oxide-Derived
HKUST	The Hong Kong University of Science and Technology	OER	Oxygen Evolution Reaction
HOF	Hydrogen-Bonded Organic Framework	OHP	Outer Helmholtz plane
HOMO	Highest Occupied Molecular Orbital	OMS	Open Metal Sites
HPLC	High Performance Liquid Chromatography	ORR	Oxygen Reduction Reaction
HR-TEM	High Resolution Transmission Electron	PC	Phthalocyanine

PCET	proton coupled electron transfer	SHE	Standard Hydrogen Electrode
PCN	Porous Coordination Network	sql	square lattice
PCPs	Porous Organic Polymers	STEM	Scanning Transmission Electron microscope
PFSA	Perfluorosulfonic acid	TAA	Thioacetamide
PMOF	Polyoxometalate Metal Organic Framework	TATB	4,4',4''-s-triazine-2,4,6-triyl-tribenzoate
PPF	porphyrin paddlewheel frameworks	TCD	Thermal Conductivity Detector
PTFE	Polytetrafluoroethylene	TEM	Transmission Electron Microscopy
<i>pcu</i>	primitive cubic lattice	TGA	Thermogravimetric Analysis
PVP	Polyvinylpyrrolidone	TMDs	Transition-Metal Dichalcogenides
PXRD	Powder X-ray Diffraction	TMSP	3-(trimethylsilyl)propionic-2,2,3,3- <i>d</i> 4 acid, sodium salt
RCSR	Reticular Chemistry Structure Resource	TOF	Turnover Frequency
RE	Reference Electrode	TRL	Technology Readiness Level
RHE	Reversible Hydrogen Electrode	TTA	Thioacetamide
RID	Refractive Index Detector	UCY	University of Cyprus
rpm	revolutions per minute	UiO	Universitetet i Oslo
SBU	Secondary Building Unit	VASP	Vienna Ab initio Simulation Package
SC-XRD	Single Crystal X-Ray Diffraction	WE	Working Electrode
SDS	Sustainable Development Scenario	XPS	X-ray Photoelectron Spectroscopy
SE	Secondary Electron	ZIF	Zeolitic Imidazolate Framework
SEM	Scanning Electron Microscopy		